Operando spectroscopic studies on reaction and regeneration mechanism of lean deNOx catalysis

Operando 分光法を用いたリーン脱硝触媒の反応機構と触媒再生機構の解明

KUBOTA Hiroe

窪田　博愛

Graduate School of Chemical Sciences and Engineering

Hokkaido University

2023

Contents

Chapter 1
General Introduction

1. General Introduction

1.1 Environmental issues for NOx

The major source of nitrogen oxides (NOx) is the combustion of fossil fuels such as petroleum in the engines of vehicles or coke in the electrical power plants and NOx is present in the atmosphere as NO, NO_2, N_2O and N_2O_3.[1,2] An internal combustion engine or power plant are essential for human life but are also associated with NOx emissions. The treatment of NOx has become indispensable for avoiding the negative impact on both human health and the environment. Every year, the number of vehicles increases, while vehicle emission control regulations are becoming stricter (**Figure 1**). Awareness of environmental issues is increasing globally, with emission controls starting in 1974 and the sustainable development goals (SDGs) being adopted in 2015. The current standards, 'Euro 6' for cars and 'Euro VI' for trucks and buses, unify the separate emission control standards and provide uniform standards for all vehicles, including electric vehicles (EVs). The European Commission published the draft new 'Euro 7/VII' emission standards for cars, which will apply from 2025.[3] A denitrification (deNOx) process through the use of lean deNOx catalysts has become the mainstream solution to remove harmful NOx from the exhaust gas emitted by the combustion.

Selective catalytic reduction of nitrogen oxides (NOx) using NH_3 as the reducing agent (NH_3-SCR) is one of the deNOx technics and commercially utilized to control the pollutant emissions from lean diesel engines[4,5] or stationary sources (thermal power plants and industrial boilers)[6–8] that relies on thermal energy produced by the combustion of fossil fuels. It is widely accepted that NH_3-SCR has been used with ammonia as a reducing reagent to convert harmful NO_x to harmless N_2 and H_2O as the equation (1-1).

$$4NH_3 + 4NO + O_2 \rightarrow 4N_2 + 6H_2O \qquad (1\text{-}1)$$

Vanadium oxide-based catalysts (V_2O_5-WO_3/TiO_2) are typically employed as industrial catalysts in stationary deNO_x systems for power plants and waste treatment plants, whereas Cu-exchanged CHA-type zeolites (Cu-CHA) are utilized in urea-based SCR systems in diesel vehicles.

However, these industrial deNOx catalyst have been put into practical use without a detailed understanding of their function. NOx purification systems for diesel engines are required to provide NOx purification performance over a wide temperature range in response to lower exhaust gas temperatures, hot starts and cold starts, as a result of improved engine efficiency and reduced vehicle weight to improve fuel consumption. The regulations to limit emissions from exhaust gas are much more stringent than ever before, and new catalyst development is attracting attention. The development of reaction mechanisms is expected to provide essential and important guidelines for the development of new catalysts.

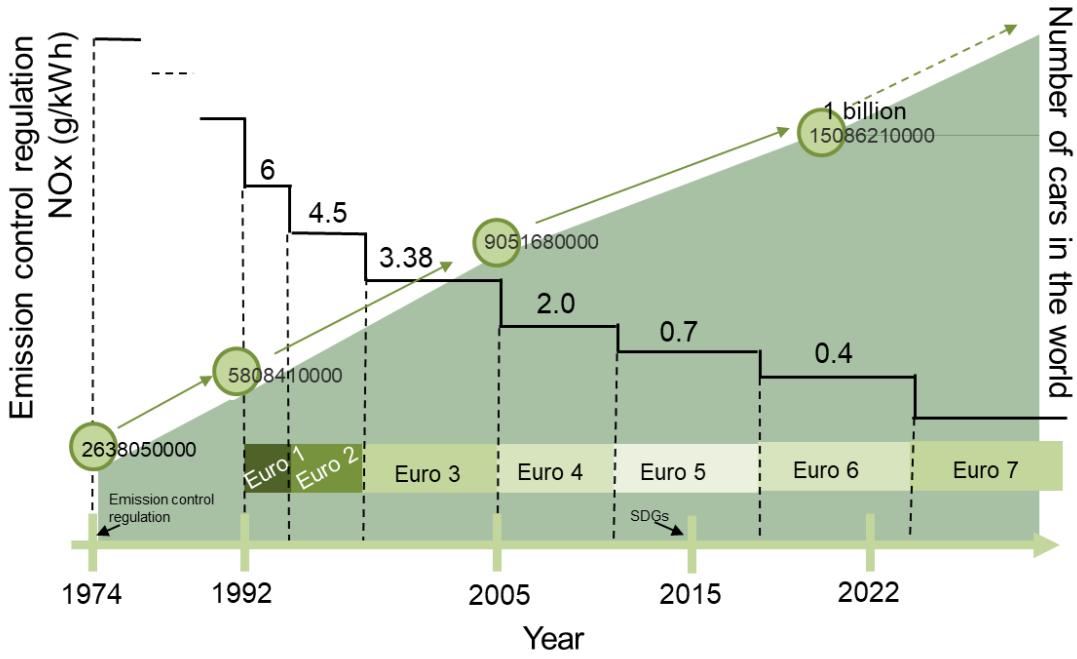

Figure 1 Emission control regulation changes of “Euro 1-7”and Number of cars in the world.

1.2 DeNOx for diesel engines

Diesel engines are widely used in automobiles and industrial machinery due to their excellent combustion efficiency and output characteristics. However, the problem is that diesel fuel is injected directly into the cylinder, resulting in high levels of particulate matter PM and NOx, which are air pollutants, in the exhaust gases. In diesel emission control systems, a diesel oxidation catalyst (DOC) located upstream of the SCR catalyst converts a portion of NO in the exhaust to NO_2, which has an important effect on the efficiency of the NH_3-SCR process. [9]

The first commercial inception of SCR in automobiles began in 2005 and required plenty of urea on-board. Though urea-SCR exhibited high NOx remediation efficiency, it suffered from technical challenges largely due to the airless system causing secondary emission of isocyanic acid. Since then, NH_3-SCR has been considered as a viable alternate to overcome issues from urea usage. It is the famous catalysts because NH_3-SCR system in diesel engines has been installed in SCR converter (**Figure 2**) of heavy-duty vehicle and passenger car.

SSZ-13 zeolite with CHA topology, shows a small-pore framework (maximum ring size of around 3.8 Å at room temperature), which consists of double-6-ring (d6r) and chabazite cages, has many contributions for NH_3-SCR reactions. According to zeolites screening by Research Association of Automotive Internal Combustion Engines (AICE),[10] it was concluded that zeolite including d6r cages, namely CHA and AFX zeolite, [11] has been described to account for the high catalytic performance and hydrothermal durability of Cu-exchanged zeolite catalysts.[12,13]

Fast SCR is known to improve deNOx activity by addiction 50% NO and 50% NO_2 below equation (1-

2).[14]

$2NH_3 + NO + NO_2 \rightarrow 2N_2 + 3H_2O$ (1-2)

It has attention on Bronsted acid site activity and the role of ammonium nitrate, which forms rapidly at low temperatures and with excess NO_2, determining a lower N_2 selectivity of the deNOx process

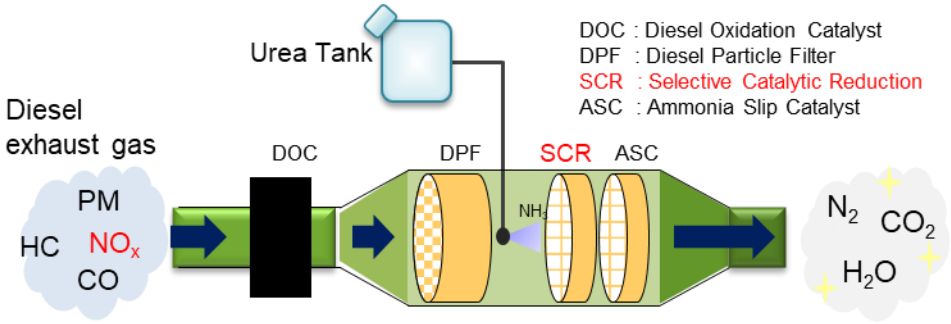

Figure 2 NH_3-SCR system for diesel engine. DOC: hydrocarbons (HC) and CO are oxidized to CO_2. DPF: PM are reduced by filter. SCR: NOx is reduced to N_2 and H_2O. ASC: Part of the excess NH_3 is oxidized to NOx and the final mixture into H_2O and N_2.

1.3 DeNOx for stationary sources

In thermal power stations, fuel is burnt in boilers to generate electricity. The flue gases generated by combustion contain nitrogen oxides (NOx), sulfur oxides (SOx) and fly dust (combustion ash), which are purified by various environmental facilities and discharged into the atmosphere. Exhaust gas from the boiler (**Figure 3**) is discharged from the chimney after (1) decomposing NOx in a denitration unit, (2) exchanging heat with combustion air in an air preheater, (3) collecting and removing dust in an electrostatic precipitator and (4) removing SOx in a desulphurization unit.

Supported vanadium(V) oxide catalysts, such as V_2O_5/TiO_2 and $V_2O_5–WO_3/TiO_2$, have been used successfully in stationary applications. The metal oxides found effective usage for the SCR of NOx from stationary sources.

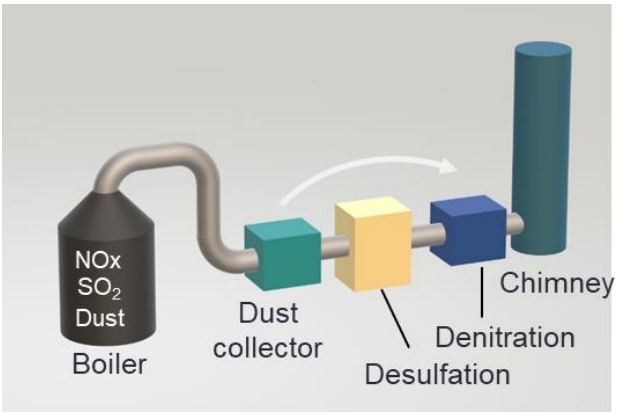

Figure 3 Design route for De-NO_x via NH_3-SCR at generation of thermal power.

1.4 NH_3-SCR study on WO_3-loaded-ceria catalyst

Ceria is an important component of rare-earth catalytic materials due to its excellent redox properties.[15] CeO_2 has been studied extensively due to its excellent oxygen storage capacity (OSC) and redox properties via the shift between Ce^{4+} and Ce^{3+} in oxidizing and reducing conditions. However, pure CeO_2 is known to be poorly thermostable and undergoes rapid sintering at higher temperatures, thereby losing OSC, which would lead to the deactivation of the catalysts. Recently, cerium-based NH_3-SCR catalysts, such as WO_3-loaded-CeO_2 (WO_3/CeO_2) have received significant attention because of high activity for NH_3-SCR. [16]

Currently, several reviews regarding the composition and mechanism of cerium-based catalysts have been reported in the literature. However, there are few studies on the NH_3-SCR mechanism and roll of CeO_2 and WO_3 over WO_3-CeO_2.

1.5 Dispersion and aggregation of single-atom catalysts (SACs)

The term “single atom catalysts (SACs)” has been widely adopted.[17] SACs with isolated metal centers are attracting great research interest because of their maximized metal utilization rates and unique structures.[18] Accordingly, the most effective way to make use of each and every metal atom of supported metal catalysts is to downsize the metal nanostructures to well-defined, atomically distributed metal active centers, which is the ultimate goal of fine dispersion. Recent studies on SACs have demonstrated that depending on the reaction conditions, the isolated metal species can be converted to metal clusters, resulting in an increased or a decreased catalytic activity. [19,20] Previous studies on the anchoring sites of γ-Al_2O_3 suggest that the anchoring sites depended on the type of metal species and that the specific anchoring sites should be determined based on multiple spectroscopic evidence, assuming various candidates for anchoring sites. Then, silver alumina catalyst has been famous for as a promising catalyst for the SCR of NOx by hydrocarbons (HC-SCR),[21] H_2-assisted HC-SCR,[22] and H_2-assisted SCR by NH_3 (H_2−NH_3-SCR).[23] It was concluded that isolated Ag(I) sites were indispensable for achieving the high-performance Ag/Al_2O_3 catalyst for SCR. However, it has been unknown to the mechanism of isolate silver regeneration on alumina surface.

1.6 *In situ/Operando* spectroscopic study

To elucidate the catalytic reaction mechanism, *in situ / operando* spectroscopy technics is powerful tool. Several spectroscopic study can provide time-resolved information, for example, electron state, changing of surface structure and instantaneous production. Specifically, X-ray absorption spectroscopy, UV-visible spectroscopy (UV-vis), and infrared spectroscopy (IR) under gas distribution conditions were performed with mass spectroscopy.

Specifically, changes in the bonding state of the catalyst surface and the presence of adsorbed species are identified by infrared spectroscopy. UV-visible spectroscopy to determine the active point by

observing changes in valence. Transmission microscopy to observe changes in particle size and determine agglomeration and dispersion states. Additional combination with density functional theory (DFT) calculations and *ab initio* thermodynamics has provided the molecular evidence.

1.7 Outline of thesis

This thesis effort on the mechanistic study of NH_3-SCR over 1) small pore Cu-zeolite catalyst, 2) V-based catalyst, 3) H-type zeolite and 4) WO_3-CeO_2 catalyst using *operando* spectroscopies, and metal dispersion mechanistic study over 5) Ag/Al_2O_3 catalyst using *in situ* spectroscopy and electronic microscopy.

Chapter 2 presents the reduction/oxidation half-cycles of NH_3-SCR reaction at 200 ˚C were investigated using in situ and operando spectroscopies to propose a general mechanism for four different catalysts (TiO_2-supported and bulk vanadium oxides and Cu-AFX and Cu-CHA zeolites). The reduction half-cycle is initiated by the reaction of NH_3 on Lewis acid sites [V(V) or Cu(II); L-NH_3] and NO, followed by the gradual reaction of NH_3 on Brønsted acid sites (B-NH_3) and NO; this results in the formation of V(IV) or Cu(I) and protons (H^+) on the surface, along with N_2 and H_2O. The UV−vis measurements for the reduction half-cycle indicate that N_2 is continuously generated until the surface V(V) or Cu(II) species is depleted. The subsequent reoxidation of the reduced catalysts under O_2 leads to the regeneration of V(V) or Cu(II) and the reaction of surface H^+, yielding H_2O (oxidation half-cycle). The higher consumption rates of B-NH_3 and L-NH_3 under NO + O_2 than those under NO, which has been previously reported in the literature, were explained based on the continuous reduction/oxidation of V(V)/V(IV) or Cu(II)/Cu(I) where the regenerated V(V) or Cu(II) site is reused in the subsequent (second) reduction half-cycle. Namely, upon the recovery of V(V) or Cu(II) via reoxidation, the leftover B-NH_3 species react with the supplied NO to yield N_2; this suggests that B-NH_3 is not a spectator but a reservoir of NH_3 to participate in the second reduction half-cycle possibly via the migration of NH_3 or HONO species. These results provide comprehensive evidence of the general mechanism of NH_3-SCR, which was found to be applicable to both V and Cu catalysts.

Chapter 3 presents the *operando* IR spectroscopy and DFT calculations were combined to investigate NH_3-SCR reaction over H-AFX zeolites. The steady-state kinetics shows that SCR reactions involving NO_2 proceed much more rapidly than those of NO. Data from in situ IR combined with online mass spectrometry under transient conditions demonstrate that Brønsted acid sites (BASs) promote the reaction of NO_2 with NH_3 to form N_2, H_2O, and NH_4NO_3 at low temperatures (50−150 ˚C). In combination with DFT results, these data suggest that NO promotes the reduction of NH_4NO_3 to NH_4NO_2, which then decomposes into N_2 and H_2O. Therefore, the accumulation of NH_4NO_3 in the zeolite is inhibited by NO. Furthermore, when NO is absent, NH_4NO_3 decomposition into N_2O and H_2O occurs only at high temperatures (>200 ˚C). A comparison of H-AFX and Cu-AFX implies that Cu sites are not active for the

reduction of NO_2 by NH_3 and that BASs are responsible for the NH_3-SCR reactions involving NO_2.

Chapter 4 presents the *operando* spectroscopies (*in situ* Ce and W L3-edge XANES, UV-vis, and IR spectroscopies, combined with online analysis of gas-phase products) were carried out to elucidate reduction/oxidation half cycles in NH_3–SCR over WO_3-loaded CeO_2. The Ce^{4+} species was reduced by NO + NH_3 to yield N_2 and Ce^{3+} species (reduction half cycle), which was then reoxidized by O_2 (oxidation half cycle). The oxidation state of the W^{6+} species remained unchanged under redox conditions. IR and theoretical results indicated that the reduction half cycle started with the reaction of W^{6+}–OH and adjacent Ce^{4+}–O with NO to afford Ce^{3+} species and gaseous HONO, which was converted to NO^+ species on the catalyst. The NO^+ species then reacted with NH_3 to generate N_2.

Chapter 5 presents the Reversible structural transformation between atomic Ag(I) and large Ag metal nanoparticles (NPs) on γ-Al_2O_3-supported Ag (Ag/Al_2O_3) catalysts for H_2-assisted NO_x selective catalytic reduction by NH_3 was monitored by *in situ* X-ray absorption spectroscopy, UV-vis spectroscopy, IR spectroscopy, and *ex situ* microscopy. Fresh Ag/Al_2O_3 was deactivated by H_2 reduction at 800 ˚C owing to sintering of the atomic Ag(I) species to form large (10−52 nm) Ag metal NPs. Reoxidation of the sintered catalyst using NO + O_2 at 400 ˚C resulted in the redispersion of Ag metal NPs to the atomic Ag(I) species, leading to the recovery of the catalytic activity. Sintering and dispersion occurred reversibly for 10 repetitive treatments of H_2 ↔ NO + O_2 at 600 ˚C. The structure of the anchoring site and the mechanism of oxidative dispersion were elucidated by kinetic studies, in situ spectroscopy, ^{27}Al nuclear magnetic resonance spectroscopy, and DFT calculations. The isolated Ag(I) cation was exchanged with H^+ of the HO- m^1-Al_{VI} site adjacent to the strong Lewis acid sites (unsaturated Al_{IV}^{3+}) on γ-Al_2O_3, and, consequently, the anchored Ag(I) species reduced the Lewis acid strength of the adjacent Al_{IV}^{3+} sites. During sintering under H_2, the isolated AgO- m^1-Al_{VI} species aggregated to form Ag metal NPs, regenerating the HO- m^1-Al_{VI} sites on the support. During oxidative dispersion under the NO + O_2 flow, the Ag metal NPs were oxidized to furnish mobile $AgNO_3$ species that moved across the support surface and reacted with the anchoring site, HO- m^1-Al_{VI}, to yield the original AgO- m^1-Al_{VI} species and HNO_3; the latter reacts with the γ-Al_2O_3 surface to yield the nitrate species. This study provides molecular level insights into the deactivation/reactivation of supported metal catalysts under reductive/oxidative conditions.

Chapter 6 presents the Ag(3 wt%)-loaded γ-Al_2O_3 (Ag/Al_2O_3) catalysts were prepared using four types of commercially available alumina powders (CTB, PUR, VGL, and CFF). Based on the support, the activity of these catalysts for the H_2-assisted selective catalytic reduction (SCR) of NO by NH_3 or C_3H_6 decreased in the order: CTB > PUR > VGL > CFF. After sintering treatment (H_2 reduction at 800 ˚C), the particle size of the Ag metal nanoparticles (NPs) changed and was found to be correlated with the catalytic activity (CTB < PUR < VGL < CFF). After the re-oxidation of H_2-reduced Ag/Al_2O_3 at 500 ˚C, the *in situ* IR spectra showed negative bands at 3762 cm^{-1} due to the HO- m^1-Al_{VI} site, where the band

intensity increased in the order: CTB > PUR > VGL > CFF. IR study of pyridine adsorbed on Ag-free γ-Al_2O_3 showed that the number of strong Lewis acid sites (unsaturated Al_{IV}^{3+}) increased in the same order: CTB > PUR > VGL > CFF, and the number of strong Lewis acid sites decreased when Ag was loaded on the supports. *In situ* XANES and UV-vis studies of Ag/Al_2O_3 sintered under NO + O_2 at 400 ˚C showed oxidative redispersion of the Ag metal NPs to regenerate atomic Ag(I) sites. The amount of re-dispersed Ag metal and the initial rates of redispersion estimated from the *in situ* UV-vis results changed in the following order: CTB > PUR > VGL > CFF. These results suggest that the HO- m^1-Al_{VI} site adjacent to the unsaturated Al_{IV}^{3+} site on γ-Al_2O_3 is the anchoring site of the atomic Ag species, and the sintering resistance of Ag/Al_2O_3 increases with the number of HO- m^1-Al_{VI} sites. During H_2-assisted SCR, where both H_2 and NO + O_2 were co-fed to the catalysts, the number of highly dispersed Ag species (active sites) increased with the number of HO- m ^{1}-Al_{VI} sites; hence, NO conversion increased with the number of HO- m^1-Al_{VI} sites on the support. The present results provide molecular-level insights into the design of sintering-resistant Ag/Al_2O_3 catalysts for SCR.

1.7 Conclusion remarks

I have developed mechanic study of deNOx catalysts. Mechanics study of combination with *operando* spectroscopy and DFT calculation provide molecular level insights into the NH_3-SCR reaction mechanism and the deactivation and reactivation of supported metal catalysts under reductive and oxidative conditions. The development of reaction mechanisms is expected to provide essential and important guidelines for the development of new catalysts.

(1) Roy, S.; Hegde, M. S.; Madras, G. Catalysis for NOx Abatement. *Applied Energy*. 2009.

(2) Skalska, K.; Miller, J. S.; Ledakowicz, S. Trends in NOx Abatement: A Review. *Science of the Total Environment*. 2010.

(3) Mulholland, E.; Miller, J.; Bernard, Y.; Lee, K.; Rodríguez, F. The Role of NOx Emission Reductions in Euro 7/VII Vehicle Emission Standards to Reduce Adverse Health Impacts in the EU27 through 2050. *Transportation Engineering* **2022**, *9*.

(4) Beale, A. M.; Gao, F.; Lezcano-Gonzalez, I.; Peden, C. H. F.; Szanyi, J. Recent Advances in Automotive Catalysis for NOx Emission Control by Small-Pore Microporous Materials. *Chemical Society Reviews*. 2015.

(5) Janssens, T. V. W.; Falsig, H.; Lundegaard, L. F.; Vennestrøm, P. N. R.; Rasmussen, S. B.; Moses, P. G.; Giordanino, F.; Borfecchia, E.; Lomachenko, K. A.; Lamberti, C.; Bordiga, S.; Godiksen, A.; Mossin, S.; Beato, P. A Consistent Reaction Scheme for the Selective Catalytic Reduction of Nitrogen Oxides with Ammonia. *ACS Catal* **2015**, *5*.

(6) Wachs, I. E. Catalysis Science of Supported Vanadium Oxide Catalysts. *Dalton Transactions*. 2013.

(7) Koebel, M.; Madia, G.; Raimondi, F.; Wokaun, A. Enhanced Reoxidation of Vanadia by NO2 in the Fast SCR Reaction. *J Catal* **2002**, *209*.

(8) Dumesic, J. A.; Topsøe, N. Y.; Topsøe, H.; Chen, Y.; Slabiak, T. Kinetics of Selective Catalytic Reduction of Nitric Oxide by Ammonia over Vanadia/Titania. *J Catal* **1996**, *163*, 409–417.

(9) Ciardelli, C.; Nova, I.; Tronconi, E.; Chatterjee, D.; Bandl-Konrad, B.; Weibel, M.; Krutzsch, B. Reactivity of NO/NO2-NH3 SCR System for Diesel Exhaust Aftertreatment: Identification of the Reaction Network as a Function of Temperature and NO2 Feed Content. *Appl Catal B* **2007**, *70*.

(10) Priya, S. V.; Ohnishi, T.; Shimada, Y.; Kubota, Y.; Masuda, T.; Nakasaka, Y.; Matsukata, M.; Itabashi, K.; Okubo, T.; Sano, T.; Tsunoji, N.; Yokoi, T.; Ogura, M. A Collective Case Screening of the Zeolites Made in Japan for High Performance NH3-SCR of NOx. *Bull Chem Soc Jpn* **2018**, *91*.

(11) Nakazawa, N.; Inagaki, S.; Kubota, Y. Novel Technique to Synthesize AFX-Type Zeolite Using a Bulky and Rigid Diquaternary Ammonium Cation. *Advanced Porous Materials* **2016**, *4*.

(12) Chokkalingam, A.; Chaikittisilp, W.; Iyoki, K.; Keoh, S. H.; Yanaba, Y.; Yoshikawa, T.; Kusamoto, T.; Okubo, T.; Wakihara, T. Ultrafast Synthesis of AFX-Type Zeolite with Enhanced Activity in the Selective Catalytic Reduction of NOx and Hydrothermal Stability. *RSC Adv* **2019**, *9*.

(13) Shibata, G.; Eijima, W.; Koiwai, R.; Shimizu, K. ichi; Nakasaka, Y.; Kobashi, Y.; Kubota, Y.; Ogura, M.; Kusaka, J. NH3-SCR by Monolithic Cu-ZSM-5 and Cu-AFX Catalysts: Kinetic Modeling and Engine Bench Tests. *Catal Today* **2019**.

(14) Eng, J.; Bartholomew, C. H. Kinetic and Mechanistic Study of NOxReduction by NH3over H-Form Zeolites. *J Catal* **1997**, *171*.

(15) Wu, Z.; Li, M.; Howe, J.; Meyer, H. M.; Overbury, S. H. Probing Defect Sites on CeO2 Nanocrystals with Well-Defined Surface Planes by Raman Spectroscopy and O2 Adsorption.

Langmuir **2010**, *26*.

(16) Liu, K.; Liu, F.; Xie, L.; Shan, W.; He, H. DRIFTS Study of a Ce-W Mixed Oxide Catalyst for the Selective Catalytic Reduction of NOx with NH3. *Catal Sci Technol* **2015**, *5*.

(17) Resasco, J.; Christopher, P. Atomically Dispersed Pt-Group Catalysts: Reactivity, Uniformity, Structural Evolution, and Paths to Increased Functionality. *Journal of Physical Chemistry Letters*. 2020.

(18) Lu, Y.; Zhang, Z.; Lin, F.; Wang, H.; Wang, Y. Single-Atom Automobile Exhaust Catalysts. *ChemNanoMat* **2020**, *6*, 1659–1682.

(19) Lang, R.; Du, X.; Huang, Y.; Jiang, X.; Zhang, Q.; Guo, Y.; Liu, K.; Qiao, B.; Wang, A.; Zhang, T. Single-Atom Catalysts Based on the Metal-Oxide Interaction. *Chemical Reviews*. 2020.

(20) Parkinson, G. S.; Novotny, Z.; Argentero, G.; Schmid, M.; Pavelec, J.; Kosak, R.; Blaha, P.; Diebold, U. Carbon Monoxide-Induced Adatom Sintering in a Pd-Fe3 O 4 Model Catalyst. *Nat Mater* **2013**, *12*.

(21) Shimizu, K.; Shibata, J.; Yoshida, H.; Satsuma, A.; Hattori, T. Silver-Alumina Catalysts for Selective Reduction of NO by Higher Hydrocarbons: Structure of Active Sites and Reaction Mechanism. *Appl Catal B* **2001**, *30*, 151–162.

(22) Shibata, J.; Shimizu, K. I.; Satokawa, S.; Satsuma, A.; Hattori, T. Promotion Effect of Hydrogen on Surface Steps in SCR of NO by Propane over Alumina-Based Silver Catalyst as Examined by Transient FT-IR. *Physical Chemistry Chemical Physics* **2003**, *5*.

(23) Shimizu, K. I.; Satsuma, A. Reaction Mechanism of H2-Promoted Selective Catalytic Reduction of NO with NH3 over Ag/Al2O3. *Journal of Physical Chemistry C* **2007**, *111*.

Chapter 2
Analogous Mechanistic Features of NH_3-SCR over Vanadium Oxide and Copper Zeolite Catalysts

2.1. Introduction

Selective catalytic reduction of nitrogen oxides (NO_x) using NH_3 as the reducing agent (NH_3–SCR) is commercially utilized to control the NOx emissions from exhausts in the presence of O_2.[1–4] Vanadium oxide-based catalysts (V_2O_5-WO_3/TiO_2) are typically employed as industrial catalysts in stationary DeNOx systems for coal-fired power plants and waste treatment plants, whereas Cu-exchanged zeolites, such as Cu-CHA, are utilized in urea-based SCR systems in diesel vehicles.[5–15] Inomata et al. recently reported that unsupported bulk vanadium oxides[16] and tungsten-doped vanadium oxides[17] exhibit higher NO-conversion capabilities than those of conventional TiO_2-supported vanadium catalysts for NH_3–SCR at low temperatures (<150 °C). Although these catalysts are considered the state-of-the-art, catalytic activities especially at low temperatures must be improved. It is therefore crucial to elucidate catalytic mechanisms, establish structure–activity relationships, and develop highly-efficient catalysts based on precise catalyst-design guidelines.[18–24]

V- and Cu-based catalysts have been thoroughly investigated for NH_3–SCR at the molecular level over the past four decades.[25–37] Although the mechanism of NH_3–SCR with these catalysts has been separately discussed, a detailed literature survey suggests mechanistic similarities between V[38–47] and Cu[48–56] catalysts as well as common unresolved issues regarding the NH_3–SCR mechanism. The common features of the NH_3–SCR mechanisms featuring V and Cu catalysts are depicted in **Figure 1A,B**. The catalytic cycles of both V and Cu catalysts are based on the redox cycles of the metal cation species [V(V)↔V(IV) and Cu(II)↔Cu(I)]. First, V(V) or Cu(II) species is reduced to V(IV) or Cu(I) species under NH_3 + NO; this is accompanied by the formation of N_2 and H_2O, presumably via NH_2NO[41,49,57–59] or NH_4NO_2[60–63] intermediate. For both V[64–69] and Cu catalysts,[70–73] there has been a long debate on the behavior of the reactive NH_3 adspecies in this step (the so-called reduction half-cycle); it is unclear whether NH_3 adsorbed on Brønsted acid sites (B-NH_3) or Lewis acid sites (L-NH_3) acts as an intermediate in NH_3–SCR. This is generally examined *via in situ* infrared (IR) spectroscopy during NH_3–SCR or after the adsorption of NH_3 on V- and Cu-based catalysts. *Operando* spectroscopic results have assisted in clarifying that L-NH_3, or in other words, NH_3 adsorbed on an oxidized metal cation, V(V) or Cu(II), is directly involved in this step.[41,68,74–76] Computational investigations of the reduction half-cycle of V[58,69] and Cu[49,77,78] catalysts have shown a common transition state in which a gas-phase (or weakly adsorbed) NO molecule directly reacts with L-NH_3 and the adjacent oxidized metal cation species, V(V) or Cu(II), to yield N_2, H_2O, a reduced cation [V(IV) or Cu(I)], and a proton on the catalyst. The formation of protons (H^+) through the reduction half-cycle has been evidenced by an increase in the number of Brønsted acid sites,[30,66] which further interact with NH_3 to form NH_4^+ on the V[69,79] and Cu[80–82] catalyst surfaces. There is an ongoing debate regarding the oxidation half-cycle; one of the widely accepted pathways involves the oxidation of the reduced cation [V(IV) or Cu(I)] by O_2 to produce oxidized cations [V(V) or Cu(II)] and H_2O.[53,61,74,83]

Although B-NH_3 does not seem to directly participate in the reduction half-cycle, B-NH_3 is likely not a spectator but a reservoir of NH_3 that migrates to metal cation sites to participate in the reduction half-cycle. However, the active role of B-NH_3 as a reservoir of NH_3 is still speculative because of the

lack of solid experimental evidence. The transient reaction of B-NH_3 and L-NH_3 under NO or NO + O_2 has been frequently utilized to investigate the reduction half-cycle. The higher reactivity of B-NH_3 under NO + O_2 than that under NO has been typically observed for V and Cu catalysts. However, the origin of the beneficial effect of O_2 on the transient reactivity of B-NH_3 remains unclear. The relatively high reactivity of B-NH_3 under NO + O_2 has been invoked in several studies to suggest the involvement of B-NH_3 on V-loaded TiO_2 in the primary catalytic cycle of NH_3–SCR.[30,65,66] Song et al. recently reported a quantitative comparison of the consumption rates of B-NH_3 and L-NH_3 on 5 wt.% V-loaded TiO_2 under NO and NO + O_2.[84] Both L-NH_3 and B-NH_3 predictably reacted faster under NO + O_2 than under NO. Interestingly, the apparent consumption rates of B-NH_3 and L-NH_3 were similar under NO (and NO + O_2), in contrast to widely reported data. Considering that the diffusion of NH_4^+ on the surface of V_2O_5 is characterized by considerably low diffusion barriers (<0.17 eV),[40] this result can be explained by the rapid migration of B-NH_3 to a V(V) site and the subsequent reaction of NH_3 on the V(V) site (L-NH_3) with NO; this indicates the active role of B-NH_3 as a mobile NH_3 reservoir.[85] Notably, Song et al. also reported that the consumption rates of B-NH_3 (and L-NH_3) in the intermediate stage of their transient reaction under NO + O_2 were nearly constant, with the rate being close to the reduction rate of NO under steady-state NH_3–SCR over the same catalyst.[84] Considering that O_2 can regenerate V(V) sites from the V(IV) species that were previously reduced by NO + NH_3, experiments on the transient reaction of adsorbed NH_3 under a flow of NO + O_2 are presumably unsuitable for analyzing the reduction half-cycle.

Summarizing these backgrounds, motivated by the previous comprehensive work by Janssens et al.,[77] we aim to propose a comprehensive mechanism of SCR. *In situ*/*operando* IR, UV–vis, and X-ray absorption spectroscopy (XAS) experiments were performed in the present study on the V(V)↔V(IV) and Cu(II)↔ Cu(I) redox cycles (reduction/oxidation half-cycles) with V- and Cu-based NH_3–SCR catalysts under transient reaction conditions. To expand the generality of the NH_3–SCR mechanism for various V- and Cu-based catalysts, two types of V-based catalysts (TiO_2-supported V_2O_5 and W-doped bulk vanadium oxide[17]) and two types of Cu zeolites (Cu-AFX[86] and Cu-CHA[87]) were investigated using the *in situ*/*operando* IR and UV–vis systems under similar conditions. The results provide comprehensive evidence for a general mechanism of NH_3–SCR that is common to V and Cu catalysts. Under transient conditions, B-NH_3 was confirmed to be a reservoir of NH_3 that migrates to the metal cation sites and participates in the (second) reduction half-cycle (**Figure 1C**). Although there is another possible mechanism where a mobile HONO intermediate, formed by the reaction with Cu(II)-OH (V(V)-OH) and NO, reacts with B-NH_3 to yield N_2 and H_2O via NH_4NO_2 intermediate,[60–63] we herein mainly discuss based on a more widely-believed mechanism given in **Figure 1A,B**.

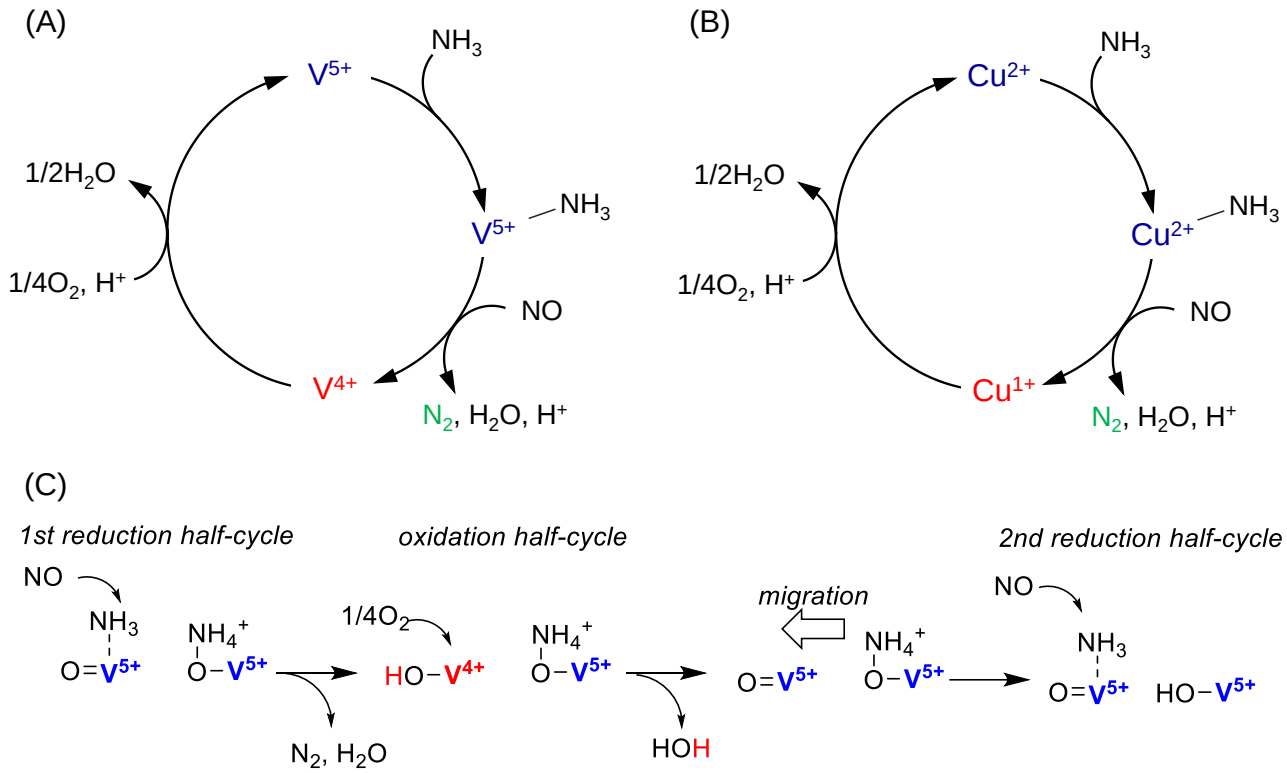

Figure 1. Typical steady-state mechanisms of standard selective catalytic reduction (SCR) with (A) vanadium oxide and (B) Cu zeolite catalysts based on previously reported results and those obtained in this study. (C) The consecutive transient reactions analyzed in this study exemplified for V-based catalysts: first reduction half-cycle, oxidation half-cycle, migration of NH_4^+, and its reaction with NO at a recovered V(V) site (second reduction half-cycle). Certain ligands and coefficients have been omitted for simplification.

2.2. Materials and methods

2.2.1 Preparation of the catalysts

A 5 wt.% V-loaded TiO_2 catalyst (V/TiO_2) was prepared by impregnating TiO_2 (P25, Evonik) with an aqueous solution of NH_4VO_3 and 3 equiv. of oxalic acid, followed by evaporation to dryness, further drying at 100 °C (12 h), and calcination at 500 °C for 4 h. Surface density of V atoms, estimated using surface area of V/TiO_2 (45 m^2/g) and V loading, is 13 V nm^{-2}. This value is larger than the monolayer coverage of V species (8 V atoms/nm),[43] suggesting that the TiO_2 surface is fully covered by V species. The 3.5 mol.% W-doped V_2O_5 catalyst ($W\text{-}V_2O_5$) was prepared using a previously reported protocol.[17] Briefly, an aqueous solution of NH_4VO_3, oxalic acid, and $(NH_4)_6H_2W_{12}O_{40}$ was heated overnight to evaporate its water content on a hot plate, followed by calcination at 300 °C for 4 h. BET specific surface area of $W\text{-}V_2O_5$ was determined to be 38 m^2/g by N_2 adsorption experiments in our previous report.[17]

The NH_4^+-form of the AFX zeolite (Si/Al = 5.3), prepared according to previously reported procedures,[88] was supplied by the Research Association of Automotive Internal Combustion Engines (AICE, Japan). The NH_4^+-form of the CHA zeolite (Si/Al = 13) was purchased from Tosoh (Japan). CHA zeolite with Si/Al = 5.6 was hydrothermally synthesized as follows. In a 125-mL Teflon beaker, aqueous solution of 1-adamantyltrimethylammonium hydroxide (TMAdaOH, Sachem Co., 1.191mmol/g, 16.793 g, 20.0 mmol), aqueous NaOH solution (3.163 mmol/g, 3.162 g, 10.0 mmol), aqueous KOH solution (2.828 mmol/g, 3.536 g, 10.0 mmol), and pure water (Milli-Q grade, 15.443 g) were mixed and stirred for ca. 5 min. To this solution, an FAU-type zeolite (9.229 g; Tosoh HSZ-350HUA, Lot#35UA3Y02, Si/Al = 5.45, SiO_2 content: 10.835 mmol/g, Al_2O_3 content：0.994 mmol/g, H_2O：13.744 mmol/g) was added and the whole mixture was lightly swirled to obtain a white suspension. The resulting mixture with a molar composition: $1.0SiO_2$ – $0.0917Al_2O_3$ – 0.20TMAdaOH – 0.10NaOH – 0.10KOH – $20H_2O$ (SiO_2：100 mmol) was taken into a 125-mL Teflon-lined autoclave and heated at 170 °C for 68 h in a convection oven equipped with a rotator. The autoclave was rotated at 20 rpm while heating. After cooling the autoclave to room temperature, the resulting solid was separated by filtration, washed several times with de-ionized water, and dried at 80 °C overnight. The as-synthesized CHA was obtained as a white powder (8.49 g). To remove the OSDA occluded in the pores, the as-synthesized sample (4.82 g) was kept in a muffle furnace and heated stepwise as follows: the temperature was raised from room temperature to 600 °C under 1.5 °C/min of the ramping rate and maintained at the same temperature for 10 h. Finally, the sample was cooled down to room temperature to give a white powder.

Cu-exchanged zeolites were prepared using an ion-exchange method with a $Cu(NO_3)_2$ solution, followed by washing with distilled water three times, drying at 100 °C for 24 h, and calcination under air at 600 °C for 1 h.[75] Cu loading was determined using energy-dispersive X-ray fluorescence spectrometry (EDX-700HS, Shimadzu Corp.). As an example, the catalyst with Cu/Al and Si/Al ratios of 0.25 and 5.3 was denoted as Cu0.25-AFX5.3, as listed in **Table 1**.

Table 1. Structural properties of the SCR catalysts[a]

Catalyst	Composition	Method of preparation
V/TiO_2	5 wt.% V	impregnation
$W\text{-}V_2O_5$	3.5 mol.% W	Precipitation
Cu0.25-AFX5.3	4.1 wt.% Cu (Si/Al = 5.3, Cu/Al = 0.25)	ion exchange
Cu0.42-CHA13	2.7 wt.% Cu (Si/Al = 13, Cu/Al = 0.42)	ion exchange
Cu0.19-CHA5.6	3.0 wt.% Cu (Si/Al = 5.6, Cu/Al = 0.19)	ion exchange

2.2.2 *In situ/operando* spectroscopic experiments

IR spectra were measured in transmission mode using the JASCO FT/IR-4100 instrument, which was equipped with a hand-made *in situ* glass cell (with CaF_2 windows)[89] containing a self-supporting disk made of 40 mg of the V or Cu catalyst. Diffuse reflectance UV–vis spectra were measured using a spectrometer (JASCO V-670) equipped with a commercial *in situ* flow cell with a quartz window (JASCO) containing 5–10 mg of the powdered catalyst. For the *in situ* IR and UV–vis experiments, a gas mixture (typically 500 or 1000 ppm NH_3, 500 or 1000 ppm NO, 5% or 10% O_2 under He) was fed to the cells through a conventional flow reaction system at a total flow rate of 100 $cm^3\ min^{-1}$. Prior to the measurements, the V and Cu catalysts were pre-oxidized *in situ* under O_2/He at 300 °C and 500 °C, respectively; time-resolved measurements were subsequently carried out at 200 °C. The *operando* IR and UV–vis measurements were obtained by monitoring the formation of N_2 and H_2O in the outlet gas mixture using a mass spectrometry (MS) apparatus (BELMass, MicrotracBEL Corp.). Detailed descriptions of the *operando* IR and UV–vis analyses have been provided in our previous study.[75]

V K-edge X-ray absorption near edge structure (XANES) measurements were performed in transmission mode using the BL14B2 beamline at SPring-8 (Harima, Japan). The storage ring was operated at 8 GeV. A Si(111) single crystal was used to obtain a monochromatic X-ray beam. A sample pellet prepared using 3.4 mg of the V/TiO_2 catalyst and 10 mg of boron nitride (φ: 7 mm) was introduced into a quartz *in situ* cell equipped with Kapton film windows and gas lines connected to the mass spectrometer. The catalyst was pretreated under a flow of 10% O_2/He (1000 $cm^3\ min^{-1}$) at 250 °C for 0.5 h. After purging with He, the reaction gas mixture (typically containing 1000 ppm NH_3, 1000 ppm NO, and 5% O_2 with He as a balance gas) was fed at a total flow rate of 1000 $cm^3\ min^{-1}$. XANES analysis was conducted using the Athena software ver. 0.9.25 included in the Demeter package.[90]

2.3. Results and discussion

2.3.1 SCR with 5 wt.% V-loaded TiO_2

The transient reaction of the B-NH_3 and L-NH_3 species adsorbed on 5 wt.% V-loaded TiO_2 (V/TiO_2) was first investigated using *operando* spectroscopic experiments (*in situ* IR and *in situ* UV–vis in combination with online analysis of the outlet gas by MS) under transient SCR conditions at 200 °C. **Figure 2** compares the time-dependent IR results of the reduction of B-NH_3 and L-NH_3 on V/TiO_2 under NO and NO + O_2, along with the MS signals of N_2 (m/z = 28). The MS intensities of N_2 correspond to the relative rates of N_2 evolution. The IR sample disk was pre-exposed to NH_3 for 900 s, followed by He purging, and collection of the IR spectra as a function of time under NO or NO + O_2 flow. The spectrum obtained prior to the NO feed (t = 0 s) shows an IR band corresponding to the adsorption of NH_3 on the V(V) sites (L-NH_3)[79,91] at 1236 cm^{-1} and a more intense peak representing NH_4^+ (B-NH_3)[79,91] at 1420 cm^{-1}. Employing an extinction coefficient ratio of L-NH_3 and B-NH_3 ($\varepsilon_L/\varepsilon_B$) of 0.73, which was experimentally determined by Song et al. for 5 wt.% V-loaded TiO_2,[84] the IR result reveals that B-NH_3 is a major NH_3 species on the V/TiO_2 sample. When NO or NO + O_2 is fed to the NH_3-adsorbed V/TiO_2, the intensity of the B-NH_3 and L-NH_3 bands are observed to decrease; the formation of N_2 is also observed. Initially (t < 100 s), consumption of L-NH_3 and formation of B-NH_3 were observed, which could be due to the formation of protons (Brønsted acid sites) through the reduction half-cycle (Figure 1C).[30,66] Then, both L-NH_3 and B-NH_3 are consumed. B-NH_3 (the primary adsorbed NH_3 species) is gradually consumed even under NO, and the formation of N_2 appears to coincide with the consumption of B-NH_3. The rates of B-NH_3 consumption and N_2 formation under NO + O_2 are higher than those under NO. As shown in **Figure 1**, the first step in NH_3–SCR involves the reduction half-cycle, that is, the reduction of NO by NH_3 coordinated to the V(V) site (L-NH_3). Based on this model, the results suggest that the reduction of NO by B-NH_3-derived mobile NH_3 species occurs on the V(V) sites to yield N_2 and V(IV). Alternatively, a mobile HONO intermediate, formed by the reduction of V(V)-OH by NO, can react with B-NH_3 to yield N_2. The higher reactivity of B-NH_3 under NO + O_2 than that under NO will be discussed further below, which essentially presumes that the rate enhancement is clearly due to the reoxidation of V(IV) by O_2 to recover the V(V) sites that can be reused in the subsequent (second) reduction half-cycle.

When the IR sample disk of V/TiO_2 is exposed to the NH_3–SCR reaction gas mixture (NO + NH_3 + O_2), B-NH_3 is noted to be the dominant NH_3 species on the catalyst (**Figure 3**). The intensity of the N_2 signal under steady-state conditions (t = 300–900 s), which corresponds to the steady-state rates of NH_3–SCR, is of the same order of magnitude as that of the maximum N_2 signals obtained in the transient reaction of adsorbed NH_3 under NO (**Figure 2B**), which corresponds to the initial rates of the reduction half-cycle. This suggests that the reduction half-cycle can semi-quantitatively account for N_2 formation during steady-state NH_3–SCR over V/TiO_2.

Figure 4 shows the changes in the surface NH_3 species present on V/TiO_2 and gas-phase products obtained during the following successive reactions at 200 °C: (A) reduction of the catalyst by NO + NH_3, (B) further reaction of L-NH_3 and B-NH_3 with NO, (C) re-oxidation of the catalyst by O_2, and (D) reaction of L-NH_3 and B-NH_3 with NO after the re-oxidation (second reduction half-cycle). The formation of N_2 and H_2O is observed under NO + NH_3, indicating the reduction of surface V(V) species

by NO + NH_3 to N_2 and V(IV) (first reduction half-cycle). The reduction of V(V) species is also evidenced by the UV–vis experiments of the same surface reaction. When the NO + NH_3-treated V/TiO_2 is exposed to NO (**Figure 4B**), the consumption (desorption) rates of L-NH_3 and B-NH_3 are slow, and N_2 and H_2O are not produced. By contrast, L-NH_3 and B-NH_3 react with NO on the as-prepared (pre-oxidized) V/TiO_2 (**Figure 2B**). These results are consistent with the mechanistic model shown in **Figure 1**. The reaction of NO with the adsorbed NH_3 species and the surface V(V) species to yield N_2, H_2O, and V(IV) is an important N_2 formation pathway in SCR with V/TiO_2. **Figure 4B** shows the lack of N_2 formation under NO after the NO + NH_3 treatment, which indicates that the surface V(V) species are completely reduced through this treatment. In other words, L-NH_3 and B-NH_3 do not react with NO in the absence of surface V(V) species. The reduced V/TiO_2 catalyst is subsequently exposed to O_2. The simultaneous re-oxidization of V(IV) by O_2 and reduction of surface protons (H^+) in the proposed mechanism is evidenced by the formation of H_2O (**Figure 4C**) as well as the UV–vis results described further below. The V/TiO_2 catalyst is exposed to NO following the oxidation half-cycle (**Figure 4D**). L-NH_3 and B-NH_3 are consumed to yield N_2 and H_2O, in contrast to the results obtained prior to reoxidation (**Figure 4B**). This result demonstrates that B-NH_3 does not participate in the reduction half-cycle in the absence of surface V(V) sites; however, it can be involved in the second reduction half-cycle after the regeneration of surface V(V) sites through the oxidation half-cycle.

In situ UV-vis spectroscopy is known to assist in quantifying the V(IV) species of V_2O_5-based catalysts under dynamic redox conditions.[92] A recent *operando* electron spin resonance (ESR) study[68] of V-loaded TiO_2 catalysts revealed the reduction of surface V(V) species to V(IV) through NO + NH_3 treatment. Based on these studies, the changes in the oxidation states of V species during the reduction/oxidation half-cycles were monitored using *operando* UV–vis measurements at 200 °C. **Figure 5** indicates that the reduction of the as-prepared V/TiO_2 under NO + NH_3 results in an increase in the broad band at ~500–800 nm, which can be assigned to the V(IV) species,[92] and the formation of N_2 and H_2O in the gas phase. After the N_2 formation is complete, He is purged, and O_2 is fed to the reduced catalyst. The intensity of the band corresponding to the reduced V species at 700 nm decreases with the duration of O_2 flow, along with the formation of H_2O (**Figure 5C**). Therefore, the *operando* IR results (**Figure 4**) and UV–vis results reveal that the reduction of surface V(V) with NO + NH_3 is the primary N_2 formation pathway of SCR, followed by the oxidization of V(IV) by O_2 to regenerate V(V). Notably, all the *operando* IR and UV–vis results of the reduction/oxidation half-cycles are consistent with the proposed NH_3-SCR mechanism depicted in **Figure 1**.

Transient reactions similar to those considered in the aforementioned IR experiment were monitored *via in situ* XANES spectroscopy, as shown in **Figure 6**. The exposure of pre-oxidized V/TiO_2 to NO + NH_3 at 250 °C causes the absorption edge to shift toward lower energies, indicating the reduction of surface V(V) to V(IV). No significant changes are observed in the XANES spectra after the subsequent exposure to NO. After purging with He, exposure to O_2 regenerates the V(V) species through the oxidation half cycle. The V/TiO_2 catalyst is exposed to NO after this oxidation half-cycle, leading to the reduction of V(V) to V(IV) even in the absence of an additional feed of NH_3. This result

clearly indicates that second reduction half-cycle occurs with NO and surface adsorbed NH_3, which is consistent with the aforementioned IR results.

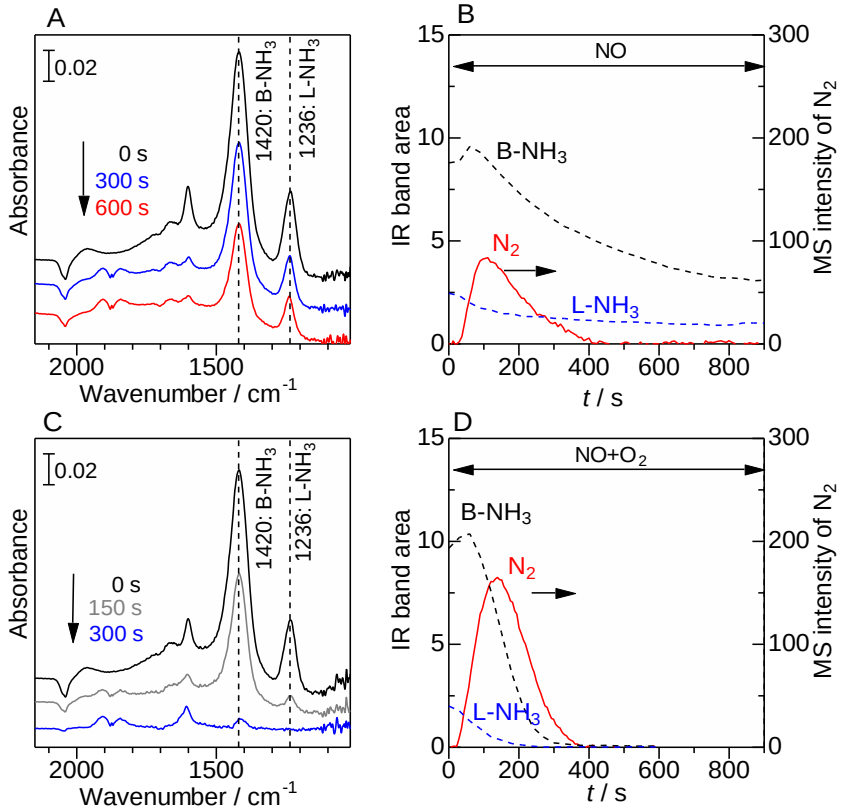

Figure 2. Time-resolved infrared (IR) data of the transient reduction of B-NH_3 and L-NH_3 on V/TiO_2 under (A,B) NO and (C,D) NO + O_2: (A,C) IR spectra; (B,D) temporal evolution of IR signals of B-NH_3 and L-NH_3 and the online mass spectrometry (MS) measurements of N_2. The sample is sequentially pre-exposed to NH_3 (900 s) and He (600 s). Conditions: 1000 ppm NO, 1000 ppm NH_3, and 5% O_2; 200 °C.

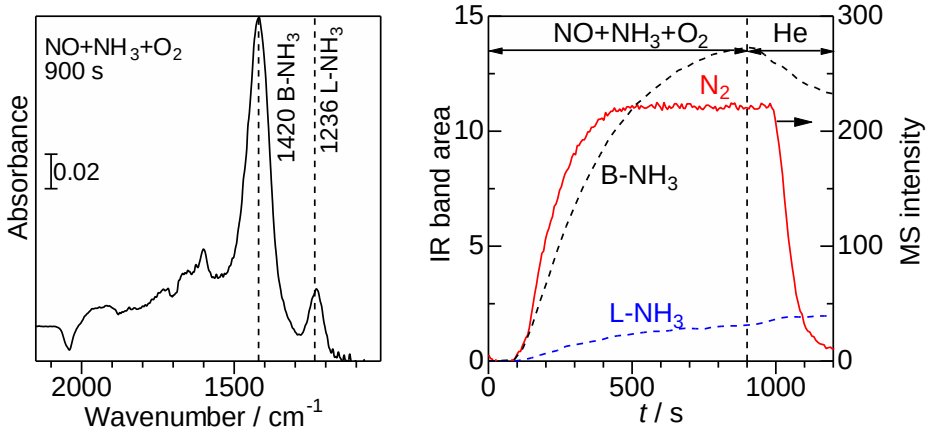

Figure 3. Typical IR spectrum (left) and time-resolved trends of IR signals representing B-NH_3 and L-NH_3 and the MS intensity of N_2 during the SCR over V/TiO_2. Conditions: 1000 ppm NO, 1000 ppm NH_3, and 5% O_2; 200 °C.

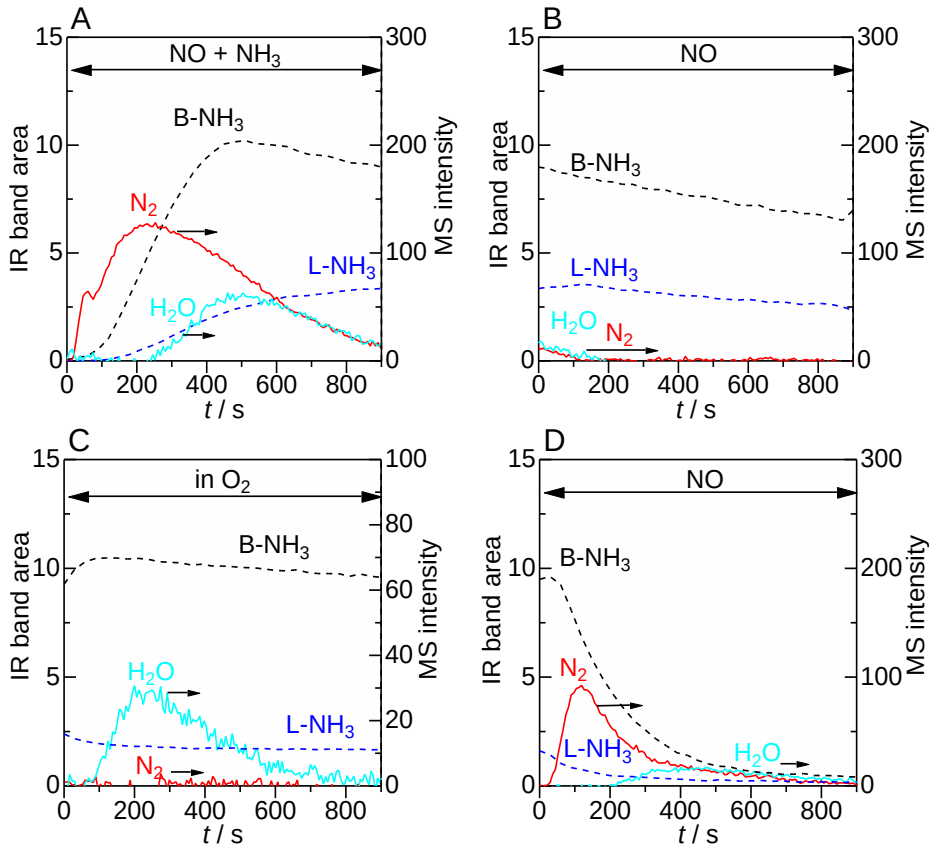

Figure 4. Time evolution of MS signals of H_2O and N_2, and IR signals of B-NH_3 (solid lines) and L-NH_3 (dashed lines) during the (A) reduction of V/TiO_2 by NO + NH_3, followed by (B) flow of NO, He purging (600 s), (C) re-oxidation of the reduced V/TiO_2 in O_2, and (D) flow of NO. Conditions: 1000 ppm NO, 1000 ppm NH_3, and 5% O_2; 200 °C.

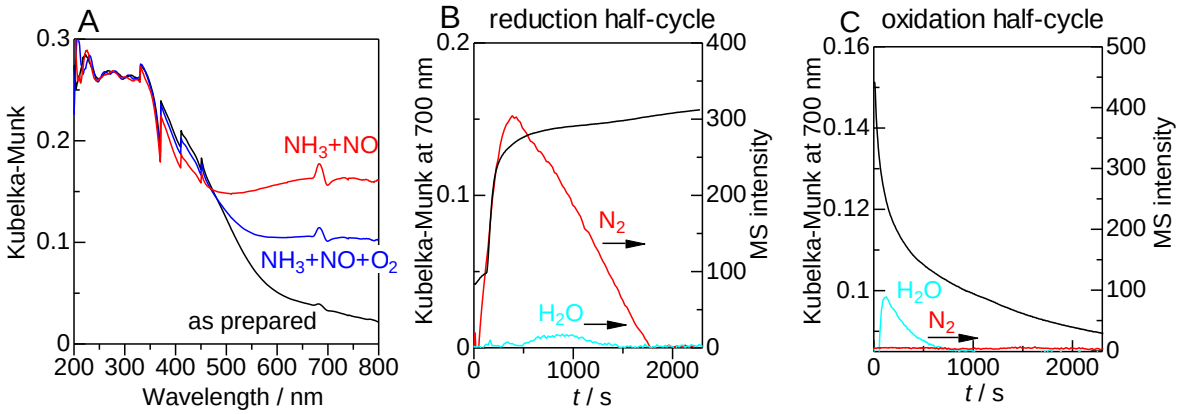

Figure 5. Changes in the UV–vis spectra of V/TiO_2 at 200 °C under sequential flow of NO + NH_3 (2300 s), He (600 s), and O_2: (A) spectra obtained before and after reduction by NO + NH_3; (B) time dependence of the UV–vis signal corresponding to V(IV) and the MS signals of N_2 and H_2O under NO + NH_3 and (C) O_2. The spectrum corresponding to NO + NH_3 + O_2 (900 s) is included in (A). Conditions: 1000 ppm NO, 1000 ppm NH_3, and 5% O_2.

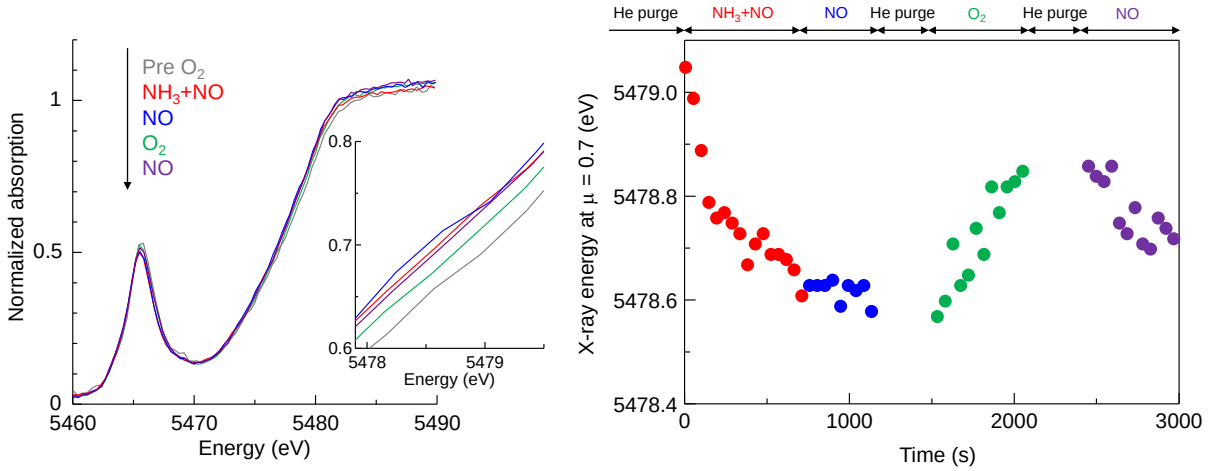

Figure 6. Changes in the V K-edge X-ray absorption near edge structure (XANES) spectra of V/TiO_2 at 200 °C under sequential flow of NO + NH_3, NO, He, O_2, He, and NO: (A) spectra obtained with various gas mixtures; (B) time dependence of the X-ray energy at a normalized absorption of 0.7. Conditions: 1000 ppm NO, 1000 ppm NH_3, and 5% O_2.

2.3.2 SCR with W-doped bulk V_2O_5

Operando spectroscopic experiments were subsequently conducted with the W-doped bulk V_2O_5 (W-V_2O_5) catalyst recently developed by Inomata et al.[17] to examine the applicability of the mechanism in **Figure 1** to a different type of V catalyst. As shown in **Figure 7**, B-NH_3 is the dominant NH_3 species on the NH_3-pre-adsorbed W-V_2O_5 sample, and the IR signals of L-NH_3 are negligible. The B-NH_3 species is consumed under NO and NO + O_2, and the rate of B-NH_3 consumption under NO + O_2 is higher than that under NO. **Figure 8** compares the kinetics of the consumption of B-NH_3 under NO (and N_2 formation) in the first (**Figure 7**) and second reduction half-cycles, that is, the reaction of B-NH_3 under NO after the first reduction half-cycle, followed by He purging, re-oxidation by O_2, and He purging. The consumption of B-NH_3 and generation of N_2 are initially observed in the first reduction half-cycle; however, a portion of B-NH_3 remains on the catalyst surface after the completion of N_2 generation. Considering the complete consumption of B-NH_3 under NO + O_2 (**Figure 7C**), the loss of the reactivity of B-NH_3 under NO can be explained by the complete consumption of surface V(V) species. After the regeneration of surface V(V) species through the re-oxidation treatment, the leftover B-NH_3 species react with NO to yield N_2 in the second reduction half-cycle. This suggests that the surface V(IV) species produced during the first reduction cycle under NO + NH_3 are oxidized by O_2 to recover the V(V) species that react with the leftover B-NH_3 and NO to yield N_2 in the second reduction half-cycle, even in the absence of an additional feed of gaseous NH_3. Similar to the results obtained for V/TiO_2, B-NH_3 adsorbed on W-V_2O_5 does not react with NO in the absence of surface V(V) species. The higher rate of B-NH_3 consumption under NO + O_2 than that under NO can be explained by the continuous reoxidation of V(IV) by O_2 to recover the V(V) sites.

In situ UV–vis measurements at 200 °C (**Figure 9**) were obtained to monitor the dynamic changes in the oxidation states of V in W-V_2O_5 under successive redox treatments, similar to the aforementioned IR experiments. The introduction of NH_3 results in a slight increase in the signal corresponding to the reduced V species. It should be noted that B-NH_3 is present on the NH_3-adsorbed sample (**Figure 7**). After purging the gas-phase NH_3 with He, NO is fed to the NH_3-adsorbed sample. The NO feed on the NH_3-adsorbed W-V_2O_5 results in an increase in the UV–vis signals representing the V(IV) species (700 nm) and the formation of N_2 in the gas phase. After the completion of N_2 formation, gas-phase NH_3 is purged with He. When the reduced sample is subsequently exposed to a flow of O_2 (**Figure 9D-F**), the intensity of the band representing the V(IV) species gradually decreases, and the formation of H_2O is confirmed by MS. Therefore, the *operando* IR results (**Figure 8**) and UV–vis results reveal that the NH_3–SCR mechanism is based on the reduction of surface V(V) with NO + NH_3 as the N_2 formation step, followed by the oxidation of V(IV) by O_2.

Note that, unlike the first reduction half-cycle, L-NH_3 is hardly observed in the on the W-V_2O_5 catalyst in the first and second reduction cycles (Figure 7), suggesting that L-NH_3 do not participate in the reduction cycles over W-V_2O_5. Unlike the SCR mechanism for V/TiO_2 (Figure 1C), the reduction half cycle for W-V_2O_5 can be the reaction of V(V) with NO and weakly adsorbed NH_3 derived from B-NH_3.

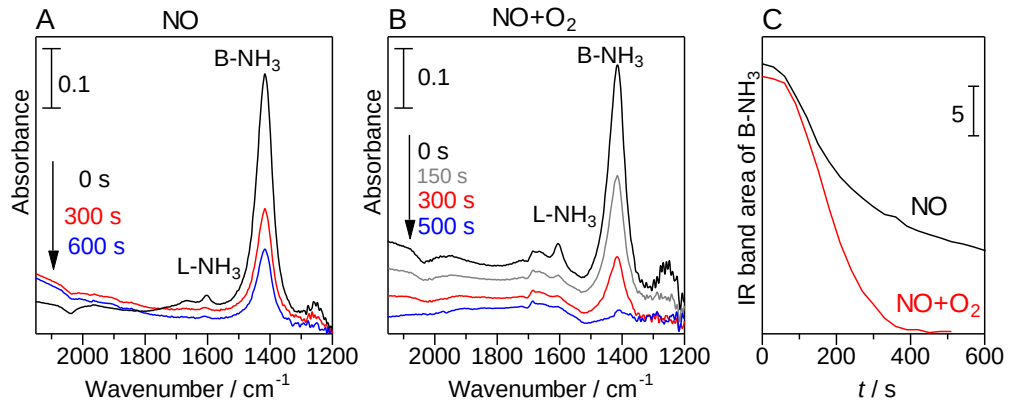

Figure 7. Time-resolved IR data (200 °C) of the transient reduction of B-NH_3 on W-V_2O_5 under NO and NO + O_2: (A, B) selected IR spectra; (C) temporal evolution of IR signals representing B-NH_3. The sample is pre-exposed to NH_3 for 900 s, followed by He purging (600 s). Conditions: 500 ppm NO, 500 ppm NH_3, and 5% O_2.

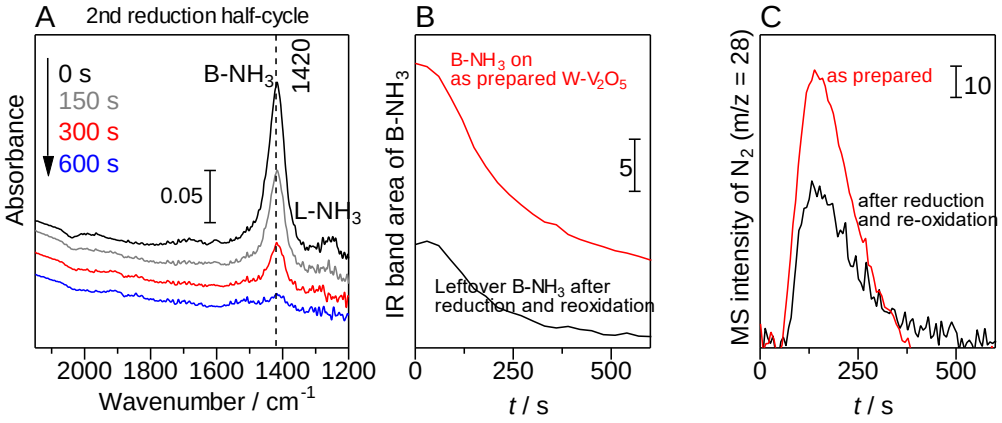

Figure 8. (A) Time-resolved IR results (200 °C) of the second reduction half-cycle: reaction of NO with B-NH_3 on W-V_2O_5 after the experiment analyzed in Figure 7A, followed by He purging, and re-oxidation under O_2. (B) Changes in the IR intensity of B-NH_3 and (C) N_2 formation in the first (red lines) and second (black lines) reduction half-cycles. Conditions: 500 ppm NO, 500 ppm NH_3, and 5% O_2.

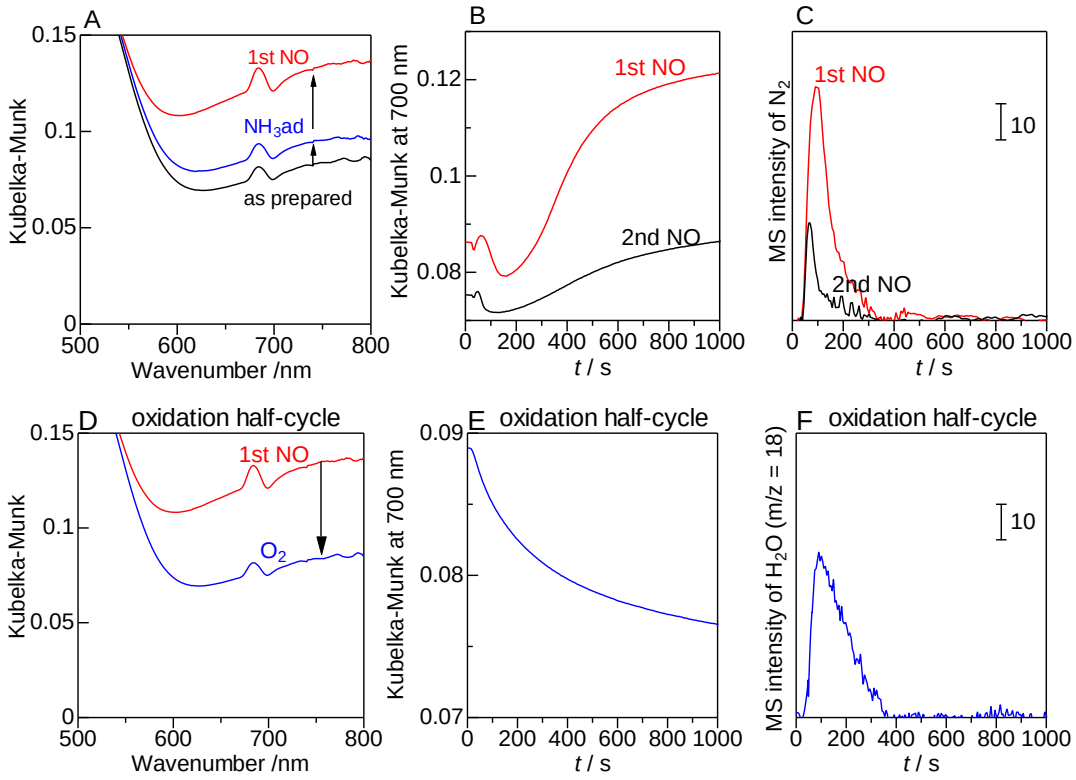

Figure 9. (A) Changes in the UV–vis spectra of W-V_2O_5 at 200 °C under successive flows of NH_3 (900 s), He (600 s), and NO (1200 s). (B) Time dependence of the UV–vis signal of V(IV) and (C) the MS signal of N_2. (D) UV–vis spectra of W-V_2O_5 obtained after the experiment analyzed in (A), followed by re-oxidation by O_2 for 1800 s. Time course of the signals representing (E) V(IV) and (F) H_2O formation during re-oxidation. Conditions: 500 ppm NO, 1000 ppm NH_3, and 5% O_2.

2.3.3 SCR with Cu-AFX

A similar research strategy employed for the V-based catalysts was applied for investigating reduction/oxidation half-cycles over Cu-exchanged zeolites with different structures (Cu-AFX and Cu-CHA) and compositions (Si/Al and Cu/Al ratios). **Figure 10** shows the results of the *operando* IR experiments with the Cu0.25-AFX5.3 catalyst at 200 °C. The addition of the NO feed on the NH_3-pre-adsorbed sample results in the consumption of NH_3 on Cu(II) sites (L-NH_3) and a slight increase in the amount of B-NH_3, as shown in **Figure 10A**, which is in agreement with our previous study.[75] Under NO + O_2 (**Figure 10B**), L-NH_3 is consumed first, followed by the consumption of B-NH_3 after 900 s (**Figure 10B, C**). The time dependences of the rates of N_2 formation under NO and NO + O_2 are compared in **Figure 10D**. The formation of N_2 under NO until 400 s is caused by the reaction of NO with NH_3 on Cu(II) (L-NH_3) to yield N_2, H_2O, and Cu(I).[75] The consumption of B-NH_3 under NO + O_2 is higher than that under NO, similar to the experiments with the V catalysts.

After the first reaction of B-NH_3 with NO (**Figure 10**), followed by He purging, the subsequent oxidation half-cycle under O_2, which is known to proceed via dimeric Cu complexes,[33,51,60] was investigated for Cu0.25-AFX5.3 (**Figure 11A**). B-NH_3 appears to be stable under O_2; however, N_2 formation is not observed *via* MS, whereas that of H_2O is observed. After the oxidation half-cycle, followed by purging with He, the reaction of the leftover B-NH_3 with NO (second reduction half-cycle) was examined. **Figure 11B-D** show the consumption of B-NH_3 and generation of N_2. These results indicate that Cu(I) produced by the first reduction half-cycle is then oxidized by O_2 to reproduce Cu(II), and Cu(II) produced by the first oxidation half-cycle reacts with the leftover B-NH_3 and NO to yield N_2 in the second reduction half-cycle.

Figure 12A,B show the *operando* UV–vis results of the first reduction half-cycles at 200 °C. The UV–vis spectrum of the as prepared Cu0.25-AFX5.3 shows a d–d band centered at ~760 nm, which is assigned to Cu(II) ions.[75] The intensity of the band corresponding to Cu(II) decreases *via* treatment of the catalyst under NO + NH_3, accompanied by N_2 formation. The band representing Cu(II) disappears at 2200 s, indicating the complete reduction of Cu(II) to Cu(I). **Figure 12C** shows the time evolution of the amount of Cu(II) species (UV–vis) and online MS analysis of the outlet gas in the subsequent oxidation half-cycle at 200 °C. The re-oxidization of Cu(I) to Cu(II) by O_2 and the simultaneous reaction of surface protons (H^+) in the proposed mechanism (**Figure 1**) is evidenced by the formation of H_2O. It should be noted that the formation of surface H^+ through the reduction half-cycle has been evidenced by the increase in the number of Brønsted acid sites that further interact with NH_3 to form NH_4^+ (**Figure 10C**); moreover, the consumption of the H^+ intermediate is confirmed by the initial decrease in the IR band of NH_4^+ under the re-oxidization step, along with the generation of H_2O (**Figure 11A**).

These *operando* IR and UV–vis results are consistent with the NH_3–SCR mechanism shown in **Figure 1**. After the oxidation half-cycle, followed by He purging, the consumption of the recovered Cu(II) under NO and the generation of N_2 are confirmed by *operando* UV–vis spectroscopy (**Figure 12D**). The *operando* IR results (**Figure 10C,D**) clearly indicate that Cu(II) (recovered by the oxidation half-cycle) is reduced again through its reaction with NO, and B-NH_3 is leftover after the reduction/oxidation half-

cycles without an additional feed of gaseous NH_3. Studies on the mobility of NH_3 in Cu zeolites have indicated that the theoretical (4.4 kJ mol^{-1})[93] and experimental (6.3 kJ mol^{-1})[94] diffusion barriers of NH_3 in zeolites are considerably low. Given the rapid diffusion of NH_4^+ in Cu-AFX, these results can be explained by the rapid migration of the B-NH_3-derived species to a Cu(II) site and the subsequent reaction of NH_3 on the Cu(II) site with NO; this suggests the active role of B-NH_3 as a mobile NH_3-reservoir. The mobile B-NH_3 species is presumably involved in the reduction half-cycle only when the neighboring Cu species are in the Cu(II) state. It is also important to note that under the conditions where migration of B-NH_3 species is slow, a mobile HONO intermediate, formed by the reaction with Cu(II)-OH and NO,[60–63] can react with B-NH_3 to yield N_2 and H_2O via NH_4NO_2.

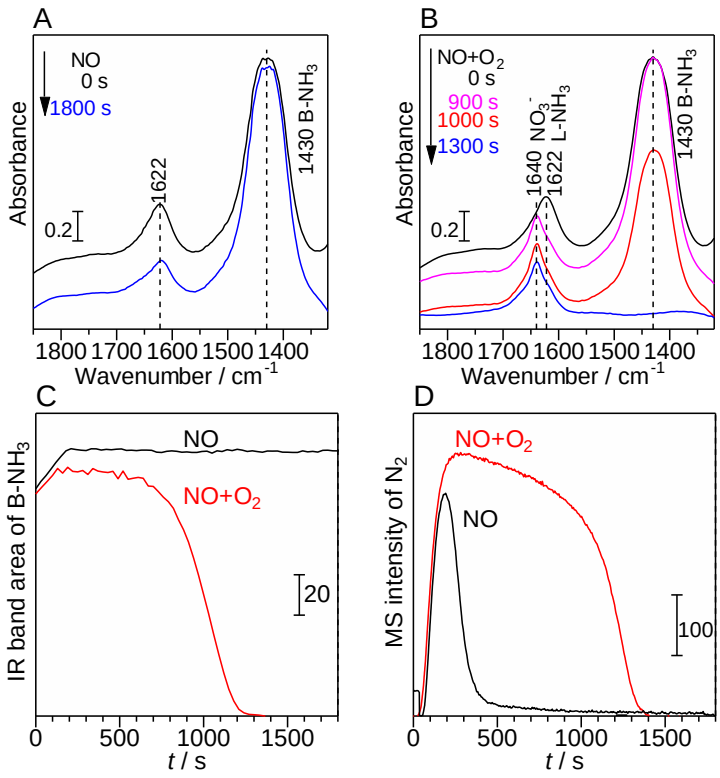

Figure 10. Time-resolved IR results of the reaction of B-NH_3 and L-NH_3 on Cu0.25-AFX5.3 at 200 °C under (A) NO and (B) NO + O_2; (C) IR intensities of B-NH_3 and (D) MS intensities of N_2 at the outlet vs. time. The sample is pre-exposed to NH_3 for 900 s, followed by He purging (600 s). Conditions: 1000 ppm NO, 1000 ppm NH_3, and 10% O_2.

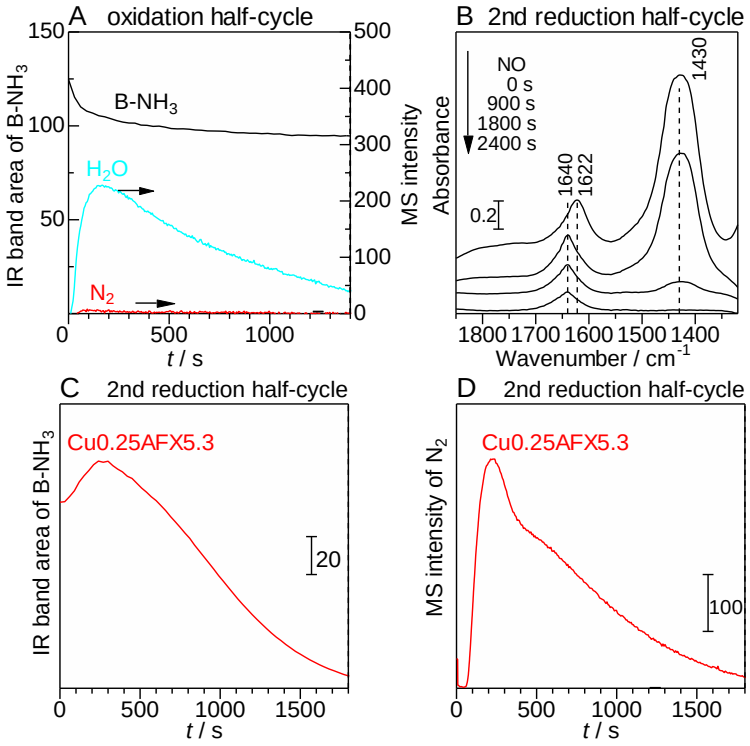

Figure 11. (A) Changes in the IR signal of B-NH_3 on Cu0.25-AFX5.3 and MS signals of N_2 and H_2O under O_2 (oxidation half-cycle) after the first reduction half-cycle (Figure 10A). Changes in the IR spectra (B, C) and formation of N_2 (D) under NO (second reduction half-cycle) with the two Cu-AFX samples. Conditions: 1000 ppm NO, 1000 ppm NH_3, and 10% O_2; 200 °C.

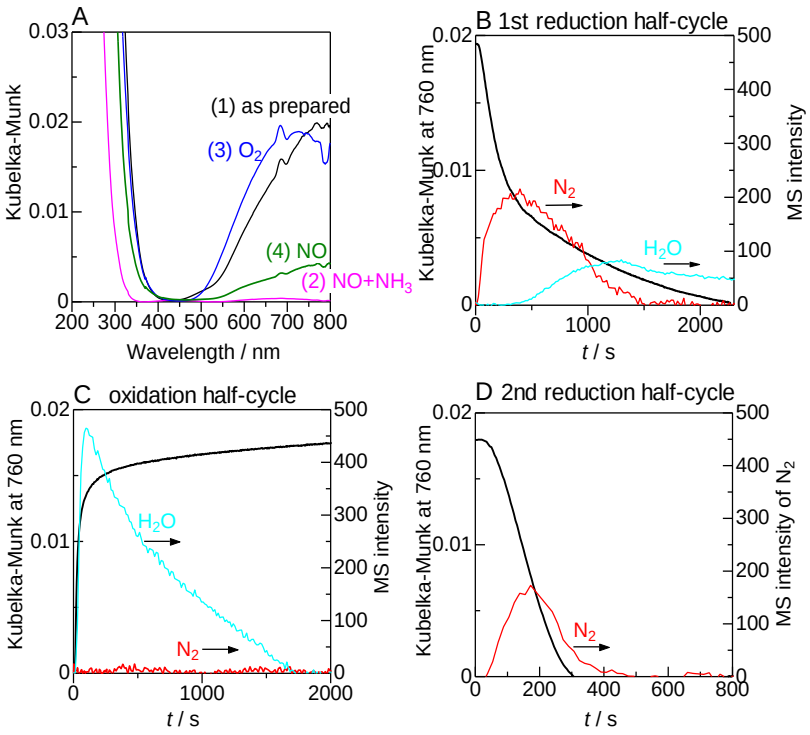

Figure 12. (A) Changes in the UV–vis spectra of Cu0.25-AFX5.3 at 200 °C under successive flows of NO + NH_3 (2400 s), He (600 s), O_2 (2000 s), and NO (800 s). Changes in the UV–vis signal of Cu(II) and the (C) MS signals of N_2 and H_2O under (B) NO + NH_3 (first reduction half-cycle), O_2 (oxidation half-cycle), and (D) NO (second reduction half-cycle). Conditions: 1000 ppm NO, 1000 ppm NH_3, and 10% O_2.

2.3.4 SCR with Cu-CHA

The *operando* IR results of the reaction of adsorbed NH_3 on Cu0.42-CHA13 under NO and NO + O_2 are compared in **Figure 13**. Similar to the results of Cu0.25-AFX5.3, the supply of the NO (+ O_2) feed to the NH_3 pre-adsorbed sample results in rapid consumption of L-NH_3 and a slight increase in the amount of B-NH_3 and N_2 formed in the initial stage (<300 s) of the transient reactions, followed by the slow consumption of B-NH_3. The rates of B-NH_3 consumption and N_2 formation under NO + O_2 appear to be higher than those under NO. As discussed above, the higher reaction rates under NO + O_2 are caused by the continuous regeneration of Cu(II), which participates in the subsequent reduction half-cycle. The relative rate of N_2 generation under NO + NH_3 + O_2 (blue line in **Figure 13D**) and steady-state conditions (>1000 s) is close to the maximum of N_2 signals obtained during the transient reactions of adsorbed NH_3 with NO (+ O_2); this indicates that the reduction half cycle in **Figure 1** accounts for the formation of N_2 under catalytic NH_3–SCR conditions.

Finally, the effect of the Si/Al ratio on the reactivity of B-NH_3 in the second reduction half-cycle was examined (**Figure 14**). Note that, unlike the first reduction half-cycle, L-NH_3 is hardly observed in the second reduction half-cycle, so that the effect of catalyst structure on the reactivity of B-NH_3 is considered in this experiment. Cu-CHA catalysts with two different Si/Al ratios and similar Cu loadings (2.7, 3 wt%) were sequentially exposed to NO + NH_3, He, O_2, and He to yield recovered Cu(II) sites and leftover B-NH_3. The results demonstrate that the reactivity of Cu(II) with NO and B-NH_3 in the second reduction half-cycle strongly depends on the Si/Al ratio; the Cu-CHA catalyst with a lower Si/Al ratio exhibits a higher reactivity. Considering that the mean distance of the nearest Al sites decreases with a decrease in the Si/Al ratio of zeolites, these results suggest that the amount of leftover B-NH_3 that reacts with NO in the second reduction half-cycle depends on the distance between the Cu(II) sites and B-NH_3; a shorter distance leads to higher reactivity in the second reduction half-cycle.

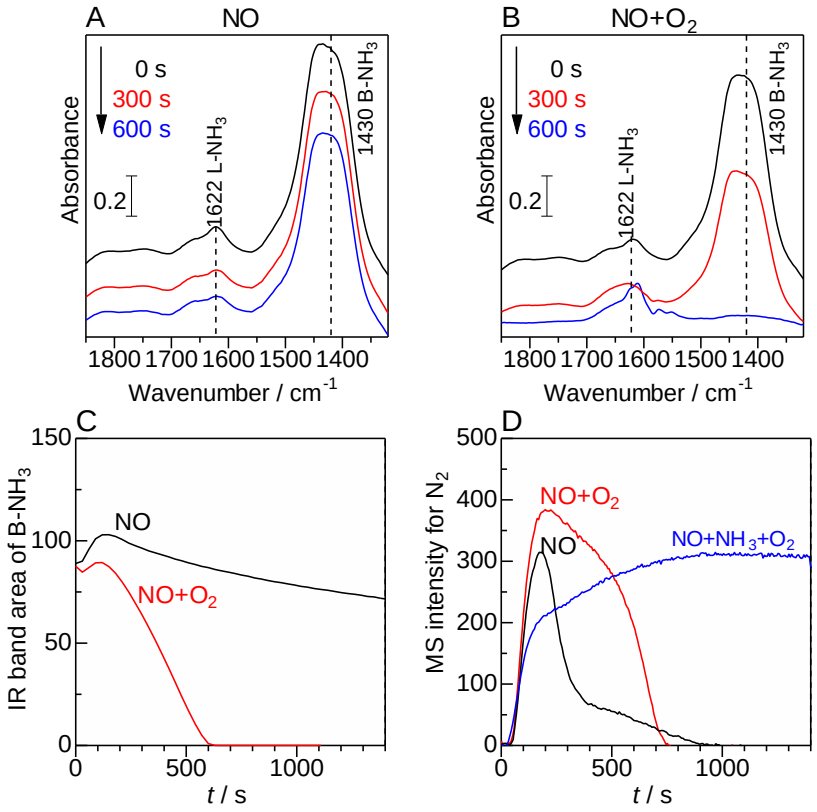

Figure 13. Time-resolved IR results of the reaction of B-NH_3 (L-NH_3) on Cu0.42-CHA13 at 200 °C under (A) NO and (B) NO + O_2; (C) IR intensities of B-NH_3 and (D) MS intensities of N_2 at the outlet vs. time. The blue line in (D) represents results obtained under a flow of NO + NH_3 + O_2. The sample is pre-exposed to NH_3 for 900 s, followed by He purging (300 s). Conditions: 1000 ppm NO, 1000 ppm NH_3, and 10% O_2.

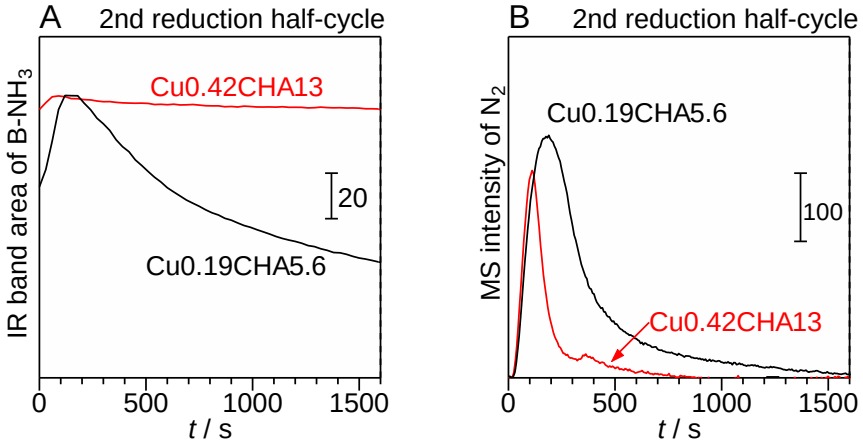

Figure 14. (A) IR intensities of B-NH_3 and (B) MS signals of N_2 obtained during the second reduction half-cycle with two Cu-CHA samples. The samples are sequentially pre-exposed to NO + NH_3 (2300 s), He (600 s), O_2 (1200 s), and He (600 s). Conditions: 1000 ppm NO, 1000 ppm NH_3, and 10% O_2.

2.4. Conclusions

Combined *in situ*/*operando* spectroscopic investigations of NH_3–SCR with vanadium oxide and Cu zeolite catalysts facilitated the analysis of a general mechanism based on reduction/oxidation half-cycles; the mechanism is described henceforth. First, NH_3 on oxidized metal cation sites [V(V), Cu(II)], conventionally known as Lewis acid sites, reacts with NO to yield reduced metal species [V(IV), Cu(I)] and H^+ on the surface, and N_2 and H_2O, presumably via an NH_2NO intermediate (reduction half-cycle). Under transient conditions, NH_3 on Brønsted acid sites (B-NH_3) could migrate to vacant V(V) or Cu(II) sites to react with NO, resulting in the formation of V(IV) or Cu(I) species, H^+, N_2, and H_2O; N_2 continues being generated until the surface V(V) or Cu(II) species is depleted. The subsequent reoxidation of reduced metal sites by O_2 regenerates the V(V) or Cu(II) sites, which accompanies the reaction of surface H^+ to yield H_2O (oxidation half-cycle). The mechanistic origin of the higher consumption rate of B-NH_3 (and L-NH_3) under NO + O_2 than that under NO was elucidated based on the continuous reoxidation of V(IV) or Cu(I) by O_2 to recover the oxidized sites. Upon the recovery of V(V) or Cu(II), the leftover B-NH_3 reacts with gaseous NO to yield N_2; therefore, B-NH_3 serves as a reservoir of NH_3 and migrates to the metal cation sites to participate in the second reduction half-cycle when the diffusion rate of B-NH_3 is higher than the rate of the reduction half-cycle. Our results suggest that a long-debated issue whether L-NH_3 or B-NH_3 is active species is not essential. Both L-NH_3 and B-NH_3 (via mobile NH_3) participate in the reduction half-cycle under transient conditions, but L-NH_3 seems more reactive because it is close to the oxidant, Cu(II) or V(V). These findings provide comprehensive evidence to support a general NH_3–SCR mechanism that is common to both V and Cu catalysts.

References

(1) Beale, A. M.; Gao, F.; Lezcano-Gonzalez, I.; Peden, C. H. F.; Szanyi, J. Recent Advances in Automotive Catalysis for NO_x Emission Control by Small-Pore Microporous Materials. *Chem. Soc. Rev.* **2015**, *44*, 7371–7405. https://doi.org/10.1039/c5cs00108k.

(2) Zhang, R.; Liu, N.; Lei, Z.; Chen, B. Selective Transformation of Various Nitrogen-Containing Exhaust Gases toward N2 over Zeolite Catalysts. *Chem. Rev.* **2016**, *116*, 3658–3721. https://doi.org/10.1021/acs.chemrev.5b00474.

(3) Han, L.; Cai, S.; Gao, M.; Hasegawa, J. Y.; Wang, P.; Zhang, J.; Shi, L.; Zhang, D. Selective Catalytic Reduction of NO_x with NH_3 by Using Novel Catalysts: State of the Art and Future Prospects. *Chem. Rev.* **2019**, *119*, 10916–10976. https://doi.org/10.1021/acs.chemrev.9b00202.

(4) Shan, Y.; Du, J.; Zhang, Y.; Shan, W.; Shi, X.; Yu, Y.; Zhang, R.; Meng, X.; Xiao, F.-S.; He, H. Selective Catalytic Reduction of NO_x with NH_3: Opportunities and Challenges of Cu-Based Small-Pore Zeolites. *Natl. Sci. Rev.* **2021**, *8*, nwab010. https://doi.org/10.1093/nsr/nwab010.

(5) Kwak, J. H.; Tonkyn, R. G.; Kim, D. H.; Szanyi, J.; Peden, C. H. F. Excellent Activity and Selectivity of Cu-SSZ-13 in the Selective Catalytic Reduction of NO_x with NH_3. *J. Catal.* **2010**, *275*, 187–190. https://doi.org/10.1016/j.jcat.2010.07.031.

(6) Marberger, A.; Elsener, M.; Ferri, D.; Kröcher, O. VO_x Surface Coverage Optimization of V_2O_5/WO_3-TiO_2 SCR Catalysts by Variation of the V Loading and by Aging. *Catalysts* **2015**, *5*, 1704–1720. https://doi.org/10.3390/catal5041704.

(7) Song, I.; Lee, H.; Jeon, S. W.; Ibrahim, I. A. M.; Kim, J.; Byun, Y.; Koh, D. J.; Han, J. W.; Kim, D. H. Simple Physical Mixing of Zeolite Prevents Sulfur Deactivation of Vanadia Catalysts for NOx Removal. *Nat. Commun.* **2021**, *12*, 901. https://doi.org/10.1038/s41467-021-21228-x.

(8) Rammelt, T.; Torkashvand, B.; Hauck, C.; Böhm, J.; Gläser, R.; Deutschmann, O. Nitric Oxide Reduction of Heavy-Duty Diesel Off-Gas by NH_3-SCR in Front of the Turbocharger. *Emiss. Control Sci. Technol.* **2017**, *3*, 275–288. https://doi.org/10.1007/s40825-017-0078-y.

(9) Priya, S. V.; Ohnishi, T.; Shimada, Y.; Kubota, Y.; Masuda, T.; Nakasaka, Y.; Matsukata, M.; Itabashi, K.; Okubo, T.; Sano, T.; et al. A Collective Case Screening of the Zeolites Made in Japan for High Performance NH_3-SCR of NO_X. *Bull. Chem. Soc. Jpn.* **2018**, *91*, 355–361. https://doi.org/10.1246/bcsj.20170352.

(10) Xu, J.; Chen, G.; Guo, F.; Xie, J. Development of Wide-Temperature Vanadium-Based Catalysts for Selective Catalytic Reducing of NOx with Ammonia: Review. *Chem. Eng. J.* **2018**, *353*, 507–518. https://doi.org/10.1016/j.cej.2018.05.047.

(11) Beretta, A.; Lanza, A.; Lietti, L.; Alcove Clave, S.; Collier, J.; Nash, M. An Investigation on the Redox Kinetics of NH_3-SCR over a V/Mo/Ti Catalyst: Evidence of a Direct Role of NO in the Re-Oxidation Step. *Chem. Eng. J.* **2019**, *359*, 88–98. https://doi.org/10.1016/j.cej.2018.11.047.

(12) Jaegers, N. R.; Lai, J. K.; He, Y.; Walter, E.; Dixon, D. A.; Vasiliu, M.; Chen, Y.; Wang, C.; Hu, M. Y.; Mueller, K. T.; et al. Mechanism by Which Tungsten Oxide Promotes the Activity of Supported V_2O_5/TiO_2 Catalysts for NO_x Abatement: Structural Effects Revealed by 51V MAS NMR Spectroscopy. *Angew. Chemie - Int. Ed.* **2019**, *58*, 12609–12616. https://doi.org/10.1002/anie.201904503.

(13) Yan, T.; Liu, Q.; Wang, S.; Xu, G.; Wu, M.; Chen, J.; Li, J. Promoter Rather than Inhibitor: Phosphorus Incorporation Accelerates the Activity of V_2O_5-$WO_3/TiO_2$2 Catalyst for Selective Catalytic Reduction of NO_x by NH_3. *ACS Catal.* **2020**, *10*, 2747−2753. https://doi.org/10.1021/acscatal.9b05549.

(14) Yan, Z.; Shan, W.; Shi, X.; He, G.; Lian, Z.; Yu, Y.; Shan, Y.; Liu, J.; He, H. The Way to Enhance the Thermal Stability of V_2O_5-Based Catalysts for NH_3-SCR. *Catal. Today* **2020**, *355*, 408–414. https://doi.org/10.1016/j.cattod.2019.07.037.

(15) Becher, J.; Sanchez, D. F.; Doronkin, D. E.; Zengel, D.; Meira, D. M.; Pascarelli, S.; Grunwaldt, J. D.; Sheppard, T. L. Chemical Gradients in Automotive Cu-SSZ-13 Catalysts for NO_x Removal Revealed by Operando X-Ray Spectrotomography. *Nat. Catal.* **2021**, *4*, 46–53. https://doi.org/10.1038/s41929-020-00552-3.

(16) Inomata, Y.; Hata, S.; Mino, M.; Kiyonaga, E.; Morita, K.; Hikino, K.; Yoshida, K.; Kubota, H.; Toyao, T.; Shimizu, K.; et al. Bulk Vanadium Oxide versus Conventional V_2O_5/TiO_2: NH_3-SCR Catalysts Working at a Low Temperature below 150 °C. *ACS Catal.* **2019**, *9*, 9327–9331. https://doi.org/10.1021/acscatal.9b02695.

(17) Inomata, Y.; Kubota, H.; Hata, S.; Kiyonaga, E.; Morita, K.; Yoshida, K.; Sakaguchi, N.; Toyao, T.; Shimizu, K. ichi; Ishikawa, S.; et al. Bulk Tungsten-Substituted Vanadium Oxide for Low-Temperature NO_x Removal in the Presence of Water. *Nat. Commun.* **2021**, *12*, 557. https://doi.org/10.1038/s41467-020-20867-w.

(18) Ek, M.; Ramasse, Q. M.; Arnarson, L.; Georg Moses, P.; Helveg, S. Visualizing Atomic-Scale Redox Dynamics in Vanadium Oxide-Based Catalysts. *Nat. Commun.* **2017**, *3*, 305. https://doi.org/10.1038/s41467-017-00385-y.

(19) Marberger, A.; Petrov, A. W.; Steiger, P.; Elsener, M.; Kröcher, O.; Nachtegaal, M.; Ferri, D. Time-Resolved Copper Speciation during Selective Catalytic Reduction of NO on Cu-SSZ-13. *Nat. Catal.* **2018**, *1*, 221–227. https://doi.org/10.1038/s41929-018-0032-6.

(20) Godiksen, A. L.; Rasmussen, S. B. Identifying the Presence of $[V=O]^{2+}$ during SCR Using in-Situ Raman and UV Vis Spectroscopy. *Catal. Today* **2019**, *336*, 45–49. https://doi.org/10.1016/j.cattod.2019.02.067.

(21) Marberger, A.; Elsener, M.; Nuguid, R. J. G.; Ferri, D.; Kröcher, O. Thermal Activation and Aging of a V_2O_5/WO_3-TiO_2 Catalyst for the Selective Catalytic Reduction of NO with NH_3. *Appl. Catal. A Gen.* **2019**, *573*, 64–72. https://doi.org/10.1016/j.apcata.2019.01.009.

(22) Kuma, R.; Kitano, T.; Tsujiguchi, T.; Tanaka, T. In Situ XANES Characterization of V_2O_5/TiO_2-SiO_2-MoO_3 Catalyst for Selective Catalytic Reduction of NO by NH_3. *Ind. Eng. Chem. Res.* **2020**, *59*, 13467−13476. https://doi.org/10.1021/acs.iecr.0c02308.

(23) Villamaina, R.; Liu, S.; Nova, I.; Tronconi, E.; Ruggeri, M. P.; Collier, J.; York, A.; Thompsett, D. Speciation of Cu Cations in Cu-CHA Catalysts for NH_3-SCR: Effects of SiO_2/Al_2O_3 Ratio and Cu-Loading Investigated by Transient Response Methods. *ACS Catal.* **2019**, *9*, 8916−8927. https://doi.org/10.1021/acscatal.9b02578.

(24) De Prins, M.; Verheyen, E.; Hoffmann, A.; Vanbutsele, G.; Sree, S. P.; Kerkhofs, S.; Van Tendeloo, L.; Schütze, F. W.; Martens, J. Structural Parameters Governing Low Temperature Activity of Small Pore Copper Zeolites in NH_3-SCR. *J. Catal.* **2020**, *390*, 224–236. https://doi.org/10.1016/j.jcat.2020.08.003.

(25) Takagi, M.; Kawai, T.; Soma, M.; Onishi, T.; Tamaru, K. The Mechanism of the Reaction between NO_x and NH_3 on V_2O_5 in the Presence of Oxygen. *J. Catal.* **1977**, *50*, 441–446. https://doi.org/10.1016/0021-9517(77)90056-2.

(26) Mizumoto, M.; Yamazoe, N.; Seiyama, T. Effects of Coexisting Gases on the Catalytic Reduction of NO with NH_3 over Cu(II) NaY Effect of Water Vapor. *J. Catal.* **1979**, *324*, 319–324.

(27) Lee, H.; Song, I.; Jeon, S. W.; Kim, D. H. Mobility of Cu Ions in Cu-SSZ-13 Determines the Reactivity of Selective Catalytic Reduction of NO_x with NH_3. *J. Phys. Chem. Lett.* **2021**, *12*, 3210–3216. https://doi.org/10.1021/acs.jpclett.1c00181.

(28) Khivantsev, K.; Kwak, J.-H.; Jaegers, N. R.; Derewinski, M. A.; Szanyi, J. Identification of the Mechanism of NO Reduction with Ammonia (SCR) on Zeolite Catalysts. *ChemRxiv* Preprint. https://doi.org/10.26434/chemrxiv.131347.

(29) Pankin, I. A.; Issa Hamoud, H.; Lomachenko, K. A.; Rasmussen, S. B.; Martini, A.; Bazin, P.; Valtchev, V.; Daturi, M.; Lamberti, C.; Bordiga, S. Cu- And Fe-Speciation in a Composite Zeolite Catalyst for Selective Catalytic Reduction of NOx: Insights from Operando XAS. *Catal. Sci. Technol.* **2021**, *11*, 846–860. https://doi.org/10.1039/d0cy01654c.

(30) Inomata, M.; Miyamoto, A.; Murakami, Y. Mechanism of the Reaction of NO and NH_3 on Vanadium Oxide Catalyst in the Presence of Oxygen under the Dilute Gas Condition. *J. Catal.* **1980**, *62*, 140–148. https://doi.org/10.1016/0021-9517(80)90429-7.

(31) Xin, Y.; Li, Q.; Zhang, Z. Zeolitic Materials for DeNOx Selective Catalytic Reduction. *ChemCatChem* **2018**, *10*, 29–41. https://doi.org/10.1002/cctc.201700854.

(32) Granger, P.; Siaka, H. W.; Umbarkar, S. B. What News in the Surface Chemistry of Bulk and Supported Vanadia Based SCR-Catalysts: Improvements in Their Resistance to Poisoning and Thermal Sintering. *Chem. Rec.* **2019**, *19*, 1813–1828. https://doi.org/10.1002/tcr.201800092.

(33) Paolucci, C.; Di Iorio, J. R.; Schneider, W. F.; Gounder, R. Solvation and Mobilization of Copper Active Sites in Zeolites by Ammonia: Consequences for the Catalytic Reduction of

Nitrogen Oxides. *Acc. Chem. Res.* **2020**, *53*, 1881–1892. https://doi.org/10.1021/acs.accounts.0c00328.

(34) Oda, A.; Shionoya, H.; Hotta, Y.; Takewaki, T.; Sawabe, K.; Satsuma, A. Spectroscopic Evidence of Efficient Generation of Dicopper Intermediate in Selective Catalytic Reduction of NO over Cu-Ion-Exchanged Zeolites. *ACS Catal.* **2020**, *10*, 12333–12339. https://doi.org/10.1021/acscatal.0c03425.

(35) Gramigni, F.; Nasello, N. D.; Usberti, N.; Iacobone, U.; Selleri, T.; Hu, W.; Liu, S.; Gao, X.; Nova, I.; Tronconi, E. Transient Kinetic Analysis of Low-Temperature NH_3-SCR over Cu-CHA Catalysts Reveals a Quadratic Dependence of Cu Reduction Rates on Cu^{II}. *ACS Catal.* **2021**, *11*, 4821–4831. https://doi.org/10.1021/acscatal.0c05362.

(36) Lv, W.; Wang, S.; Wang, P.; Liu, Y.; Huang, Z.; Li, J.; Dong, M.; Wang, J.; Fan, W. Regulation of Al Distributions and Cu^{2+} Locations in SSZ-13 Zeolites for NH_3-SCR of NO by Different Alkali Metal Cations. *J. Catal.* **2021**, *393*, 190–201. https://doi.org/10.1016/j.jcat.2020.11.027.

(37) Ma, Y.; Wu, X.; Ding, J.; Liu, L.; Jin, B.; Walter, E. D.; Ran, R.; Si, Z.; Gao, F.; Weng, D. Quasi-Operando Quantification of Cu(II) Ions in Cu-SSZ-13 Catalyst by an NH_3 Temperature-Programmed Reduction Method. *Chem. Commun.* **2021**, *57*, 1891–1894. https://doi.org/10.1039/d0cc07346f.

(38) Busca, G.; Lietti, L.; Ramis, G.; Berti, F. Chemical and Mechanistic Aspects of the Selective Catalytic Reduction of NO(x) by Ammonia over Oxide Catalysts: A Review. *Appl. Catal. B Environ.* **1998**, *18*, 1–36. https://doi.org/10.1016/S0926-3373(98)00040-X.

(39) Forzatti, P. Present Status and Perspectives in De-NO_x SCR Catalysis. *Appl. Catal. A Gen.* **2001**, *222*, 221–236. https://doi.org/10.1016/S0926-860X(01)00832-8.

(40) Gruber, M.; Hermann, K. Elementary Steps of the Catalytic NO_x Reduction with NH_3: Cluster Studies on Adsorbate Diffusion and Dehydrogenation at Vanadium Oxide Substrate. *J. Chem. Phys.* **2013**, *138*, 194701. https://doi.org/10.1063/1.4804160.

(41) Marberger, A.; Ferri, D.; Elsener, M.; Kröcher, O. The Significance of Lewis Acid Sites for the Selective Catalytic Reduction of Nitric Oxide on Vanadium-Based Catalysts. *Angew. Chemie - Int. Ed.* **2016**, *55*, 11989–11994. https://doi.org/10.1002/anie.201605397.

(42) Zhu, M.; Lai, J. K.; Tumuluri, U.; Ford, M. E.; Wu, Z.; Wachs, I. E. Reaction Pathways and Kinetics for Selective Catalytic Reduction (SCR) of Acidic NO_x Emissions from Power Plants with NH_3. *ACS Catal.* **2017**, *7*, 8358–8361. https://doi.org/10.1021/acscatal.7b03149.

(43) Lai, J. K.; Wachs, I. E. A Perspective on the Selective Catalytic Reduction (SCR) of NO with NH_3 by Supported V_2O_5-WO_3/TiO_2 Catalysts. *ACS Catal.* **2018**, *8*, 6537–6551. https://doi.org/10.1021/acscatal.8b01357.

(44) He, G.; Lian, Z.; Yu, Y.; Yang, Y.; Liu, K.; Shi, X.; Yan, Z.; Shan, W.; He, H. Polymeric Vanadyl Species Determine the Low-Temperature Activity of V-Based Catalysts for the SCR of NO_x with NH_3. *Sci. Adv.* **2018**, *4*, eaau4637. https://doi.org/10.1126/sciadv.aau4637.

(45) Nuguid, R. J. G.; Ferri, D.; Marberger, A.; Nachtegaal, M.; Kröcher, O. Modulated Excitation Raman Spectroscopy of V_2O_5/TiO_2: Mechanistic Insights into the Selective Catalytic Reduction of NO with NH_3. *ACS Catal.* **2019**, *9*, 6814–6820. https://doi.org/10.1021/acscatal.9b01514.

(46) Doronkin, D. E.; Benzi, F.; Zheng, L.; Sharapa, D. I.; Amidani, L.; Studt, F.; Roesky, P. W.; Casapu, M.; Deutschmann, O.; Grunwaldt, J. D. NH_3-SCR over V-W/TiO_2 Investigated by Operando X-Ray Absorption and Emission Spectroscopy. *J. Phys. Chem. C* **2019**, *123*, 14338−14349. https://doi.org/10.1021/acs.jpcc.9b00804.

(47) Lian, Z.; Deng, H.; Xin, S.; Shan, W.; Wang, Q.; Xu, J.; He, H. Significant Promotion Effect of the Rutile Phase on V_2O_5/TiO_3 Catalysts for NH_3-SCR. *Chem. Commun.* **2021**, *57*, 355--358. https://doi.org/10.1039/d0cc05938b.

(48) Lomachenko, K. A.; Borfecchia, E.; Negri, C.; Berlier, G.; Lamberti, C.; Beato, P.; Falsig, H.; Bordiga, S. The Cu-CHA DeNOx Catalyst in Action: Temperature-Dependent NH_3-Assisted Selective Catalytic Reduction Monitored by Operando XAS and XES. *J. Am. Chem. Soc.* **2016**, *138*, 12025–12028. https://doi.org/10.1021/jacs.6b06809.

(49) Paolucci, C.; Parekh, A. A.; Khurana, I.; Di Iorio, J. R.; Li, H.; Albarracin Caballero, J. D.; Shih, A. J.; Anggara, T.; Delgass, W. N.; Miller, J. T.; et al. Catalysis in a Cage: Condition-Dependent Speciation and Dynamics of Exchanged Cu Cations in SSZ-13 Zeolites. *J. Am. Chem. Soc.* **2016**, *138*, 6028–6048. https://doi.org/10.1021/jacs.6b02651.

(50) Ueda, K.; Ohyama, J.; Satsuma, A. Investigation of Reaction Mechanism of NO-C_3H_6-CO-O_2 Reaction over $NiFe_2O_4$ Catalyst. *ACS Omega* **2017**, *2*, 3135−3143.

(51) Paolucci, C.; Khurana, I.; Parekh, A. A.; Li, S.; Shih, A. J.; Li, H.; Di Iorio, J. R.; Albarracin-Caballero, J. D.; Yezerets, A.; Miller, J. T.; et al. Dynamic Multinuclear Sites Formed by Mobilized Copper Ions in NOx Selective Catalytic Reduction. *Science (80-.).* **2017**, *357*, 898–903. https://doi.org/10.1126/science.aan5630.

(52) Greenaway, A. G.; Lezcano-Gonzalez, I.; Agote-Aran, M.; Gibson, E. K.; Odarchenko, Y.; Beale, A. M. Operando Spectroscopic Studies of Cu–SSZ-13 for NH_3–SCR $DeNO_x$ Investigates the Role of NH_3 in Observed Cu(II) Reduction at High NO Conversions. *Top. Catal.* **2018**, *61*, 175–182. https://doi.org/10.1007/s11244-018-0888-3.

(53) Liu, C.; Kubota, H.; Toyao, T.; Maeno, Z.; Shimizu, K. I. Mechanistic Insights into the Oxidation of Copper(I) Species during NH_3-SCR over Cu-CHA Zeolites: A DFT Study. *Catal. Sci. Technol.* **2020**, *10*, 3586–3593. https://doi.org/10.1039/d0cy00379d.

(54) Jones, C. B.; Khurana, I.; Krishna, S. H.; Shih, A. J.; Delgass, W. N.; Miller, J. T.; Ribeiro, F. H.; Schneider, W. F.; Gounder, R. Effects of Dioxygen Pressure on Rates of NO_x Selective Catalytic Reduction with NH_3 on Cu-CHA Zeolites. *J. Catal.* **2020**, *389*, 140–149. https://doi.org/10.1016/j.jcat.2020.05.022.

(55) Ohata, Y.; Kubota, H.; Toyao, T.; Shimizu, K.; Ohnishi, T.; Moteki, T.; Ogura, M. Kinetic and Spectroscopic Insights into the Behaviour of Cu Active Site for NH3-SCR over Zeolites with

Several Topologies. *Catal. Sci. Technol.* **2021**, *11*, 2718–2733. https://doi.org/10.1039/d0cy01838d.

(56) Feng, Y.; Janssens, T. V. W.; Vennestrøm, P. N. R.; Jansson, J.; Skoglundh, M.; Grönbeck, H. The Role of H^+- and Cu^+-Sites for N_2O Formation during NH_3-SCR over Cu-CHA. *J. Phys. Chem. C* **2021**, *125*, 4595−4601.

(57) Greenaway, A. G.; Marberger, A.; Thetford, A.; Lezcano-González, I.; Agote-Arán, M.; Nachtegaal, M.; Ferri, D.; Kröcher, O.; Catlow, C. R. A.; Beale, A. M. Detection of Key Transient Cu Intermediates in SSZ-13 during NH_3-SCR DeNOx by Modulation Excitation IR Spectroscopy. *Chem. Sci.* **2020**, *11*, 447–455. https://doi.org/10.1039/c9sc04905c.

(58) Gruber, M.; Hermann, K. Elementary Steps of the Catalytic NO_x Reduction with NH_3: Cluster Studies on Adsorbate Diffusion and Dehydrogenation at Vanadium Oxide Substrate. *J. Chem. Phys.* **2013**, *139*, 244701. https://doi.org/10.1063/1.4849556.

(59) Zhao, P.; Boekfa, B.; Shimizu, K. I.; Ogura, M.; Ehara, M. Selective Catalytic Reduction of NO with NH_3 over Cu-Exchanged CHA, GME, and AFX Zeolites: A Density Functional Theory Study. *Catal. Sci. Technol.* **2021**, *11*, 1780–1790. https://doi.org/10.1039/d0cy02342f.

(60) Gao, F.; Mei, D.; Wang, Y.; Szanyi, J.; Peden, C. H. F. Selective Catalytic Reduction over Cu/SSZ-13: Linking Homo- and Heterogeneous Catalysis. *J. Am. Chem. Soc.* **2017**, *139*, 4935–4942. https://doi.org/10.1021/jacs.7b01128.

(61) Usberti, N.; Gramigni, F.; Nasello, N. D.; Iacobone, U.; Selleri, T.; Hu, W.; Liu, S.; Gao, X.; Nova, I.; Tronconi, E. An Experimental and Modelling Study of the Reactivity of Adsorbed NH_3 in the Low Temperature NH_3-SCR Reduction Half-Cycle over a Cu-CHA Catalyst. *Appl. Catal. B Environ.* **2020**, *279*, 119397. https://doi.org/10.1016/j.apcatb.2020.119397.

(62) Hu, W.; Zou, R.; Dong, Y.; Zhang, S.; Song, H.; Liu, S.; Zheng, C.; Nova, I.; Tronconi, E.; Gao, X. Synergy of Vanadia and Ceria in the Reaction Mechanism of Low-Temperature Selective Catalytic Reduction of NO_x by NH_3. *J. Catal.* **2020**, *391*, 145–154. https://doi.org/10.1016/j.jcat.2020.08.002.

(63) Hu, W.; Selleri, T.; Gramigni, F.; Fenes, E.; Rout, K. R.; Liu, S.; Nova, I.; Chen, D.; Gao, X.; Tronconi, E. On the Redox Mechanism of Low-Temperature NH_3-SCR over Cu-CHA: A Combined Experimental and Theoretical Study of the Reduction Half Cycle. *Angew. Chemie - Int. Ed.* **2021**, *60*, 7197–7204. https://doi.org/10.1002/anie.202014926.

(64) He, Y.; Ford, M. E.; Zhu, M.; Liu, Q.; Tumuluri, U.; Wu, Z.; Wachs, I. E. Influence of Catalyst Synthesis Method on Selective Catalytic Reduction (SCR) of NO by NH_3 with V_2O_5-WO_3/TiO_2 Catalysts. *Appl. Catal. B Environ.* **2016**, *193*, 141–150. https://doi.org/10.1016/j.apcatb.2016.04.022.

(65) Topsøe, N. Y.; Topsøe, H.; Dumesic, J. A. Vanadia/Titania Catalysts for Selective Catalytic Reduction (SCR) of Nitric-Oxide by Ammonia. I. Combined Temperature-Programmed in-Situ FTIR and on-Line Mass-Spectroscopy Studies. *J. Catal.* **1995**, *151*, 226–240. https://doi.org/10.1006/jcat.1995.1024.

(66) Topsøe, N. Y.; Dumesic, J. A.; Topsøe, H. Vanadia-Titania Catalysts for Selective Catalytic Reduction of Nitric-Oxide by Ammonia. II. Studies of Active Sites and Formulation of Catalytic Cycles. *J. Catal.* **1995**, *151*, 241–252. https://doi.org/10.1006/jcat.1995.1025.

(67) Arnarson, L.; Falsig, H.; Rasmussen, S. B.; Lauritsen, J. V.; Moses, P. G. A Complete Reaction Mechanism for Standard and Fast Selective Catalytic Reduction of Nitrogen Oxides on Low Coverage $VO_x/TiO_2(001)$ Catalysts. *J. Catal.* **2017**, *346*, 188–197. https://doi.org/10.1016/j.jcat.2016.12.017.

(68) Godiksen, A. L.; Funk, M. H.; Rasmussen, S. B.; Mossin, S. Assessing the Importance of V(IV) During NH_3−SCR Using Operando EPR Spectroscopy. *ChemCatChem* **2020**, *12*, 4893–4903. https://doi.org/10.1002/cctc.202000802.

(69) Mason, M. M.; Lee, Z. R.; Vasiliu, M.; Wachs, I. E.; Dixon, D. A. Initial Steps in the Selective Catalytic Reduction of NO with NH_3 by TiO_2-Supported Vanadium Oxides. *ACS Catal.* **2020**, *10*, 13918–13931. https://doi.org/10.1021/acscatal.0c03693.

(70) Zhu, H.; Kwak, J. H.; Peden, C. H. F.; Szanyi, J. In Situ DRIFTS-MS Studies on the Oxidation of Adsorbed NH3 by NOx over a Cu-SSZ-13 Zeolite. *Catal. Today* **2013**, *205*, 16–23. https://doi.org/10.1016/j.cattod.2012.08.043.

(71) Ma, L.; Cheng, Y.; Cavataio, G.; McCabe, R. W.; Fu, L.; Li, J. In Situ DRIFTS and Temperature-Programmed Technology Study on NH_3-SCR of NOx over Cu-SSZ-13 and Cu-SAPO-34 Catalysts. *Appl. Catal. B Environ.* **2014**, *156–157*, 428–437. https://doi.org/10.1016/j.apcatb.2014.03.048.

(72) Lezcano-Gonzalez, I.; Deka, U.; Arstad, B.; Van Yperen-De Deyne, A.; Hemelsoet, K.; Waroquier, M.; Van Speybroeck, V.; Weckhuysen, B. M.; Beale, A. M. Determining the Storage, Availability and Reactivity of NH_3 within Cu-Chabazite-Based Ammonia Selective Catalytic Reduction Systems. *Phys. Chem. Chem. Phys.* **2014**, *16*, 1639–1650. https://doi.org/10.1039/c3cp54132k.

(73) Su, W.; Chang, H.; Peng, Y.; Zhang, C.; Li, J. Reaction Pathway Investigation on the Selective Catalytic Reduction of NO with NH3 over Cu/SSZ-13 at Low Temperatures. *Environ. Sci. Technol.* **2015**, *49*, 467–473. https://doi.org/10.1021/es503430w.

(74) Paolucci, C.; Di Iorio, J. R.; Ribeiro, F. H.; Gounder, R.; Schneider, W. F. Catalysis Science of NOx Selective Catalytic Reduction With Ammonia Over Cu-SSZ-13 and Cu-SAPO-34. *Adv. Catal.* **2016**, *59*, 1–107. https://doi.org/10.1016/bs.acat.2016.10.002.

(75) Liu, C.; Kubota, H.; Amada, T.; Kon, K.; Toyao, T.; Maeno, Z.; Ueda, K.; Ohyama, J.; Satsuma, A.; Tanigawa, T.; et al. In Situ Spectroscopic Studies on the Redox Cycle of NH_3−SCR over Cu−CHA Zeolites. *ChemCatChem* **2020**, *12*, 3050–3059. https://doi.org/10.1002/cctc.202000024.

(76) Krishna, S. H.; Jones, C. B.; Miller, J. T.; Ribeiro, F. H.; Gounder, R. Combining Kinetics and Operando Spectroscopy to Interrogate the Mechanism and Active Site Requirements of NOx

Selective Catalytic Reduction with NH3 on Cu-Zeolites. *J. Phys. Chem. Lett.* **2020**, *11*, 5029–5036. https://doi.org/10.1021/acs.jpclett.0c00903.

(77) Janssens, T. V. W.; Falsig, H.; Lundegaard, L. F.; Vennestrøm, P. N. R.; Rasmussen, S. B.; Moses, P. G.; Giordanino, F.; Borfecchia, E.; Lomachenko, K. A.; Lamberti, C.; et al. A Consistent Reaction Scheme for the Selective Catalytic Reduction of Nitrogen Oxides with Ammonia. *ACS Catal.* **2015**, *5*, 2832–2845. https://doi.org/10.1021/cs501673g.

(78) Chen, L.; Janssens, T. V. W.; Vennestrøm, P. N. R.; Jansson, J.; Skoglundh, M.; Grönbeck, H. A Complete Multisite Reaction Mechanism for Low-Temperature NH_3-SCR over Cu-CHA. *ACS Catal.* **2020**, *10*, 5646–5656. https://doi.org/10.1021/acscatal.0c00440.

(79) Rasmussen, S. B.; Portela, R.; Bazin, P.; Ávila, P.; Bañares, M. A.; Daturi, M. Transient Operando Study on the NH3/NH4+ Interplay in V-SCR Monolithic Catalysts. *Appl. Catal. B Environ.* **2018**, *224*, 109–115. https://doi.org/10.1016/j.apcatb.2017.10.026.

(80) Chen, P.; Khetan, A.; Jabłońska, M.; Simböck, J.; Muhler, M.; Palkovits, R.; Pitsch, H.; Simon, U. Local Dynamics of Copper Active Sites in Zeolite Catalysts for Selective Catalytic Reduction of NO_x with NH_3. *Appl. Catal. B Environ.* **2018**, *237*, 263–272. https://doi.org/10.1016/j.apcatb.2018.05.091.

(81) Chen, P.; Moos, R.; Simon, U. Metal Loading Affects the Proton Transport Properties and the Reaction Monitoring Performance of Fe-ZSM-5 and Cu-ZSM-5 in NH3-SCR. *J. Phys. Chem. C* **2016**, *120* (44), 25361–25370. https://doi.org/10.1021/acs.jpcc.6b07353.

(82) Zhang, Y.; Peng, Y.; Li, K.; Liu, S.; Chen, J.; Li, J.; Gao, F.; Peden, C. H. F. Using Transient FTIR Spectroscopy to Probe Active Sites and Reaction Intermediates for Selective Catalytic Reduction of NO on Cu/SSZ-13 Catalysts. *ACS Catal.* **2019**, *9*, 6137–6145. https://doi.org/10.1021/acscatal.9b00759.

(83) Ganjkhanlou, Y.; Janssens, T. V. W.; Vennestrøm, P. N. R.; Mino, L.; Paganini, M. C.; Signorile, M.; Bordiga, S.; Berlier, G. Location and Activity of VO_x Species on TiO_2 Particles for NH_3-SCR Catalysis. *Appl. Catal. B Environ.* **2020**, *278*, 119337. https://doi.org/10.1016/j.apcatb.2020.119337.

(84) Song, I.; Lee, H.; Jeon, S. W.; Kim, T.; Kim, D. H. Time-Resolved Observation of V_2O_5/TiO_2 in NH_3-SCR Reveals the Equivalence of Brønsted and Lewis Acid Sites. *Chem. Commun.* **2020**, *56*, 15450–15453. https://doi.org/10.1039/d0cc06006b.

(85) Song, I.; Youn, S.; Lee, H.; Lee, S. G.; Cho, S. J.; Kim, D. H. Effects of Microporous TiO_2 Support on the Catalytic and Structural Properties of V_2O_5/Microporous TiO_2 for the Selective Catalytic Reduction of NO by NH_3. *Appl. Catal. B Environ.* **2017**, *210*, 421–431. https://doi.org/10.1016/j.apcatb.2017.04.016.

(86) Ogura, M.; Shimada, Y.; Ohnishi, T.; Nakazawa, N.; Kubota, Y.; Yokoi, T.; Ehara, M.; Shimizu, K.; Tsunoji, N. AFX Zeolite for Use as a Support of NH_3-SCR Catalyst Mining through AICE Joint Research Project of Industries-Academia- Academia. *Catalysts* **2021**, *11*, 163. https://doi.org/10.3390/catal11020163.

(87) Peden, C. H. F. Cu/Chabazite Catalysts for 'Lean-Burn' Vehicle Emission Control. *J. Catal.* **2019**, *373*, 384–389. https://doi.org/10.1016/j.jcat.2019.04.046.

(88) Nakazawa, N.; Inagaki, S.; Kubota, Y. Novel Technique to Synthesize AFX-Type Zeolite Using a Bulky and Rigid Diquaternary Ammonium Cation. *Adv. Porous Mater.* **2016**, *4*, 219–229. https://doi.org/10.1166/apm.2016.1114.

(89) Satsuma, A.; Shimizu, K. I. In Situ FT/IR Study of Selective Catalytic Reduction of NO over Alumina-Based Catalysts. *Prog. Energy Combust. Sci.* **2003**, *29*, 71–84. https://doi.org/10.1016/S0360-1285(02)00033-3.

(90) Ravel, B.; Newville, M. ATHENA, ARTEMIS, HEPHAESTUS: Data Analysis for X-Ray Absorption Spectroscopy Using IFEFFIT. *J. Synchrotron Radiat.* **2005**, *12*, 537–541. https://doi.org/10.1107/S0909049505012719.

(91) Song, I.; Lee, J.; Lee, G.; Han, J. W.; Kim, D. H. Chemisorption of NH_3 on Monomeric Vanadium Oxide Supported on Anatase TiO_2: A Combined DRIFT and DFT Study. *J. Phys. Chem. C* **2018**, *122*, 16674–16682. https://doi.org/10.1021/acs.jpcc.8b02291.

(92) Argyle, M. D.; Chen, K.; Resini, C.; Krebs, C.; Bell, A. T.; Iglesia, E. Extent of Reduction of Vanadium Oxides during Catalytic Oxidation of Alkanes Measured by In-Situ UV-Visible Spectroscopy. *J. Phys. Chem. B* **2004**, *108* (7), 2345–2353. https://doi.org/10.1021/jp030989m.

(93) O'Malley, A. J.; Hitchcock, I.; Sarwar, M.; Silverwood, I. P.; Hindocha, S.; Catlow, C. R. A.; York, A. P. E.; Collier, P. J. Ammonia Mobility in Chabazite: Insight into the Diffusion Component of the NH3-SCR Process. *Phys. Chem. Chem. Phys.* **2016**, *18* (26), 17159–17168. https://doi.org/10.1039/c6cp01160h.

(94) Nakasaka, Y.; Kanda, T.; Shimizu, K.; Kon, K.; Shibata, G.; Masuda, T. Micropore Diffusivities of NO and NH_3 in Cu-ZSM-5 and Their Effect on NH_3-SCR. *Catal. Today* **2019**, *332*, 64–68. https://doi.org/10.1016/j.cattod.2018.06.056.

Chapter 3

Formation and Reactions of NH_4NO_3 during Transient and Steady-State NH_3-SCR of NO_x over H-AFX Zeolites: Spectroscopic and Theoretical Studies

3.1. Introduction

The catalytic selective reduction of nitrogen oxides (NO_x) by NH_3 (NH_3–SCR) is a widely used process to control NO_x emissions from stationary and sources and diesel vehicles.[1–3] Transition metal (Fe and Cu) cation-exchanged zeolites have been promising catalysts for NH_3–SCR. It is generally accepted that the exchanged transition metal cations are the main catalytically active species for the reaction of equimolar amounts of NO and NH_3 in the presence of oxygen, so-called "standard SCR":[1,2,4]

$4NH_3 + 4NO + O_2 \rightarrow 4N_2 + 6H_2O$ (1)

Since the commercialization of Cu-exchanged chabazites (Cu-CHA) for NO_x aftertreatment systems,[5,6] attention has been focused on the Cu-exchanged zeolites. It has been established that the catalytic cycle of standard SCR is composed of the reduction of isolated Cu(II) to Cu(I) and the subsequent reoxidation of Cu(I) to Cu(II).[1–4,7] In comparison with Cu-CHA, the NO reduction activity of Cu-free H-CHA is negligibly low, and it has been suggested the Brønsted acid sites (BAS) of zeolites offer the exchange site of Cu cations but do not play a significant role in the standard SCR.[8]

In the emission control system for diesel vehicles, a diesel oxidation catalyst (DOC) located upstream of the SCR catalyst converts a fraction of NO to NO_2, and the participation of NO_2 in NH_3–SCR shows an important effect on the SCR performance.[9–20] For H-[9,10,13] or Fe-exchanged[14–16] zeolites and V-based catalysts,[17,18] the SCR activity is enhanced significantly when NO_2/NO molar is ratio of 1/1 (so-called "fast SCR reaction"):

$2NH_3 + NO + NO_2 \rightarrow 2N_2 + 3H_2O$ (2)

In addition, the catalytic reduction of NO_2 by NH_3 can occur without NO.[14] When N_2 selectivity is 100%, the reaction could be described as follows, so called "NO_2 SCR" or "slow SCR":[1]

$8NH_3 + 6NO_2 \rightarrow 7N_2 + 12H_2O$ (3)

The SCR activity of H-type zeolites depends strongly on the NO_2 feed. Vartuli et al. reported that the reaction rate of NO_2 SCR is several hundred times faster than that of standard SCR over H-ZSM-5 catalyst.[13] In contrast, NO_2 does not improve the NO reduction activity of Cu-zeolites.[16,21,22] He et al. recently found NO_2 can even inhibit NO conversions at low temperatures over Cu-CHA.[23] Moreover, it was suggested that NO_2 formed in the DOC upstream of the SCR converter can lead to the accumulation of ammonium nitrate (NH_4NO_3) in zeolite pores, which causes catalyst deactivation [23] as well as the formation of undesirable N_2O byproduct.[24]

The BAS of zeolites play a significant role in the NH_3–SCR reactions involving NO_2 (fast SCR and NO_2 SCR), in which Cu sites are not of essential importance.[9,10] Considering the fact that Cu sites can catalyze NO_2 decomposition to NO and O_2,[25] Cu-zeolites are not ideal model catalysts for studying the role of NO_2 in NH_3–SCR. Pioneering kinetic and theoretical studies on fast or NO_2 SCR utilized H-ZSM-5 zeolites,[9,12] and very few studies[19] focused on the NO_2 effect on SCR by small-pore H-type zeolites.[19] To the best of our knowledge, little is known about the difference of the reaction rates for standard, fast, and NO_2 SCR by H-type small-pore zeolites.[26]

AFX zeolite is one of the 8-membered ring (small-pore) zeolites with AFT cage (0.55 × 1.35 nm) and small GME cage (0.33 × 0.74 nm). Conventionally, AFX zeolites, known as SSZ-16, were synthesized using a flexible organic structure-directing agent (OSDA).[27] Recently, Kubota and co-workers developed a highly durable AFX zeolite using a bulky and non-flexible OSDA ($TEBOP^{2+}$).[28] In this study, we employ the H-type AFX (H-AFX) to perform *operando* IR spectroscopy, kinetic, and DFT studies on the role of NO_2 in NH_3–SCR under steady-states and transient conditions. First, we propose transformation pathways of NO_2 to N_2 or N_2O via NH_4NO_3 over H-AFX on the basis of the experimental evidences. Then, we discuss molecular-level insights into the role of BAS and NO_2 based on the theoretical results. The clarified mechanism will be useful for the rational control of NH_4NO_3 deposition and N_2O emission under NH_3–SCR operations in the practical system.

3.2. Experimental details

3.1.1 Sample preparation

NH4 + -form of AFX (Si/Al = 5.3), prepared using the method by Kubota et al., 1 was supplied from the Research Association of Automotive Internal Combustion Engines (AICE), Japan. H+ -exchanged AFX was prepared by calcining NH_4^+ -AFX at 600 ˚C for 1 h under air. Cu-AFX was prepared by ion-exchanging method using $Cu(NO_3)_2$ solution at a pH 5.5, followed by washing with distilled water (200 mL) three times, drying at 100 ˚C for 24 h, and by calcination under air at 600 ˚C for 1 h. Energy-dispersive X-ray fluorescence (EDX-700HS, Shimadzu Corp.) showed the Cu/Al of 0.13.

3.2.2 NH_3-SCR reaction

Catalytic reaction experiments were carried out in a fixed-bed flow reactor (quartz glass tube with an inner diameter of 4 mm) at atmospheric pressure suing powder samples of H-AFX (0.25 to 0.053 mm in size, 2-200 mg). The reaction temperature was measured by a thermocouple, whose tip was inside the upper side of the catalyst bed. The feed gas composition was regulated by the mass flow controllers of each individual gas line. The total flow rate was maintained at 100 mL min^{-1}, which resulted in a gas hourly space velocity (GHSV) of 501672 h^{-1} based on the packing density of the catalysts at 5.98 g cm^{-3} and catalyst weight at 2 mg. Concentrations of the feed gas and products were measured by an online IR spectrometer (JASCO Corp., FT/IR-4600) equipped with an 8 m gas cell (JASCO, LPC-8M-S) that was heated at 200 ˚C. Prior to steady-state reaction measurements, the catalyst was pretreated for 1 h at 600 ˚C under flowing 10% O_2/He. Standard SCR reaction was tested with a feed of 500 ppm NO, 500 ppm NH_3, 10% O_2, and balance He. Fast SCR was tested with a feed of 250 ppm NO, 250 ppm NO_2, 500 ppm NH_3, 10% O_2. For NO_2 SCR, a mixture of 500 ppm NO_2, 500 ppm NH_3, 10% O_2 was fed to the catalyst. The NOx conversion was determined by the following equation.

$$\text{NOx conversion (\%)} = \frac{(\text{NOx})\text{inlet} - (\text{NOx})\text{outlet}}{(\text{NOx})\text{inlet}} \times 100\%$$

For kinetic experiments, the rates of NOx reduction were evaluated under the conditions where conversions of NOx and NH_3 were below 60%.

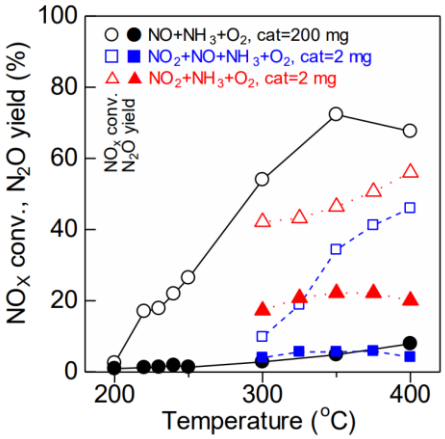

Figure 1. NOx conversion and N_2O yield for standard SCR, fast SCR, and NO_2 SCR over H-AFX. Standard SCR: 500 ppm NO, 500 ppm NH3, 10% O_2, 200 mg catalyst. Fast SCR: 250 ppm NO, 250 ppm NO_2, 500 ppm NH_3, 10% O_2, 2 mg catalyst. NO_2 SCR 500 ppm NO_2, 500 ppm NH_3, 10% O_2, 2 mg catalyst.

3.2.3 In situ IR and on-line MS

A transmission infrared (IR) spectroscopy was studied for in situ probing of the formation and reaction of adsorbed species on H-AFX. In situ IR spectra were recorded using a JASCO FT/IR4200 with a TGS (Triglycine sulfate) detector. H-AFX powder sample was pressed to obtain selfsupporting pellets (20 mmϕ, 40 mg), which were placed in the quartz IR cell with CaF_2 windows connected to a conventional gas flow system (100 mL min^{-1}). Spectra were measured accumulating 20 scans at a resolution of 4 cm^{-1}. A reference spectrum taken at a reaction temperature under He flow was subtracted from each spectrum. Prior to the measurements, the IR disc was heated under a flow of 10% O_2/He at 500 ˚C for 1 h and was cooled to a measuring temperature under a flow of 10% O_2/He, and by purging with He for 15 min. Note that preliminary IR results showed that adsorbed water and adsorbed NH_3 species were completely removed by the pretreatment. A mass spectrometer (BELMass, MicrotracBEL Corp.) was used for analyzing effluent gas (N_2 and N_2O). The MS signals were calibrated by flowing pure compound (N_2 or N_2O in He) of known concentrations.

3.2.4 TPSR

TPSR (temperature-programmed surface reaction) experiments were performed using the H-AFX powder (40 mg) placed in the flow reaction system (100 mL min^{-1}) connected to the IR gas analyzer

(JASCO FT/IR-4600 with the gas cell of 8 m path) and MS. The concentrations of NO and NO_2 were analyzed by IR: NO (1913-1910 cm^{-1}), NO_2 (2938-2854 cm^{-1}). The concentrations of N_2 and N_2O were analyzed by MS.

3.3. Results and Discussion

3.3.1 NO_2 effect on steady-states SCR on H-AFX

To explore the effect of NO_2 on the reaction rates of SCR over H-AFX catalysts, we carried out steady-state catalytic experiments under "standard SCR" (NO_2/NO_x = 0), "fast SCR" (NO_2/NO_x = 1/2), and "NO_2 SCR" (NO_2/NO_x = 1) conditions in a temperature range from 150 to 400 °C. An online IR spectrometer was used to measure the concentrations of the feed gas and products. It was found that the reaction rates of fast and NO_2 SCR reactions are significantly higher than those of standard SCR, and the NO conversions for standard SCR reaction are negligibly low under the same contact time condition. As the NO_2/NO_x ratio increases, the NO_x reduction rates at 200 °C increase in the following order: 0.02 mmol g^{-1} h^{-1} (NO_2/NO_x = 0), 2.89 mmol g^{-1} h^{-1} (NO_2/NO_x = 1/2), 27.36 mmol g^{-1} h^{-1} (NO_2/NO_x = 1). It is noteworthy that the NO_x reduction rate for fast SCR and NO_2 SCR is more than two orders of magnitude higher than that for standard SCR. This result is similar to the earlier report by Stevenson et al. for NH_3–SCR by H-ZSM-5, in which the rate of NO_2 SCR is several hundred times higher than that of standard SCR.[13]

Figure 2 depicts the Arrhenius plots with estimated apparent activation energies (E_a) for standard, fast, and NO_2 SCR reactions. The reaction rates were measured under the conditions with NO_x and NH_3 conversions between 20 and 55%. For standard SCR, the Arrhenius plot is a straight line in a temperature range of 150–400 ˚C, which gives an estimated E_a of 71 kJ mol^{-1}. This value is larger than the literature data for standard SCR by H-ZSM-5 (56.4 kJ mol^{-1}). For fast SCR, there are two kinetic regimes with distinct apparent activation energies. The E_a is 59 kJ mol^{-1} in the high temperature regime (275–350 ˚C), which becomes lower (12 kJ mol^{-1}) in the low temperature regime (150–225 ˚C). Similar temperature-dependent kinetic regimes for fast SCR over H-CHA were reported by Schneider et al.,[19] and this phenomenon was explained to associate with the dynamic change of active sites at different temperature. The kinetic experiment of NO_2 SCR gave the lowest E_a (3.8 kJ mol^{-1}). These results indicate that the presence of NO_2 in the feed gas decreases the apparent activation energy, thereby increasing the reduction rates of NO_x. For the product selectivity, the standard and fast SCR selectively convert NO_x to N_2, whereas half of N balance with NO_2 SCR yields N_2O between 300 and 400 °C. A significant amount of N_2O product during NO_2 SCR was previously reported for H-ZSM-5,[13,29] and the following reaction involving O_2 was suggested for N_2O production:

$$2NO_2 + 2NH_3 + O_2 \rightarrow 2N_2O + 3H_2O \qquad (4)$$

A separate experiment for NO oxidation by H-AFX was also performed. The rate of NO oxidation to NO_2 at 230 ˚C is 0.12 mmol g^{-1} h^{-1}, which is close to that of the standard SCR reaction (0.11 mmol g^{-1} h^{-1}). Considering the higher rate of fast SCR and NO_2 SCR than standard SCR, the

result suggests that NO_2 is a key intermediate of standard SCR by H-AFX, and NO oxidation is the rate-limiting step of standard SCR by H-AFX.

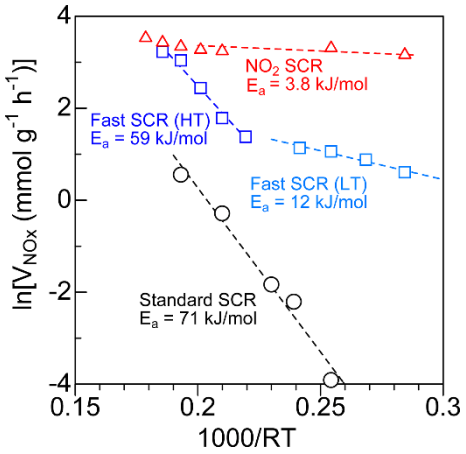

Figure 2. Arrhenius plots for standard SCR, fast SCR at high and low temperature (HT and LT) regimes, and NO_2 SCR over H-AFX zeolites.

3.3.2 Surface species during standard, fast, and NO_2 SCR

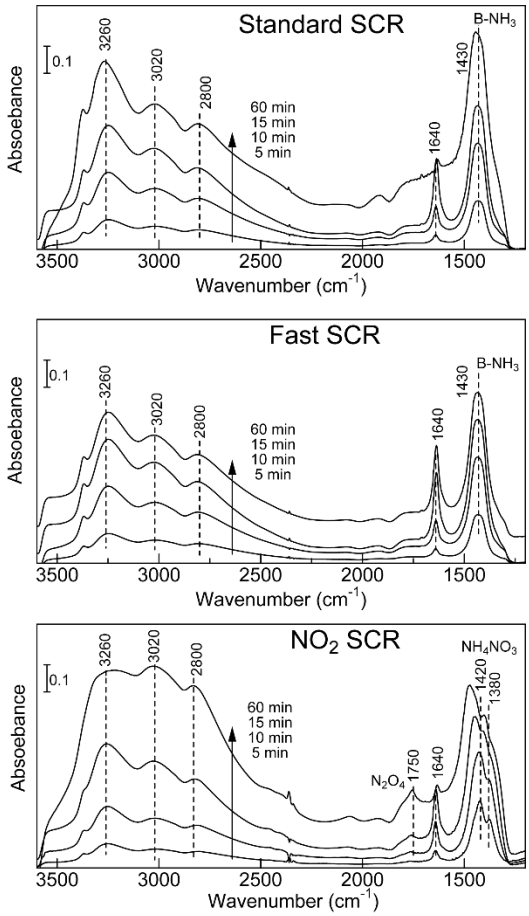

Figure 3. *In situ* IR spectra of adsorbed species on H-AFX (40 mg) during standard, fast, and NO_2 SCR at 150 ˚C.

In situ IR measurements were then carried out to characterize the surface species during standard, fast, and NO_2 SCR. The experiments were conducted at 150 ˚C using a disc of H-AFX (40 mg). As shown in **Figure 3**, strong IR bands due to NH_3 adsorbed on the BAS (NH_4^+ on zeolite oxygen, designated as B-NH_3) were observed at 1430, 2800, 3020, 3260 cm^{-1} during standard and fast SCR reactions. For standard SCR, the band probably due to adsorbed NO_2 (1640 cm^{-1}) was initially observed, and then its intensity decreased with time. Under the steady-state standard SCR conditions (t = 60 min), the B-NH_3 is the dominant adsorbed species. During fast SCR, the amount of the adsorbed NO_2 (1640 cm^{-1}) increased with reaction time, and the B-NH_3 and the adsorbed NO_2 co-exist in H-AFX under the steady-states (t = 60 min). In contrast to standard and fast SCR, bands at 1420 and 1380 cm^{-1} were observed during NO_2 SCR. Based on the previous reports,[17,30] these bands are assigned to NH_4NO_3 accumulated on the catalyst. The band due to N–H stretching vibrations of NH_4^+ (2800, 3020, 3250 cm^{-1}) are similar to those for standard and fast SCR, indicating that the B-NH_3 is also present in the catalyst under the NO_2 SCR conditions. After 60 min, a band at 1750 cm^{-1} probably due to N_2O_4 species[31] was observed.

3.3.3 Transient reaction of adsorbed NH_3 with NO_x + O_2 on H-AFX and Cu-AFX

To monitor the dynamic changes of the adsorbed species on H-AFX and the evolved gas products, we carried out time-resolved *in situ* IR experiments at 230 ˚C while monitoring mass spectroscopy (MS) signals of outlet gas (*in situ* IR-MS, i.e. *operando* IR). The flow type IR cell was connected on-line to the MS apparatus. The IR disc of H-AFX was first exposed to 0.1% NH_3/He flow for 10 min, followed by purging with He flow for 15 min. Then, *in situ* IR spectra were collected as a function of time with NO + O_2 or NO_2 + O_2 flowing (**Figure 4**). After purging with He, the B-NH_3 at 1430 cm^{-1} was observed, while NH_3 adsorbed on Lewis acid sites (around 1620 cm^{-1}) was not observed. Followed by NO + O_2 flowing (**Figure 4a**), the IR band due to B-NH_3 did not change markedly for 1000 s, and then the band intensity decreased with time. Simultaneously, the MS signal of N_2 (m/e = 28) was observed. Note that the MS intensities for N_2 correspond to the relative rates of N_2 formation. The N_2 formation continued until the adsorbed NH_3 was completely consumed. The induction period of 1000 s may be due to the blocking of active site (Brønsted acid site) by NH_3.[32]

When the NH_3-exposed H-AFX was exposed to a flow of NO_2 + O_2 for 1000 s (**Figure 4b**), IR spectrum assignable to NH_4NO_3 (NH_4^+ ,1420 cm^{-1}; NO_3^-, 1380 cm^{-1}) was observed. Using the reference spectra of NH_3 on BAS (B-NH_3) and NH_4NO_3, the spectra in a range of 1365-1560 cm^{-1} were deconvoluted to these two components (**Figure 1**). Then, the area of each component was plotted as a function of time in **Figure 4b** (right). After the induction period of 500 s, the intensity of B-NH_3 band decreased together with N_2 formation and the accumulation of NH_4NO_3. The maximum intensity of N_2 signal, which is the initial rate of N_2 formation, under NO_2 + O_2 is higher than that under NO + O_2, indicating that the NO_x reduction by adsorbed NH_3 is faster under NO_2 + O_2. Taking

into account the fact that NO_2 is produced by NO + O_2 on BAS of zeolites,[15] the N_2 formation over H-AFX is interpreted as the reduction of NO_2 by adsorbed NH_3 to yield N_2. As noted above, the rate of NO oxidation to NO_2 on H-AFX is relatively slow, which results in the slower rate of the transient N_2 formation under NO + O_2 than under NO_2 + O_2.

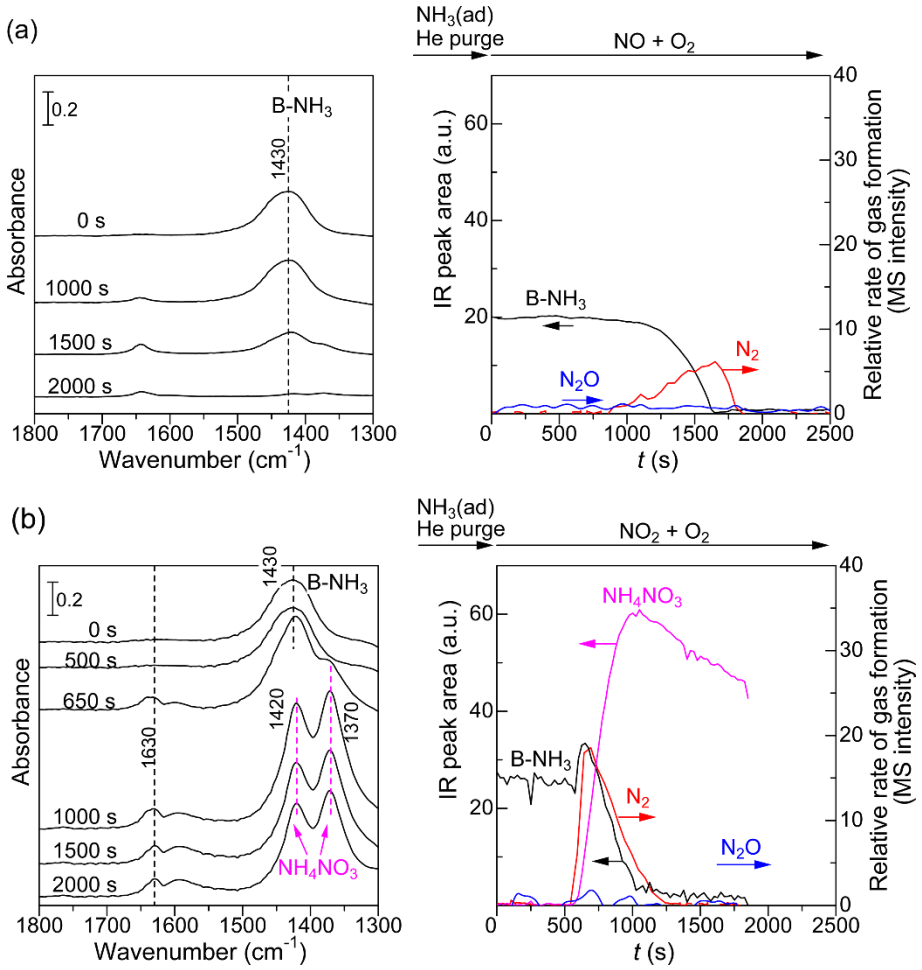

Figure 4. *In situ* IR spectra (left) of adsorbed species on H-AFX during the reaction of adsorbed NH_3 with NO_x at 230 ˚C (a) under 500 ppm NO + 10% O_2 and (b) under 500 ppm NO_2 + 10% O_2. The right figures show the time dependence of the IR peak area for surface species and the MS intensity of N_2.

The same experiments were then performed using the NH_3-exposed Cu-AFX. The IR-MS results under NO + O_2 and NO_2 + O_2 are shown in **Figure 5a and 5b**, respectively. After the He purge, the IR spectra show a peak at 1620 cm^{-1} due to NH_3 adsorbed on Cu(II) sites (designated as Cu-NH_3) together with a strong band due to NH_3 on BAS (B-NH_3, 1430 cm^{-1}). When the catalyst was exposed to a flow of NO + O_2 (**Figure 5a**), the intensity of these bands decreased, and simultaneously N_2 formation was observed by MS analysis. Within 800 s, these NH_3 species were completely consumed to give N_2.

In contrast to the results for H-AFX (**Figure 4**), the transient reaction of B-NH_3 under NO_2 + O_2 over Cu-AFX is much shower than the reaction under NO + O_2 (**Figure 5**). For Cu-AFX, the

lower rates of both B-NH_3 consumption and the N_2 formation were observed under NO_2 + O_2 than under NO + O_2. The completion of N_2 formation under NO_2 + O_2 required more than 2000 s, while N_2 formation was completed within 800 s under NO + O_2. Comparison of the results for the NO_2-involved SCR reactions over H-AFX and Cu-AFX (**Figure 4b** vs. **Figure 5b**) indicates that Cu sites show negative effect on the transient reaction of adsorbed NH_3 under NO_2 + O_2. This implies that BAS are the active site for the reduction of NO_2 by adsorbed NH_3, while Cu sites do not play an active role in this transient reaction. The comparison for H-AFX and Cu-AFX under NO + O_2 condition (**Figure 4a** vs. **Figure 5a**) indicates that Cu-AFX shows higher rates of N_2 formation and B-NH_3 consumption than H-AFX, which may be due to a higher rate of NO oxidation to NO_2 on Cu sites than on H^+ sites.

Additionally, IR bands due to the nitrate species on Cu^{n+} sites were observed at 1570, 1596, and 1620 cm^{-1} [33] for Cu-AFX under NO_2 + O_2 condition (**Figure 5b**). The accumulation of these nitrates on Cu-AFX catalyst suggests that the reaction of B-NH_3 with nitrate species on Cu sites is relatively slow. The role of such Cu nitrates in SCR reaction remains not fully unraveled, particularly whether they are involved in reaction cycle. [34,35] Nevertheless, recent time-resolved IR[35] and X-ray absorption spectroscopy (XAS)[36] studies on Cu-CHA show that the Cu nitrates are kinetically insignificant under typical low-temperature SCR conditions, indicative of their less important role in SCR cycle.

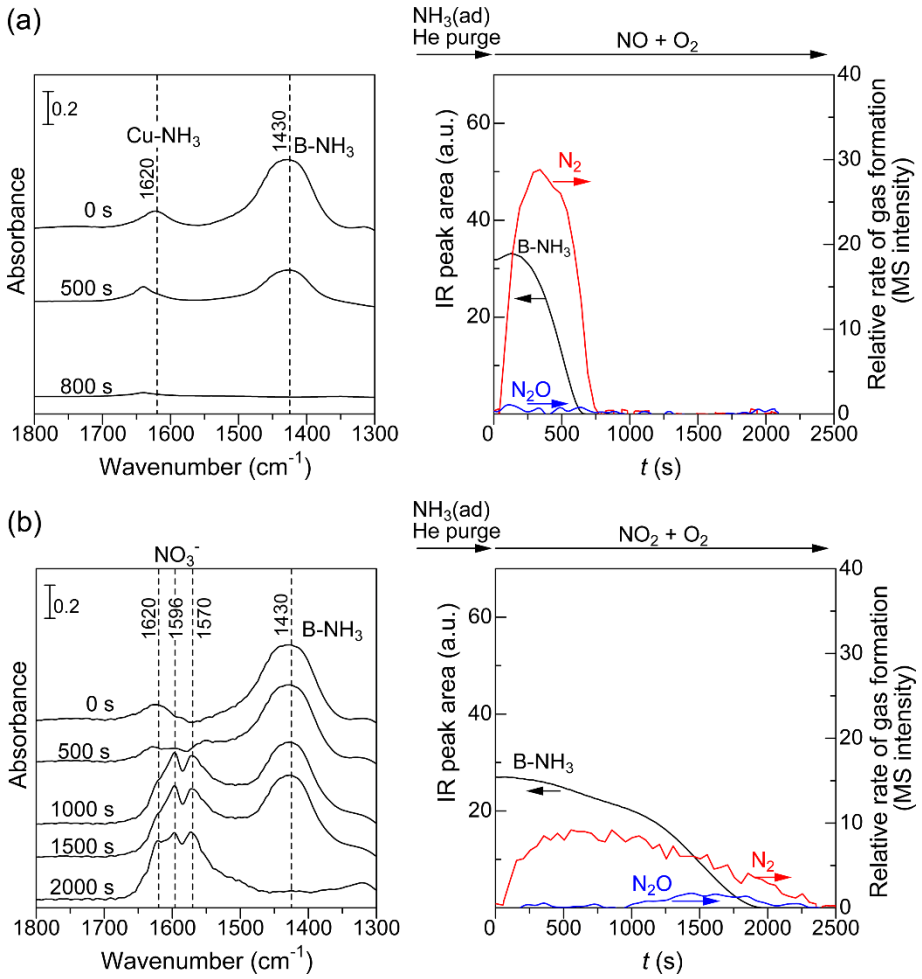

Figure 5. *In situ* IR spectra (left) of adsorbed species on Cu-AFX during the reaction of adsorbed NH_3 with NO_x at 230 ˚C (a) under 500 ppm NO + 10% O_2 and (b) under 500 ppm NO_2 + 10% O_2. The right figures show time dependence of IR peak area for surface species and the MS intensity of N_2.

3.3.4 Transient reaction of adsorbed NH_3 with NO_x on H-AFX

We then studied the H-AFX catalyzed reaction of B-NH_3 with NO_x in the absence of O_2. Transient experiments were performed at 150 ˚C for NH_3-exposed H-AFX to a flow of NO + NO_2 or NO_2 (**Figure 6**). Under NO + NO_2, B-NH_3 was consumed by NO + NO_2 to yield N_2 after the induction period of 500 s. In contrast, the reaction under NO_2 shows a higher rate of N_2 production and the significant amount of NH_4NO_3 accumulated on H-AFX. The absence of NH_4NO_3 accumulation under NO + NO_2 flow suggests that NO promotes decomposition of NH_4NO_3 [37,38] or NO inhibits the formation of NH_4NO_3.[30,37,38] The experimental observations suggest that NH_3 adsorbed on H^+ sites reacts with NO_2 to produce N_2 and NH_4NO_3 (Eqn. (5)). The produced NH_4NO_3 can further react with NO to yield N_2, NO_2 and H_2O (Eqn. (6)).

$$2NH_{3ad} + 2NO_2 \rightarrow N_2 + NH_4NO_3 + H_2O \quad (5)$$

$$NH_4NO_3 + NO \rightarrow N_2 + NO_2 + 2H_2O \quad (6)$$

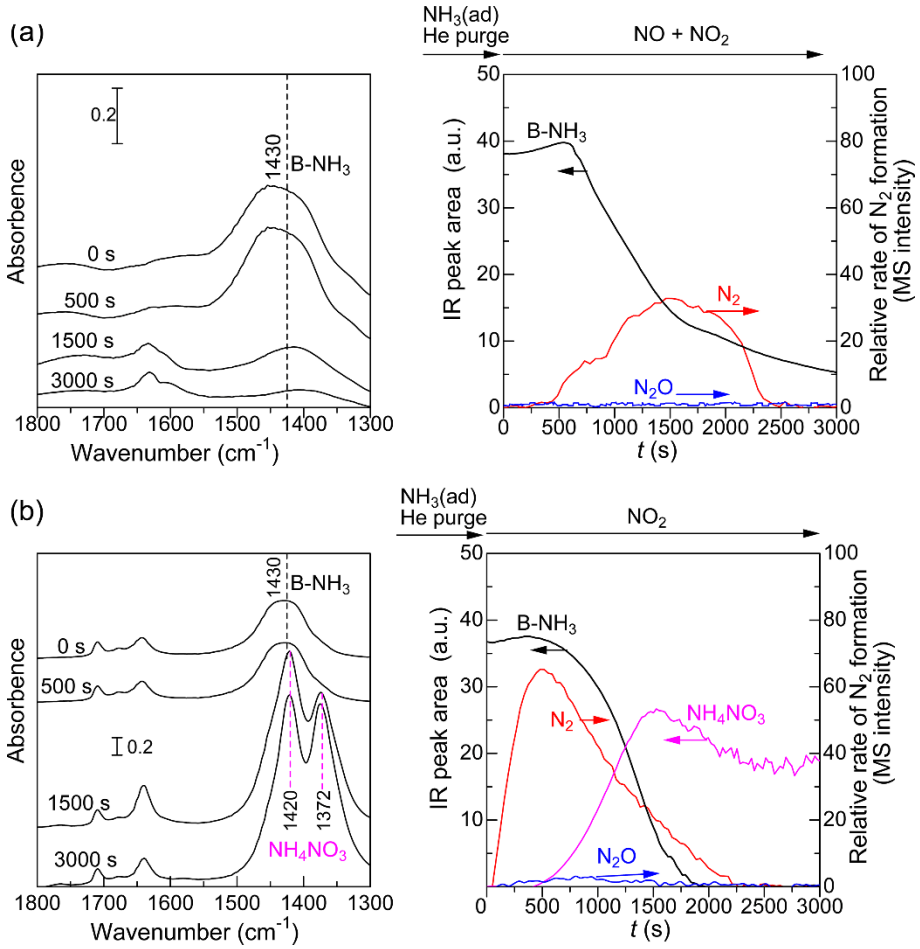

Figure 6. *In situ* IR spectra (left) of adsorbed species on H-AFX during the reaction of adsorbed NH_3 at 150 ˚C (a) under 250 ppm NO + 250 ppm NO_2 and (b) under 500 ppm NO_2. The right figures show time dependence of IR peak area for surface species and the MS intensity of N_2.

To better understand the temperature effect on reaction (5), we studied the temperature-programmed surface reaction (TPSR) of adsorbed NH_3 on H-AFX under a flow of NO_2 (**Figure 7**). IR disc of H-AFX was first exposed to 0.1% NH_3 for 0.5 h at 30 ˚C and followed by purging with He. Then, the catalyst was heated up to 500 ˚C (10 ˚C min^{-1}) under 500 ppm NO_2. The adsorbed species and outlet gas were monitored by IR and MS signals, respectively. Above 50 ˚C, B-NH_3 consumption, N_2 formation, and NH_4NO_3 accumulation on H-AFX were observed simultaneously. At 280 ˚C, NH_4NO_3 consumption and N_2O formation occurred simultaneously. The result shows that the reaction (5) occurs at temperature range of 50–150 ˚C. The reaction paths for NH_4NO_3 conversion to N_2O and the decomposition of NH_4NO_3 with NO to yield N_2 (Eqn. (6)) are discussed in the following section.

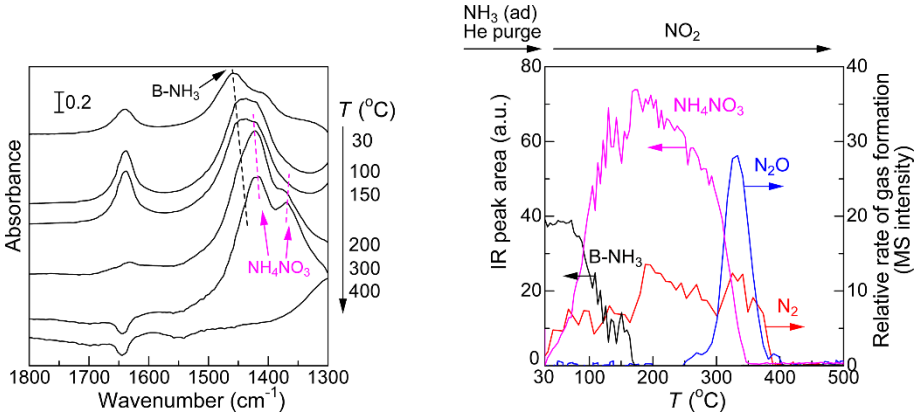

Figure 7. *In situ* IR spectra (left) during the temperature-programmed surface reaction (TPSR) of adsorbed NH_3 under 500 ppm NO_2 over H-AFX, pre-exposed to 500 ppm NH_3 at 30 ˚C (0.5 h). The right figures show time dependence of IR peak area for surface species and the MS intensity of N_2.

3.3.5 Conversion of NH_4NO_3 to N_2 or N_2O

To provide direct evidence of the reaction (6), we carried out *in situ* IR experiment of NH_4NO_3-loaded H-AFX in flowing NO at elevated temperatures. Following the methods in the literature[39–41], NH_4NO_3-loaded H-AFX (NH_4NO_3 loading of 1 mmol g^{-1}) was prepared by the impregnation method: 200 μL of 0.2 M NH_4NO_3 solution was added dropwise to 40 mg of H-AFX, followed by drying in an oven at 80 °C for 5 h. After obtaining the background IR spectrum of NH_4NO_3-impregnated H-AFX at 30 °C under He, the IR cell was heated (10 °C min^{-1}) under a flow of 500 ppm NO/He. **Figure 8** shows the IR difference spectra of NH_4NO_3-impregnated H-AFX at various temperature. As temperature increases, the negative peaks appeared at 1420, 1380, 3020, and 3260 cm^{-1}, indicating the consumption of adsorbed NH_4NO_3. Above 200 °C, the intensity of the negative peaks leveled off. The NO-assisted decomposition of NH_4NO_3 on SCR catalysts has been also reported by previous studies.[3842]

For the NH_4NO_3-impregnated H-AFX, the shape of the negative band is close to that of the positive bands appeared when NH_3-exposed H-AFX is exposed to a flow of NO_2 (**Figure S1**), which suggests that the impregnated NH_4NO_3 species in H-AFX is basically the same as the NH_4NO_3 formed by the reaction of NO_2 with NH_3. We also compared the IR spectra of physically mixed NH_4NO_3 and H-AFX, for which NH_4NO_3 particles are mainly present at the external surface of H-AFX. The comparison of IR spectra (**Figure S2**) suggests the physically mixed NH_4NO_3 gives different IR spectroscopic features as the one from NH_3 + NO_2 flow or impregnated NH_4NO_3, indicative of their different adsorption states. The NH_4NO_3 species generated from the reaction of NH_3 and NO_2 or impregnated from NH_4NO_3 solution are more likely adsorbed on the BAS rather than at the external surface of zeolite. The above comparisons show the NH_4NO_3 sample prepared from impregnation method is more appropriate to represent the state of accumulated NH_4NO_3 during the NH_3–SCR over H-AFX, and thus we used such a sample to further perform the TPSR as a model reaction of NH_4NO_3 inside the H-AFX zeolite. A lower amount of impregnated NH_4NO_3

(1.0 mmol g^{-1}) than the number of Al atoms in the H-AFX catalyst (2.7 mmol g^{-1}) was employed, which helps avoid the deposition of over-loaded NH_4NO_3 at the external surface of zeolite.

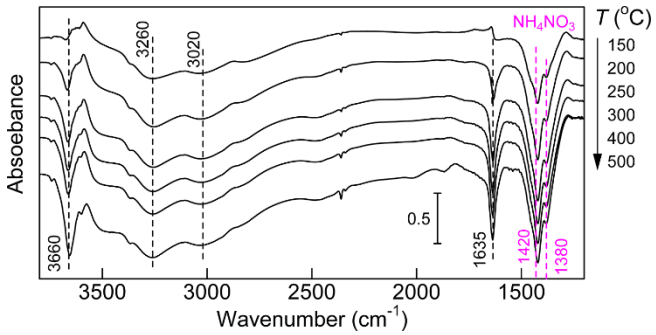

Figure 8. *In situ* IR spectra of 1 mmol g^{-1} NH_4NO_3-loaded H-AFX (40 mg) during heating (from 30°C to 500°C, 10 min^{-1}) under 500 ppm NO.

In a separate flow reactor, the TPSR experiments of NH_4NO_3(1 mmol g^{-1})-impregnated H-AFX (powder) were carried out in flowing of various gas mixture (**Figure 9**). N_2 and N_2O in the outlet gas were quantified using MS. As NO_2 was quantified by IR equipped with a long path (8 m) gas cell, the time response of NO_2 was slower than the other gases. The result under flowing NO **(Figure 9a**) shows the formation of N_2 and NO_2 in a temperature range of 50-200 ˚C. The tailing of NO_2 concentration above 200 ˚C can be due to slower response of the IR detector than MS. The formation of NO_2 indicates that NH_4NO_3 is reduced by NO to yield NO_2 and ammonium nitrite (NH_4NO_2), which is consistent with the pathway proposed by Weitz et al.[38,43,44] It is well known that NH_4NO_2 readily decomposes to N_2 and H_2O at low temperatures (< 100 ˚C).[43,44] Combined with the corresponding IR result in **Figure 8**, it is shown that the reaction (6) is composed of the following two reactions.

$$NH_4NO_3 + NO \rightarrow NO_2 + NH_4NO_2 \qquad (7)$$

$$NH_4NO_2 \rightarrow N_2 + H_2O \qquad (8)$$

In the absence of NO, the decomposition of NH_4NO_3 can afford N_2O.[37,45] The TPSR profile (**Figure 9b**) under He flow (in the absence of NO) shows N_2O formation in a temperature range of 200-350 ˚C with only trace amount of N_2. This indicates that N_2O is produced by NH_4NO_3 decomposition in the absence of NO (Eqn. (9)).[37]

$$NH_4NO_3 \rightarrow N_2O + 2H_2O \qquad (9)$$

The TPSR profile under NO_2 flow (**Figure 9c**) shows that N_2O is the main product, which is explained as follows. NO_2 decomposition to NO is slow over H-AFX, resulting in higher rate of the reaction (9) than the reaction (7).

In the NH_3–SCR conditions, NH_3 co-exsists in the gas mixture. We also studied the effect of NH_3 on the reactivity NH_4NO_3 under NO (**Figure 9d**). The TPSR profile of NH_4NO_3-loaded H-AFX in flowing NO + NH_3 results in lower amount of N_2 formation than the TPSR result under NO. Additinally, N_2O formation was accelerated by the NH_3 addition. It is obvious that NH_3 inhibits the

reaction (6), most likely the reaction (7), and consequently the reaction (9) is accelerated. Previously, Weitz et al.[38] studied the role of BAS of zeolite on the reduction of NH_4NO_3 by NO and showd that BAS catalytically promote the reaction (8). Under NO + NH_3 at low temperatures, NH_3 can be readily adsorbed on the BAS of H-AFX, which results in decrease in the number of the BAS available for the reaction (8), leading to lower amount of N_2 formation than the TPSR result. The TPSR experiment for NH_4NO_3-SiO_2 under NO shows no formation of N_2 and N_2O (result not shown), indicating that BAS are active sites for the key reactions for the formation of N_2 and N_2O, e.g. the reactions (7) and (9).

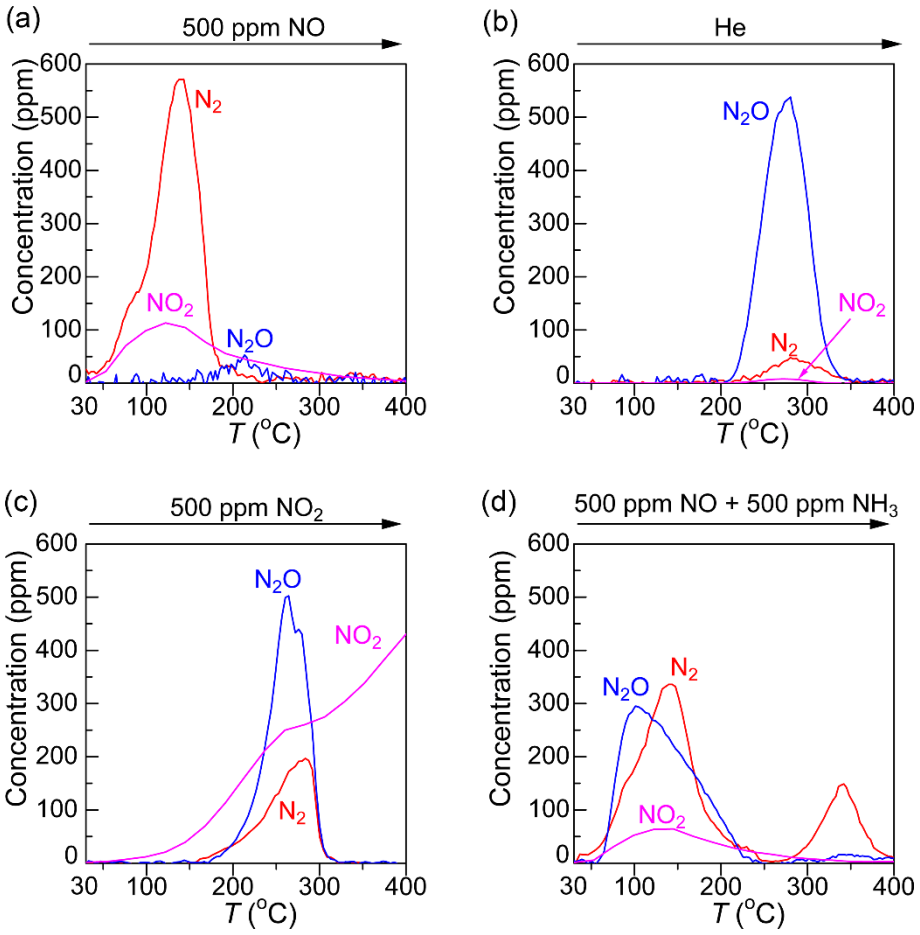

Figure 9. TPSR profile of 1 mmol g^{-1} NH_4NO_3-loaded H-AFX (40 mg) during heating (from 30 °C to 400 °C, 10 °C min^{-1}) under (a) 500 ppm NO, (b) He, (c) 500 ppm NO_2, and (d) 500 ppm NO + 500 ppm NH_3.

3.3.6 DFT study on NH_4NO_3 decomposition

To provide molecular-level insights into the elementary steps of NH_4NO_3 conversion over H-AFX, we further performed DFT calculations using a 48T hexagonal unit cell (**Figure S2**). First, the formation of N_2O from NH_4NO_3 was investigated (**Figure 10a**). The adsorption of NH_4NO_3 on the protonic H-AFX zeolite leads to the proton transfer from the BAS to the nitrate moiety, giving HNO_3

and NH_4^+, which are stabilized by hydrogen-bonding interactions at the negative oxygen sites of the zeolite framework. The decomposition of NH_4NO_3 into N_2O proceeds via two sequential dehydration reactions. The first dehydration occurs via a proton transfer from NH_4^+ to the OH moiety of the protonated nitrate group, which produces the H_2NNO_2 intermediate with a synchronous proton backdonation to the zeolite framework oxygen (Int_H_2NNO_2). This reaction is endothermic by 84 kJ/mol with an activation barrier of 138 kJ/mol. In the corresponding transition state (TS1), water molecule is already generated, and the NO_2 moiety interacts with the NH_3 fragment at a N–N distance ($d_{N–N}$) of 2.67 Å. The production of H_2NNO_2 intermediate is accompanied with N–N bond formation ($d_{N–N}$ = 1.48 Å) and the regeneration of BAS. The reorientation of H_2NNO_2 intermediate (Int_H_2NNO_2(reo)) decreases the system energy by -38 kJ/mol, which initializes the second dehydration reaction. With the participation of both the BAS and the water generated from the first dehydration, the conversion of H_2NNO_2 via TS2 proceeds with an activation barrier of 52 kJ/mol, and the production of N_2O strongly stabilizes the system by -91 kJ/mol. For this BAS catalyzed decomposition of NH_4NO_3 into N_2O and H_2O, the first dehydration to produce H_2NNO_2 intermediate is the rate-determining step with an activation barrier of 138 kJ/mol. When H-AFX is absent, the non-catalytic decomposition of NH_4NO_3 requires a much higher barrier of 181 kJ/mol for the first dehydration (**Figure S5**), indicative of the essential catalytic role of BAS during the conversion of NH_4NO_3 into N_2O.

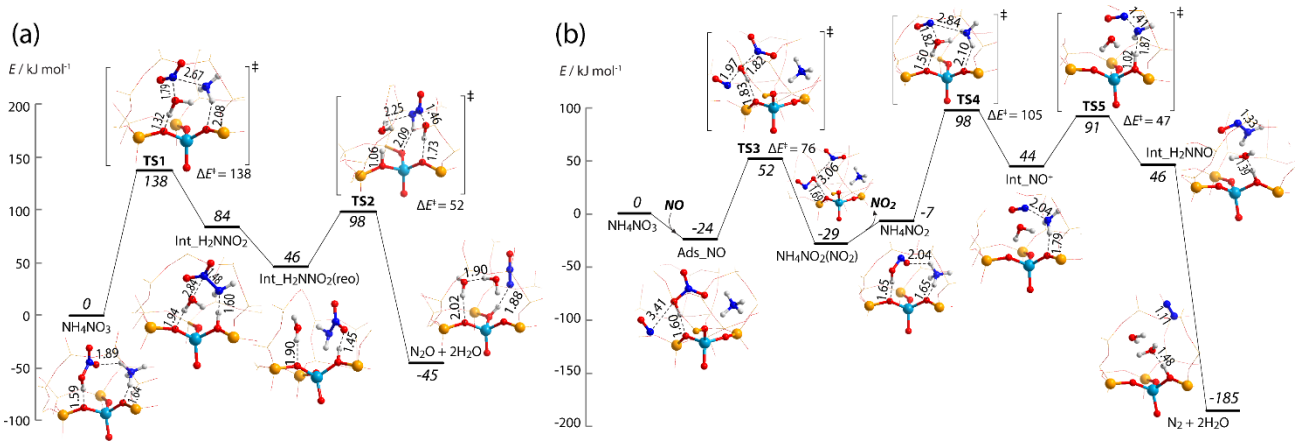

Figure 10. Energy profiles for the decomposition of NH_4NO_3 on protonic H-AFX zeolite: (a) direct decomposition of NH_4NO_3; (b) NO-assisted NH_4NO_3 decomposition via NH_4NO_2 intermediate. Atomic distances are indicated in angstrom (Å).

The NO-assisted NH_4NO_3 decomposition was then investigated and compared (**Figure 10b**). Based on our experimental evidences, it is assumed that NO first reacts with NH_4NO_3 to generate NO_2 and NH_4NO_2, which then decomposes into N_2 and H_2O. DFT results suggest the production of NH_4NO_2 is realized by the hydroxyl group transfer from the protonated nitrate group (HNO_3) to the adsorbed NO, which generates a nitrous acid (HNO_2) and a free NO_2 (HNO_3 + NO → HNO_2 + NO_2). This reaction occurs via TS3 with an activation barrier of 76 kJ/mol. The release

of NO_2 leads to the formation of HNO_2 moiety and NH_4^+ stabilized at the negative sites of zeolite, which can be considered as adsorbed NH_4NO_2 with its nitrite group protonated by the BAS. During such a conversion from ammonium nitrate to nitrite species, the NH_4^+ moiety is not directly involved but only acts as a spectator. The further decomposition reaction of NH_4NO_2 is similar to that of NH_4NO_3. However, the activation barrier for the first dehydration is much lower for NH_4NO_2 (TS4, $\Delta E^{\ddagger}$ = 105 kJ/mol) than for NH_4NO_3 (TS1, $\Delta E^{\ddagger}$ = 138 kJ/mol). Different from NH_4NO_3 decomposition where the H_2NNO_2 is produced in a single elementary step, the decomposition of NH_4NO_2 to H_2NNO occurs via a stepwise mechanism, in which a NO^+ intermediate is formed (Int_NO^+ in Figure 9b). The cationic nature of such a NO^+ intermediate was confirmed by Bader charge analysis (**Figure S4**). Comparison with the free gaseous NO (Q_N = +0.52 e) or its adsorption state in siliceous AFX framework (Q_N = +0.50 e), the cationic NO^+ possesses a much higher positive charge on the N terminal (Q_N = +0.80 e, Int_NO^+ in **Figure S4**), which is similar to the case (Q_N = +0.86 e) when the surrounding ammonia and water adsorbents were removed and only NO^+ was present at the negative site of $1Al^{3+}$ substituted AFX as charge-compensation cation. Such a NO^+ intermediate shows a high reactivity towards further reaction with NH_3, which only requires an activation barrier of 47 kJ/mol (TS5) to afford H_2NNO intermediate and a Brønsted proton connected back to the zeolite framework oxygen. The decomposition of H_2NNO occurs via proton transfers,[46,47] which affords the final product of N_2 and H_2O with a strong exothermicity. The results for the reactions of NH_4NO_3 over H-AFX are summarized in Scheme 2.

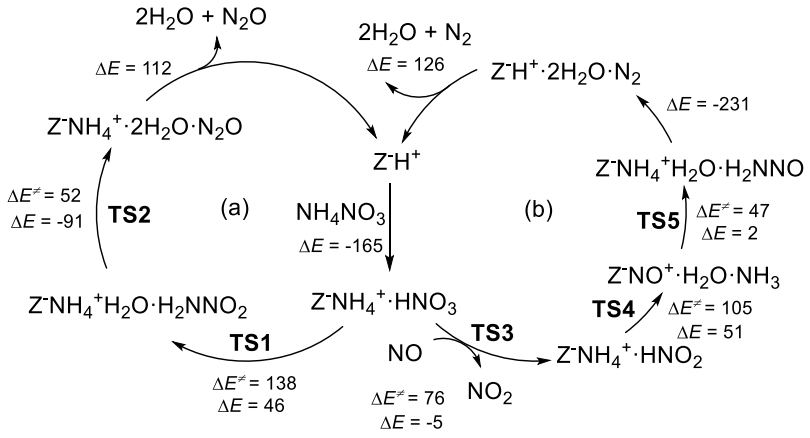

Scheme 1. DFT-calculated reaction paths of NH_4NO_3 under (a) non-NO-assisted and (b) NO-assisted conditions during NH_3–SCR reaction over H-AFX.

The comparison of the reaction profiles (**Figure 10** and **Scheme 1**) indicates that the direct NH_4NO_3 decomposition requires a much higher reaction barrier than the case of NO-assisted NH_4NO_3 decomposition. To further account for the temperature and entropy effect, we considered the Gibbs free energies of the key elementary steps (**Table S1**). The thermodynamic data were calculated using the results of frequency analysis. At the reaction temperature of 150 °C, the computed Gibbs free activation energies are 113 and 96 kJ/mol (TS1 and TS4) for the first

dehydration reaction of NH_4NO_3 and NH_4NO_2, respectively. For the reaction of NO with NH_4NO_3, the Gibbs free activation barrier of TS3 was calculated using the reference state of NH_4NO_3 and gaseous NO. The obtained barrier is 99 kJ/mol, which contains significant translational and rotational entropic contributions of free-state NO as the adsorption process has a strong negative entropy effect. The Gibbs free energy calculations show the reaction of NO and NH_4NO_3 to afford NO_2 and NH_4NO_2 requires a similar barrier (99 kJ/mol) as the further dehydration of NH_4NO_2 (96 kJ/mol), and these free energy barriers are lower than that of the first dehydration reaction of NH_4NO_3 (113 kJ/mol), which is the rate-determining step of the direct NH_4NO_3 decomposition. The presented data point that NO-assisted NH_4NO_3 decomposition to produce N_2 is more favorable than the direct NH_4NO_3 decomposition to N_2O, which is consistent with our experimental observation.

3.3.7 Reaction pathways of NH_3–SCR over H-AFX zeolite via NH_4NO_3

Summarizing the above experimental and theoretical results, the reaction pathways of NH_3–SCR via NH_4NO_3 over H-AFX is shown in **Scheme 2**. The first important role of BAS is to storage NH_3 forming NH_4^+. Then, BAS catalytically promotes the reaction of the adsorbed NH_3 with NO_2 to yield N_2, H_2O, and adsorbed NH_4NO_3 in a temperature range of 50–150 ˚C (**Figure 7**). The rate of NO reduction under the NO_2-free (standard) SCR conditions is two orders of magnitude lower than the NO_x reduction rates under fast SCR and NO_2 SCR conditions (**Figure 2**), possibly because NO_2 formation from BAS-catalyzed NO oxidation is too slow. Hence, addition of NO_2 significantly enhance the NO_x reduction rate. When NO is present (in fast SCR condition), the reduction of NH_4NO_3 by NO yields gas-phase NO_2 (**Figure 9a**) and NH_4NO_2, which then decompose into N_2 (**Figure 9a**) and H_2O at low temperatures. Hence, NH_4NO_3 accumulation in the zeolite is retarded by NO (**Figure 3, Figure 6a, and Figure 10a**). NH_3 inhibits this process by blocking the BAS as active sites of NH_4NO_3 reduction with NO (**Figure 9d**). In the absence of NO, NH_4NO_3 decomposition into N_2O and H_2O is catalyzed by BAS above 200 ˚C (**Figure 7, Figure 9b, and Figure 10b**). During steady-state fast SCR, NH_4NO_3 once formed on the catalyst are quickly consumed by its reaction with NO, so that NH_4NO_3 does not accumulate on the catalyst (**Figure 3**). In the case of NO_2 SCR, the NH_4NO_3 intermediate cannot react with NO and decomposes into N_2O and H_2O above 200℃. Consequently, nearly half of the reduced product is N_2O in steady-state NO_2 SCR. It should be pointed out that NH_4NO_3 may be continuously accumulated on the catalyst below 200℃, which makes it difficult to measure the steady-state reaction rates of NO_2 SCR below 200℃. In the metal-exchanged SCR catalyst, Cu (or Fe) sites catalyzes the oxidation of NO to NO_2, which results in higher rates of NH_4^+ consumption under NO + O_2 (**Figure 5a**). This pathway may contribute to the removal of NO under transient operation of the SCR system.

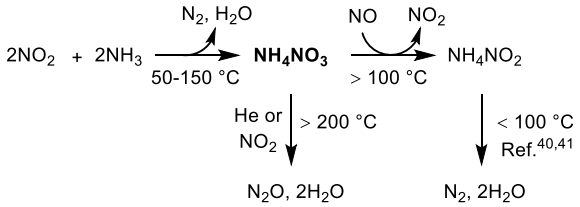

Scheme 2. Proposed mechanism for NH_3–SCR reaction over H-AFX.

3.4. Conclusion

We have investigated the formation and reactions of NH_4NO_3 during transient and steady-state NH_3–SCR of NO_x over H-AFX zeolites using *operando* IR spectroscopy, kinetic, and DFT studies. Steady-state kinetics shows that the SCR of NO_2 or NO/NO_2 mixture is more than two orders of magnitude faster than the SCR of NO. For NO_2 involved SCR over H-AFX, Brønsted acid sites (BAS) play an essential role, which promote the reaction of the adsorbed NH_3 with NO_2 to yield N_2, H_2O, and adsorbed NH_4NO_3 at low temperatures (50–150 ˚C). Transient *operando* IR and DFT studies suggest that when NO is present, NH_4NO_3 is reduced by NO to yield NO_2 and NH_4NO_2, and then NH_4NO_2 decomposes into N_2 and H_2O. Thus, NH_4NO_3 accumulation in zeolite is retarded by NO. In the absence of NO, the decomposition of NH_4NO_3 into N_2O and H_2O is more difficult, which is catalyzed by BAS at high temperatures (> 200 ˚C). The comparison of the SCR performance between H-AFX and Cu-AFX suggests that Cu sites only promote NH_3–SCR under NO + O_2 but show a negative effect under NO_2 + O_2, indicating the BAS rather than the Cu sites are the active site for the reduction of NO_2 by adsorbed NH_3. The presented results emphasize the essential roles of BAS and NO_2 in SCR by zeolite catalysts.

References

(1) Paolucci, C.; Di Iorio, J. R.; Ribeiro, F. H.; Gounder, R.; Schneider, W. F. *Catalysis Science of NOx Selective Catalytic Reduction With Ammonia Over Cu-SSZ-13 and Cu-SAPO-34*, 1st ed.; Elsevier Inc., 2016; Vol. 59. https://doi.org/10.1016/bs.acat.2016.10.002.

(2) Beale, A. M.; Gao, F.; Lezcano-Gonzalez, I.; Peden, C. H. F.; Szanyi, J. Recent Advances in Automotive Catalysis for NOx Emission Control by Small-Pore Microporous Materials. *Chem. Soc. Rev.* **2015**, *44* (20), 7371–7405. https://doi.org/10.1039/c5cs00108k.

(3) Liu, F.; Yu, Y.; He, H. Environmentally-Benign Catalysts for the Selective Catalytic Reduction of NOx from Diesel Engines: Structure-Activity Relationship and Reaction Mechanism Aspects. *Chem. Commun.* **2014**, *50* (62), 8445–8463. https://doi.org/10.1039/c4cc01098a.

(4) Xin, Y.; Li, Q.; Zhang, Z. Zeolitic Materials for DeNOx Selective Catalytic Reduction. *ChemCatChem* **2018**, *10* (1), 29–41. https://doi.org/10.1002/cctc.201700854.

(5) Luo, J.; Tang, Y.; Joshi, S.; Kamasamudram, K.; Currier, N.; Yezerets, A. The Impact of Ammonium Nitrate Species on Low Temperature NOx Conversion Over Cu/CHA SCR Catalyst. *SAE Int. J. Engines* **2017**, *10* (4). https://doi.org/10.4271/2017-01-0953.

(6) Ottinger, N.; Xi, Y.; Keturakis, C.; Liu, Z. G. Impact of Hydrothermal Aging on the Formation and Decomposition of Ammonium Nitrate on a Cu/Zeolite SCR Catalyst. *SAE Int. J. Engines* **2017**, *10* (4). https://doi.org/10.4271/2017-01-0946.

(7) Mao, Y.; Wang, Z.; Wang, H. F.; Hu, P. Understanding Catalytic Reactions over Zeolites: A Density Functional Theory Study of Selective Catalytic Reduction of NOx by NH_3 over Cu-SAPO-34. *ACS Catal.* **2016**, *6* (11), 7882–7891. https://doi.org/10.1021/acscatal.6b01449.

(8) Bates, S. A.; Verma, A. A.; Paolucci, C.; Parekh, A. A.; Anggara, T.; Yezerets, A.; Schneider, W. F.; Miller, J. T.; Delgass, W. N.; Ribeiro, F. H. Identification of the Active Cu Site in Standard Selective Catalytic Reduction with Ammonia on Cu-SSZ-13. *J. Catal.* **2014**, *312*, 87–97. https://doi.org/10.1016/j.jcat.2014.01.004.

(9) Eng, J.; Bartholomew, C. H. Kinetic and Mechanistic Study of NO x Reduction by NH_3 over H-Form Zeolites I. Kinetic and Mechanistic Insights into NO Reduction over H-ZSM-5. *J. Catal.* **1997**, *171* (1), 14–26. https://doi.org/10.1006/jcat.1997.1769.

(10) Eng, J.; Bartholomew, C. H. Kinetic and Mechanistic Study of NO x Reduction by NH_3 over H-Form Zeolites II. Semi-Steady-State and In Situ FTIR Studies. *J. Catal.* **1997**, *44* (2), 27–44.

(11) Brüggemann, T. C. Theoretical Investigation of the Selective Catalytic Reduction of Nitrogen Oxides with Ammonia on Fe/H-ZSM5. *J. Phys. Chem. C* **2008**, *112* (44), 17378–17387.

(12) Brüggemann, T. C.; Keil, F. J. Theoretical Investigation of the Mechanism of the Selective Catalytic Reduction of Nitric Oxide with Ammonia in the Presence of Oxygen on H-Form

Zeolites. *J. Phys. Chem. C* **2010**, *114* (14), 6567–6587.

(13) Stevenson, S. A.; Vartuli, J. C. The Selective Catalytic Reduction of NO_2 by NH_3 over HZSM-5. *J. Catal.* **2002**, *208* (1), 100–105. https://doi.org/10.1006/jcat.2002.3542.

(14) Long, R. Q.; Yang, R. T. Temperature-Programmed Desorption/Surface Reaction (TPD/TPSR) Study of Fe-Exchanged ZSM-5 for Selective Catalytic Reduction of Nitric Oxide by Ammonia. *J. Catal.* **2001**, *198* (1), 20–28. https://doi.org/10.1006/jcat.2000.3118.

(15) Long, R. Q.; Yang, R. T. Reaction Mechanism of Selective Catalytic Reduction of NO with NH_3 over Fe-ZSM-5 Catalyst. *J. Catal.* **2002**, *207* (2), 224–231. https://doi.org/10.1006/jcat.2002.3528.

(16) Colombo, M.; Nova, I.; Tronconi, E. A Comparative Study of the NH_3-SCR Reactions over a Cu-Zeolite and a Fe-Zeolite Catalyst. *Catal. Today* **2010**, *151* (3–4), 223–230. https://doi.org/10.1016/j.cattod.2010.01.010.

(17) Tronconi, E.; Nova, I.; Ciardelli, C.; Chatterjee, D.; Weibel, M. Redox Features in the Catalytic Mechanism of the “Standard” and “Fast” NH_3-SCR of NO_x over a V-Based Catalyst Investigated by Dynamic Methods. *J. Catal.* **2007**, *245* (1), 1–10. https://doi.org/10.1016/j.jcat.2006.09.012.

(18) Koebel, M.; Madia, G.; Elsener, M. Selective Catalytic Reduction of NO and NO_2 at Low Temperatures. *Catal. Today* **2002**, *73* (3–4), 239–247. https://doi.org/10.1016/S0920-5861(02)00006-8.

(19) Li, S.; Zheng, Y.; Gao, F.; Szanyi, J.; Schneider, W. F. Experimental and Computational Interrogation of Fast SCR Mechanism and Active Sites on H-Form SSZ-13. *ACS Catal.* **2017**, *7* (8), 5087–5096. https://doi.org/10.1021/acscatal.7b01319.

(20) Li, J.; Li, S. New Insight into Selective Catalytic Reduction of Nitrogen Oxides by Ammonia over H-Form Zeolites: A Theoretical Study. *Phys. Chem. Chem. Phys.* **2007**, *9* (25), 3304–3311. https://doi.org/10.1039/b700161d.

(21) Grossale, A.; Nova, I.; Tronconi, E.; Chatterjee, D.; Weibel, M. The Chemistry of the NO/NO_2-NH_3 “Fast” SCR Reaction over Fe-ZSM5 Investigated by Transient Reaction Analysis. *J. Catal.* **2008**, *256* (2), 312–322. https://doi.org/10.1016/j.jcat.2008.03.027.

(22) Xie, L.; Liu, F.; Liu, K.; Shi, X.; He, H. Inhibitory Effect of NO2 on the Selective Catalytic Reduction of NO_x with NH3 over One-Pot-Synthesized Cu-SSZ-13 Catalyst. *Catal. Sci. Technol.* **2014**, *4* (4), 1104–1110. https://doi.org/10.1039/c3cy00924f.

(23) Shan, Y.; Shi, X.; He, G.; Liu, K.; Yan, Z.; Yu, Y.; He, H. Effects of NO_2 Addition on the NH_3-SCR over Small-Pore Cu-SSZ-13 Zeolites with Varying Cu Loadings. *J. Phys. Chem. C* **2018**, *122* (45), 25948–25953. https://doi.org/10.1021/acs.jpcc.8b05930.

(24) Szanyi, J.; Kollár, M.; Peden, C. H. F.; Wang, Y.; Washton, N. M.; Gao, F. Effects of Si/Al Ratio on Cu/SSZ-13 NH_3-SCR Catalysts: Implications for the Active Cu Species and the Roles of Brønsted Acidity. *J. Catal.* **2015**, *331*, 25–38. https://doi.org/10.1016/j.jcat.2015.08.004.

(25) Morpurgo, S. The Mechanism of NO and N_2O Decomposition Catalyzed by Short-Distance Cu(I) Pairs in Cu-ZSM-5: A DFT Study on the Possible Role of NO and NO_2 in the $[Cu–O–Cu]^{2+}$ Active Site Reduction. *J. Catal.* **2018**, *366* (2), 189–201. https://doi.org/10.1016/j.jcat.2018.08.006.

(26) Iwasaki, M.; Shinjoh, H. A Comparative Study of “Standard”, “Fast” and “NO_2” SCR Reactions over Fe/Zeolite Catalyst. *Appl. Catal. A Gen.* **2010**, *390* (1–2), 71–77. https://doi.org/10.1016/j.apcata.2010.09.034.

(27) Fickel, D. W.; D’Addio, E.; Lauterbach, J. A.; Lobo, R. F. The Ammonia Selective Catalytic Reduction Activity of Copper-Exchanged Small-Pore Zeolites. *Appl. Catal. B Environ.* **2011**, *102* (3–4), 441–448. https://doi.org/10.1016/j.apcatb.2010.12.022.

(28) Nakazawa, N.; Inagaki, S.; Kubota, Y. Novel Technique to Synthesize AFX-Type Zeolite Using a Bulky and Rigid Diquaternary Ammonium Cation. *Adv. Porous Mater.* **2016**, *4* (3), 219–229. https://doi.org/10.1166/apm.2016.1114.

(29) Wallin, M.; Karlsson, C. J.; Skoglundh, M.; Palmqvist, A. Selective Catalytic Reduction of NOx with NH3 over Zeolite H-ZSM-5: Influence of Transient Ammonia Supply. *J. Catal.* **2003**, *218* (2), 354–364. https://doi.org/10.1016/S0021-9517(03)00148-9.

(30) Ciardelli, C.; Nova, I.; Tronconi, E.; Chatterjee, D.; Bandl-Konrad, B.; Weibel, M.; Krutzsch, B. Reactivity of NO/NO_2-NH_3 SCR System for Diesel Exhaust Aftertreatment: Identification of the Reaction Network as a Function of Temperature and NO_2 Feed Content. *Appl. Catal. B Environ.* **2007**, *70* (1–4), 80–90. https://doi.org/10.1016/j.apcatb.2005.10.041.

(31) Penkova, A.; Hadjiivanov, K.; Mihaylov, M.; Daturi, M.; Saussey, J.; Lavalley, J. C. FTIR Spectroscopic Study of Low Temperature NO Adsorption and NO + O_2 Coadsorption on H-ZSM-5. *Langmuir* **2004**, *20* (13), 5425–5431. https://doi.org/10.1021/la0496643.

(32) Grossale, A.; Nova, I.; Tronconi, E. Ammonia Blocking of the “Fast SCR” Reactivity over a Commercial Fe-Zeolite Catalyst for Diesel Exhaust Aftertreatment. *J. Catal.* **2009**, *265* (2), 141–147. https://doi.org/10.1016/j.jcat.2009.04.014.

(33) Ruggeri, M. P.; Nova, I.; Tronconi, E.; Pihl, J. A.; Toops, T. J.; Partridge, W. P. In-Situ DRIFTS Measurements for the Mechanistic Study of NO Oxidation over a Commercial Cu-CHA Catalyst. *Appl. Catal. B Environ.* **2015**, *166–167* (2), 181–192. https://doi.org/10.1016/j.apcatb.2014.10.076.

(34) Janssens, T. V. W.; Falsig, H.; Lundegaard, L. F.; Vennestrøm, P. N. R.; Rasmussen, S. B.; Moses, P. G.; Giordanino, F.; Borfecchia, E.; Lomachenko, K. A.; Lamberti, C.; et al. A Consistent Reaction Scheme for the Selective Catalytic Reduction of Nitrogen Oxides with Ammonia. *ACS Catal.* **2015**, *5* (5), 2832–2845. https://doi.org/10.1021/cs501673g.

(35) Zhang, Y.; Peng, Y.; Li, K.; Liu, S.; Chen, J.; Li, J.; Gao, F.; Peden, C. H. F. Using Transient FTIR Spectroscopy to Probe Active Sites and Reaction Intermediates for Selective Catalytic Reduction of NO on Cu/SSZ-13 Catalysts. *ACS Catal.* **2019**, 6137–6145. https://doi.org/10.1021/acscatal.9b00759.

(36) Marberger, A.; Petrov, A. W.; Steiger, P.; Elsener, M.; Kröcher, O.; Nachtegaal, M.; Ferri, D. Time-Resolved Copper Speciation during Selective Catalytic Reduction of NO on Cu-SSZ-13. *Nat. Catal.* **2018**, *1* (3), 221–227. https://doi.org/10.1038/s41929-018-0032-6.

(37) Shan, Y.; Shi, X.; He, G.; Liu, K.; Yan, Z.; Yu, Y.; He, H. Effects of NO_2 Addition on the NH_3-SCR over Small-Pore Cu-SSZ-13 Zeolites with Varying Cu Loadings. *J. Phys. Chem. C* **2018**, *122* (45), 25948–25953. https://doi.org/10.1021/acs.jpcc.8b05930.

(38) Savara, A.; Li, M. J.; Sachtler, W. M. H.; Weitz, E. Catalytic Reduction of NH_4NO_3 by NO: Effects of Solid Acids and Implications for Low Temperature DeNOx Processes. *Appl. Catal. B Environ.* **2008**, *81* (3–4), 251–257. https://doi.org/10.1016/j.apcatb.2007.12.008.

(39) Xie, L.; Liu, F.; Liu, K.; Shi, X.; He, H. Inhibitory Effect of NO_2on the Selective Catalytic Reduction of NO_x with NH_3 over One-Pot-Synthesized Cu-SSZ-13 Catalyst. *Catal. Sci. Technol.* **2014**, *4* (4), 1104–1110. https://doi.org/10.1039/c3cy00924f.

(40) Tronconi, E.; Nova, I.; Nováková, J.; Bernauer, M.; Sazama, P.; Sobalík, Z. Mechanistic Study of the NO + NH_4NO_3 Reaction on H- and Fe/H-BEA Zeolites Using 15N and 18O Labeled Species. *Top. Catal.* **2018**, *61* (18–19), 1967–1973. https://doi.org/10.1007/s11244-018-1026-y.

(41) Pereira, M. V. L.; Berthout, D.; Petitto, C.; Delahay, G.; Raux, S.; Rousseau, S. Ammonium Nitrate Temperature-Programmed Decomposition on Fe–Zeolite Catalysts: Effect of Deposition Method. *ChemCatChem* **2017**, *9* (12), 2339–2343. https://doi.org/10.1002/cctc.201700147.

(42) Selleri, T.; Gramigni, F.; Nova, I.; Tronconi, E. NO Oxidation on Fe- and Cu-Zeolites Mixed with BaO/Al_2O_3: Free Oxidation Regime and Relevance for the NH_3-SCR Chemistry at Low Temperature. *Appl. Catal. B Environ.* **2018**, *225* (September 2017), 324–331. https://doi.org/10.1016/j.apcatb.2017.11.068.

(43) Li, M.; Henao, J.; Yeom, Y.; Weitz, E.; Sachtler, W. M. H. Low Activation Energy Pathway for the Catalyzed Reduction of Nitrogen Oxides to N_2 by Ammonia. *Catal. Letters* **2004**, *98* (1), 5–9. https://doi.org/10.1007/s10562-004-6441-y.

(44) Li, M.; Yeom, Y.; Weitz, E.; Sachtler, W. M. H. An Acid Catalyzed Step in the Catalytic Reduction of NO x to N_2. *Catal. Letters* **2006**, *112* (3–4), 129–132. https://doi.org/10.1007/s10562-006-0191-y.

(45) Chen, H. Y.; Wei, Z.; Kollar, M.; Gao, F.; Wang, Y.; Szanyi, J.; Peden, C. H. F. A Comparative Study of N_2O Formation during the Selective Catalytic Reduction of NOx with NH_3 on Zeolite Supported Cu Catalysts. *J. Catal.* **2015**, *329*, 490–498. https://doi.org/10.1016/j.jcat.2015.06.016.

(46) Sun, D.; Schneider, W. F.; Adams, J. B.; Sengupta, D. Molecular Origins of Selectivity in the Reduction of NO_x by NH_3. *J. Phys. Chem. A* **2004**, *108* (43), 9365–9374. https://doi.org/10.1021/jp049079a.

(47) Paolucci, C.; Verma, A. A.; Bates, S. A.; Kispersky, V. F.; Miller, J. T.; Gounder, R.;

Delgass, W. N.; Ribeiro, F. H.; Schneider, W. F. Isolation of the Copper Redox Steps in the Standard Selective Catalytic Reduction on Cu-SSZ-13. *Angew. Chemie - Int. Ed.* **2014**, *53* (44), 11828–11833. https://doi.org/10.1002/anie.201407030.

Result details

Curve fitting for IR spectra analysis

For analysis of IR spectra, we employed Python 3.2 using the Spyder (Anaconda3) integrated development environment. After measurement of *in situ* IR on-line MS and reference spectra (see Section 1.3 here above), we fitted each experimental *in situ* IR spectra as a linear combination of the two reference spectra, and denotes each experimental point in fitted wavenumber range from 1300 to 1500 cm^{-1}. The reference of B-NH_3 which was shown as red line in Figure S1 is the condition which H-AFX catalysis disc was introduced 0.1% NH_3(800s) next to He purge. The reference of NH_4NO_3 which was shown as blue line in Figure S1 is the condition which H-AFX catalysis disc was pre-exposed to NH_3 (800 s), was exposed to 500 ppm NO_2+10% O_2 for 2000 s, in other words, the condition shows that adsorbed species of NH_4NO_3 is completely saturated over H-AFX catalysis disc.

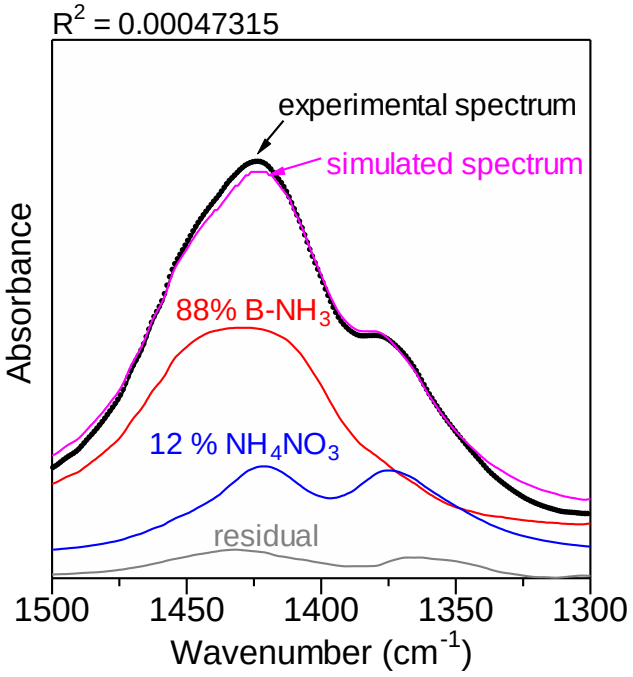

Figure S1. Curve-fitting of the IR spectrum (N–H stretching and N–O stretching regions) for a mixture of NH_3 on BAS and NH_4NO_3 at 230 ˚C. H-AFX, pre-exposed to NH_3 (800 s), was exposed to 500 ppm NO_2+10% O_2 for 881 s.

Verification of NH_4NO_3 impregnated in zeolite

As shown in Figure 7, NH_4NO_3-loaded H-AFX (NH_4NO_3 loading of 1 mmol g^{-1}) was prepared by the impregnation method. The spectrum (a) in Figure S2 was measured the sample of mixture 5 wt% NH_4NO_3 and KBr powder under the air and room temperature after taking background KBr disc and using by KBr windows. The spectrum (b) in Figure S2 was measured the sample of mixture 5 wt% NH_4NO_3 and H-AFX under the air and room temperature after taking background only H-AFX disc

and without using window. The spectrum (c) in Figure S2 is NH_4NO_3 over BAS on H-AFX by NH_3+NO gas. Three spectra indicate that these situation are difference between only NH_4NO_3(Figure S2(a)), NH_4NO_3 particles outside the zeolite(Figure S2(b)) and NH_4NO_3 adsorbed BAS (Figure S2(c)).

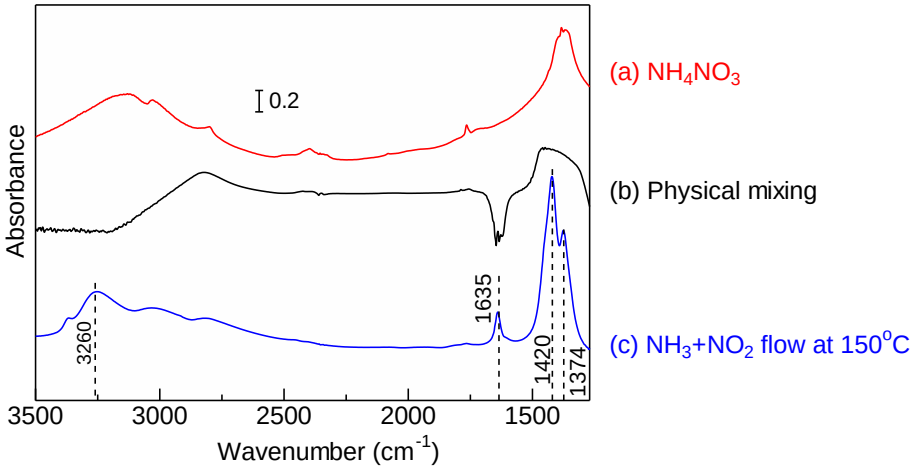

Figure S2. *In situ* IR spectra at 150 ˚C of samples (a) was prepared by physical mixing 5wt% NH_4NO_3 powder and KBr (40 mg); (b) was prepared by physical mixing 5wt% NH_4NO_3 powder and H-AFX (40 mg); (c) was introduced by 0.1 % NH_3+500 ppm NO_2/He (100 mL min^{-1}) to H-AFX (40 mg).

DFT calculation

Method of DFT calculation

Periodic DFT calculations were performed using the Vienna Ab initio Simulation Package (VASP) version 5.4.4.[456] The Perdew-Burke-Ernzerhof (PBE) functional[7] with the projector augmented wave (PAW) method[89] was used. The cut-off energy of the plane wave basis sets was set to 500 eV. The Brillouin zone sampling was restricted to the Γ point.[10] To account for the van der Waals interactions, the dispersion-corrected DFT-D3 (BJ) method was employed.[11] Geometries were assumed to be converged when the force on each atom was below 0.05 eV $Å^{-1}$. The climbing image nudged elastic band (CI-NEB) method was applied to determine the minimum-energy reaction paths and to locate the corresponding transition states.[12] Vibrational frequency calculations using the finite difference method (0.02 Å atomic displacements) were performed to confirm the nature of transition states, which show a single imaginary frequency corresponding to the reaction path. For the reaction of ammonia nitrate with NO, spin-polarized calculations were applied to account for the unpaired elections in the reaction system.

AFX zeolite was modelled by a 48T hexagonal unit cell.[13] The cell parameters were optimized for the all-silica zeolite cell ($Si_{48}O_{96}$). The optimized lattice parameters are a = b = 13.70 Å, c = 19.73 Å, which show good agreement with the experimental values (a = b = 13.67 Å, c = 19.70 Å). To introduce the Brønsted acid site (BAS), one lattice Si was substituted by an Al atom, and a Brønsted proton was located on the neighboring oxygen site as charge-compensating cation (Figure 1). Then full geometry optimizations were performed with fixed lattice parameters.

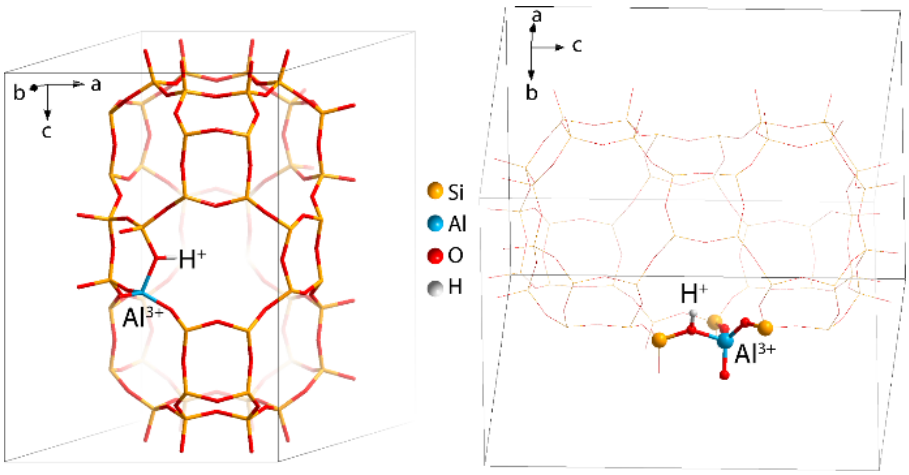

Figure S3. Computational model of protonic AFX zeolite (views from different directions).

Additional DFT results

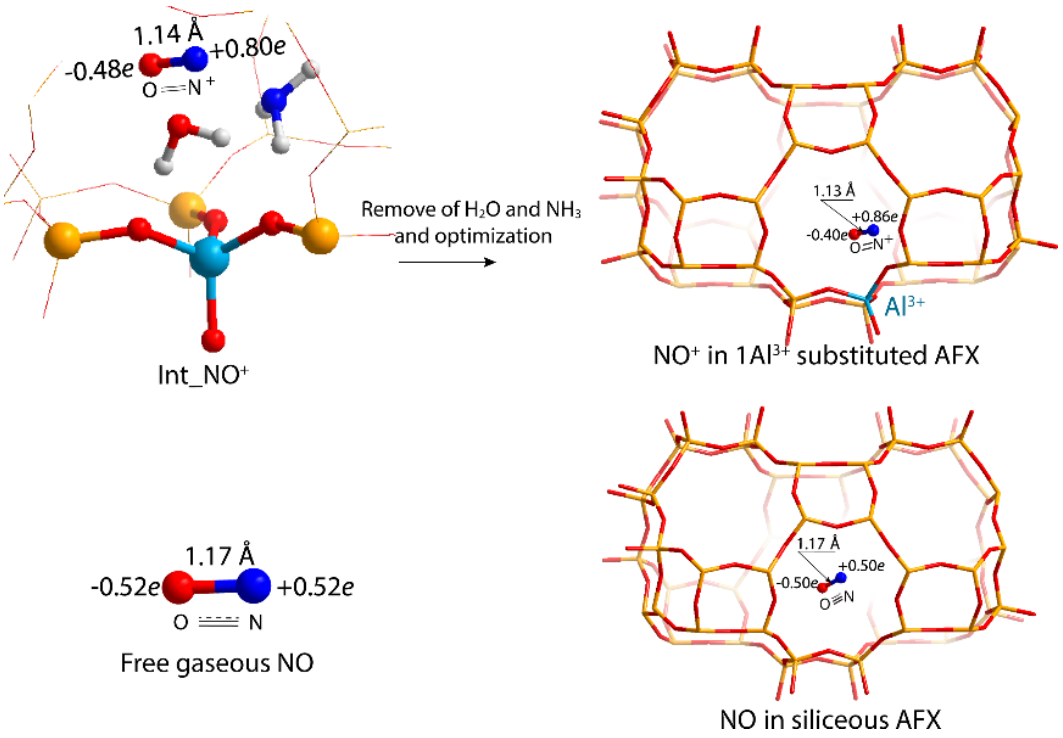

Figure S4. Bader charge analysis of NO^+ cation and neutral NO molecule during SCR process.

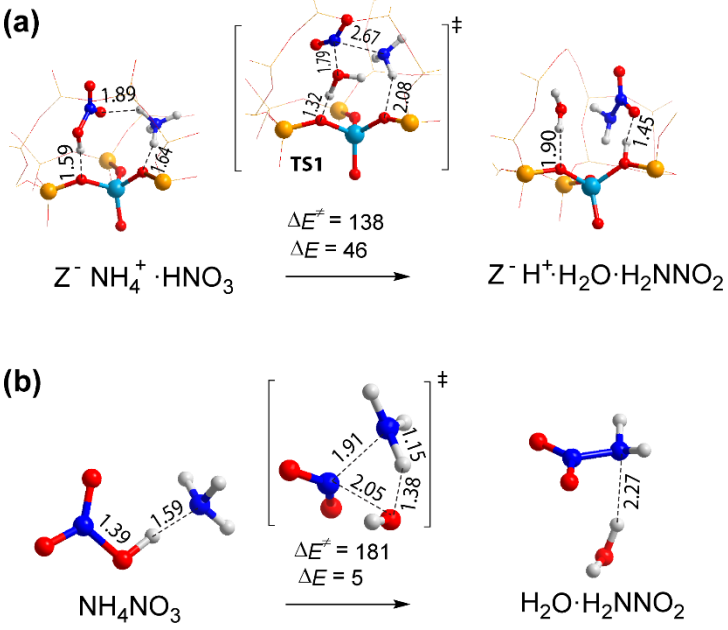

Figure S5. Effect of protonic AFX zeolite on the decomposition of NH_4NO_3: (a) BAS promoted dehydration; (b) non-catalytic dehydration. Activation and reaction energies ($\Delta E^{\ddagger}$ and ΔE) are given in kJ/mol.

Table S1. Activation Gibbs free energies ($\Delta G^{\ddagger}$) of the key elementary steps during NH_4NO_3 decomposition. Energies are given in kJ/mol.

Transition state	$\Delta E^{\ddagger}$	$\Delta G^{\ddagger}$ (150 °C)
TS1	138	113
TS3	52	99[a]
TS4	105	96

[a] For the reaction of NO with NH_4NO_3 (TS3), the $\Delta G^{\ddagger}$ was calculated using the reference state of NH_4NO_3 and gaseous free-state NO.

Chapter 4

Operando Spectroscopic Study of Reduction and Oxidation Half Cycles in NH_3–SCR over CeO_2-Supported WO_3

4.1. Introduction

The selective catalytic reduction of NO_x using NH_3 (NH_3–SCR) catalyzed by Cu- or Fe-exchanged zeolites is a state-of-the-art technology for NO_x purification in diesel vehicles.[1] V-based oxide catalysts have been widely utilized for NO_x emission control from stationary sources for a long time.[2] Among V-free oxide catalysts, which have been reported as a new class of NH_3–SCR catalysts,[3–7] CeO_2-based catalysts modified with acidic oxides[8–24] (such as WO_3, MoO_3, and TiO_2) have recently attracted considerable attention. W–Ce oxides are of particular interest[9–14] owing to their high NO_x conversion over a wide temperature range at high gas hourly space velocity (GHSV), adequate H_2O/SO_2 durability, and high N_2 selectivity (low N_2O emission). He et al. reported that a Ce–W mixed oxide ($CeWO_x$) prepared using the homogeneous precipitation method showed 100% NO_x conversion over a wide temperature range of 250–425 °C at a GHSV of 500000 h^{-1}.[11] This was a pioneering work demonstrating that a V-free oxide catalyst exhibits higher NO_x conversion than commercial catalysts (V_2O_5–WO_3/TiO_2 and Fe-ZSM-5). Iwasaki et al.[12,13] showed that WO_3-loaded CeO_2 (WO_3/CeO_2) catalysts prepared using the conventional impregnation method were effective for NH_3–SCR. They showed detailed structure-activity relationship study on NH_3–SCR over WO_3/CeO_2 as a function of the effect of W content (W surface density) and proposed that interface sites between WO_3 clusters (NH_3 adsorption sites) and CeO_2 (redox sites) are active sites for NH_3–SCR.[13] Moreover, they proposed that NO oxidation is a key reaction in the NH_3–SCR by WO_3/CeO_2. Interestingly, the number of redox active sites for NO oxidation increased with increasing loading of WO_3 clusters (acidic sites).[12] He et al.[9,10] reported mechanistic studies on NH_3–SCR over $CeWO_x$ and reported two types of N_2 formation pathways: the reaction between NO and NH_4NO_3 to form N_2, H_2O, and NO_2 (termed the NH_4NO_3 path) and the reaction between nitrite and adsorbed NH_3 to form N_2 and H_2O (termed the nitrite path). The mechanistic details of NH_3–SCR using Ce–W oxide catalysts remain unclear and are the subject of the present study.

Compared with the number of studies on V-free oxide catalysts, a larger number of studies have been devoted to the molecular-level understanding of NH_3–SCR mechanisms over Cu-zeolite[1,25–36] and V-oxide[2,36–39] catalysts. Although the mechanisms for the two types of SCR catalysts have been separately discussed, a literature survey suggests that there is a common principle in the NH_3–SCR mechanism over these catalysts.[36] Based on *in situ* and *operando* spectroscopic evidence combined with previous proposals in the literature, we demonstrated an analogous mechanistic feature of the NH_3–SCR over Cu-zeolites and V_2O_5-based catalysts, which is based on the redox couple of the metal cation species, $Cu^{2+} \leftrightarrow Cu^{+}$ or $V^{5+} \leftrightarrow V^{4+}$ (**Figure S1**).[36] For example, for the Cu-zeolite catalyst, the initial step of the catalytic cycle is the reduction of $Cu^{2+}(OH^-)$ species by NH_3 + NO to afford Cu^+, N_2, and H_2O, the so-called reduction half cycle (RHC). The Cu^+ species then undergoes oxidation half cycle (OHC) by O_2 and hydration to regenerate the $Cu^{2+}(OH^-)$ species. The detailed mechanism of RHC remains unclear; however, a possible route is the nitrous acid (HONO) route[25–30] where reduction of $Cu^{2+}(OH^-)$ by NO yields Cu^+ and HONO, which reacts with NH_3 to yield N_2 and H_2O possibly via ammonium nitrite (NH_4NO_2). Gao et al.[39]

reported experimental and theoretical evidence of the HONO route in NH_3–SCR over V_2O_5-loaded CeO_2. In the redox cycle, the oxidation state of the V species remained V^{5+}; however, the $V^{5+}(OH^-)$ species promoted the reduction of Ce^{4+} by NO to yield Ce^{3+} and HONO. Instead of Cu- and V-based catalysts, few studies have focused on molecular insights into RHC and OHC over V-free CeO_2-based catalysts.

Based on this background, we hypothesized that the catalytic cycle of NH_3–SCR by WO_3/CeO_2 also involves the redox reaction of surface species (**Figure S1c**). To verify this hypothesis, RHC and OHC over WO_3/CeO_2 under transient reaction conditions were studied using time-resolved *operando* IR, UV-vis, and X-ray absorption spectroscopy (XAS) in combination with the observation of gas-phase products. The $Ce^{4+} \leftrightarrow Ce^{3+}$ or $W^{6+} \leftrightarrow W^{5+}$ redox couple can be involved in the catalytic cycle; therefore, we conducted *operando* XAS studies at the Ce L_3- and W L_3-edge. Combined with theoretical studies, the molecular-level mechanisms of NH_3–SCR over WO_3/CeO_2 are discussed.

4.2. Materials and methods

4.2.1 Catalyst preparation

CeO_2 (Type B) was supplied by Daiichi Kigenso Kagaku Kogyo Co. Ltd. The WO_3-loaded CeO_2 catalysts were prepared by impregnating CeO_2 with an aqueous solution of ammonium metatungstate hydrate and 3 equiv. of oxalic acid, followed by evaporation to dryness, drying at 100 °C (12 h), and calcination at 600 °C (3 h). A V_2O_5 and WO_3 co-loaded TiO_2 catalyst, V(1)W(5)/TiO_2 (V = 1 wt%; W = 5 wt%), was prepared using a sequential impregnation method. TiO_2 (P25) was impregnated with an aqueous solution of ammonium metatungstate hydrate and 3 equiv. of oxalic acid, followed by evaporation to dryness, drying at 100 °C (12 h), and calcination at 600 °C (3 h). Thereafter, the powder was impregnated with an aqueous solution of NH_4VO_3, followed by evaporation to dryness, drying at 100 °C (12 h), and calcination at 600 °C (3 h). The $NH4^+$ form of the CHA zeolite (Si/Al = 13) was procured from Tosoh (Japan). CHA zeolite was calcined in air at 600 °C to obtain H-type CHA. In **Table 1**, the catalysts are designated as WO_3(*x*)/CeO_2, where *x* denotes the W loading (wt%).

Table 1. Structural properties of the catalysts.

Catalysts	W loading (wt%)	S_{BET} (m^2 g^{-1})	W density (nm^{-2})
CeO_2	0	148	0
WO_3(1)/CeO_2	1	136	0.24
WO_3(5)/CeO_2	5	82	1.99
WO_3(10)/CeO_2	10	68	4.75

4.2.2 *In situ/operando* spectroscopic experiments

IR spectra were collected in the transmission mode using an FT/IR-4100 (JASCO) unit with an MCT detector. A self-supporting disk of the samples (90 mg) was placed in a handmade *in situ* glass cell with CaF_2 windows. Diffuse reflectance UV-vis spectra were acquired using a spectrometer (JASCO V-670) equipped with a commercial *in situ* flow cell with a quartz window (JASCO) containing 20 mg of the powdered catalyst. For the *in situ* IR and UV-vis experiments, a gas mixture (typically 0.1% NH_3, 0.1% NO, and 10% O_2 under He) was fed to the cells through a conventional flow reaction system at a total flow rate of 100 cm^3 min^{-1}. Prior to the measurements, the catalysts were pre-oxidized *in situ* under O_2/He at 500 °C. Subsequently, time-resolved measurements were performed at 200 °C. The *operando* IR and UV-vis measurements were performed by monitoring the formation of N_2 in the outlet gas mixture using a mass spectrometry (MS) apparatus (BELMass, MicrotracBEL Corp.). Detailed descriptions of the *operando* IR and UV-vis analyses are provided in our previously published report.[35]

Ce L_3- and W L_3-edge X-ray absorption near-edge structure (XANES) spectra were collected in the transmission mode using the BL14B2 beamline at SPring-8 (Harima, Japan). The storage ring was operated at 8 GeV. A Si(111) single crystal was used to obtain monochromatic X-ray beams. A sample pellet prepared using 1.36 mg of the WO_3(10)/CeO_2 catalyst diluted in boron nitride 42 mg (φ: 7 mm) was introduced into a quartz *in situ* cell equipped with Kapton film windows and gas lines connected to the mass spectrometer. The catalyst was pre-treated under a flow of 10% O_2/He (1000 cm^3 min^{-1}) at 200 °C for 0.5 h. After purging with He, the reaction gas mixture (typically containing 0.1% NH_3, 0.1% NO, and 10% O_2 with He as a balance gas) was fed at a total flow rate of 1000 cm^3 min^{-1}. XANES analysis was conducted using Athena software ver. 0.9.25, which is included in the Demeter package.[40]

Ambient-pressure X-ray photoelectron spectroscopy (AP-XPS) measurements were conducted at beamline 13 B of the Photon Factory (PF) at the High Energy Accelerator Research Organization (KEK). Powder WO_3(10)/CeO_2 catalysts were coated onto a Si substrate using deionized water as a dispersant via a drop-and-dry method. The sample temperatures were measured using a thermocouple directly attached to the sample holder in the analysis chamber. The gases were introduced into the chamber using variable leak valves. The sample was heated to 200 °C under exposure to 0.1 Torr O_2 at a heating rate of 10 °C min^{-1}. W 4f and Ce 3d measurements were performed at a photon energy of 630 eV under various gas conditions. The binding energy was calibrated using the C 1s peak (284.5 eV). The W 4f and Ce 3d XPS profiles were analyzed by the convolution of Gaussian and Lorentzian with a Shirley background in the ranges of 33–39 and 876–895 eV, respectively.

4.2.3 Catalytic tests for NH_3–SCR

The catalytic tests for NH_3–SCR were conducted using a fixed-bed flow reactor (Pyrex tube; inner diameter of 4 mm) by feeding a gas mixture of 1000 ppm NO, 1000 ppm NH_3, and 10% O_2 with He (balance gas) at a total flow rate of 100 cm^3 min^{-1}. The outlet concentrations of NO, NO_2, N_2O, and NH_3 were quantified using an online IR spectrometer (JASCO FT/IR-4600, TGS detector, 20 scans) with a homemade gas cell (CaF_2 windows) based on the calibration data for each gas. The NO_x reduction rates were evaluated under conditions wherein the conversion of NO and NH_3 was below 40%.

4.2.4 Other characterization

X-ray diffraction (XRD) patterns were obtained using a Rigaku MiniFlex II/AP diffractometer with Cu-Kα radiation. Bright-field scanning transmission electron microscopy (BF-STEM) and high-angle annular dark-field STEM (HAADF-STEM) combined with energy dispersive X-ray spectroscopy (EDX) mapping observation were conducted using a JEOL JEM-ARM200F microscope (JEOL).

4.2.5 Computational methods

Periodic DFT calculations were performed using the Vienna ab initio simulation package (VASP, version 5.4.4)[41,42] and Matlantis. For VASP, the Perdew–Burke–Ernzerhof functional revised for solids (PBEsol)[43] was employed in combination with the projector-augmented wave (PAW) method.[44] A kinetic energy cutoff of 400 eV was used for the plane-wave basis sets. Gaussian smearing with a width of 0.2 eV was applied to occupy the electronic levels. The k-point mesh includes only the gamma point of the Brillouin zone (1 × 1 × 1). Van der Waals interactions were described using a dispersion-corrected DFT-D3 (BJ) function.[45] The convergence of the force on each atom was set to 0.03 eV $Å^{-1}$. The effect of adding Hubbard U was considered based on Dudarev's formulation.[46] The effective *U* value (denoted as U_{eff}) of $U - J$ was set to 5 eV for Ce and 3 eV for W.[47]

For universal neural network potential (NNP) calculations using Matlantis (version 2.0.0)[48], all all-atom energy optimizations were conducted using the Broyden–Fletcher–Goldfarb–Shanno (BFGS) algorithm with a force threshold of 0.01 eV $Å^{-1}$.

The CeO_2(111) surface was simulated using supercell slab models (**Figure S4**). The repeated slabs along the surface-normal direction were separated by a minimum vacuum region thickness of 15 Å. The two bottom layers were fixed at their original bulk positions.

The O vacancy formation energy (E_{Ovac}) is defined as:

$$E_{Ovac} = E_{removed} - E_{perfect} + \frac{1}{2}E_{O_2}, \quad (1)$$

where $E_{removed}$ and $E_{perfecct}$ are the slab energies after and before removal of one O atom, respectively. E_{O2} is the total energy of an isolated O_2 molecule.

The differential charge density ($\Delta\rho$) of the supported tungsten oxide species is defined as

$$\Delta\rho = \rho_{WO_x/CeO_2} - \rho_{WO_x} - \rho_{CeO_2}, \quad (2)$$

where $\rho_{WOx/CeO2}$, ρ_{WOx}, and ρ_{CeO2} are the charge densities of the CeO_2-supported tungsten oxide, free-state tungsten oxide, and bare CeO_2(111) surfaces, respectively. Bader charge analysis was also performed to evaluate the valence state of tungsten on the surfaces of metal oxides.[48]

4.2.6 *Ab initio* thermodynamic analyses

Ab initio thermodynamic analysis was performed to investigate the effects of reaction gases (O_2 and H_2O) and temperature on the tungsten oxide species on the CeO_2(111) surface. The enthalpy and entropy at each temperature and standard state pressure (1 atm) were obtained from the NIST-JANAF Thermochemical Tables.[49] Tungsten acid (H_2WO_4) was used to determine the energy of the tungsten oxide species. The energies of the gas molecules were obtained using a large empty unit cell (25 Å × 25 Å × 25 Å) to mimic the isolated species. The equilibrium reaction,

energy change (Δ*E*), Gibbs free energy change (Δ*G*), and chemical potential change (Δ*μ*) under H_2 and H_2O atmospheres are given by Eq. (3)–(6).

$$x\mathrm{H_2WO_4} + \mathrm{CeO_2} + \left(-x + \frac{1}{2}z\right)\mathrm{H_2O} + \left(-\frac{3}{2}x + \frac{1}{2}y - \frac{1}{4}z\right)\mathrm{O_2} \rightarrow \left(\mathrm{W_xO_yH_z}\right)/\mathrm{CeO_2} \quad (3)$$

$$\Delta E = E\left[\left(\mathrm{W_xO_yH_z}\right)/\mathrm{CeO_2}\right] - xE[\mathrm{H_2WO_4}] - \left(-x + \frac{1}{2}z\right)E[\mathrm{H_2O}] - \left(-\frac{3}{2}x + \frac{1}{2}y - \frac{1}{4}z\right)E[\mathrm{O_2}] \quad (4)$$

$$\Delta G(T,p) = \Delta E - \left(-x + \frac{1}{2}z\right)\Delta\mu_{H_2O} - \left(-\frac{3}{2}x + \frac{1}{2}y - \frac{1}{4}z\right)\Delta\mu_{O_2} \quad (5)$$

$$\Delta\mu_{gas} = \Delta\mu_{gas}(T,p^0) + RTln\left(\frac{p_{gas}}{p^0}\right) \ (\mathrm{gas} = \mathrm{O_2 \ and \ H_2O}) \quad (6)$$

Here, $W_xO_yH_z/CeO_2$ is the CeO_2-supported tungsten oxide species, $E[W_xO_yH_z/CeO_2]$ is the total energy of the species, $E(CeO_2)$ is the total energy of the $CeO_2(111)$ slab model, $E(O_2)$ and $E(H_2O)$ represent the total energies of the gas molecules, $\Delta\mu_{gas}$ is the change in the chemical potential of the gases involved in the reaction (Eq. (6)), T is the temperature (K), p^0 is the atmospheric pressure, and p_{gas} is the partial pressure of the reaction gas.

4.2.7 Diffuse reflectance infrared Fourier transform (DRIFT) using a phase-sensitive detection analysis technique

DRIFT spectra were collected using a Vertex70 spectrometer (Bruker) equipped with an MCT detector. The spectra were recorded from 4000 to 1000 cm^{-1} at a resolution of 4 cm^{-1} and scanner velocity of 80 kHz. The sample and background spectra were obtained by averaging 10 and 50 scans, respectively. Approximately 50 mg of the sample was loaded into a custom-built spectroscopic cell[50], which was equipped with a 2-mm-thick calcium fluoride window (Crystran) and attached to a Praying Mantis™ diffuse reflection accessory (Harrick).

Time-resolved DRIFT spectra from at least five equilibrated modulation periods were converted into phase-resolved spectra using the following equation:

A (φ^{PSD}) = $\frac{2}{T}$ $\int_0^T A(t)$ sin ($k\omega t + \varphi^{PSD}$) dt,

(7)

where $A(\varphi^{PSD})$ is the absorbance in the phase-resolved spectra, T is the modulation period, A(t) is the absorbance in the time-resolved spectra, k is the demodulation index (k = 1 in this study), ω is the stimulation frequency, and φ is the phase angle.

4.3. Results and discussion

4.3.1 Structure–activity relationship

To elucidate the effects of the W content (W surface density) of WO_3-loaded CeO_2 (WO_3/CeO_2) catalysts on their structure, acid–base properties, and catalytic activity for NH_3–SCR, the sample details listed in **Table 1** display the W loading, surface area, and W density of WO_3/CeO_2 catalysts. The catalyst acidity was tested by IR observation of NH_3 species adsorbed on the WO_3/CeO_2 catalysts at 200 °C (**Figure 1a**). W-free CeO_2 ($WO_3(0)/CeO_2$) and the low-W-loading sample ($WO_3(1)/CeO_2$) show a band at 1150 cm^{-1} assignable to NH_3 adsorbed on Lewis acid sites (exposed cation sites). The $WO_3(1)/CeO_2$ sample exhibits a shoulder peak at 1184 cm^{-1}. For the high-W-loading samples ($WO_3(5)/CeO_2$ and $WO_3(10)/CeO_2$), the band at 1150 cm^{-1} is not observed; however, the band at 1184 cm^{-1} is clearly observed. Therefore, the bands at 1150 and 1184 cm^{-1} can be assigned to NH_3 adsorbed on the Ce^{4+} and W^{6+} sites, respectively. The IR band at 1418 cm^{-1} assignable to NH_3 adsorbed on Brønsted acid sites is observed for the high-W-loading samples ($WO_3(5)/CeO_2$ and $WO_3(10)/CeO_2$). According to Iwasaki et al., the basic sites of CeO_2 serve as NOx adsorption sites.[13] Using this information, the relative number of basic sites (in other words, uncovered CeO_2 surface) can be estimated by exposing the IR disk to NO + O_2 at 200 °C (**Figure 1b**). Bare CeO_2 without W loading shows strong bands at 1560, 1530, 1250, and 1210 cm^{-1} assignable to nitrates (NO_3^-), that is, NO_2 species adsorbed on the basic sites (negative oxygen sites) of CeO_2.[51] The intensity of these bands decreases with W loading, and the sample with the highest W loading ($WO_3(10)/CeO_2$) shows no band due to the presence of NO_3^- on CeO_2. The intensity of the NH_3 adsorbed on the W^{6+} sites (hereafter named L-NH_3) at 1184 cm^{-1} as well as the Brønsted acid sites (B-NH_3) and NO_3^- on CeO_2 are plotted in **Figure 1c** as a function of W density. These results indicate that the basic surface of the CeO_2 support is covered by an acidic oxide (WO_3), consistent with the results reported by Iwasaki et al.[13]

Figure 2a plots the temperature dependence of NO conversions for $WO_3(0)/CeO_2$, $WO_3(10)/CeO_2$, and V_2O_5 and WO_3 co-loaded TiO_2 ($V(1)$-$W(5)/TiO_2$) as a standard catalyst for NH_3–SCR.[2] The NO conversions of $WO_3(10)/CeO_2$ are considerably higher than those of W-free CeO_2 ($WO_3(0)/CeO_2$), indicating that WO_3 is an indispensable structural element for NH_3–SCR catalysis. The NO conversions for $WO_3(10)/CeO_2$ are higher than those for $V(1)$-$W(5)/TiO_2$, demonstrating that the high-W-loading WO_3/CeO_2 catalyst can replace the well-established V-based NH_3–SCR catalysts. Kinetic results for NH_3–SCR by these catalysts at 200 °C are shown in **Figure 2a**. By adjusting the catalyst weight, NH_3–SCR rates were measured under the conditions where the NO conversions were below 40%. The NO reduction rates linearly increase with W density, indicating that WO_3 species are involved in the rate determining step of the catalytic cycle. The amount of Brønsted acid sites increases with W density; however, those of Lewis acid sites and the uncovered CeO_2 surface show different trends (**Figure 2b**). Therefore, it can be concluded that the Brønsted acid sites of WO_3 species (W^{6+}-OH sites) play an essential role in NH_3–SCR.

Experimental structural analysis was performed to reveal the structures of the supported WO_3 species. The XRD patterns of a series of WO_3/CeO_2 samples with different loading amounts

of WO_3 are identical to that of bare CeO_2 (**Figure S2**), irrespective of the loading amount of tungsten. HAADF-STEM and EDX mapping observations were conducted for $WO_3(10)/CeO_2$ (**Figure 3**). Clearly, WO_3 is highly dispersed over the ceria surface.

A computational study was conducted to further clarify the plausible structures of the supported W oxide species. An *ab initio* thermodynamic approach was employed.[52] This method enables the assessment of system stabilities under reaction conditions by calculating the relative Gibbs free energies (ΔG). Various W oxide clusters with 1–4 W atoms were considered possible structures, as shown in **Figure S6**. Note that only the most stable structures for each chemical formulation obtained are shown for clarity. The valence state of W was set to 6^+ for all structures considered to be consistent with the experimental observations. **Figure 4** shows the phase diagram of the W oxide species, with the lowest relative ΔG values in terms of the temperature and partial pressure of H_2O. The trimeric species, $W_3O_{12}H_6$, is the most stable around the reaction temperature (below 300 °C), whereas the tetrameric species, $W_4O_{13}H_2$, is the most stable at higher temperatures (and lower H_2O partial pressures). The other structures considered, including monomeric and dimeric structures, are relatively unstable under these conditions.

The same *ab initio* thermodynamic analysis was performed using computational results calculated by Matlantis instead of VASP. Matlantis employs universal NNPs called PreFerred Potentials (PFPs), which support various elements and material types with an accuracy comparable to that of DFT calculations and significantly lower computational costs.[48] If rational results were obtained with Matlantis, it would enable us to significantly reduce the computational time even for unknown systems. **Figure S5** displays the phase diagram of the W oxide species, with the lowest relative ΔG values, in terms of the temperature and partial pressure of H_2O obtained from the computational results calculated by Matlantis. This result is similar to that obtained using VASP, confirming its high reliability. These results obtained through the *ab initio* thermodynamic approach indicate that trimeric species can be produced under the current reaction conditions, consistent with the results of the XAS, XRD, and STEM-EDX investigations.

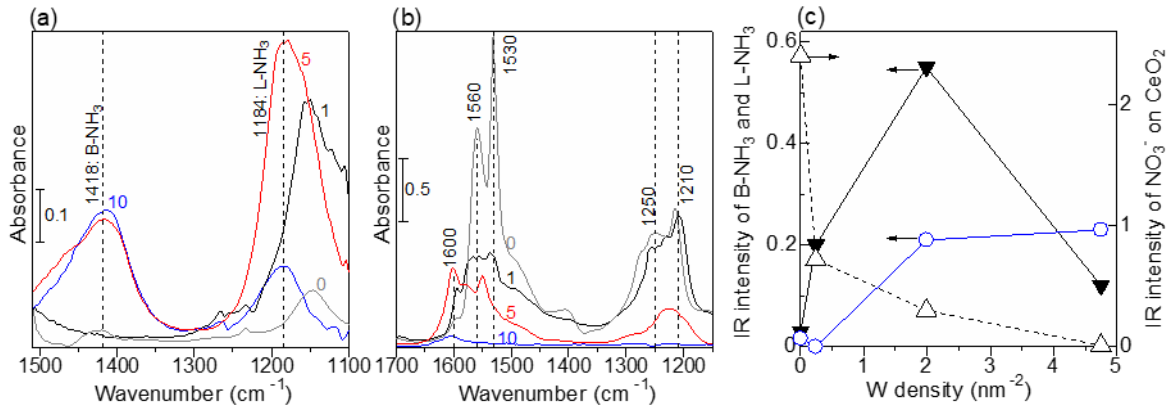

Figure 1. IR spectra of adsorbed species on the catalysts under (a) 0.1% NH_3 (600 s) and (b) 0.1% NO + 10% O_2 (600 s) at 200 °C. (c) IR peak height of B-NH_3 (1418 cm^{-1}), L-NH_3 (1184 cm^{-1}), and NO_3^- on CeO_2 (1530 cm^{-1}) versus W density.

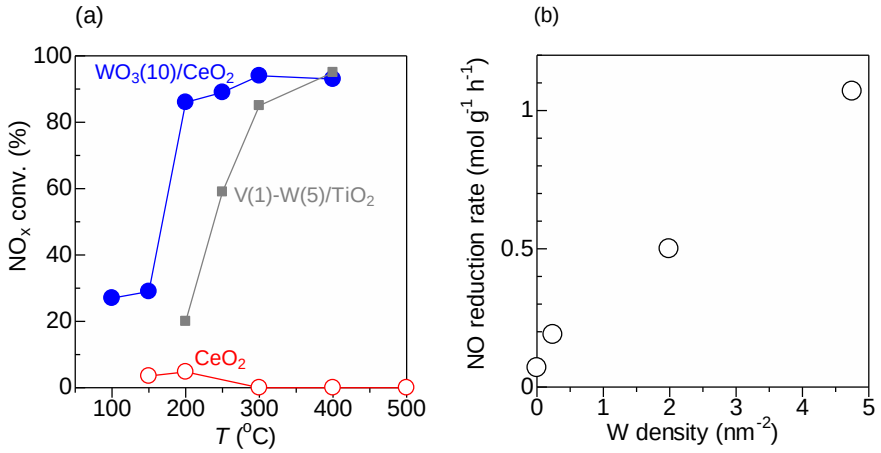

Figure 2. (a) NOx conversions versus temperature for standard SCR by $WO_3(10)/CeO_2$ and conventional catalysts. (b) Rates of standard SCR by $WO_3(x)/CeO_2$ catalysts at 200 °C versus W density.

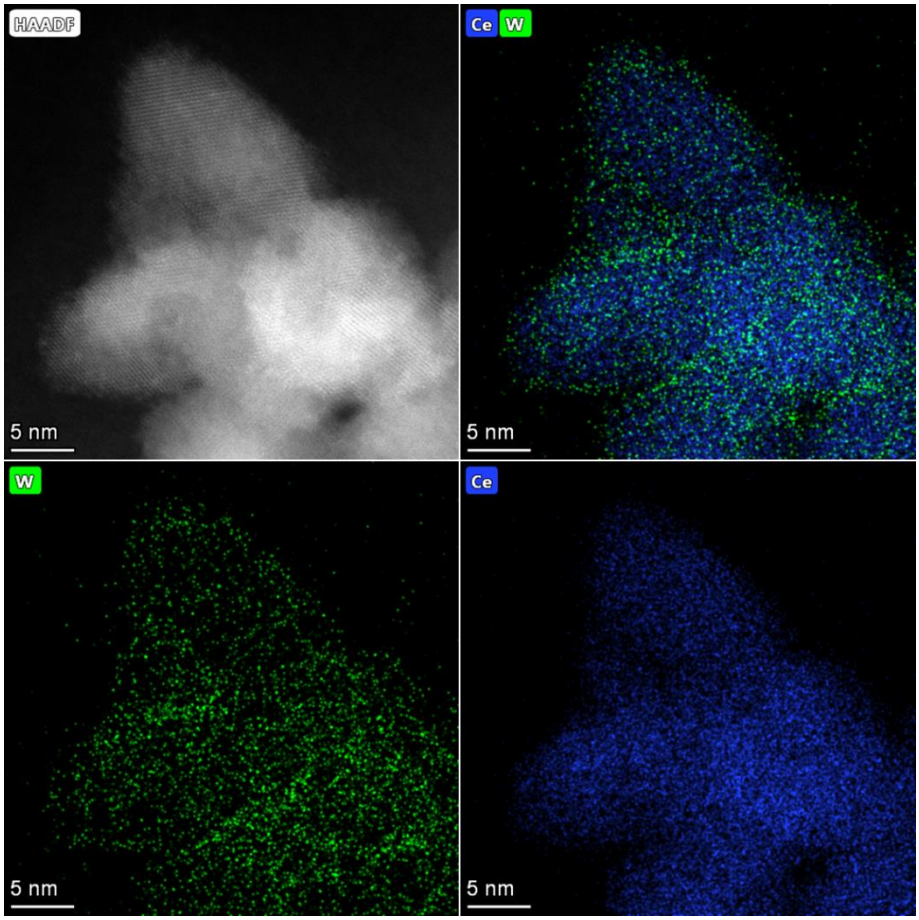

Figure 3. HAADF-STEM image and EDX mapping of $WO_3(10)/CeO_2$.

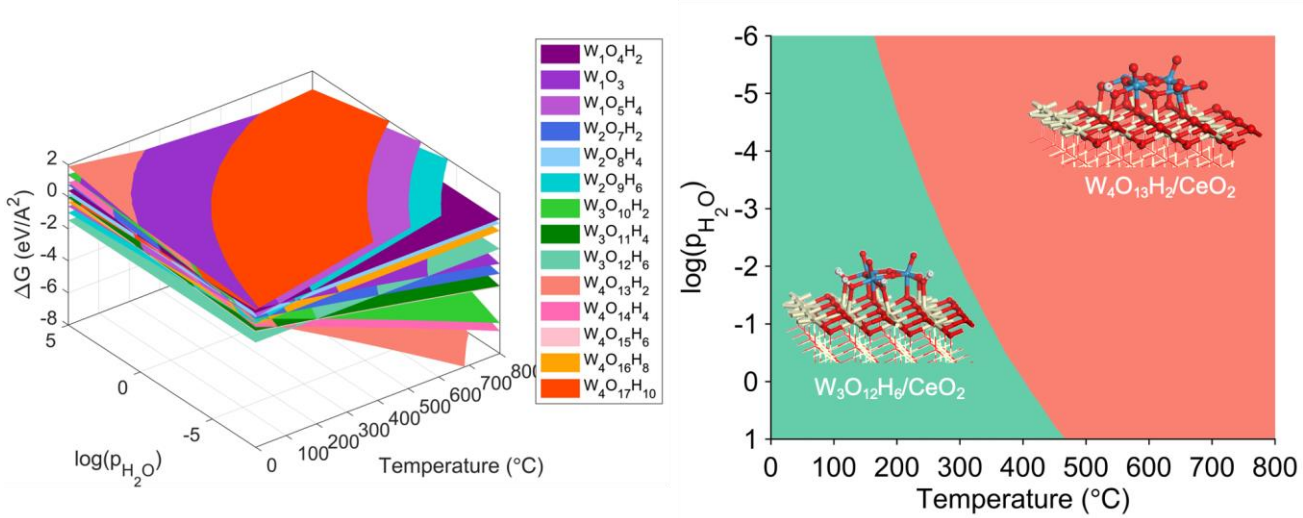

Figure 4. (a) 3D and (b) 2D phase diagrams showing the species with the lowest relative Gibbs free energy (Δ*G*) in terms of temperature and H_2O partial pressure (log scale) and two possible structures: trimeric species $W_3O_{12}H_6/CeO_2(111)$ and tetrameric species $W_4O_{13}H_2/CeO_2(111)$. All calculations were performed using VASP (yellow: Ce; red: O; blue: W; and white: H).

4.3.2 *Operando* XANES, UV-vis, and IR studies for RHC and OHC

Based on a literature survey on the NH_3–SCR mechanism, we assumed a hypothetical NH_3–SCR mechanism for WO_3/CeO_2 in **Figure S1c**. According to this mechanism, one of two different types of redox couples, Ce^{4+}/Ce^{3+} and W^{6+}/W^{5+}, can be involved in the catalytic cycle. When oxidized WO_3/CeO_2 is exposed to NO + NH_3, the reduction of the metal species accompanying N_2 formation (RHC) can be observed by *operando* spectroscopic experiments. When the reduced WO_3/CeO_2 is exposed to O_2, oxidation of the metal species (OHC) can be observed using the same methods. To verify these hypothetical redox cycles (RHC ↔OHC), we conducted *operando* spectroscopic experiments (*in situ* XANES, UV-vis, and IR combined with the online MS analysis of outlet N_2) on $WO_3(10)/CeO_2$ at 200 °C under flowing NO + NH_3 (RHC) followed by flowing O_2 (OHC). Before the measurements, $WO_3(10)/CeO_2$ was oxidized in 10% O_2/He at 500 °C (0.5 h), followed by He purging (600 s) at 200 °C.

First, we performed a time-resolved *operando* Ce L_3-edge XANES experiment to monitor the Ce^{4+} ↔ Ce^{3+} redox cycle over pre-oxidized $WO_3(10)/CeO_2$. **Figure 5** shows the XANES spectra before and after exposure to NO + NH_3 (1496 s) at 200 °C. The spectral features of the pre-oxidized $WO_3(10)/CeO_2$, which are close to those of Ce(IV) compounds in the literature,[53] are not markedly changed by the NO + NH_3 treatment. However, a close look at the absorption edge (**Figure 5b**) shows that it is shifted to a lower energy by the NO + NH_3 treatment. Further, the reduction of Ce^{4+} to Ce^{3+} is indicated by the gradual disappearance of the characteristic second peak at 5737.[54] Considering that the XANES spectrum corresponds to an averaged structural feature of Ce species in the bulk and surface of the $WO_3(10)/CeO_2$ particles, this result indicates that bulk Ce species remained in Ce^{4+} states and a part of the surface Ce species was reduced to Ce^{3+} species. Changes in energies at an absorption of 0.9 under NO + NH_3 are plotted in **Figure 5c,** in addition to the MS intensity for N_2 monitored by online MS analysis. The decrease in the edge energy coincides with N_2 formation, indicating the reduction of surface Ce^{4+} species by NO + NH_3 to yield N_2 (RHC). After purging with He, the gas was switched to O_2, and the XANES spectra were acquired as a function of the oxidation time. As shown in **Figure 5d**, the edge energy increases within 100 s, whereas the MS signal of N_2 is not observed. These results indicate that the surface Ce^{3+} species are oxidized by O_2 regenerating the Ce^{4+} species (OHC), which is not involved in the N_2 formation.

The same time-resolved *operando* XANES experiment was performed at the W L_3-edge. The energies of the normalized absorption of 2 under NO + NH_3 (**Figure 6a**) and subsequent oxidation (**Figure 6b**) remain unchanged within the experimental error and are close to the edge energy of WO_3 as a model compound of W(VI) species. This indicates that the oxidation state of the WO_3 species did not change under reductive (NO + NH_3) and oxidative (O_2) conditions.

In situ UV-vis experiments have been utilized for monitoring the Ce^{4+} ↔ Ce^{3+} redox cycles of CeO_2-based catalysts under a reductive/oxidative atmosphere in a previous study.[55] The reduced CeO_2 showed a broad visible absorption band at 500–800 nm assignable to Ce^{3+} species.[55] We investigated the formation/consumption of the Ce^{3+} species under RHC/OHC

conditions by *in situ* UV-vis experiments of $WO_3(10)/CeO_2$ during successive redox treatments under NO + NH_3 (**Figure 7a,b**), He, and then O_2 (**Figure 7e**) at 200 °C. Upon exposure of the pre-oxidized $WO_3(10)/CeO_2$ to NO + NH_3, a broad band in the range of 500–800 nm appears in the UV-vis spectrum (**Figure 7a**). The difference spectra shown in **Figure 7b** were obtained by subtracting each spectrum from the spectrum at t = 0 s. The intensity of the difference spectra (ΔKM) at 600 nm is plotted in **Figure 7b** together with the MS intensity of outlet N_2, which corresponds to the N_2 formation rate. Below 250 s, ΔKM at 600 nm, corresponding to the amount of Ce^{3+} species, steeply decreases with increasing time of NO + NH_3 flow; simultaneous N_2 formation was monitored by MS. The results provide direct evidence for the reduction of surface Ce^{4+} species by NO + NH_3 to yield N_2 (RHC). After purging with He, the reduced catalyst was exposed to O_2 while monitoring the UV-vis spectra. As shown in **Figure 7d**, the ΔKM value at 600 nm (relative number of Ce^{3+} species) decreases sharply below 250 s, indicating that the Ce^{3+} species were oxidized by O_2 regenerating the Ce^{4+} species (OHC).

In a separate *in situ* UV-vis experiment, the pre-oxidized $WO_3(10)/CeO_2$ was exposed to NO at 200 °C. The difference spectra under NO (**Figure 7e**) were similar to those under NO + NH_3, indicating the formation of Ce^{3+} species. The ΔKM value at 600 nm decreases steeply below 250 s (**Figure 7f**), indicating that the Ce^{4+} species were reduced by NO to yield Ce^{3+} species.

AP-XPS was performed to investigate the redox behavior of the W and Ce species in the $WO_3(10)/CeO_2$ catalyst. **Figure 8** shows the XPS profiles of the W 4f and Ce 3d regions obtained under successive exposure to 0.1 Torr O_2, vacuum, 0.05 Torr NH_3 + 0.05 NO, and 0.1 Torr O_2. The oxidation state of W was W^{6+}, which remained unchanged during the experiment. By contrast, Ce^{3+} and Ce^{4+} were found in the Ce 3d region under a 0.1 Torr O_2 atmosphere, followed by further Ce reduction under vacuum even without any reductants. This result indicates that photoreduction occurred during the measurement owing to the reducible nature of CeO_2.[56,57] The concentrations of the surface Ce^{4+} and Ce^{3+} detected are listed in **Table 2**. Only Ce^{4+} and Ce^{3+} species were observed during the entire measurement period. The concentration of Ce^{3+} in the profile of $WO_3(10)/CeO_2$ under exposure to 0.05 Torr NH_3 + 0.05 NO (58%) was slightly higher than that in the profile obtained under vacuum (56%). After treatment with 0.05 Torr NH_3 + 0.05 NO and 10 min of evacuation, O_2 was introduced into the XPS chamber. Upon exposure to 0.1 Torr O_2, the intensities of the peaks ascribed to Ce^{3+} species decreased, and the peaks of Ce^{4+} species increased, indicating that the catalyst surface was oxidized by O_2. Although the photoreduction during the measurement hindered a clear observation of the redox behavior of the surface Ce species, the obtained results suggest that the RHC and OHC occurred by flowing NO + NH_3 and O_2, respectively, and that the redox couple was Ce^{4+} and Ce^{3+}. Notably, the W^{6+} species remained unchanged during this process. This result is consistent with those of other *in situ/operando* spectroscopic experiments described above.

Changes in the O vacancy formation energy (E_{Ovac}) of the $CeO_2(111)$ surface supported by trimeric W oxide species ($W_3O_{12}H_6$) were theoretically investigated. **Figure 9A** shows E_{Ovac}

versus the minimum distance to a W atom. The O sites close to W show a small E_{Ovac}, indicating that the presence of the W oxide species makes the formation of O vacancies easier. The same investigation was performed using Matlantis instead of VASP (**Figure 9B**). Although the absolute values of E_{Ovac} are different from those obtained with VASP, the overall trend of E_{Ovac} versus the minimum distance to a W atom is the same, confirming the high reliability of the analyses.

Figure S7 shows the partial electronic density of states (DOS) projected for each element in CeO_2(111) and $W_3O_{12}H_6/CeO_2$(111) with and without O vacancies on the CeO_2(111) surface. To clarify the contribution of the tungsten oxide species supported on CeO_2(111), the local DOS of $W_3O_{12}H_6$ in $W_3O_{12}H_6/CeO_2$(111) is also shown. Note that the O vacancy with the smallest E_{Ovac} value (O vacancy that is most likely to be formed) was considered here. All DOSs were aligned at the vacuum level. Creating an O vacancy forms a defect state in the bandgap of CeO_2. The position of the defect state was lowered by the presence of $W_3O_{12}H_6$ species. In particular, $W_3O_{12}H_6$ stabilizes the defect state, resulting in the easier formation of O vacancies on the $W_3O_{12}H_6/CeO_2$(111) surface than on the bare CeO_2(111) surface. Similar phenomena are widely observed for supported metal catalysts, particularly at metal/oxide support perimeter sites, where supported metals serve as electron scavengers to accept excess electrons upon O removal.[58,59]

To further investigate the effect of O vacancy formation on the electronic structure of the $W_3O_{12}H_6/CeO_2$(111) surface, the charge density distribution was analyzed (**Figure S8**). The electrons generated by the formation of the O vacancy transferred to the oxygen of the $W_3O_{12}H_6$ species and neighboring Ce sites. Bader charge analysis was performed to investigate the valence change of Ce. The valence of Ce decreased before and after the formation of O vacancies, indicating that Ce^{4+} was reduced to Ce^{3+} upon the formation of O vacancies, whereas the valence of the W^{6+} species remained unchanged. This result was consistent with the experimental results obtained in this study.

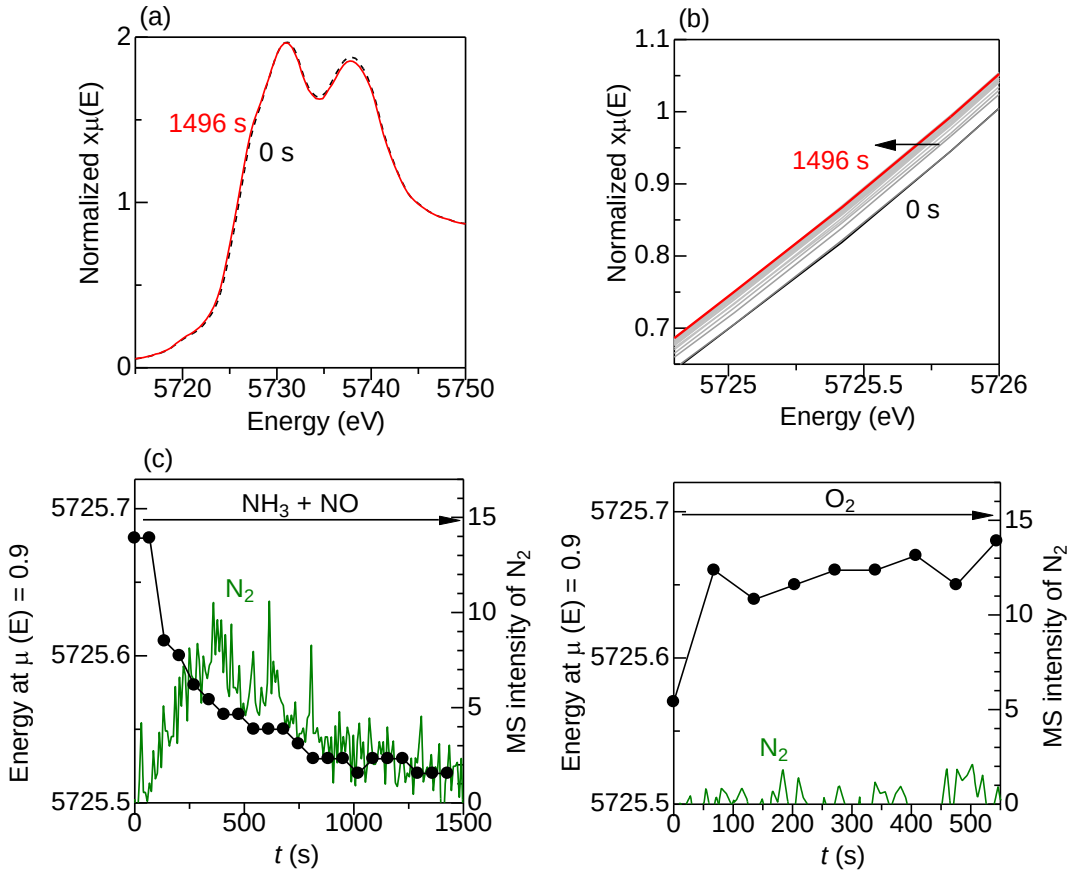

Figure 5. Changes in the Ce L_3-edge XANES spectra of $WO_3(10)/CeO_2$ under NO + NH_3 (a,b) and time course of MS intensity for N_2 and the energy at normalized absorption of 0.9 during successive feed of 0.1% NO + 0.1% NH_3 (c), He, and 10% O_2 (d) at 200 °C.

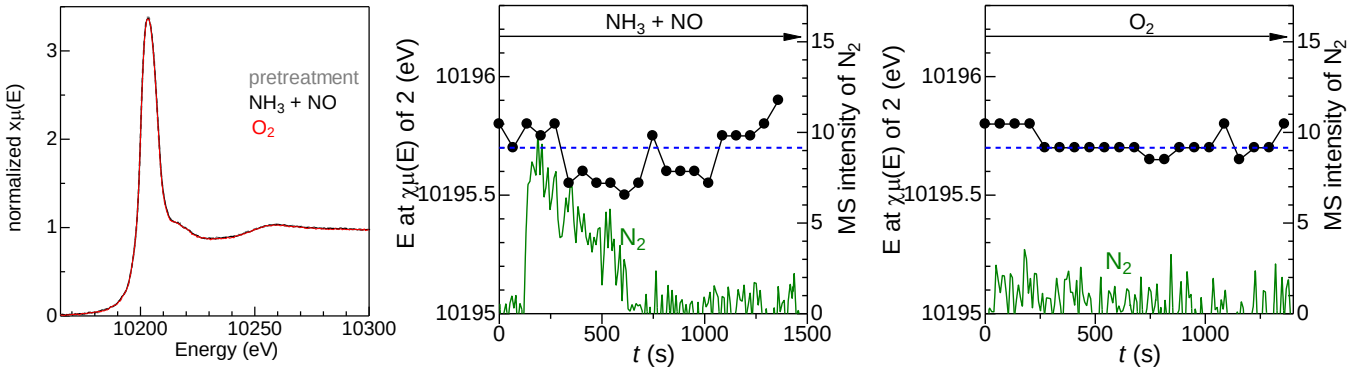

Figure 6. Time-resolved W L_3-edge XANES analysis. Time course of MS intensity for N_2 and the energy at normalized absorption of 2 during successive feed of 0.1% NO + 0.1% NH_3 (c), He, and 10% O_2 (d) at 200 °C.

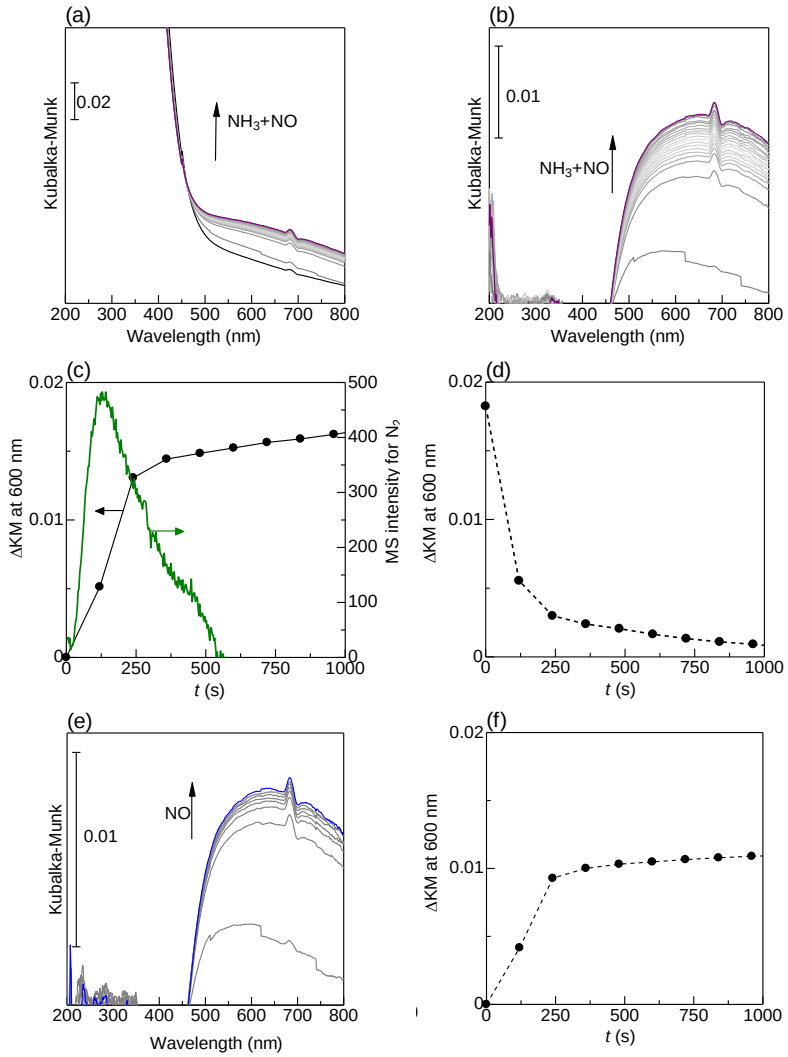

Figure 7. Evolution of UV-vis spectra of (a) $WO_3(10)/CeO_2$ and (b) difference spectra based on the spectrum at 0 s. Time course of the MS signal of N_2 and UV-vis intensity at 600 nm under (c) NO + NH_3, followed by He purge and (d) by O_2. (e) Evolution of difference UV-vis spectra and (f) time course of the intensity at 600 nm under 0.1% NO. Conditions: 0.1% NO; 0.1% NH_3; 10% O_2; and 200 °C.

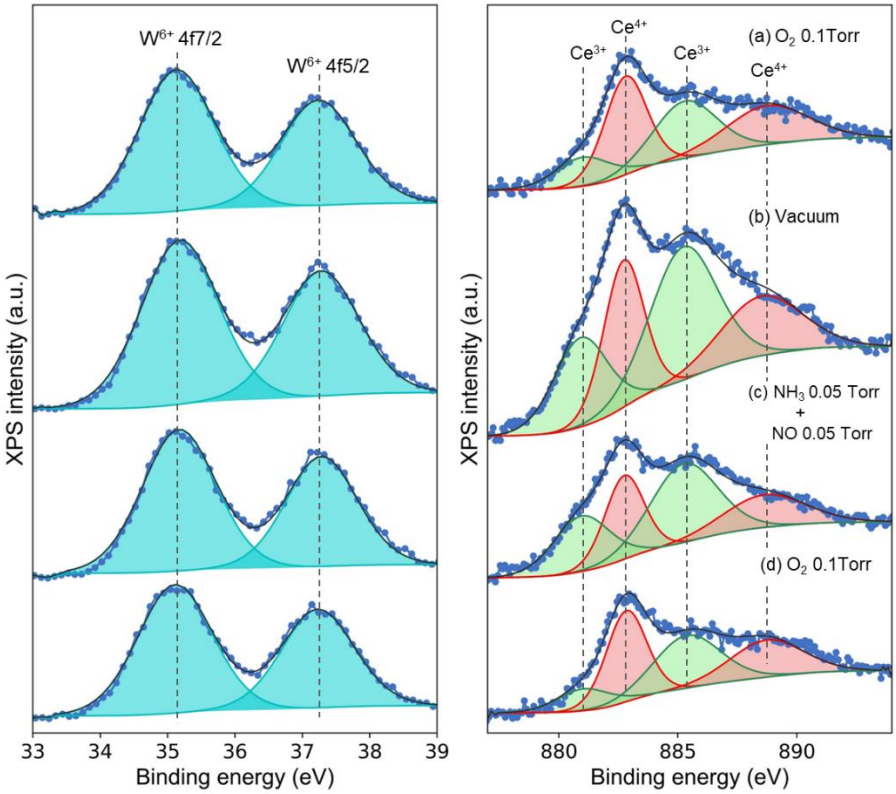

Figure 8. Ce3d AP-XPS profiles of $WO_3(10)/CeO_2$ under exposure to (a) 0.1 Torr O_2, (b) vacuum, (c) 0.05 Torr NH_3 + 0.05 NO, and (d) 0.1 Torr O_2 at 200 °C. Blue dots: raw spectrum; gray line: sum; green: Ce^{3+} species; and red: Ce^{4+} species.

Table 2. Peak concentrations in the Ce3d AP-XPS profiles of $WO_3(10)/CeO_2$ at 200 °C under various gas conditions.

Condition	Peak concentration / %	
	Ce^{3+}	Ce^{4+}
(a) 0.1 Torr O_2	43	57
(b) Vacuum	56	44
(c) 0.05 Torr NH_3+ 0.05 Torr NO	58	42
(d) 0.1 Torr O_2	42	58

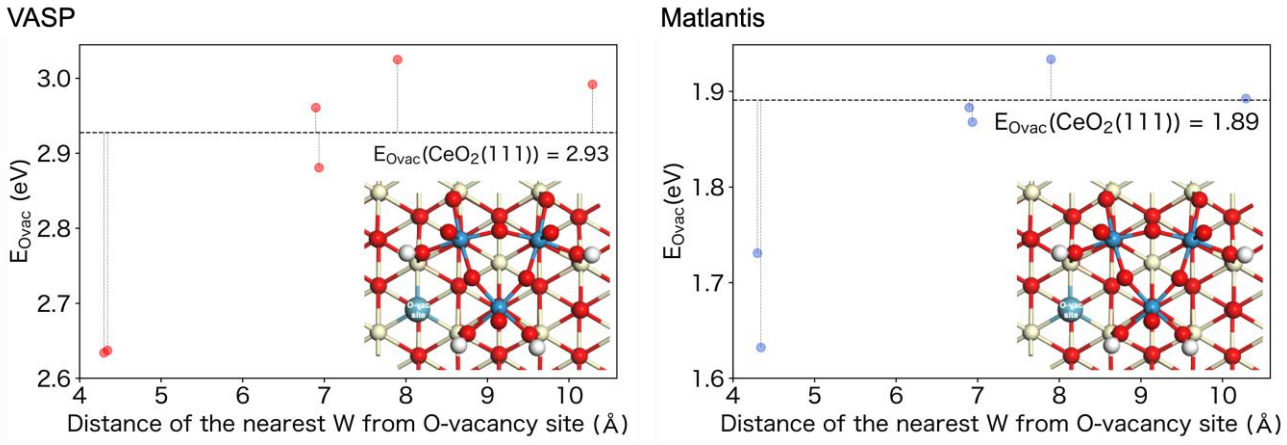

Figure 9. E_{Ovac} versus minimum distance to a W atom from the O site obtained using VASP (left) and Matlantis (right); yellow: Ce; red: O; blue: W; and white: H.

The formation and consumption of adsorbed molecules under the transient RHC reaction were monitored by *operando* IR experiments of $WO_3(10)/CeO_2$ at 200 °C under successive flows of NO + NH_3, NO, O_2, He, and then NO. Under NO + NH_3 (**Figure 10a,b**), N_2 formation was confirmed by MS analysis, and the formation of NH_3 adsorbed on the W^{6+} sites (L-NH_3; 1180 cm^{-1}) and Brønsted acid sites (B-NH_3; 1180 cm^{-1}) was observed by IR. When the gas was switched from NO + NH_3 to NO, N_2 formation was not observed by MS, and the IR intensities of L-NH_3 and B-NH_3 did not change significantly (dashed lines in **Figure 10c**). The IR disk of $WO_3(10)/CeO_2$ was then exposed to O_2, followed by He purging. As the gas was switched from He to NO, L-NH_3 and B-NH_3 were almost completely consumed, accompanied by N_2 formation (solid lines in **Figure 10c**). Combined with the XANES and UV-vis results showing that Ce^{3+} species are oxidized by O_2 to regenerate the Ce^{4+} species, the IR results in **Figure 10c** clearly demonstrate that the adsorbed NH_3 species on $WO_3(10)/CeO_2$ (B-NH_3 and L-NH_3) cannot react with NO in the absence of surface Ce^{4+} species, whereas adsorbed NH_3 can react with NO after regeneration of the surface Ce^{4+} species by OHC.

Figure 11 compares time-resolved *operando* IR results for the transient reaction of adsorbed NH_3 under NO and NO + O_2 at 200 °C. The IR disk of the pre-oxidized $WO_3(10)/CeO_2$ was exposed to NH_3, followed by He purging, resulting in the formation of B-NH_3 and L-NH_3 on the surface. When the sample was exposed to NO and NO + O_2, B-NH_3 and L-NH_3 were consumed to yield N_2. The slopes of the curves for B-NH_3 and L-NH_3, or in other words, the reaction rates of B-NH_3 and L-NH_3 are close to each other, suggesting that these two NH_3 species show similar reactivity. The co-presence of O_2 does not markedly affect the N_2 formation rate, indicating that O_2 does not play an important role in the N_2 formation step. In the literature on NH_3–SCR, the transient reactions of B-NH_3 and L-NH_3 under NO + O_2 have generally been studied. Our results demonstrate that the transient reaction of B-NH_3 and L-NH_3 under NO is essential for understanding the N_2 formation step.

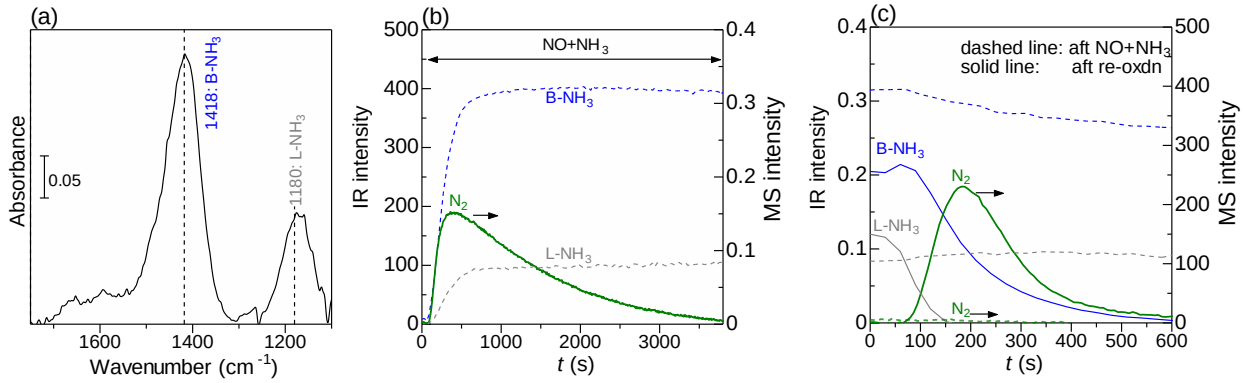

Figure 10. (a) IR spectrum of adsorbed species on $WO_3(10)/CeO_2$ under NO + NH_3 (3800 s). Time course of MS signal of N_2 and IR intensity of adsorbed NH_3 on W10Ce under (b) NO + NH_3 (3800 s),

followed by NO (dashed lines in (c)), O_2 (1800 s), and NO (solid lined in (c). Conditions: 0.1% NO; 0.1% NH_3; 10% O_2; 200 °C.

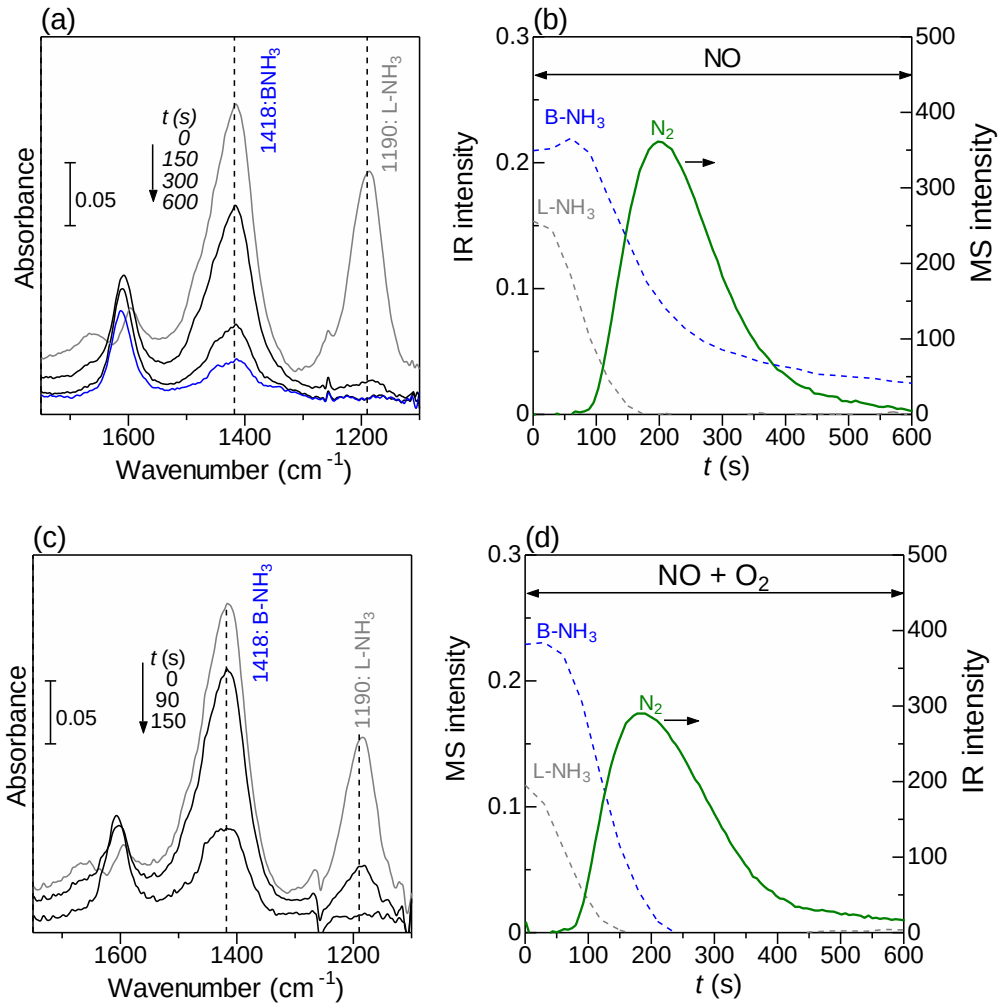

Figure 11. Time-resolved IR-MS results for the reaction of NH_3 species pre-adsorbed on WO_3(10)/CeO_2 under (top) NO and (bottom) NO + O_2: (a, c) typical IR spectra and (b, d) IR intensity of B-NH_3 and L-NH_3 and MS signal of outlet N_2 versus time. The sample was oxidized in O_2 at 500 °C (0.5 h), followed by pre-exposure to NH_3 (600 s) at 200 °C, followed by He purge (600 s). Conditions: 0.1% NO; 0.1% NH_3; 10% O_2; 200 °C.

4.3.3 N_2 formation via the HONO intermediate

As shown in **Figure 7e,f**, a small number of the Ce^{4+} species on $WO_3(10)/CeO_2$ can be reduced by NO at 200 °C. Gao et al.[39] reported that Ce^{4+} species on V_2O_5/CeO_2 was reduced by NO at 200 °C to afford a mobile HONO. Tronconi et al.[26] and our group[60] also reported a similar elementary step as the initial step of NH_3–SCR by Cu-CHA; reduction of $Cu^{2+}(OH^-)$ by NO yields Cu^+ and HONO, which react with NH_3 to yield N_2 and H_2O. The NH_3–SCR mechanism via a mobile HONO intermediate can explain the improved NOx conversions by simply mixing a redox catalyst (such as CeO_2–ZrO_2) and Brønsted acidic catalysts (such as H-zeolites).[61,62] Inspired by these experimental observations, we performed *operando* IR experiments on the formation and reaction of NO^+ intermediates at a low temperature (30 °C) using the IR disk of a physical mixture of $WO_3(1)/CeO_2$ and H-type CHA ($WO_3(1)/CeO_2$+H-CHA). The IR disk of $WO_3(1)/CeO_2$+H-CHA was exposed to NO for 600 s (**Figure 12a**). A strong band assignable to NO^+ adsorbed on the zeolite (2174 cm^{-1})[63] and a weak band attributed to NO_3^- species on CeO_2 (1590 cm^{-1})[64] can be observed. In this experiment, $WO_3(1)/CeO_2$ with a lower W loading was used because of the ease of IR measurements. The intrinsic roles of W species in $WO_3(1)/CeO_2$ and $WO_3(10)/CeO_2$ are expected to be the same as the results of the NO reduction activity dependence on the W density (**Figure 2a**). These bands were not observed in the same experiments using CeO_2, and the experiment with H-CHA gave a small peak due to NO^+, suggesting that the NO^+ on the zeolite via mobile species such as HONO and NO_2. A mobile intermediate produced by reaction (8), HONO (9), can account for the formation of NO^+ on the zeolite.

$$M^{n+}(OH^-) + NO \rightarrow M^{(n-1)+} + HONO \qquad (8)$$

$$HONO + H^+O_Z^- \rightarrow NO^+O_Z^- + H_2O \qquad (9)$$

After purging, the IR disk of $WO_3(1)/CeO_2$+H-CHA was exposed to the NH_3 flow. As shown in **Figure 12b,c**, the IR band due to NO^+ decreased with time of NH_3 flow, and N_2 formation was observed by MS. We reported a combined experimental and theoretical study on the reaction of NO^+ on H-CHA with NH_3 and proposed the N_2 formation mechanism via reactions (10) and (11).[63] $NO^+O_Z^-$ reacts with NH_3 to yield a nitrosamide (H_2NNO) intermediate, which is thermally decomposed to N_2 and H_2O.

$$NO^+O_Z^- + NH_3 \rightarrow H_2NNO + H^+O_Z^- \qquad (10)$$

$$H_2NNO \rightarrow N_2 + H_2O \qquad (11)$$

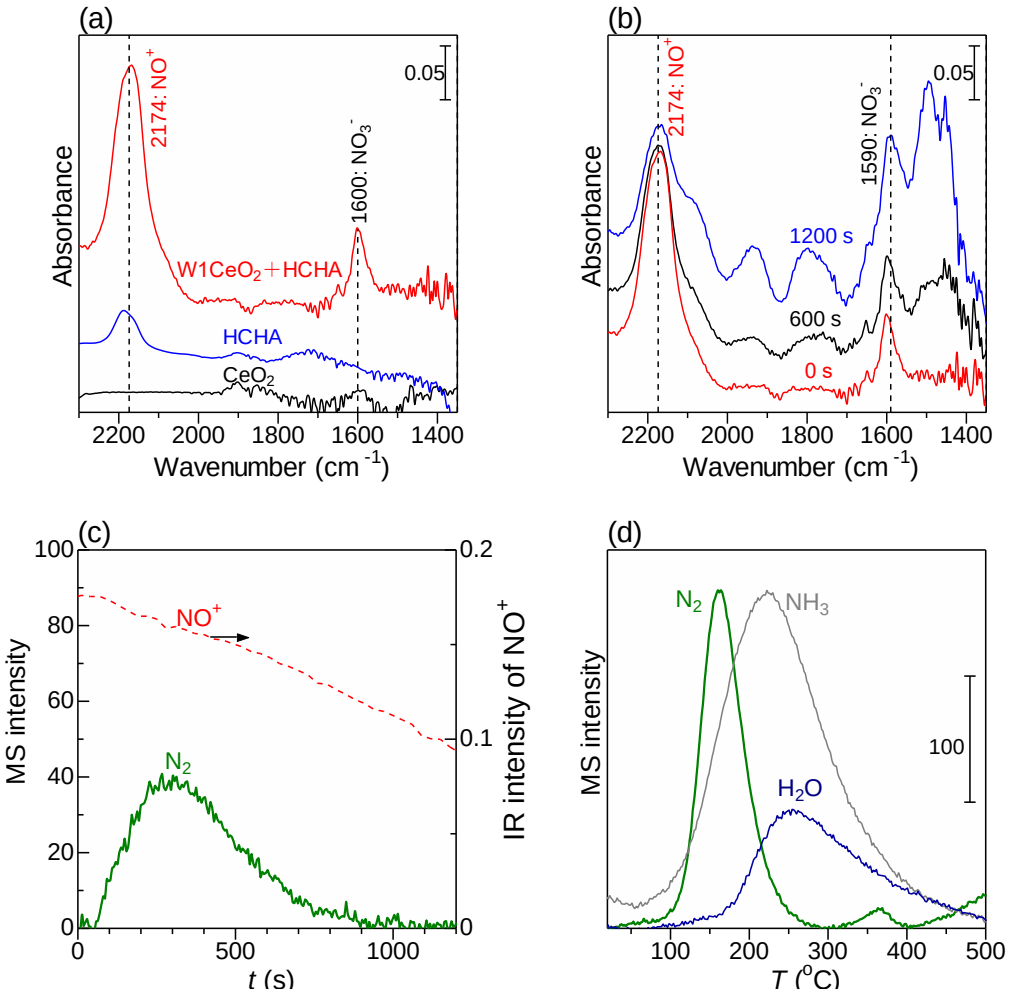

Figure 12. (a) IR spectra of adsorbed species on WO_3(1)/CeO_2 (30 mg)/H-CHA (40 mg) mixture, pre-exposed to 0.1% NO (600 s), followed by He purge (600 s), under 0.1% NH_3 at 30 °C. (b) Time course of IR peak height for NO^+ (2174 cm^{-1}) and MS intensity of outlet N_2. (c) TPSR (20 °C min^{-1}) of adsorbed species under He monitored by *in situ* IR and MS of outlet gas.

For the direct measurement of NO^+ species on CeO_2-supported WO_3 catalysts, we conducted an ME DRIFTS experiment with a WO_3(5)/CeO_2 catalyst. After pretreatment under O_2/Ar flow at 300 °C, the catalyst was periodically exposed to NO + O_2 (30 s) and O_2 (30 s) at 150 °C. The averaged time-resolved spectra obtained at the end of both NO + O_2 (30 s) and O_2 (30 s) pulses are shown in **Figure 13a**. A weak peak assignable to NO^+ (2200 cm^{-1}) is observed as a minor peak, while strong bands attributed to nitrates are observed as major features. Enhanced sensitivity toward changeable surface species that may not be visible by inspecting time-resolved DRIFT data was obtained using phase-sensitive detection (PSD). In the phase-resolved spectra shown in **Figure 13b**, the intensity of the shoulder peak assignable to NO^+ (2140 cm^{-1}) is close to

that of nitrates. These results suggest that NO^+ (a minor species) is more reactive than nitrates (a dominant species) under periodic NO + O_2/O_2.

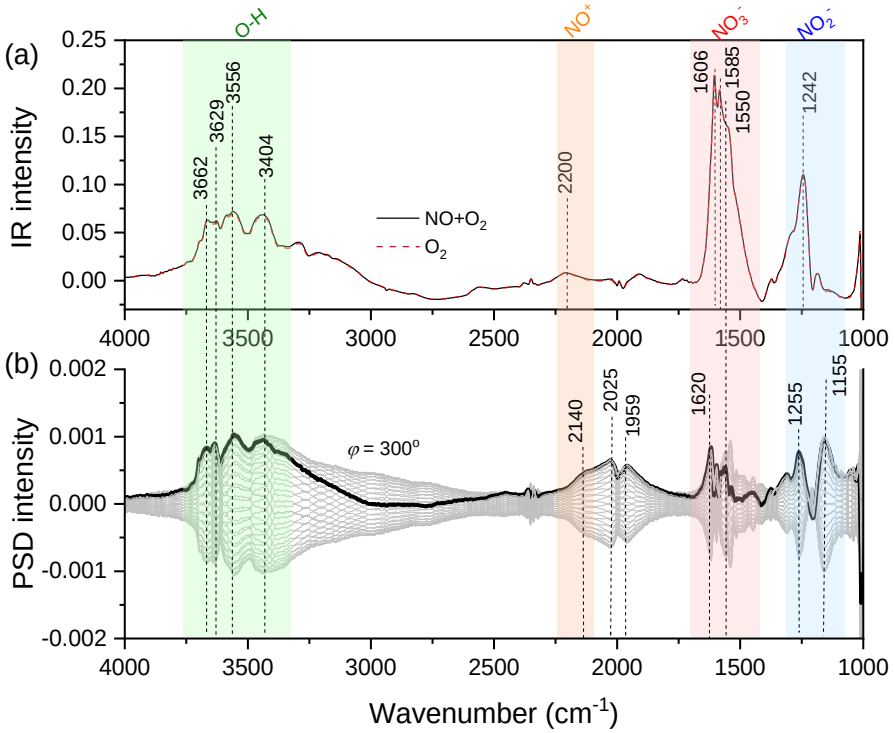

Figure 13. (a) Time-resolved spectra and (b) phase-resolved spectra (PSD) as results of 30 s pulses of 250 ppm NO in a gas feed containing 10% O_2 in Ar at 150 °C using ME DRIFTS experiment over WO_3(5)/CeO_2 catalyst.

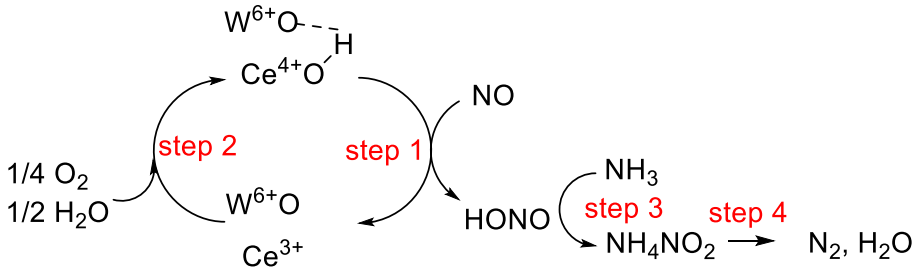

Scheme 1. Proposed NH_3–SCR mechanism for WO_3/CeO_2.

To summarize the mechanistic results of this study, an NH_3–SCR mechanism for WO_3/CeO_2 is proposed in **Scheme 1**. The first step was the reduction of the surface $Ce^{4+}O$ species by NO to yield Ce^{3+}. Considering that the dominant surface sites of the most active catalyst (WO_3(10)/CeO_2) are Brønsted acid sites (**Figure 2**), the protonic H atoms of the W^{6+}-OH species adjacent to the $Ce^{4+}O$ species may participate in the formation of HONO. The Ce^{3+} species is reoxidized by O_2 to

regenerate the initial Ce^{4+} species. The mobile intermediate HONO can react with NH_3 to yield NH_4NO_2, which decomposes into N_2 and H_2O.

4.4. Conclusions

Operando spectroscopies and DFT calculations clarified the reduction/oxidation half cycles in the selective catalytic reduction of NO with NH_3 (NH_3–SCR) over WO_3-loaded CeO_2. The Ce^{4+} species was reduced by NO + NH_3 to yield N_2 and Ce^{3+} species (RHC), which was then reoxidized by O_2 (oxidation half cycle). The oxidation state of the W^{6+} species remained unchanged under redox conditions. IR and theoretical results suggested that the RHC started with the reaction of W^{6+}–OH and adjacent Ce^{4+}–O with NO to afford Ce^{3+} species and gaseous HONO, which was converted to NO^+ species on the catalyst. Thereafter, the NO^+ species reacted with NH_3 to generate N_2.

References

(1) Beale, A. M.; Gao, F.; Lezcano-Gonzalez, I.; Peden, C. H. F.; Szanyi, J. Recent Advances in Automotive Catalysis for NOx Emission Control by Small-Pore Microporous Materials. *Chem Soc Rev*. Royal Society of Chemistry October 21, 2015, pp 7371–7405.

(2) Lai, J. K.; Wachs, I. E. A Perspective on the Selective Catalytic Reduction (SCR) of NO with NH3 by Supported V2O5-WO3/TiO2 Catalysts. *ACS Catal* **2018**, *8*, 6537–6551.

(3) Xu, J.; Yu, H.; Zhang, C.; Guo, F.; Xie, J. Development of Cerium-Based Catalysts for Selective Catalytic Reduction of Nitrogen Oxides: A Review. *New J Chem* **2019**, *43*, 3996–4007.

(4) Zhou, J.; Guo, R. T.; Zhang, X. F.; Liu, Y. Z.; Duan, C. P.; Wu, G. L.; Pan, W. G. Cerium Oxide-Based Catalysts for Low-Temperature Selective Catalytic Reduction of NOxwith NH3: A Review. *Energy and Fuels* **2021**, *35*, 2981–2998.

(5) Zeng, Y.; Haw, K. G.; Wang, Y.; Zhang, S.; Wang, Z.; Zhong, Q.; Kawi, S. Recent Progress of CeO2−TiO2 Based Catalysts for Selective Catalytic Reduction of NOx by NH3. *ChemCatChem*. Wiley Blackwell January 20, 2021, pp 491–505.

(6) Andana, T.; Rappé, K. G.; Gao, F.; Szanyi, J.; Pereira-Hernandez, X.; Wang, Y. Recent Advances in Hybrid Metal Oxide–Zeolite Catalysts for Low-Temperature Selective Catalytic Reduction of NOx by Ammonia. *Appl Catal, B.* Elsevier B.V. August 15, 2021.

(7) Han, L.; Cai, S.; Gao, M.; Hasegawa, J. Y.; Wang, P.; Zhang, J.; Shi, L.; Zhang, D. Selective Catalytic Reduction of NOx with NH3 by Using Novel Catalysts: State of the Art and Future Prospects. *Chem Rev*. American Chemical Society October 9, 2019, pp 10916–10976.

(8) Michalow-Mauke, K. A.; Lu, Y.; Kowalski, K.; Graule, T.; Nachtegaal, M.; Kröcher, O.; Ferri, D. Flame-Made WO3/CeOx-TiO2 Catalysts for Selective Catalytic Reduction of NOx by NH3. *ACS Catal* **2015**, *5*, 5657–5672.

(9) Liu, K.; He, H.; Yu, Y.; Yan, Z.; Yang, W.; Shan, W. Quantitative Study of the NH3-SCR Pathway and the Active Site Distribution over CeWOx at Low Temperatures. *J Catal* **2019**, *369*, 372–381.

(10) Liu, K.; Liu, F.; Xie, L.; Shan, W.; He, H. DRIFTS Study of a Ce-W Mixed Oxide Catalyst for the Selective Catalytic Reduction of NOx with NH3. *Catal Sci Technol* **2015**, *5*, 2290–2299.

(11) Shan, W.; Liu, F.; He, H.; Shi, X.; Zhang, C. Novel Cerium-Tungsten Mixed Oxide Catalyst for the Selective Catalytic Reduction of NOx with NH3. *Chem Commun* **2011**, *47*, 8046–8048.

(12) Iwasaki, M.; Iglesia, E. Mechanistic Assessments of NO Oxidation Turnover Rates and Active Site Densities on WO3-Promoted CeO2 Catalysts. *J Catal* **2016**, *342*, 84–97.

(13) Iwasaki, M.; Dohmae, K.; Nagai, Y.; Sudo, E.; Tanaka, T. Experimental Assessment of the Bifunctional NH3-SCR Pathway and the Structural and Acid-Base Properties of WO3 Dispersed on CeO2 Catalysts. *J Catal* **2018**, *359*, 55–67.

(14) Peng, Y.; Li, K.; Li, J. Identification of the Active Sites on CeO2-WO3 Catalysts for SCR of NOx with NH3: An in Situ IR and Raman Spectroscopy Study. *Appl Catal B* **2013**, *140–141*, 483–492.

(15) Li, Y.; Cheng, H.; Li, D.; Qin, Y.; Xie, Y.; Wang, S. WO3/CeO2-ZrO2, a Promising Catalyst for Selective Catalytic Reduction (SCR) of NOx with NH3 in Diesel Exhaust. *Chem Commun* **2008**, *12*, 1470–1472.

(16) Xu, H.; Liu, J.; Zhang, Z.; Liu, S.; Lin, Q.; Wang, Y.; Dai, S.; Chen, Y. Design and Synthesis of Highly-Dispersed WO3 Catalyst with Highly Effective NH3-SCR Activity for NOx Abatement. *ACS Catal* **2019**, *9*, 11557–11562.

(17) Liu, S.; Yao, P.; Lin, Q.; Xu, S.; Pei, M.; Wang, J.; Xu, H.; Chen, Y. Optimizing Acid Promoters of Ce-Based NH3-SCR Catalysts for Reducing NOx Emissions. *Catal Today* **2021**, *382*, 34–41.

(18) Qu, R.; Peng, Y.; Sun, X.; Li, J.; Gao, X.; Cen, K. Identification of the Reaction Pathway and Reactive Species for the Selective Catalytic Reduction of NO with NH3 over Cerium-Niobium Oxide Catalysts. *Catal Sci Technol* **2016**, *6*, 2136–2142.

(19) Huo, Y.; Liu, K.; Liu, J.; He, H. Effects of SO2 on Standard and Fast SCR over CeWOx: A Quantitative Study of the Reaction Pathway and Active Sites. *Appl Catal B* **2022**, *301*.

(20) Ji, J.; Jing, M.; Wang, X.; Tan, W.; Guo, K.; Li, L.; Wang, X.; Song, W.; Cheng, L.; Sun, J.; Song, W.; Tang, C.; Liu, J.; Dong, L. Activating Low-Temperature NH3-SCR Catalyst by Breaking the Strong Interface between Acid and Redox Sites: A Case of Model Ce2(SO4)3-CeO2 Study. *J Catal* **2021**, *399*, 212–223.

(21) Liu, Z.; Zhu, J.; Zhang, S.; Ma, L.; Woo, S. I. Selective Catalytic Reduction of NOx by NH3 over MoO3-Promoted CeO2/TiO2 Catalyst. *Catal Commun* **2014**, *46*, 90–93.

(22) Li, L.; Tan, W.; Wei, X.; Fan, Z.; Liu, A.; Guo, K.; Ma, K.; Yu, S.; Ge, C.; Tang, C.; Dong, L. Mo Doping as an Effective Strategy to Boost Low Temperature NH3-SCR Performance of CeO2/TiO2 Catalysts. *Catal Commun* **2018**, *114*, 10–14.

(23) Mosrati, J.; Atia, H.; Eckelt, R.; Huyen Vuong, T.; Rabeah, J.; Mhamdi, M.; Armbruster, U. Ta and Mo Oxides Supported on CeO2-TiO2 for the Selective Catalytic Reduction of NOx with NH3 at Low Temperature. *J Catal* **2021**, *395*, 325–339.

(24) Xu, W.; Yu, Y.; Zhang, C.; He, H. Selective Catalytic Reduction of NO by NH3 over a Ce/TiO2 Catalyst. *Catal Commun* **2008**, *9*, 1453–1457.

(25) Gao, F.; Mei, D.; Wang, Y.; Szanyi, J.; Peden, C. H. F. Selective Catalytic Reduction over Cu/SSZ-13: Linking Homo- and Heterogeneous Catalysis. *J Am Chem Soc* **2017**, *139*, 4935–4942.

(26) Hu, W.; Selleri, T.; Gramigni, F.; Fenes, E.; Rout, K. R.; Liu, S.; Nova, I.; Chen, D.; Gao, X.; Tronconi, E. On the Redox Mechanism of Low-Temperature NH3-SCR over Cu-CHA: A Combined Experimental and Theoretical Study of the Reduction Half Cycle. *Angew Chem, Int Ed* **2021**, *60*, 7197–7204.

(27) Mao, Y.; Wang, Z.; Wang, H. F.; Hu, P. Understanding Catalytic Reactions over Zeolites: A Density Functional Theory Study of Selective Catalytic Reduction of NOx by NH3 over Cu-SAPO-34. *ACS Catal* **2016**, *6*, 7882–7891.

(28) Chen, L.; Janssens, T. V. W.; Vennestrøm, P. N. R.; Jansson, J.; Skoglundh, M.; Grönbeck, H. A Complete Multisite Reaction Mechanism for Low-Temperature NH3-SCR over Cu-CHA. *ACS Catal* **2020**, *10*, 5646–5656.

(29) Yang, G.; Ran, J.; Du, X.; Wang, X.; Ran, Z.; Chen, Y.; Zhang, L.; Crittenden, J. Understanding the Nature of NH3-Coordinated Active Sites and the Complete Reaction Schemes for NH3-SCR Using Cu-SAPO-34 Catalysts. *Phys Chem Chem Phys* **2021**, *23*, 4700–4710.

(30) Daya, R.; Keturakis, C. J.; Trandal, D.; Kumar, A.; Joshi, S. Y.; Yezerets, A. Alternate Pathway for Standard SCR on Cu-Zeolites with Gas-Phase Ammonia. *React Chem Eng* **2021**, *6*, 1042–1052.

(31) Greenaway, A. G.; Marberger, A.; Thetford, A.; Lezcano-González, I.; Agote-Arán, M.; Nachtegaal, M.; Ferri, D.; Kröcher, O.; Catlow, C. R. A.; Beale, A. M. Detection of Key Transient Cu Intermediates in SSZ-13 during NH3-SCR DeNOx by Modulation Excitation IR Spectroscopy. *Chem Sci* **2020**, *11*, 447–455.

(32) Clark, A. H.; Nuguid, R. J. G.; Steiger, P.; Marberger, A.; Petrov, A. W.; Ferri, D.; Nachtegaal, M.; Kröcher, O. Selective Catalytic Reduction of NO with NH3 on Cu−SSZ-13: Deciphering the Low and High-Temperature Rate-Limiting Steps by Transient XAS Experiments. *ChemCatChem* **2020**, *12*, 1429–1435.

(33) Paolucci, C.; di Iorio, J. R.; Schneider, W. F.; Gounder, R. Solvation and Mobilization of Copper Active Sites in Zeolites by Ammonia: Consequences for the Catalytic Reduction of Nitrogen Oxides. *Acc Chem Res* **2020**, *53*, 1881–1892.

(34) Krishna, S. H.; Jones, C. B.; Miller, J. T.; Ribeiro, F. H.; Gounder, R. Combining Kinetics and Operando Spectroscopy to Interrogate the Mechanism and Active Site Requirements of NOxSelective Catalytic Reduction with NH3on Cu-Zeolites. *J Phys Chem Lett*. American Chemical Society July 2, 2020, pp 5029–5036.

(35) Liu, C.; Kubota, H.; Amada, T.; Kon, K.; Toyao, T.; Maeno, Z.; Ueda, K.; Ohyama, J.; Satsuma, A.; Tanigawa, T.; Tsunoji, N.; Sano, T.; Shimizu, K. ichi. In Situ Spectroscopic Studies on the Redox Cycle of NH3−SCR over Cu−CHA Zeolites. *ChemCatChem* **2020**, *12*, 3050–3059.

(36) Kubota, H.; Toyao, T.; Maeno, Z.; Inomata, Y.; Murayama, T.; Nakazawa, N.; Inagaki, S.; Kubota, Y.; Shimizu, K. I. Analogous Mechanistic Features of NH3-SCR over Vanadium Oxide and Copper Zeolite Catalysts. *ACS Catal* **2021**, *11*, 11180–11192.

(37) Marberger, A.; Ferri, D.; Elsener, M.; Kröcher, O. The Significance of Lewis Acid Sites for the Selective Catalytic Reduction of Nitric Oxide on Vanadium-Based Catalysts. *Angew Chem* **2016**, *128*, 12168–12173.

(38) He, G.; Lian, Z.; Yu, Y.; Yang, Y.; Liu, K.; Shi, X.; Yan, Z.; Shan, W.; He, H. *Polymeric Vanadyl Species Determine the Low-Temperature Activity of V-Based Catalysts for the SCR of NO x with NH 3*; 2018; Vol. 4.

(39) Hu, W.; Zou, R.; Dong, Y.; Zhang, S.; Song, H.; Liu, S.; Zheng, C.; Nova, I.; Tronconi, E.; Gao, X. Synergy of Vanadia and Ceria in the Reaction Mechanism of Low-Temperature Selective Catalytic Reduction of NOx by NH3. *J Catal* **2020**, *391*, 145–154.

(40) Ravel, B.; Newville, M. ATHENA, ARTEMIS, HEPHAESTUS: Data Analysis for X-Ray Absorption Spectroscopy Using IFEFFIT. *J Synchrotron Radiat* **2005**, *12*, 537–541.

(41) Kresse, G.; Furthmüller, J. Efficient Iterative Schemes for Ab Initio Total-Energy Calculations Using a Plane-Wave Basis Set. *Phys Rev B Condens Matter Mater Phys* **1996**, *54*, 11169–11186.

(42) Kresse, G.; Furthmüller, J. Efficiency of Ab-Initio Total Energy Calculations for Metals and Semiconductors Using a Plane-Wave Basis Set. *Comput Mater Sci* **1996**, *6*, 15–50.

(43) Perdew, J. P.; Ruzsinszky, A.; Csonka, G. I.; Vydrov, O. A.; Scuseria, G. E.; Constantin, L. A.; Zhou, X.; Burke, K. Restoring the Density-Gradient Expansion for Exchange in Solids and Surfaces. *Phys Rev Lett* **2008**.

(44) Blöchl, P. E. Projector Augmented-Wave Method. *Phys Rev B* **1994**, *50*, 17953–17979.

(45) Grimme, S.; Ehrlich, S.; Goerigk, L. Effect of the Damping Function in Dispersion Corrected Density Functional Theory. *J Comput Chem* **2011**, *32*, 1456–1465.

(46) Dudarev, S.; Botton, G. Electron-Energy-Loss Spectra and the Structural Stability of Nickel Oxide: An LSDA+U Study. *Phys Rev B Condens Matter Mater Phys* **1998**, *57*, 1505.

(47) Hinuma, Y.; Toyao, T.; Kamachi, T.; Maeno, Z.; Takakusagi, S.; Furukawa, S.; Takigawa, I.; Shimizu, K. I. Density Functional Theory Calculations of Oxygen Vacancy Formation and Subsequent Molecular Adsorption on Oxide Surfaces. *J Phys Chem C* **2018**, *122*, 29435–29444.

(48) Takamoto, S.; Shinagawa, C.; Motoki, D.; Nakago, K.; Li, W.; Kurata, I.; Watanabe, T.; Yayama, Y.; Iriguchi, H.; Asano, Y.; Onodera, T.; Ishii, T.; Kudo, T.; Ono, H.; Sawada, R.; Ishitani, R.; Ong, M.; Yamaguchi, T.; Kataoka, T. et al. Towards Universal Neural Network Potential for Material Discovery Applicable to Arbitrary Combination of 45 Elements. *Nat Commun* **2022**, *13*.

(49) Chase, M.W.; C.A.D Jr.; Downey, J.J.R.; Frurip, D.J.; McDonald, R.A. A. N. S. NIST-JANAF Thermochemical Tables (2nd Ed.). *The U.S. Department of Commerce, Washington* **1985**.

(50) Nuguid, R. J. G.; Ortino-Ghini, L.; Suskevich, V. L.; Yang, J.; Lietti, L.; Kröcher, O.; Ferri, D. Interconversion between Lewis and Brønsted-Lowry Acid Sites on Vanadia-Based Catalysts. *Phys Chem Chem Phys* **2022**, *24*.

(51) Peng, Y.; Li, K.; Li, J. Identification of the Active Sites on CeO2-WO3 Catalysts for SCR of NOx with NH3: An in Situ IR and Raman Spectroscopy Study. *Appl Catal B* **2013**, *140–141*.

(52) Reuter, K.; Scheffler, M. Composition, Structure, and Stability of RuO_2(110) as a Function of Oxygen Pressure. *Phys Rev B Condens Matter Mater Phys* **2002**, *65*, 1–11.

(53) Moog, I.; Prestipino, C.; Figueroa, S.; Majimel, J.; Demourgues, A. Dual Ce4+/Fe3+ Redox Phenomena into Nanocrystalline Ce1-XFexO2-x/2 Solid Solution. *J Phys Chem C* **2014**, *118*, 22746–22753.

(54) Rothensteiner, M.; Bonk, A.; Vogt, U. F.; Emerich, H.; van Bokhoven, J. A. Structural Changes in Ce0.5Zr0.5O2-Δ under Temperature-Swing and Isothermal Solar Thermochemical Looping Conditions Determined by in Situ Ce K and Zr K Edge X-Ray Absorption Spectroscopy. *J Phys Chem C* **2016**, *120*.

(55) Kondratenko, E. v.; Sakamoto, Y.; Okumura, K.; Shinjoh, H. Time-Resolved in Situ UV/Vis Spectroscopy for Analyzing the Dynamics of Surface and Bulk Redox Processes in Materials Used as Oxygen Storage Capacitors. In *Catal Today*; 2011; Vol. 164, pp 46–51.

(56) Park, P. W.; Ledford, J. S. Effect of Crystallinity on the Photoreduction of Cerium Oxide: A Study of CeC2 and Ce/Al2O3 Catalysts. *Langmuir* **1996**, *12*.

(57) Schmitt, R.; Nenning, A.; Kraynis, O.; Korobko, R.; Frenkel, A. I.; Lubomirsky, I.; Haile, S. M.; Rupp, J. L. M. A Review of Defect Structure and Chemistry in Ceria and Its Solid Solutions. *Chem Soc Rev*. **2020**.

(58) Puigdollers, A. R.; Schlexer, P.; Tosoni, S.; Pacchioni, G. Increasing Oxide Reducibility: The Role of Metal/Oxide Interfaces in the Formation of Oxygen Vacancies. *ACS Catal* **2017**.

(59) Hinuma, Y.; Toyao, T.; Hamamoto, N.; Takao, M.; Shimizu, K. I.; Kamachi, T. Changes in Surface Oxygen Vacancy Formation Energy at Metal/ Oxide Perimeter Sites: A Systematic Study on Metal Nanoparticles Deposited on an In2O3(111) Support. *J Phys Chem C* **2020**, *124*.

(60) Liu, C.; Yasumura, S.; Toyao, T.; Maeno, Z.; Shimizu, K. I. Mechanism of Standard NH3-SCR over Cu-CHA via NO+and HONO Intermediates. *J Phys Chem C* **2022**, *126*, 11594–11601.

(61) Mytareva, A. I.; Stakheev, A. Y.; Baeva, G. N.; Bokarev, D. A.; Kustov, A. L.; Thøgersen, J. R. New Insights into the Mechanism of Synergistic Effect for [CeO2–ZrO2 + H-Beta] CombiCat in NH3–SCR. *Top Catal* **2016**, *59*, 919–924.

(62) Stakheev, A. Y.; Mytareva, A. I.; Bokarev, D. A.; Baeva, G. N.; Krivoruchenko, D. S.; Kustov, A. L.; Grill, M.; Thøgersen, J. R. Combined Catalytic Systems for Enhanced Low-Temperature NOx Abatement. *Catal Today* **2015**, *258*, 183–189.

(63) Yasumura, S.; Liu, C.; Toyao, T.; Maeno, Z.; Shimizu, K. I. Lean NOxCapture and Reduction by NH3via NO+Intermediates over H-CHA at Room Temperature. *J Phys Chem C* **2021**, *125*, 1913–1922.

(64) Mihaylov, M. Y.; Ivanova, E. Z.; Vayssilov, G. N.; Hadjiivanov, K. I. Revisiting Ceria-NOx Interaction: FTIR Studies. *Catal Today*. Elsevier B.V. November 1, 2020, pp 613–620.

Supplementary Results

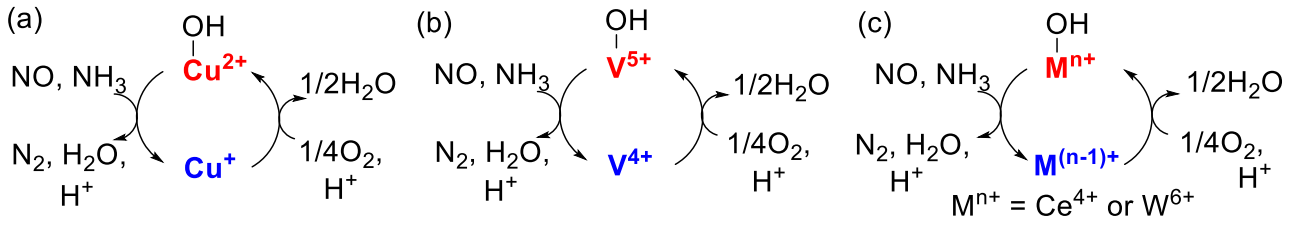

Figure S1. Reported mechanisms of NH_3-SCR for (a) Cu-CHA and (b) V_2O_5-based catalysts, and (c) hypothetical NH_3-SCR mechanism for WO_3/CeO_2.

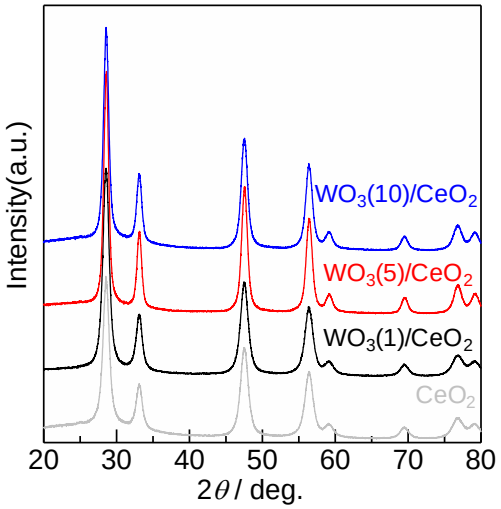

Figure S2. XRD patterns of CeO_2, $WO_3(1)/CeO_2$, $WO_3(5)/CeO_2$ and $WO_3(10)/CeO_2$.

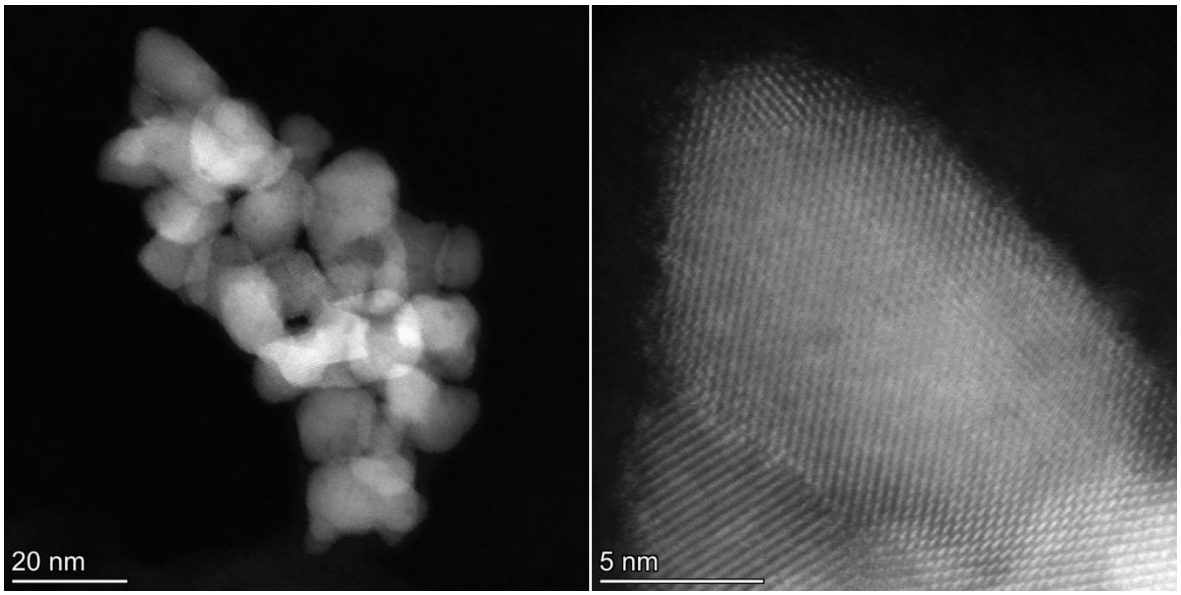

Figure S3. HAADF-STEM images of $WO_3(10)/CeO_2$.

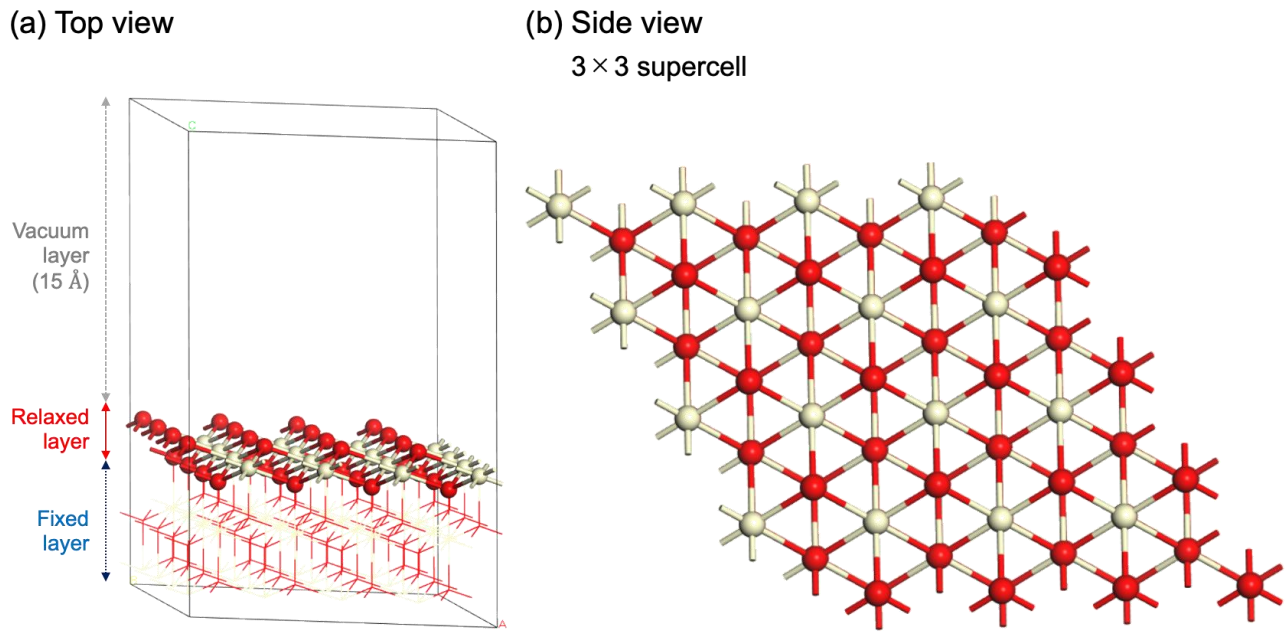

Figure S4. Top and side views of the slab models used for computational study of the $CeO_2(111)$ surface; yellow: Ce; red: O.

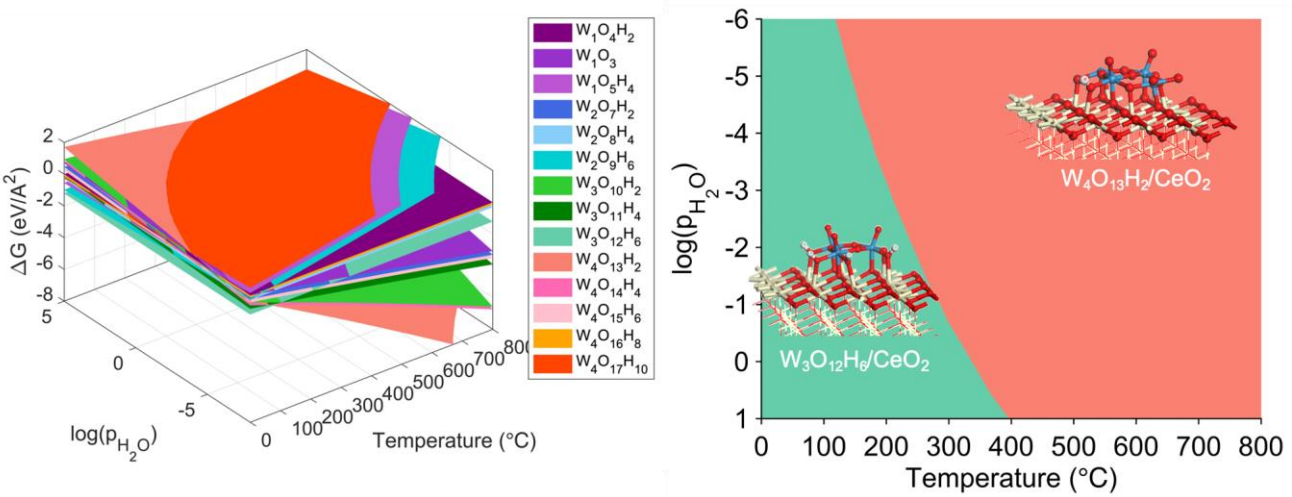

Figure S5. (a) 3D and (b) 2D Phase diagrams showing the species with the lowest relative Gibbs free energy (Δ*G*) in terms of temperature and H_2O partial pressure (log scale) and the two possible structures: trimeric species $W_3O_{12}H_6/CeO_2(111)$ and tetrameric species $W_4O_{13}H_2/CeO_2(111)$. All calculations were performed by Matlantis; yellow: Ce; red: O; blue: W; white: H.

Number of W atoms	Surface structure of $W_xO_yH_z/CeO_2(111)$
1	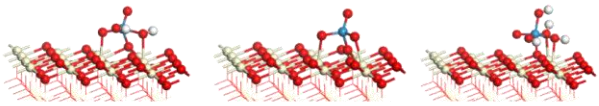
2	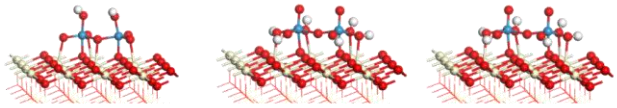
3	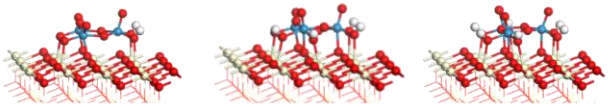
4	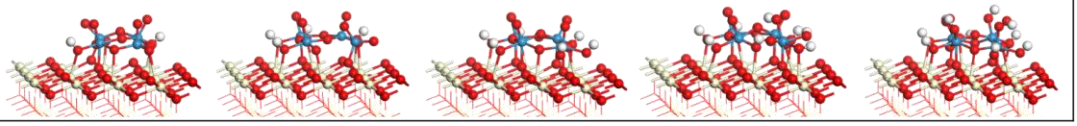

Figure S6. Side views of the slab models used for computational study of the W oxide species on $CeO_2(111)$; yellow: Ce; red: O; blue: W; white: H.

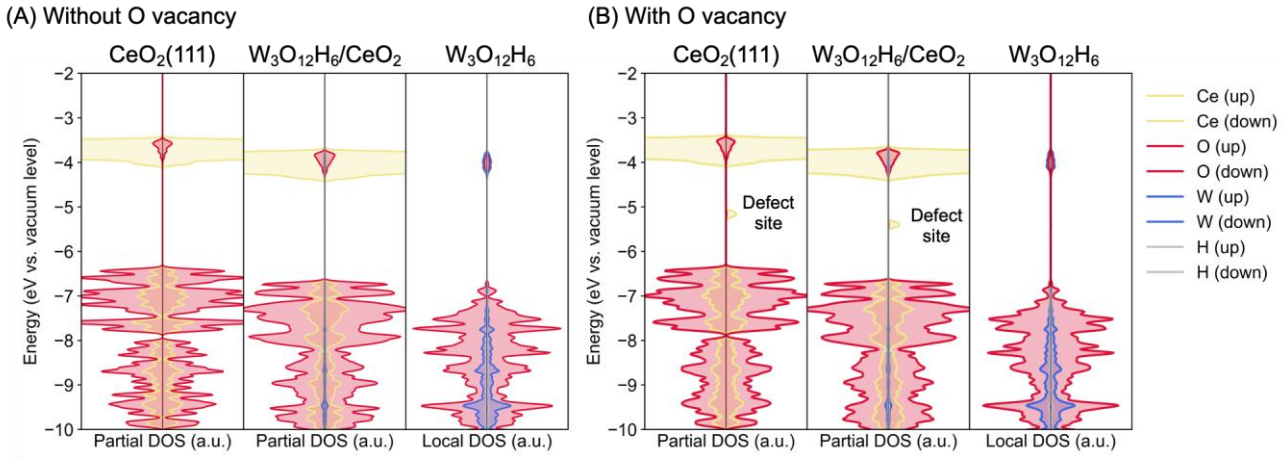

Figure S7. Partial DOS of the $CeO_2(111)$ surface, $W_3O_{12}H_6/CeO_2(111)$, and local DOS of $W_3O_{12}H_6$ of $W_3O_{12}H_6/CeO_2(111)$ without O vacancy (a) and with O vacancy (b). The energies are aligned at the vacuum level.

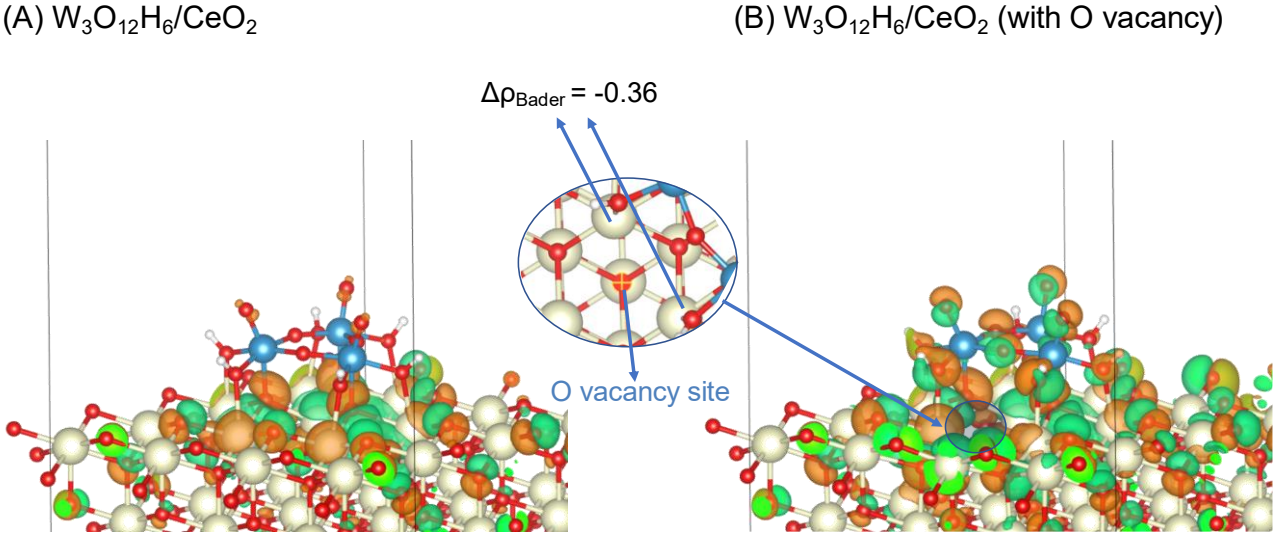

Figure S8. Differential charge densities of the $W_3O_{12}H_6$ species on $CeO_2(111)$ surface. The charge density represented in orange and green shows the positive and negative phases, respectively. The isosurface was set to 0.02 |e|/Bohr^3. The numbers represent the Bader charge; yellow: Ce; red: O; blue: W; white: H.

Chapter 5

Redox-Driven Reversible Structural Evolution of Isolated Silver Atoms Anchored to Specific Sites on γ-Al_2O_3

5.1. INTRODUCTION

Appropriate designing of sintering resistant (or regenerable) noble metal catalysts with 100% dispersion of the active component is crucial for the development of efficient industrial catalysts such as automotive catalysts.[1–3] In this context, supported atomically dispersed metal catalysts, also known as single-atom catalysts (SACs), have received significant attention over the past decade as heterogeneous catalysts.[4–6] SACs can maximize the utilization of expensive precious metals and can tune the reactivity and stability of metal species by the virtue of the strong interactions between the metal center and the support.[7] However, if the metal–support interaction is not strong enough to immobilize the isolated metals during a catalytic reaction, the isolated atoms are sintered to reduce the surface energy.[8] Recent studies on SACs have demonstrated that depending on the reaction conditions, the isolated metal species can be converted to metal clusters,[9] resulting in increased or decreased catalytic activity.[3,10–12] For example, Piccolo et al.[10] revealed that single Pt^{m+} atoms anchored on Pt/Al_2O_3, which otherwise exhibit poor activity for CO oxidation, aggregate during CO oxidation to form highly active Pt metal clusters, thus demonstrating that SACs can be a precursor of classical metal catalysts. Despite significant efforts to develop SACs, only a few SACs have been utilized in commercial catalytic processes. Atomically dispersed Pt^{m+} atoms on CeO_2-based support for automotive catalysis is a rare example of commercialized SACs;[3] however, the actual active species are the Pt metal clusters and nanoparticles (NPs) generated by sintering of the Pt^{m+} atoms under reducing environments.[3,7]

Alumina-supported silver (Ag/Al_2O_3) catalysts are another example of commercialized SACs. Ag/Al_2O_3 has long been studied as a promising catalyst for the selective catalytic reduction of NO*x* by hydrocarbons (HC–SCR),[13–16] H_2-assisted HC–SCR,[17–24] and H_2-assisted SCR by NH_3 (H_2–NH_3–SCR).[25–31] Recently, HC–SCR in the presence of Ag/Al_2O_3 has been commercialized by Hino Motors Ltd. for NO*x* removal from diesel exhaust.[1] After a long debate on the active Ag species in HC-SCR reactions,[13,17,24,28] it was concluded that isolated Ag(I) sites were indispensable for achieving high performance-Ag/Al_2O_3 catalysts for SCR.[24] Small $Ag_n^{\delta+}$ clusters generated from the *in situ* reduction of Ag(I) species by H_2 or HCs during SCR promoted the reaction under some conditions, while Ag metal NPs had an adverse effect on NO*x* conversion as they promoted the nonselective oxidation of reductants.[28,29] Our previous study on H_2–NH_3–SCR[31] showed that isolated Ag(I) sites and small $Ag_n^{\delta+}$ clusters co-exist under the reaction conditions play important roles. In commercial SCR systems, the Ag/Al_2O_3 catalysts are exposed to high temperature conditions, thus lowering the NO*x* conversion because of the sintering of the isolated Ag(I) species to Ag metal NPs. The supported single-atom Ag and small Ag clusters can be sintered at lower temperatures than other transition metals.[32–35] A density functional theory (DFT) study on the binding of various single metal atoms on θ-Al_2O_3 (010) showed that the binding strength decreases

in the order Pd > Pt > Ni > Cu > Au > Ag.[33] Plessow et al. calculated the adhesion energies at various metal-oxide interfaces and found that the strength of the metal-support interaction decreased with a decrease in the adsorption energies of the atomic oxygen on clean metal surfaces in the order Ru > Os > Ni > Rh > Ir > Pd > Cu > Pt > Ag > Au.[34] These results suggest that the designing of sintering-resistant Ag SACs is principally challenging.

Sintering of small metal NPs is a long-standing problem in heterogeneous catalysis. Recent advances in experimental and theoretical techniques have provided insights into the sintering mechanism at the atomic level.[36,37] Sintering can occur via two pathways. One is based on the migration and coalescence of metal NPs driven by the decrease in surface energy, and the other is the atomic (Ostwald) ripening, in which mobile atomic species detach from one NP, diffuse over the support surface (or gas phase), and finally attach to another NP, resulting in the growth of large particles and disappearance of small particles owing to the difference in the stability of surface atoms.[38–40] Recent microscopic[41–44] and DFT[45–47] studies have shown that Ostwald ripening is the dominant process in the growth of metal NPs. When the binding strength between the mobile adatom and support is higher than the cohesive energy of the metal NPs, the mobile adatom liberated from the metal NPs is trapped by the anchoring site of the support, leading to redispersion of the metal NPs to SACs. Recent studies have provided experimental evidence on the redispersion of metal NPs to isolated metal species.[42] The nature of the adatom during the Ostwald ripening-based sintering and/or redispersion of Pt[48,49], Pd[50–53], and Ag[54–56] catalysts was studied, and it was revealed that the mobile species were oxidized metal species generated by oxidation of the metal NPs under an oxidative environment. We have previously reported the oxidative dispersion of large Ag metal particles to isolated Ag(I) cations on θ-Al_2O_3;[57] however, the precise dispersion mechanism and the nature of the anchoring site remain elusive.

There has been a long debate on the structure of the metal anchoring sites on γ-Al_2O_3 surfaces.[58,59] Among the various anchoring sites, the penta-coordinated (Al_V^{3+}) ions as anchoring sites for various metal clusters have been exclusively focused on recently in some studies employing Al nuclear magnetic resonance (NMR) spectroscopy,[60–64] as the surface Al_V^{3+} ions can be exclusively characterized. However, Al NMR is not sufficient for the complete characterization of the metal anchoring sites as this technique cannot identify surface octahedral (Al_{VI}^{3+}) and tetrahedral Al (Al_{IV}^{3+}) sites and other anchoring sites such as the OH groups. In this regard, infrared (IR) spectroscopy using basic probe molecules[65–71] is useful for characterizing the surface Al sites with different coordination environments (Al_{VI}^{3+}, Al_V^{3+}, and Al_{IV}^{3+}) and different OH groups.[72,73] The IR study of NH_3 adsorbed on Ag-loaded and unloaded γ-Al_2O_3 by Zeng et al.[24] proposed that the terminal hydroxyl (OH) groups on the (100) surface were the anchoring sites of the isolated Ag(I) cations, which acted as catalytic sites for the H_2-assisted HC–SCR. Previous studies on the anchoring sites of γ-Al_2O_3 suggest that the anchoring sites depended on the type of metal species

and that the specific anchoring sites should be determined based on multiple spectroscopic evidences assuming various candidates for anchoring sites. We have previously shown that Ag metal particles undergo oxidative dispersion to afford isolated Ag(I) cations on γ-Al_2O_3.[57] Based on this, we hypothesized that the γ-Al_2O_3-supported Ag (Ag/Al_2O_3) catalytic system would be suitable for investigating the anchoring sites for Ag(I) using multiple spectroscopic techniques. Herein, we report the reversible structural transformation between atomic Ag(I) and large Ag metal NPs on Ag/Al_2O_3. *In situ* X-ray absorption spectroscopy (XAS), ultraviolet-visible (UV-vis) spectroscopy, and IR spectroscopy, *ex situ* microscopy, and theoretical calculations were employed to identify the structure of the anchoring site and the mechanism of oxidative dispersion and reductive aggregation.

5.2. METHODS

Preparation of catalysts

Ag/Al_2O_3 catalysts were prepared by impregnating γ-AlOOH (Pural SB supplied by Sasol) with an aqueous solution of $AgNO_3$, followed by evaporation to dryness at 60 °C, drying at 100 °C (12 h), and calcination in air at 600 °C for 1 h. The Ag/Al_2O_3 catalysts were designated as Ag*x*/Al_2O_3, where *x* is the silver loading (wt%). Sintered Ag/Al_2O_3 was prepared by reducing fresh Ag/Al_2O_3 in H_2 at 800 °C for 1 h, while re-oxidized Ag/Al_2O_3 was prepared by exposing the sintered Ag/Al_2O_3 to NO + O_2 at 400 °C for 1 h. γ-Al_2O_3 was prepared by calcination of γ-AlOOH at 600 °C for 1 h. Ag^+-exchanged CHA zeolite (Ag-CHA) which is consist of Si/Al =11, Ag/Al = 0.58 was prepared by stirring NH_4-type CHA (Tosoh, Si/Al = 11) in an aqueous $AgNO_3$ solution at room temperature for 3 h, followed by washing with water, drying at 100 °C for 12 h, and calcining at 600 °C for 1 h. The Ag/Al ratio was determined by X-ray fluorescence spectroscopy (Shimadzu, EDX-700HS). Furthermore, α,θ-Al_2O_3 (34 m^2 g^{-1}) was prepared by calcining γ-AlOOH at 1100 °C (1 h), and a 10 wt% Ag-loaded low-surface-area α,θ-Al_2O_3 was prepared by impregnating the α,θ-Al_2O_3 with an aqueous solution of $AgNO_3$, followed by evaporation to dryness at 60 °C, drying at 100 °C, and calcination in air at 600 °C (1 h).

In situ UV-vis spectroscopy

In situ diffuse reflectance UV-vis spectroscopy was performed on a JASCO V-750 UV-vis spectrometer. The sintered $Ag3/Al_2O_3$ (15 mg) catalyst powder was placed in a diffuse reflectance cell with a quartz window connected to a gas flow system (100 mL min^{-1}). The light source was

directed to the center of an integrating sphere through an optical fiber. Reflectance was converted to pseudo-absorbance using the Kubelka-Munk function. $BaSO_4$ was used to collect the background spectra. The spectrum of fresh Ag3/Al_2O_3 under a He atmosphere was subtracted from each spectrum.

In situ IR spectroscopy

In situ IR spectra were recorded on a JASCO FT/IR-4600 instrument equipped with a quartz IR cell connected to flow system (totally 100 mL min^{-1}). The sample was pressed into a 40 mg self-supporting wafer and mounted on an IR cell with CaF_2 windows. Twenty spectra were collected at a resolution of 4 cm^{-1} to obtain the final spectrum. The spectrum of the catalyst wafer acquired at the measurement temperature under He atmosphere was subtracted from each spectrum. *In situ* diffuse reflectance infrared Fourier transform (DRIFT) spectra of the powder sample (40 mg) were recorded on a JASCO FT/IR-4600 instrument equipped with an *in situ* flow cell with a CaF_2 window.

Catalytic reactions

The H_2–NH_3–SCR (H_2 + NO + NH_3 + O_2) reaction was performed in a fixed-bed flow reactor in the presence of Ag3/Al_2O_3 at a flow rate of 100 mL min^{-1}. The composition of the feed gas H_2/NO/NH_3/O_2/He was 1%/500 ppm/500 ppm/10%/balance. The concentrations of the feed gas and products were measured using an online IR spectrometer (JASCO FT/IR-4600) equipped with a home-built gas cell. The concentrations of NO, NO_2, N_2O, and NH_3 were calculated based on the calibration results. Reaction rates were estimated by changing the catalyst loading under conditions where the NO and NH_3 conversions were below 30%.

In situ XAS

Ag K-edge X-ray absorption experiments were performed in the transmission mode using the BL-14B2 beamline at the SPring-8 synchrotron radiation facility (Harima, Japan). A Si(311) single crystal was used to obtain a monochromatic X-ray beam. A self-supporting wafer of the sample (diameter: ca. 7 mm) was placed in an *in situ* quartz cell under a flow of gas mixture diluted with He (500 mL min^{-1}) at atmospheric pressure. Normalization and linear combination fitting (LCF) analysis of the X-ray absorption near edge structure (XANES) and analysis of the extended X-ray absorption fine structure (EXAFS) were performed using the Athena software package. For the LCF analysis, Ag^+-exchanged Ag-CHA (Si/Al =11) and 10 wt% Ag-loaded Al_2O_3 were used as reference compounds for isolated Ag(I) and the Ag metal NPs, respectively.

Other characterization techniques

X-ray diffraction (XRD) patterns were obtained using a Rigaku MiniFlex II/AP diffractometer with Cu Kα radiation. Transmission electron microscopy (TEM) was performed on a JEOL JEM-2200FS electron microscope. Bright-field scanning transmission electron microscopy (BF-STEM) and high-angle annular dark-field STEM (HAADF-STEM) were performed on a JEM-ARM200F microscope (JEOL). ^{27}Al magic-angle spinning (MAS) NMR (^{27}Al-NMR) measurements were carried out on a Bruker DSX-300 spectrometer operating at 300 MHz with a 4 mm rotor.

DFT calculations

All calculations were carried out based on the spin-polarized DFT using the Vienna ab initio simulation package (VASP.5.4.1).[74,75] The core-valence electron interaction was described by the projector augmented wave method.[76] The Perdew−Burke−Ernzerhof functional[77] was used for calculating the structural relaxation and vibration frequency of the surface and pyridine adsorption models, and the DFT-D3 method with the Becke−Johnson damping dispersion correction was employed to account for the dispersion interaction.[78,79]

The γ-Al_2O_3 bulk structure was adopted from a previous study by Raybaud and co-workers.[80] Many studies have been conducted recently on the surface structures of γ-Al_2O_3. Batista et al.[80,81] reported the high reactivity of the edge sites on the (110) and (100) surfaces using experimental studies and DFT calculations. TEM studies by Rozita et al.[82,83] suggested that γ-Al_2O_3 (110) was energetically unstable and that the (100) and (111) surface step-edge structures were formed by surface reconstruction. Based on these recent studies, we constructed step-edge models that included two different surface terminations in the supercell. **Figure S1** shows the γ-Al_2O_3 (110)–(100) step-edge model and the γ-Al_2O_3 (100)–(111) step-edge model. **Table S1** lists the lattice parameters and composition of each model. The OH groups were placed on all coordinatively unsaturated Al_{III} and Al_{IV} sites (edge sites, (110), and (111) surfaces) of γ-Al_2O_3 as well as on one of the Al_V sites located near the edge site of the (100) surface, as shown in **Figures S2**; H^+ as a counter-cation was placed on the adjacent surface lattice oxygen. The Al_{IV} edge site was selected as the adsorption site for pyridine, and the vibrational frequency and adsorption energy (ΔE_{ads}) were calculated. ΔE_{ads} was calculated using the following equation:

$$\Delta E_{ads} = E_{pyr+\gamma\text{-}Al2O3} - (E_{\gamma\text{-}Al2O3} + E_{pyr}), \quad (1)$$

Here, $E_{pyr+\gamma\text{-}Al2O3}$ is the total energy of the system after the structural relaxation of the pyridine adsorbed on the Al_{IV} edge sites. $E_{\gamma\text{-}Al2O3}$ and E_{pyr} represent the total energy of the γ-Al_2O_3 step-edge model and pyridine, respectively; E_{pyr} was calculated by constructing an isolated model with pyridine molecules in a cube of 25 Å per side and by performing structural relaxation. Furthermore, to correct the energy error due to d electron delocalization, the effect of addition of Hubbard *U* was investigated based on Dudarev's formulation.[84] The effective *U* value (denoted as U_{eff}) of $U - J$ was set to be 5 eV in Ag. This value is the same as that used by Stevanovic et al.[85] to determine the elemental phase reference energy. All the step-edge models were calculated with a 1 × 1 × 1 k-points mesh and an energy cutoff of 400 eV. The criterion for convergence is that the maximum value of the Hellmann–Feynman force should be smaller than 0.05 eV/Å. Bader charge analysis was also performed to evaluate the valence of Ag.[86–88]

For comparison, the anchoring of Ag on aγ-Al_2O_3 (100) surface was also investigated. γ-Al_2O_3 (100) contains a (1 × 1) supercell, a four-layer-thick slab, and 15 Å of vacuum with 40 atoms (lattice parameters for the surface: a = 5.59 Å, b = 8.41 Å). The OH groups produced by dissociative adsorption of H_2O were placed on the Al_V site. Ag was anchored by exchanging the H of HO-μ^1-Al_{VI} on theγ-Al_2O_3 (100) surface. During structural relaxation, the bottom two layers were fixed. All the calculation condition is the same as for the step-edge model, except that the k-points mesh is changed to 4 × 3 × 1 (see **Figure S3**). All the structures obtained by DFT calculations are presented in the CIF format in the Supporting Information (see Associated contents).

Ab initio thermodynamic analysis

Ab initio thermodynamic analysis[52,89] was performed to study the effect of reaction gases (H_2, O_2, and $NO+O_2$) and temperature on the AgO-μ^1-Al_{VI} species on the γ-Al_2O_3 (110)–(100) step-edge surface (see **Figure S1b** for the structures considered). Enthalpies and entropies at each temperature and the standard state pressure (1 atm) were obtained from the NIST-JANAF Thermochemical Tables.[90] The Ag bulk model (containing four Ag atoms in unit cell) was used to obtain the energy of the Ag atom. The energies of the gas molecules were obtained using a large empty unit cell (25 × 25 × 25 Å) to mimic the isolated species. The equilibrium reaction, energy change (ΔE), Gibbs free energy change (ΔG), and chemical potential change ($\Delta\mu$) under (a) H_2+H_2O, (b) O_2+H_2O, and (c) $NO+O_2+HNO_3$ atmospheres are given by Eqs. (2)–(11).

(a) H_2 + (H_2O) atmosphere:

$x\mathrm{Ag_{bulk}}$ + 10(H+OH)/γ-Al_2O_3 + $\left(-y+\frac{1}{2}z\right)H_2$ + $(y-10)H_2O$ ⇄ ($Ag_xO_yH_z$)/γ-Al_2O_3 (2)

$\Delta E = E((Ag_xO_yH_z)/\gamma\text{-}Al_2O_3) - E(10(H+OH)/\gamma\text{-}Al_2O_3)$

$$- xE(\mathrm{Ag_{bulk}}) - \left(-y+\frac{1}{2}z\right)E(H_2) - (y-10)E(H_2O) \quad (3)$$

$$\Delta G(T,p) = \frac{1}{A}\left[\Delta E - \left(-y+\frac{1}{2}z\right)\Delta\mu_{H2} - (y-10)\Delta\mu_{H2O}\right] \quad (4)$$

(b) <u>O_2 + (H_2O) atmosphere:</u>

$x\mathrm{Ag_{bulk}}$ + 10(H+OH)/γ-Al_2O_3 + $\left(\frac{1}{2}y-\frac{1}{4}z\right)O_2$ + $\left(\frac{1}{2}z-10\right)H_2O$ ⇄ ($Ag_xO_yH_z$)/γ-Al_2O_3 (5)

$\Delta E = E((Ag_xO_yH_z)/\gamma\text{-}Al_2O_3) - E(10(H+OH)/\gamma\text{-}Al_2O_3)$

$$- xE(\mathrm{Ag_{bulk}}) - \left(\frac{1}{2}y-\frac{1}{4}z\right)E(O_2) - \left(\frac{1}{2}z-10\right)E(H_2O) \quad (6)$$

$$\Delta G(T,p) = \frac{1}{A}\left[\Delta E - \left(\frac{1}{2}y-\frac{1}{4}z\right)\Delta\mu_{O2} - \left(\frac{1}{2}z-10\right)\Delta\mu_{H2O}\right] \quad (7)$$

(c) <u>NO + O_2 + (HNO_3) atmosphere:</u>

$x\mathrm{Ag_{bulk}}$ + 10(H+OH)/γ-Al_2O_3 + $(-z+20)NO$ + $\left(\frac{1}{2}y-z+15\right)O_2$ + $(z-20)HNO_3$

$$\rightleftarrows (Ag_xO_yH_z)/\gamma\text{-}Al_2O_3 \quad (8)$$

$\Delta E = E((Ag_xO_yH_z)/\gamma\text{-}Al_2O_3) - E(10(H+OH)/\gamma\text{-}Al_2O_3)$

$$- xE(\mathrm{Ag_{bulk}}) - (-z+20)E(NO) - \left(\frac{1}{2}y-z+15\right)E(O_2) - (z-20)E(HNO_3) \quad (9)$$

$$\Delta G(T,p) = \frac{1}{A}\left[\Delta E - (-z+20)\Delta\mu_{NO} - \left(\frac{1}{2}y-z+15\right)\Delta\mu_{O2} - (z-20)\Delta\mu_{HNO3}\right] \quad (10)$$

$$\Delta\mu_{gas} = \Delta\mu_{gas}(T,p^0) + RTln\left(\frac{P_{gas}}{P^0}\right) \quad \text{(gas = } H_2, O_2, H_2O, NO, N_2O, \text{ and } HNO_3) \quad (11)$$

Here, ($Ag_xO_yH_z$)/γ-Al_2O_3 is a chemical species that includes AgO-μ^1_H-μ^3/γ-Al_2O_3 (x = 2, y = 10, z = 18) and (Ag NPs)+H_OH/γ-Al_2O_3 (x = 4, y = 10, z = 20). These correspond to dispersed and aggregated (sintered) species, respectively. $E((Ag_xO_yH_z)/\gamma\text{-}Al_2O_3)$ is the total energy of the species. E(10(H + OH)/γ-Al_2O_3) is the total energy of the γ-Al_2O_3 (110)–(100) step-edge surface, where H_2O

molecules are dissociatively adsorbed. $E(Ag_{bulk})$ is the total energy of the Ag bulk model (containing four Ag atoms in unit cell); $E(H_2)$, $E(O_2)$, $E(NO)$, $E(H_2O)$, and $E(HNO_3)$ represent the total energy of the gas molecules. $\Delta\mu_{gas}$ is defined as the change in the chemical potential of the gases involved in the reaction (Eq. (11)); T is the temperature (K), p^0 is the atmospheric pressure, and p_{gas} is the partial pressure of the reaction gases. H_2O, which appears in Eq. (2) and (5), and HNO_3, which appears in Eqs. (8), are not detected under the experimental conditions but are assumed to be present in small quantities (100 ppm) for stoichiometric reasons.

5.3. RESULTS AND DISCUSSION

Dispersion and regeneration of sintered Ag species on Ag/Al_2O_3 for H_2-assisted NH_3–SCR

The fresh, sintered, and re-oxidized Ag species on $Ag3/Al_2O_3$ were studied by XRD (**Figure 1a**), XAS (**Figure 1b,c**), HAADF-STEM (**Figure 2**), and activity tests (**Figure 3**). The full range of XRD patterns are shown in **Figure S4**.

The XRD pattern of fresh $Ag3/Al_2O_3$ showed no peaks corresponding to crystalline metallic and oxidized silver compounds (**Figure 1a**). HAADF-STEM images of fresh $Ag3/Al_2O_3$ showed the presence of atomically dispersed silver species and small clusters/nanoparticles with diameters less than 2 nm (**Figure 2a**). The edge position as well as the shape of the XANES spectrum of fresh Ag_3/Al_2O_3 correspond well to those of the $AgNO_3$ used as a reference (**Figure 1b**),[13] suggesting that the Ag species in $Ag3/Al_2O_3$ existed as monovalent Ag^+ ions.[56] Fitting (**Table 1**) of the EXAFS spectrum (**Figure 1c**) revealed the Ag–O bond at a distance (*R*) of 2.0 Å, with a coordination number (CN) of 3.7, and a relatively small contribution from the Ag–Ag coordination (CN = 2.6; *R* = 2.90 Å). The XANES/EXAFS analyses were consistent with the HAADF-STEM analysis—isolated Ag(I) species were the dominant Ag species, and metallic Ag clusters were the minor Ag species on fresh Ag_3/Al_2O_3. Upon high-temperature aging treatment under 100% H_2 at 800 °C for 1 h, an XRD peak was observed at 38.1°; this was attributed to Ag metal (111)[31] (**Figure 1a**). Atomic Ag species were not observed in the HAADF-STEM images of sintered $Ag3/Al_2O_3$ (**Figure 2b**). The size of the Ag metal NPs ranged from 10 to 52 nm. This demonstrates that high temperature (800 °C)-reduction of fresh $Ag3/Al_2O_3$ causes the isolated Ag(I) species to aggregate to Ag metal NPs. When sintered $Ag3/Al_2O_3$ was reoxidized by O_2 or NO + O_2 at 400 °C for 1 h, the intensity of the XRD peak of Ag metal decreased. XRD peaks due to silver oxides were not observed (**Figure 1a**). The HAADF-STEM images of $Ag3/Al_2O_3$ after oxidation by NO + O_2 revealed atomically dispersed silver species and small clusters and NPs with diameters of 2–18 nm, indicating the oxidative dispersion of large (10–52 nm) Ag metal NPs to small (2–18 nm) NPs and atomic Ag species (**Figure 2c**). The XRD peak of the Ag metal was less intense after oxidation by NO + O_2 than by O_2. The XANES features and EXAFS results (1.2 Ag–O bonds at 2.00 Å) of re-oxidized $Ag3/Al_2O_3$ are distinct from those of sintered $Ag3/Al_2O_3$ but similar to those of fresh Ag_3/Al_2O_3. These results suggest that the atomically dispersed Ag(I) species are regenerated by the oxidative transformation of the Ag metal NPs, and the re-dispersion by O_2 is promoted by NO.

The Ag species of fresh Ag_3/Al_2O_3 show high dispersion as monovalent Ag^+ over the alumina support and high catalytic activity in H_2–NH_3–SCR. Previous studies[21,24,31] have established that atomically dispersed Ag(I) species and small AgO*x* clusters are the dominant Ag species on the calcined Ag/Al_2O_3 catalysts with low Ag loading (typically below 2–3 wt%). The characterization results of the fresh (calcined) $Ag3/Al_2O_3$ are consistent with this structural model, as described above.

The above results suggest that the atomically dispersed Ag species, once converted to 10–52 nm Ag metal particles by the reduction in H_2 at 800 °C, can be regenerated by NO + O_2 treatment. The deactivation and regeneration of the Ag3/Al_2O_3 catalyst for the De-NO_x reaction were investigated by comparing the catalytic activity of the fresh, sintered, and regenerated Ag3/Al_2O_3 in the H_2–NH_3–SCR. The sintered Ag3/Al_2O_3 catalyst showed lower NOx conversions than fresh catalyst for H_2–NH_3–SC (**Figure S5**). Steady-state rates of NO reduction (at 150–225 °C) are plotted in **Figure 3**. The results show that the catalytic activity of Ag3/Al_2O_3 decreased upon high-temperature reduction-induced sintering of Ag but was recovered upon NO + O_2 treatment. In combination with the structural analysis, the following conclusions can be drawn: the fresh Ag3/Al_2O_3 is deactivated by H_2-reduction at 800 °C because the atomically dispersed Ag(I) species and Ag clusters, which are the active species of H_2–NH_3–SCR,[13] are aggregated to large (10–52 nm) Ag metal particles. The activity of the deactivated catalyst was recovered by re-oxidation under NO + O_2 atmosphere at 400 °C because the Ag metal NPs were transformed to the atomically dispersed Ag(I) species, which were the active species in the H_2–NH_3–SCR.

Table 1. Ag K-edge EXAFS Curve-fitting Analysis of Ag3/Al_2O_3

Sample	Shell	CN [a]	R [b] / Å	σ^2 [c] / Å^2	R_f [d] / %
Fresh Ag3/Al_2O_3	Ag–O	3.7	2.09	0.019	2.2
	Ag–Ag	2.6	2.94	0.030	2.8
Sintered Ag3/Al_2O_3	Ag–Ag	10	2.94	0.021	2.8
Re-oxidized Ag3/Al_2O_3	Ag–O	1.2	2.09	0.010	2.1

[a] Coordination number. [b]Bond distance. [c] Debye-Waller factor. [d] Residual factor.

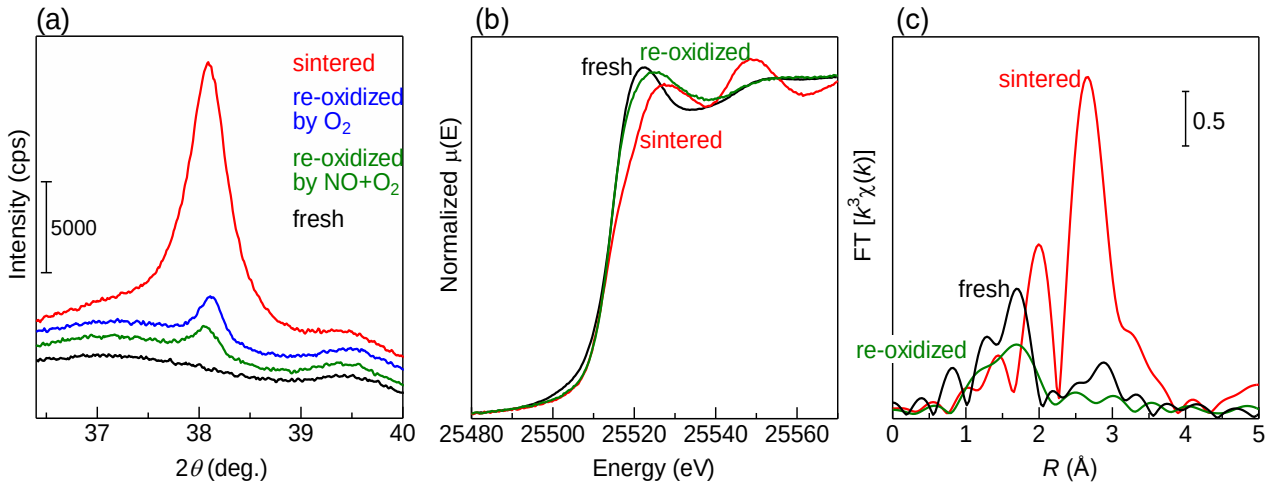

Figure 1 (a) XRD patterns, (b) XANES spectra, and (c) EXAFS Fourier transforms (FTs) of Ag_3/Al_2O_3 after consecutive redox treatments: black, fresh (calcined); red, reduced (sintered) in H_2

at 800 ˚C; green, re-oxidized in NO + O_2; and blue, re-oxidized in O_2 at 400 ˚C for 0.5 h. The XANES/EXAFS data of reduced and re-oxidized samples were acquired *in situ* at 400 ˚C.

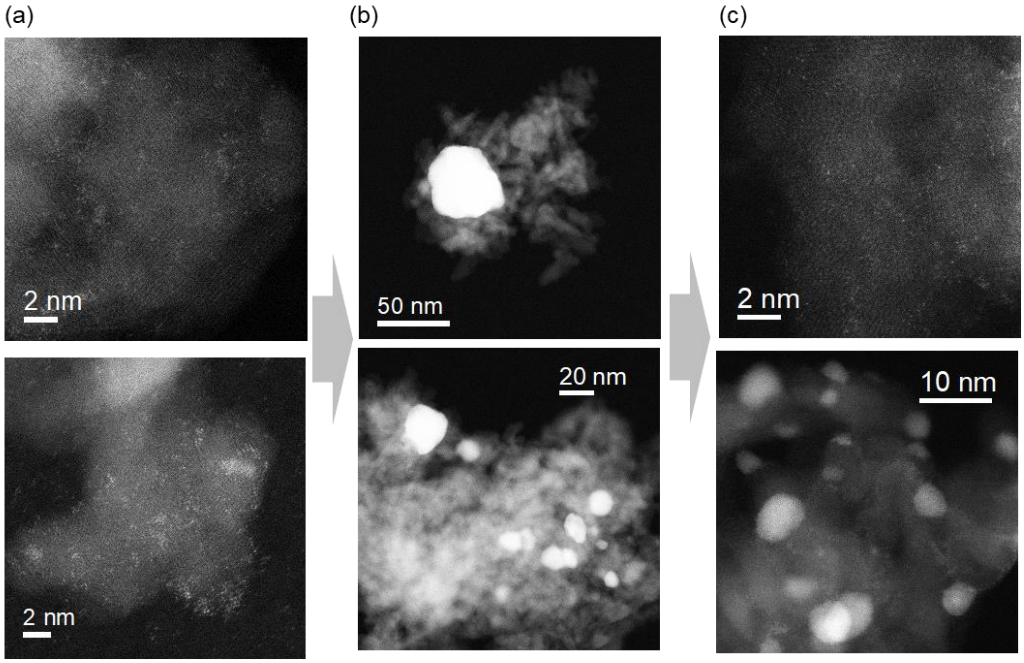

Figure 2 HAADF-STEM images of Ag3/Al_2O_3 after successive redox treatments: (a) fresh, (b) reduced (sintered) in H_2 at 800 ˚C, and (c) re-oxidized in NO + O_2 at 400 ˚C.

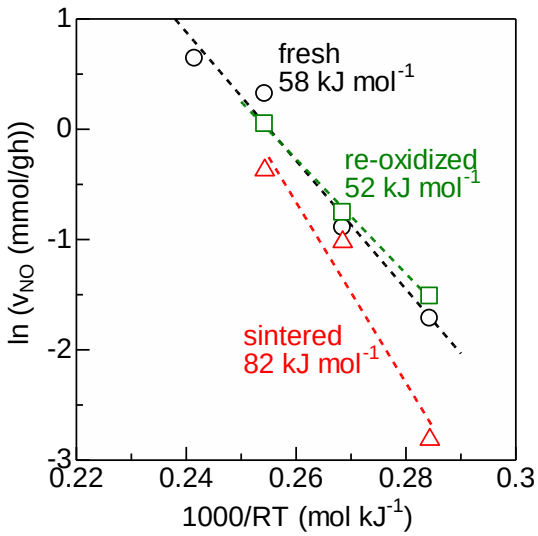

Figure 3 Arrhenius plots for the H_2–NH_3–SCR by Ag3/Al_2O_3 after successive redox treatments: black, fresh; red, reduced (sintered) in H_2 at 800 ˚C; and green, re-oxidized in NO + O_2 at 400˚C.

***Ex situ* observation of reductive aggregation and oxidative dispersion**

Changes in the particle size distribution after reductive aggregation and oxidative re-dispersion were monitored by *ex situ* microscopy. Representative TEM images and particle size distributions are shown in **Figure 4**. To improve the accuracy of the particle size analysis, we used a high loading (10 wt%) sample ($Ag10/Al_2O_3$). TEM was used to analyze the Ag metal NPs (> 3 nm), while HAADF-STEM was used to observe the atomically dispersed Ag(I) species and the small Ag clusters. TEM images of the fresh $Ag10/Al_2O_3$ sample show Ag NPs with a diameter of 3-30 nm and mean size of 10 ± 9 nm (**Figure 4a**). HAADF-STEM images of this sample show isolated Ag(I) species and small Ag clusters (**Figure 4e**). The reduction of $Ag10/Al_2O_3$ in H_2 at 800 °C increased the mean size of the Ag NPs (60 ± 34 nm) and resulted in a broader size distribution (6-188 nm) (**Figure 4b**). Isolated Ag(I) species were not observed by HAADF-STEM (**Figure 4f**). The XRD pattern of this sample shows an intense peak at 38.1° owing to the aggregated Ag metal (**Figure 4i**). The sintered sample was oxidized by NO and O_2 at 400 °C for 135 s (followed by quick cooling of the sample to room temperature under NO and O_2 flow), and this led to a decrease in the XRD peak intensity of the Ag metal. The mean size of the Ag NPs, as estimated from the TEM analysis, decreased from 60 ± 34 nm (**Figure 4b**) to 43 ± 21 nm (**Figure 4c**). HAADF-STEM images of this sample show small Ag NPs and isolated Ag(I) species. Interestingly, the isolated Ag(I) species were observed near the Ag metal NPs (**Figure 4g**). After the NO + O_2 treatment for 1 h, the mean size of the Ag NPs (12 ± 8 nm) and the size distribution histogram (**Figure 4d**) were similar to those of the fresh $Ag10/Al_2O_3$ sample, and the isolated Ag(I) species were regenerated (**Figure 4h**). The XRD peak of Ag metal for the NO + O_2 treated sample was similar to that of the fresh sample. This *ex situ* characterization reveals the oxidative dispersion of large (60 nm) Ag NPs to small Ag NPs, Ag clusters, and isolated Ag(I) species on Al_2O_3 upon NO + O_2 treatment at 400 °C. An increase in the NO + O_2 treatment time resulted in a decrease in the mean size of Ag NPs and the generation of a larger number of isolated Ag(I) species. The STEM images show that the remaining Ag NPs are surrounded by isolated Ag(I) species in the initial stage of the oxidative dispersion (**Figure 4g**), and the temporal evolution suggests that the dispersion is not driven by the migration of small Ag clusters or NPs but by the movement of atomic Ag species.

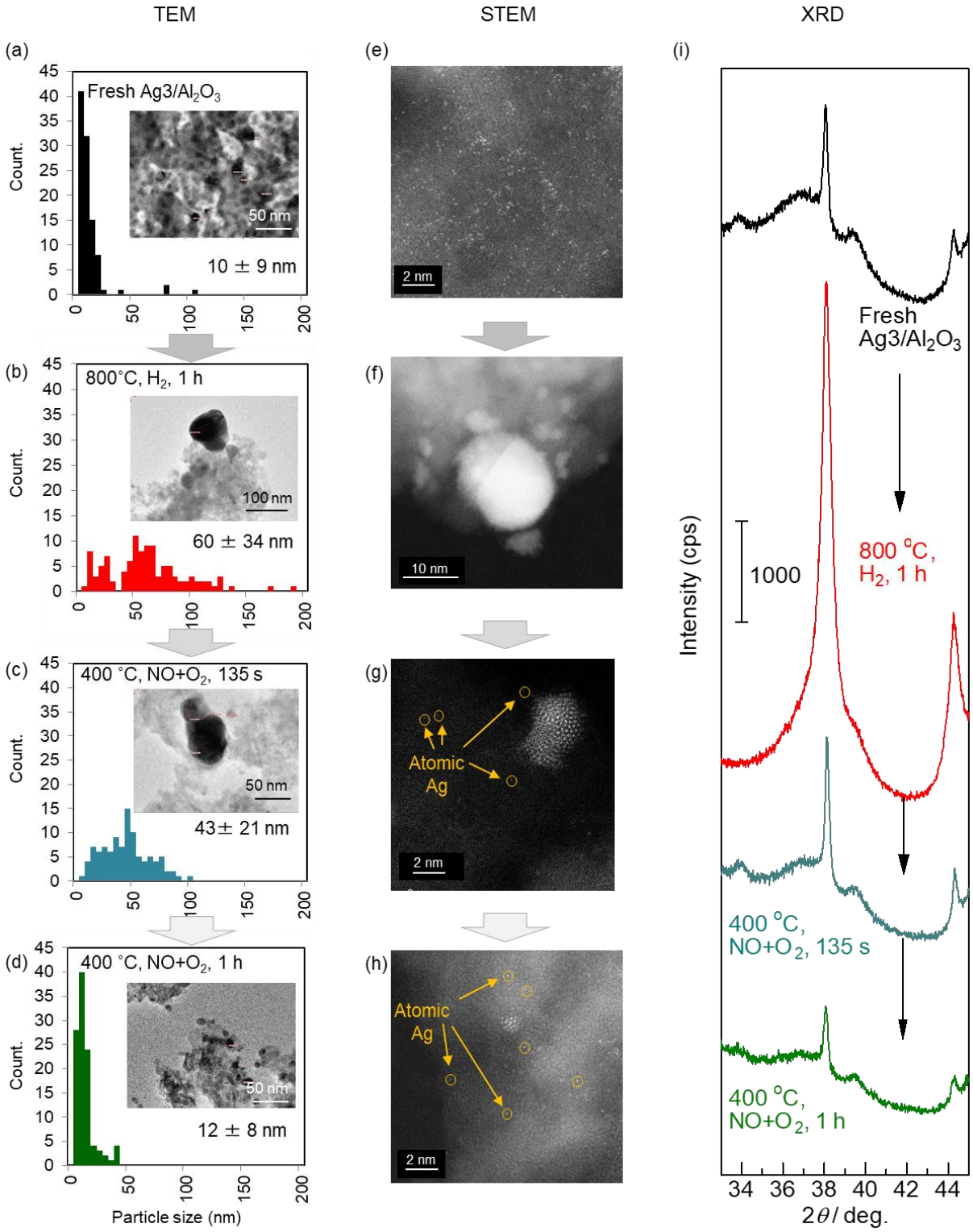

Figure 4 (a-d) TEM images and particle size distribution, (e-h) HAADF-STEM images, and (i) XRD patterns of the high loading (10 wt%) sample ($Ag10/Al_2O_3$) after successive redox treatments.

***In situ* kinetic study on oxidative dispersion**

Dynamic structural changes of the Ag species during oxidative dispersion were monitored by *in situ* time-resolved Ag K-edge XANES spectroscopy. The Ag3/Al_2O_3 sample pre-reduced under H_2 at 800 °C shows XANES and EXAFS (10.1 Ag-Ag bonds at 2.91 Å; **Table 1**) features similar to those of a model compound for Ag metal (**Figure 5**). The XANES peak intensity of the Ag(I) species at 25516 eV[56] increased with increasing NO + O_2 treatment time at 400 °C (**Figure 5a**). To quantify the species based on the *in situ* XANES spectra, LCF analysis of these spectra was carried out in the energy range 25480–25570 eV using the spectra of the two reference samples: Ag(I) ion-exchanged CHA zeolite for isolated Ag(I) species and Ag(10 wt%)-loaded low surface area *α*, *θ*-Al_2O_3 for Ag metal NPs. As shown in **Figure 5b**, the *in situ* XANES spectrum under NO + O_2 flow at 400 °C is nearly consistent with the simulated spectrum, indicating that the Ag species on Al_2O_3 are Ag NPs and isolated Ag(I) species. The fraction of the isolated Ag(I) species increased with time while that of the metal NPs decreased, indicating the oxidative dispersion of Ag NPs to isolated Ag(I) species (**Figure 5c**). After the NO + O_2 treatment for 1000 s, the Ag–Ag coordination of the EXAFS disappeared, accompanied by the appearance of Ag–O coordination (**Figure 1c, Table 1**). The fraction of the isolated Ag(I) species in the re-oxidized sample is much higher than that of the sintered catalyst but rather close to that of the fresh sample. Assuming that the isolated Ag(I) species is indispensable species for H_2–NH_3–SCR,[31] the XANES result is consistent with the catalytic results in Figure 3.

In situ diffuse reflectance UV-vis spectroscopy was used to characterize Ag clusters and small Ag NPs under redox conditions.[31,55] The UV-vis spectrum of Ag3/Al_2O_3 after *ex situ* reduction under H_2 at 800 °C, followed by *in situ* reduction under 1% H_2/He at 400 °C, shows a broad band centered at 400 nm assignable to small Ag NPs (**Figure 6**). Then, the intensity of the UV-vis band at 400 nm was monitored as a function of the oxidation time under NO, O_2, or NO + O_2 atmosphere at 400 °C. The consumption rates of Ag NPs, as estimated by the initial slope of the kinetic curve ($\Delta KM/\Delta t$), depend on the gas mixture; the rates of oxidative dispersion change in the order NO + O_2 > O_2 > NO. The initial rates of oxidative dispersion under O_2 and NO + O_2 atmospheres at different temperatures were also estimated in a similar manner. With prolonged dispersion (4000 s) under NO + O_2 or O_2 atmosphere at 400 °C, the intensity of the UV-vis band at 400 nm assignable to the Ag NPs decreased. However, the extent of decrease was higher for the NO + O_2 treatment than for the O_2 treatment (**Figure S6**). **Figure 7** shows the Arrhenius plots of the oxidative dispersion of the Ag NPs under NO + O_2 and O_2 atmospheres. The $\Delta KM/\Delta t$ values were -1.0×10^{-3} under NO + O_2 atmosphere and -2.8×10^{-4} under O_2 atmosphere at 400 °C. At 300 °C, these

values were -5.0×10^{-4} under NO + O_2 atmosphere and -5.4×10^{-5} under O_2 atmosphere. Notably, the value of the initial slope in the UV-vis kinetic curve at 400 nm ($\Delta KM/\Delta t$) indicates the rate of oxidative dispersion as well as the consumption rate of the Ag NPs. The rate of oxidative dispersion at 300 °C under NO + O_2 was 10 times higher than that under O_2. Below 450 °C, the apparent activation energy under NO + O_2 (16 kJ mol^{-1}) was lower than that under O_2 (49 kJ mol^{-1}). This indicates that the oxidative dispersion was significantly enhanced by NO, and *in situ* IR spectroscopy suggested that the formation of silver nitrate as the mobile Ag(I) species promoted the oxidative dispersion under NO. Similar sets of experiments were performed at 400 °C by changing the concentrations of NO and O_2. The rates of oxidative dispersion under 500 ppm NO with different O_2 concentrations and those under 10% O_2 with different NO concentrations are plotted in **Figure 8**. The reaction orders with respect to NO and O_2, as estimated from the slopes, were 0.47 and 0.26, respectively. The positive values suggest that both NO and O_2 are involved in the kinetically important steps in the oxidative dispersion of Ag NPs into isolated Ag(I) species. The higher reaction order for NO suggests that NO is involved in the rate-limiting step.

Figure 9a shows the time-resolved *in situ* IR spectra of the adsorbed species on the sintered Ag3/Al_2O_3 catalysts during the oxidative dispersion of Ag NPs under the NO + O_2 atmosphere at 400 °C. Exposure of the sintered Ag3/Al_2O_3 to NO + O_2 for 300 s resulted in the formation of nitrate (NO_3^-) species (as evident from the new peaks at 1630, 1545, 1290, 1245 cm^{-1}).[20,28] The relative concentration of nitrates was estimated from the peak areas in the range of 1470–1672 cm^{-1}. The formation rate of nitrates corresponded to the initial slope of the IR peak area ($\Delta area/\Delta t$) in this wavelength range. The values of $\Delta area/\Delta t$ were 2.5×10^{-2} and 2.5×10^{-3} for sintered Ag3/Al_2O_3 and fresh Ag3/Al_2O_3, respectively. Additionally, no formation of nitrate was in γ-Al_2O_3. It is evident that the formation rate of nitrates for sintered Ag3/Al_2O_3 was 10 times higher than those for fresh Ag3/Al_2O_3 and γ-Al_2O_3 (**Figure 9b)**. This indicates that the Ag metal NPs (major Ag species in sintered Ag3/Al_2O_3) promote the oxidation of NO to nitrates more efficiently than isolated Ag(I) species (major Ag species in fresh Ag3/Al_2O_3) and γ-Al_2O_3 alone. Generally, oxidation of NO on metal surfaces involves reductive activation of O_2 by the surface metal sites.[91] Based on the *in situ* XANES/EXAFS data and *in situ* UV-vis data for the oxidative dispersion of the Ag NPs under the NO + O_2 atmosphere, the higher rate of nitrate formation by sintered Ag3/Al_2O_3 than by fresh Ag3/Al_2O_3 can be attributed to the higher activity of the Ag metal NPs for the reductive activation of O_2 than the isolated Ag(I) sites. Kinetic analysis (**Figure 8**) suggests that both NO and O_2 are involved in the key steps of the redispersion process, while *in situ* XANES results (**Figure 5c**) suggest that metallic Ag^0 species are directly converted to Ag(I) species and that the initial step of the redispersion process can be described as a stoichiometric reaction (12):

$$Ag^0 + NO + 1/2O_2 \rightarrow AgNO_3 \quad (12)$$

The $AgNO_3$ species thus formed on the surface of the Ag metal NPs have a melting point of 212 °C, which is lower than the temperature of reoxidation, and hence, migrate to the surface of γ-Al_2O_3 owing to the concentration gradient of $AgNO_3$. Then, $AgNO_3$ is anchored by the Al-OH site to form Al-OAg and HNO_3 (reaction 13), following which HNO_3 either evaporates or reacts with a Lewis acid-base pair (Al-O) site of γ-Al_2O_3 to form nitrates on γ-Al_2O_3 (reaction 14). The structure of the Al-OH site for anchoring Ag (I) is discussed in the following section.

$$AgNO_3 + \text{Al-OH} \rightarrow \text{Al-OAg} + HNO_3 \quad (13)$$

$$HNO_3 + \text{Al-O} \rightarrow NO_3^- \text{Al-OH} \quad (14)$$

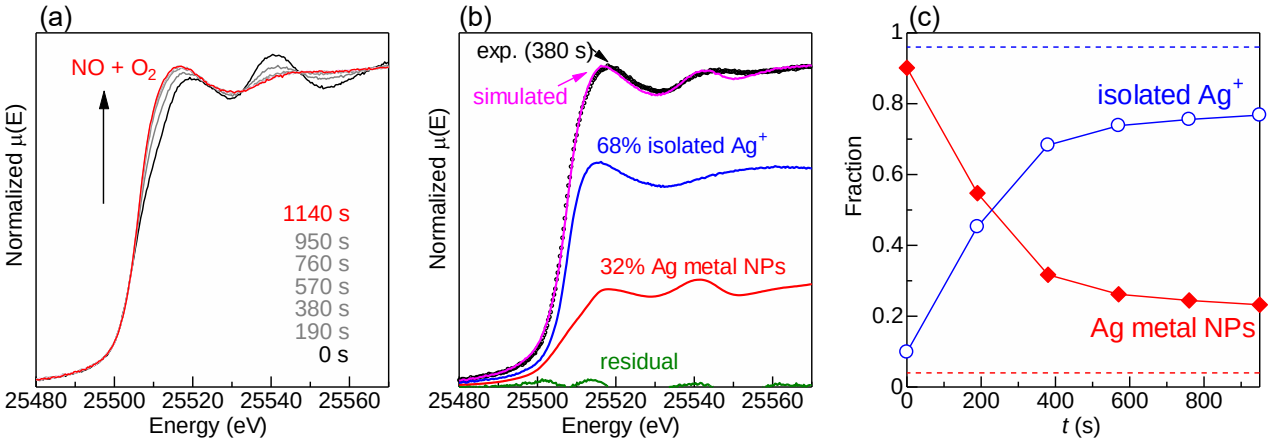

Figure 5 (a) *In situ* Ag K-edge XANES spectra of H_2-reduced (sintered) $Ag3/Al_2O_3$ during reoxidation by NO + O_2 at 400 ˚C. (b) LCF analysis after treatment in NO + O_2 for 380 s. (c) Time course of the fractions of Ag metal NPs and isolated Ag^+. EXAFS data at t = 0 s (sintered) and 1140 s (re-oxidized) are shown in **Figure 1c**. Fractions of Ag metal NPs (red) and isolated Ag^+ (blue) in the fresh $Ag3/Al_2O_3$ are shown as dashed lines.

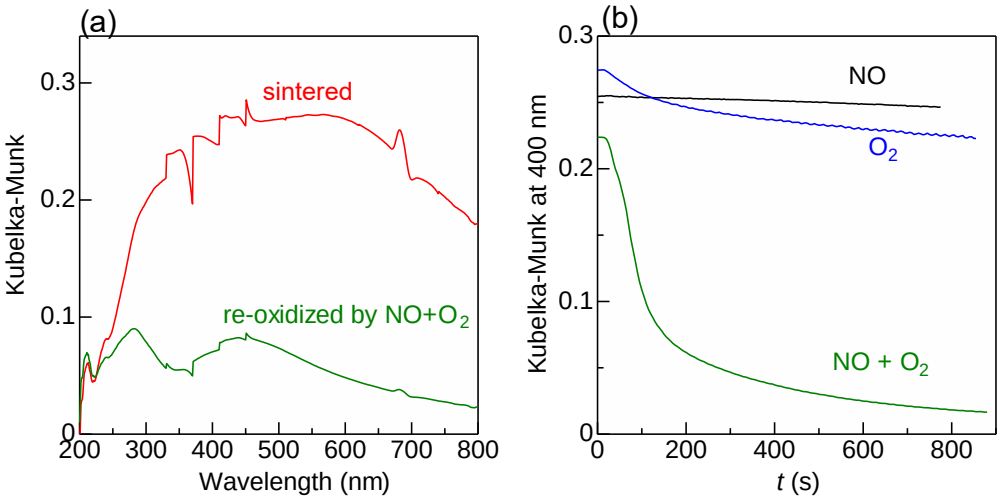

Figure 6 (a) *In situ* UV-vis spectra of sintered Ag3/Al_2O_3 (difference spectrum after reduction by H_2 at 800 ˚C) and spectra after subsequent re-oxidation at 400 ˚C by 500 ppm NO + 10% O_2 (800 s). (b) Time dependence of the UV-vis signal intensity due to Ag NPs during re-oxidation by (black) 500 ppm NO, (blue) 10% O_2, and (green) 500 ppm NO + 10% O_2 at 400 ˚C.

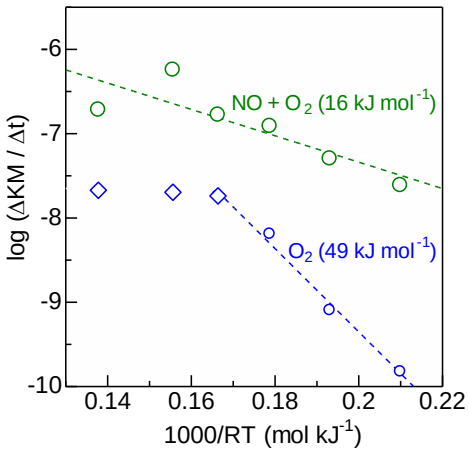

Figure 7 Arrhenius plots (300–500 ˚C) for the consumption of Ag NPs during re-oxidation of sintered Ag3/Al_2O_3 (pre-reduced by H_2 at 800 ˚C) by (blue) 10% O_2 and (green) 500 ppm NO + 10% O_2. The rate of Ag NPs consumption was estimated from the initial slope ($-\Delta KM/\Delta t$) of the kinetic curve (**Figure 6b**).

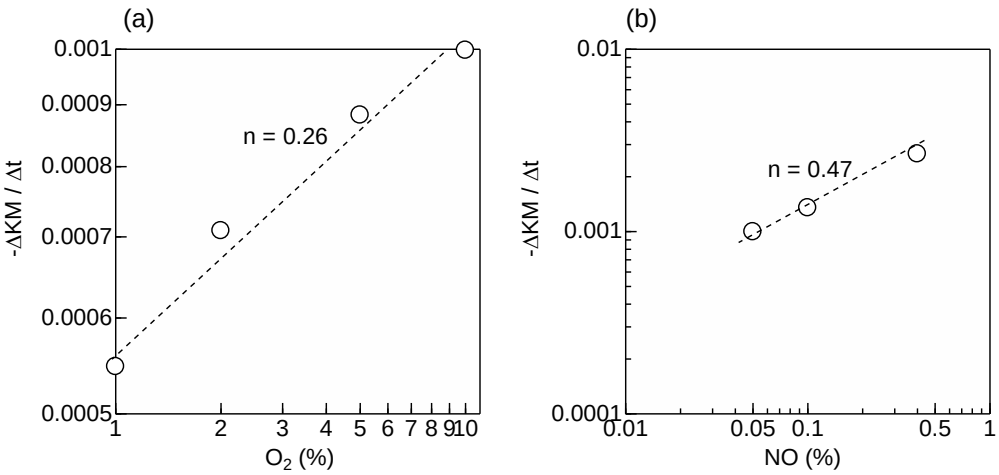

Figure 8 Rate of consumption of Ag NPs versus the partial pressure of (a) NO and (b) O_2 during re-oxidation of sintered Ag3/Al_2O_3 under (a) 500 ppm NO + 1-20% O_2 and (b) 500-4000 ppm NO + 10% O_2.

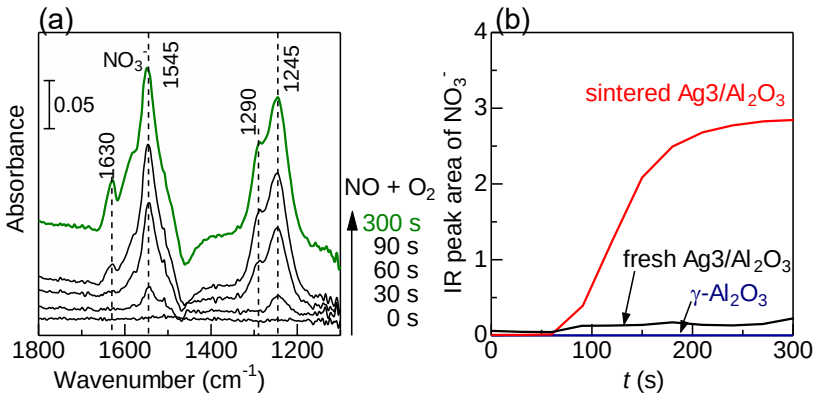

Figure 9 (a) *In situ* IR spectra of the adsorbed species on sintered Ag3/Al_2O_3 under NO + O_2 flow at 400 ˚C. (b) Kinetic curves for the formation of nitrates on *γ*-Al_2O_3 and fresh and sintered Ag3/Al_2O_3 under NO + O_2 flow at 400 ˚C.

Structure of the anchoring site

Next, we shall discuss the structure of the anchoring sites of the atomically dispersed Ag(I) species on *γ*-Al_2O_3. Among the various metal anchoring sites on *γ*-Al_2O_3, significant attention has been paid recently on the penta-coordinated (Al_V^{3+}) ions as anchoring sites for various metal clusters, metal oxides, and isolated metal cations. Kwak et al.[61,92] reported that the Al_V^{3+} sites on the *γ*-Al_2O_3 surface interact strongly with atomic Pt (or small Pt oxide species), BaO, and La_2O_3, thereby inhibiting the sintering of the supported metal species in an oxidative environment. Some studies have also reported the interaction of unsaturated Al_V^{3+} sites with WOx, PdO, and PtSn clusters supported on *γ*-Al_2O_3.[64,93,94] These conclusions are based on the fact that the NMR signal

intensity of the Al_V^{3+} center decreases with increased loading of the metal species on γ-Al_2O_3. However, Zeng et al.[24] reported no change in the NMR signal of Al_V^{3+} upon loading of Ag on γ-Al_2O_3 and proposed that the anchoring sites for Ag(I) species are not Al_V^{3+}. Based on the changes in the ^{1}H NMR and IR spectra upon Ag loading, they proposed that the terminal hydroxyl (OH) groups on the (100) γ-Al_2O_3 surface. These studies suggest that the anchoring sites on γ-Al_2O_3 depend on the type of the metal species, and the specific anchoring sites should be determined based on multiple spectroscopic evidence assuming various candidates for anchoring sites. The aforementioned results indicate that the anchoring and de-anchoring of the isolated Ag(I) cations on γ-Al_2O_3 can be controlled by exposing Ag-loaded γ-Al_2O_3 under reductive and oxidative environments. Based on this, we hypothesized that the present system is suitable for investigating the anchoring sites of the Ag(I) species using multiple spectroscopic techniques. The candidates for the binding sites are the coordinatively unsaturated Al (surface Al^{3+} Lewis acid) sites such as Al_V^{3+}, tetra-coordinated Al^{3+} (Al_{IV}^{3+}) sites, and various OH groups.

First, we investigated the ^{27}Al NMR spectra of bare γ-Al_2O_3. Previous studies on ^{27}Al NMR of γ-Al_2O_3 have established that Al_V^{3+} ions are present only on the first surface layer.[61] As shown in **Figure S8**, an ^{27}Al NMR signal of Al_V^{3+} centered around 33 ppm was observed for the γ-Al_2O_3 sample dehydrated at 500 °C. The ^{27}Al NMR signal of Al_V^{3+} disappeared after exposure to ambient conditions for 1 h. This result is consistent with the previous conclusion that the Al_V^{3+} ions are present on the first surface layer of γ-Al_2O_3 and that the coordination of water to the unsaturated Al_V^{3+} sites on the surface yields hexacoordinated (octahedral) Al^{3+} (Al_{VI}^{3+}) sites. **Figure 10** shows the ^{27}Al NMR spectra of γ-Al_2O_3 and fresh, sintered, and reoxidized Ag3/Al_2O_3, pre-dehydrated under N_2 at 500 °C for 1 h. The peaks with chemical shifts centered at 10, 33, and 67 ppm were assigned to Al_{IV}^{3+}, Al_V^{3+}, and Al_{VI}^{3+}, respectively. The intensity of the Al_V^{3+} peak for the fresh Ag3/Al_2O_3 is lower than that of γ-Al_2O_3, indicating that some of the surface Al_V^{3+} sites interact with the isolated Ag(I) species. After the sintering of the isolated Ag(I) species to the Ag NPs, the intensity of the Al_V^{3+} peak reached that of γ-Al_2O_3. When the sintered Ag3/Al_2O_3 was oxidized by NO + O_2 at 400 °C, the intensity of the Al_V^{3+} peak decreased to that of fresh Ag3/Al_2O_3. The combined XANES, EXAFS, UV-vis spectroscopy, and NMR spectroscopy data indicate that free Al_V^{3+} sites were recovered by the aggregation of the anchored Ag (I) species to Ag NPs (de-anchoring), and after oxidation by NO + O_2, the redispersed isolated Ag(I) ions interacted again with the Al_V^{3+} sites. These results suggest that the surface Al_V^{3+} sites of γ-Al_2O_3 may be one of the binding sites for the atomic Ag(I) species. However, the changes in the NMR signal corresponding to the Al_V^{3+} sites are very minor; thus, we conclude that ^{27}Al NMR is not the best method for

monitoring the dynamic changes in the anchoring sites for the Ag(I) species upon de-anchoring (sintering of Ag) and anchoring (re-dispersion of Ag(I)). Moreover, the ^{27}Al NMR signal from tetrahedral Al^{3+} (Al_{IV}^{3+}) provides structural information on both surface and bulk alumina; accordingly, this method is not suitable for determining the role of the other low-coordinated Al^{3+} sites (Al_{IV}^{3+}) in the binding of metal species. In other words, the previous studies on ^{27}Al NMR on metal anchoring sites have excluded the possible role of the Al_{IV}^{3+} sites.

To probe the interaction of the Ag species with various surface Al^{3+} sites, we carried out a conventional pyridine adsorption IR experiment. Previous IR studies have established that the 8a mode of pyridine coordinated to Al^{3+} Lewis acid sites is useful for identifying Al^{3+} Lewis acid sites in different coordination environments.[67] Based on the fact that pyridine with a higher wavenumber of the 8a band desorbs at a higher temperature, Lennon et al. assigned the bands at 1595, 1613, and 1623 cm^{-1} to weak, medium, and strong Lewis acid sites, respectively.[67] **Figure 11** shows the IR spectra of pyridine adsorbed at 200 °C on γ-Al_2O_3 and the fresh, sintered, and re-dispersed Ag3/Al_2O_3 samples after redox treatment at 500 °C. It is to be noted that the redispersed catalyst was prepared by oxidization of the sintered catalyst with 10% O_2 instead of using NO + O_2, because IR bands due to nitrates were observed on the Ag3/Al_2O_3 sample prepared with NO + O_2. A peak at 1613 cm^{-1} with a shoulder at 1621 cm^{-1} was observed for all the samples, indicating the presence of medium and weak Lewis acid sites. No shoulder peak at 1597 cm^{-1} was observed for γ-Al_2O_3 and sintered Ag3/Al_2O_3 but was observed for fresh and re-oxidized (re-dispersed) Ag3/Al_2O_3. Since the XANES, EXAFS, and STEM analyses suggest that isolated Ag(I) species are present on fresh and re-oxidized Ag3/Al_2O_3 but not on γ-Al_2O_3 and sintered Ag3/Al_2O_3, it can be concluded that the weak Lewis acid sites (1597 cm^{-1}) are related to the presence of Ag(I) ions on γ-Al_2O_3. Although the band at 1621 cm^{-1} can be assigned to the tricoordinated Al^{3+} (Al_{III}^{3+}) site, the dehydration conditions of γ-Al_2O_3 in this study (500 °C under He flow for 1h), which is milder than the high-temperature evacuation conditions required for the generation of Al_{III}^{3+} sites,[59] suggest that the band at 1621 cm^{-1} can be assigned to the Al_{IV}^{3+} sites. In summary, the bands at 1597, 1613, and 1623 cm^{-1} can be assigned to weak, medium, and strong Lewis acid sites, respectively. The medium and strong Lewis acid sites corresponded to the surface Al_{VI}^{3+} and Al_{V}^{3+} sites, respectively.[71] The structure of the weak Lewis acid sites (1597 cm^{-1}), related to the presence of Ag(I) on γ-Al_2O_3, was determined from the DFT calculations, as discussed in the following section.

Upon adsorption of pyridine on the samples, a negative band at 3766 cm^{-1} appeared in the region of the OH groups of alumina, and the intensity of this negative band depended strongly on the conditions (γ-Al_2O_3 or sintered Ag3/Al_2O_3). Previous studies have shown that this OH group

corresponding to the peak at 3770 cm^{-1} is reactive toward both acidic and basic probe molecules, indicating that this OH group is both acidic and basic.[70,73,95] Digne et al. conducted the DFT study on γ-Al_2O_3 and assigned the band at 3777 cm^{-1} to the on-top OH group on octahedral Al (HO-μ^1-Al_{VI}).[71] Based on this assignment, Zeng et al. recently showed that the ^1H NMR and IR signal intensities of HO-μ^1 decreased with increasing Ag loading on γ-Al_2O_3 and proposed that the HO-μ^1 site is the anchoring site for the isolated Ag(I) ions.[24] This implies that the anchoring of Ag on γ-Al_2O_3 is basically the cation exchange of the proton (H^+) to Ag(I) cation on the surface of the HO-μ^1 group. The IR band intensity at 3770 cm^{-1} decreased upon Na^+ loading on γ-Al_2O_3,[66] indicating the high capacity of this OH group to exchange with monovalent metal cations. Liu et al. reported that the negative band of HO-μ^1-Al_{VI} (3766 cm^{-1}) coincides with the positive band due to the pyridine adsorbed on the strong Lewis acid (Al_{IV}^{3+}) sites (1621 cm^{-1}) and concluded that the HO-μ^1-Al_{VI} site is adjacent to the Al_{IV}^{3+} site.[71] The result in **Figure 11c** is consistent with this proposal; the intensity corresponding to the pyridine on the Al_{IV}^{3+} (1621 cm^{-1}) site increases with an increase in the intensity of the negative band from HO-μ^1-Al_{VI} (3766 cm^{-1}). Based on the above discussion, we concluded that the negative band at 3766 cm^{-1} can be assigned to the HO-μ^1-Al_{VI} sites adjacent to the strong Lewis acid sites (unsaturated Al_{IV}^{3+} sites). The poor correlation between the band intensities of the medium Lewis acid (Al_V^{3+}) sites (1613 cm^{-1}) and the HO-μ1-Al_{VI} site suggests that these sites are not related to each other. The number of weak Lewis acid sites (1597 cm^{-1}), related to the presence of Ag(I) on γ-Al_2O_3, decreased with an increase in the intensity of the negative band due to HO-μ^1-Al_{VI}. In the following section, we present a DFT-based structural model of the Ag(I)-anchoring sites that is consistent with these IR observations.

Based on the band assignments discussed above, the changes in the IR spectra in **Figure 11** support the following models of the anchoring sites of the Ag(I) species on γ-Al_2O_3. The negative band of HO-μ^1-Al_{VI} (3766 cm^{-1}) for fresh Ag3/Al_2O_3 is less intense than that for γ-Al_2O_3, indicating that the isolated Ag (I) cations are exchanged with H^+ of this OH group. The positive bands of pyridine on the strong Lewis acid (Al_{IV}) sites (1621 cm^{-1}) of fresh Ag3/Al_2O_3 are less intense than those on γ-Al_2O_3, suggesting that the exchanged Ag (I) cations decrease the Lewis acidity of the adjacent Al_{IV}^{3+} sites, possibly due to the electronic effect of Ag(I). Considering that the cation exchange site, HO-μ^1-Al_{VI}, is adjacent to the Al_{IV}^{3+} site, the most acceptable model is that in which the Ag (I) cations are exchanged with H^+ of this OH group to yield anchored Ag(I) species, AgO-μ^1-Al_{VI}, resulting in a decrease in the Lewis acidity of the adjacent strong Lewis acid (Al_{IV}^{3+}) sites. The negative band of HO-μ^1-Al_{VI} (3766 cm^{-1}) for sintered Ag3/Al_2O_3 is more intense than that for fresh Ag3/Al_2O_3, indicating that the HO-μ^1-Al_{VI} sites are recovered upon de-anchoring of the

isolated Ag (I) cations ($AgO\text{-}\mu^1\text{-}Al_{VI}$) during the reductive aggregation under H_2, accompanied by the exchange of Ag^+ to H^+ (reaction 15).

$$AgO\text{-}\mu^1\text{-}Al_{VI} + 1/2\ H_2 \rightarrow HO\text{-}\mu^1\text{-}Al_{VI} + Ag^0 \quad (15)$$

The negative band of $HO\text{-}\mu^1\text{-}Al_{VI}$ for re-oxidized $Ag3/Al_2O_3$ was less intense than that for sintered $Ag3/Al_2O_3$, indicating that the $HO\text{-}\mu^1\text{-}Al_{VI}$ sites were consumed again upon the oxidative redispersion of the Ag metal NPs to the isolated Ag (I) cations in the original anchoring site (reaction 16).

$$HO\text{-}\mu^1\text{-}Al_{VI} + Ag^0 + 1/4\ O_2 \rightarrow AgO\text{-}\mu^1\text{-}Al_{VI} + 1/2\ H_2O \quad (16)$$

The IR band of pyridine on Al_{IV} (1621 cm^{-1}) for sintered $Ag3/Al_2O_3$ was more intense than that for fresh $Ag3/Al_2O_3$, and that for reoxidized $Ag3/Al_2O_3$ was less intense than that for sintered $Ag3/Al_2O_3$. This can be explained by the negative effect of the anchored Ag(I) species on the Lewis acidity of the Al_{IV}^{3+} sites adjacent to the $AgO\text{-}\mu^1\text{-}Al_{VI}$ sites.

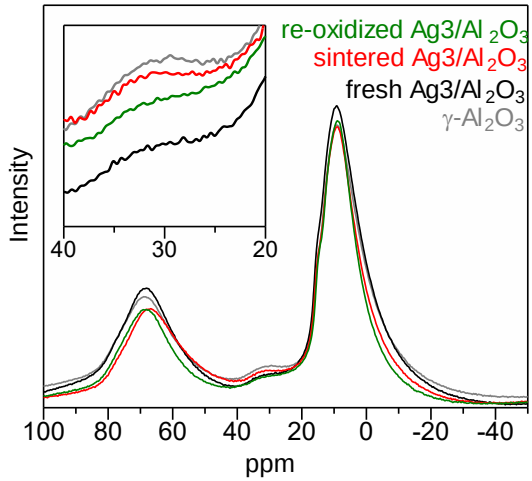

Figure 10 ^{27}Al NMR spectra of γ-Al_2O_3 and fresh, sintered (H_2, 800 ˚C), and re-oxidized ($NO + O_2$, 400 ˚C) $Ag3/Al_2O_3$ samples. The samples were dehydrated under N_2 at 500 ˚C before the measurements.

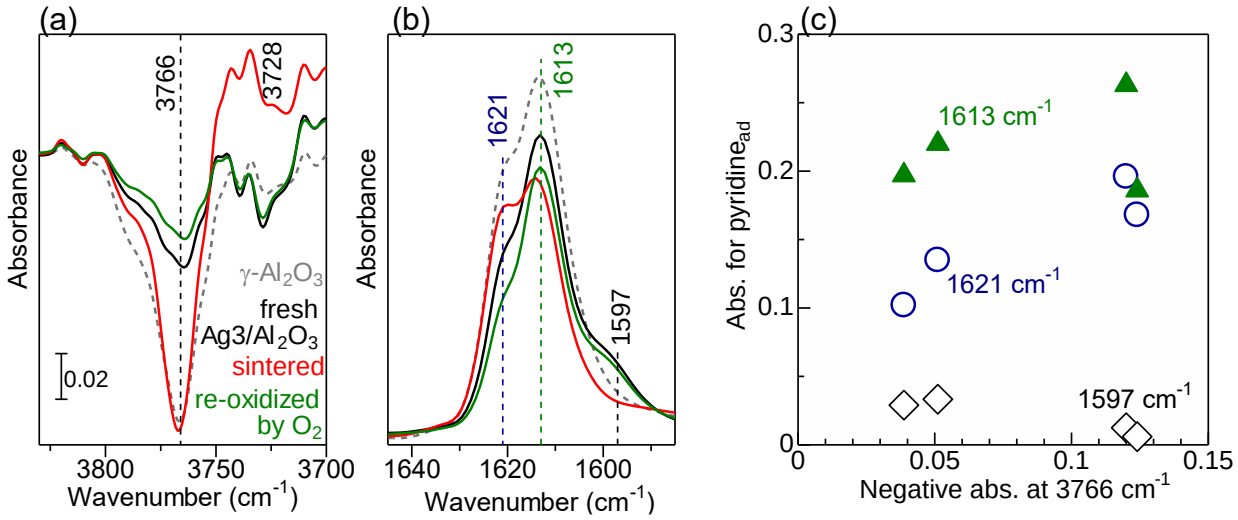

Figure 11 (a) OH stretching and (b) 8a (pyridine) regions in the IR spectra of pyridine adsorbed on *γ*-Al_2O_3 and $Ag3/Al_2O_3$ after successive redox treatments: (black) fresh $Ag3/Al_2O_3$, (red) $Ag3/Al_2O_3$ reduced in H_2 at 800 ˚C for 1 h (sintered $Ag3/Al_2O_3$), and (green) $Ag3/Al_2O_3$ re-oxidized in NO + O_2 at 400˚C for 0.5 h. (c) Intensities of the $pyridine_{ad}$ bands for weak (1597 cm^{-1}), medium (1613 cm^{-1}), and strong (1621 cm^{-1}) Lewis acid sites versus the negative intensity of the on-top (μ^1) OH group on Al_{VI} (HO-μ^1-Al_{VI}).

Reversibility of Ag dispersion over *γ*-Al_2O_3

To verify the reversibility of the sintering/dispersion phenomena on $Ag3/Al_2O_3$ under reductive/oxidative environments, we carried out *in situ* diffuse reflectance UV-vis and *in situ* DRIFT experiments. By using identical *in situ* reactors for the diffuse reflectance UV-vis and IR experiments, the time dependence of the UV-vis and IR signals (**Figure 12**) could be directly compared. After *in situ* oxidation of fresh $Ag3/Al_2O_3$ under 10% O_2 at 600 °C, the background data were recorded, and the reductive gas (1% H_2; 300 s) and oxidative gas (500 ppm NO + 10% O_2; 300 s) were repeatedly fed to the sample in the *in situ* cell at 600 °C, while recording the reflectance at 400 nm (UV-vis) and IR spectra of the adsorbed species. The UV-vis intensity for the Ag metal NPs increased under H_2 and then decreased upon NO + O_2 treatment (**Figure S9**), and reversible changes were observed for 10 cycles. The results clearly demonstrate that the reductive aggregation of isolated Ag(I) to Ag metal NPs and the oxidative dispersion of the Ag NPs to isolated Ag(I) are reversible processes. The time-resolved *in situ* IR analysis under the same periodic conditions showed that the IR intensity (KM) for HO-μ^1-Al_{VI} (3766 cm^{-1}) increased under H_2 and then decreased upon NO + O_2 treatment, while the IR intensity for bidentate nitrates (1548 cm^{-1})

increased upon NO + O_2 treatment and then decreased under H_2 (**Figure S10**). These phenomena were continuously observed for 10 cycles. Based on the UV-vis and IR spectroscopic analyses, a plausible mechanism of the reversible sintering/dispersion phenomena on Ag3/Al_2O_3 was proposed. Under a H_2 atmosphere, isolated Ag(I) cations anchored as AgO-μ^1-Al_{VI} species aggregate to form Ag metal NPs and HO-μ^1-Al_{VI} sites on the supports (reaction (2)). When the gas is changed to NO + O_2, the surface Ag^0 species, most likely at the interface of the Ag metal NPs, γ-Al_2O_3 surface, and gas phase, are oxidized by NO and O_2 (reaction (1)) to yield monomeric $AgNO_3$ species. The $AgNO_3$ species at the boundary of the Ag NPs and γ-Al_2O_3 surface move across the support surface owing to the concentration gradient of the mobile $AgNO_3$ species. The $AgNO_3$ species react with the anchoring site, HO-μ^1-Al_{VI}, to yield the original AgO-μ^1-Al_{VI} species and HNO_3, which then reacts with the alumina surface to yield the adsorbed nitrate species.

$$AgNO_3 + HO\text{-}\mu^1\text{-}Al_{VI} \rightarrow Ag\text{-}O\text{-}\mu^1\text{-}Al_{VI} + HNO_3 \quad (17)$$

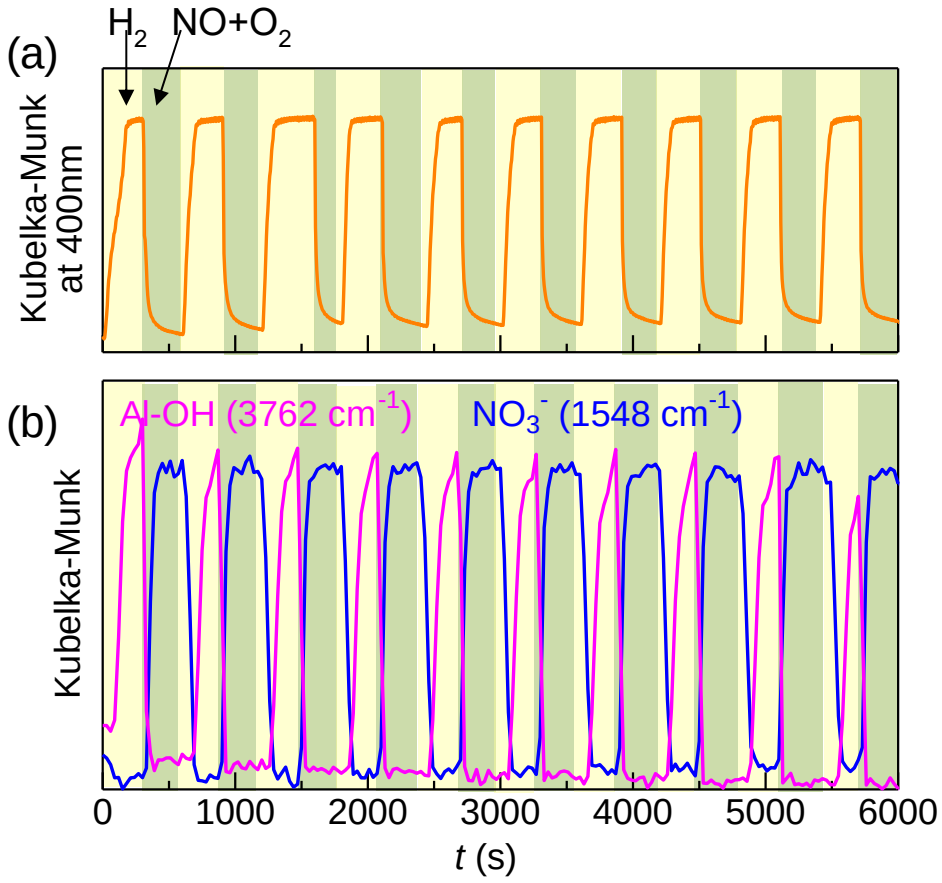

Figure 12 Dynamic changes in the (a) UV-vis intensity of Ag NPs (400 nm) and (b) *in situ* DRIFT signal intensity for HO-μ^1-Al_{VI} (3762 cm^{-1}) and nitrates (1548 cm^{-1}) under the periodic feed of 1% H_2 and 500 ppm NO + 10% O_2 for 10 cycles at 600˚C over Ag3/Al_2O_3.

DFT modeling of the anchoring sites over the *γ*-Al_2O_3 surface

The aforementioned results suggest that during oxidative dispersion, the Ag^+ cation is exchanged with H^+ at the HO-μ^1-Al_{VI} site adjacent to Al_{IV}^{3+}, resulting in a decrease in the Lewis acid strength of the Al_{IV}^{3+} site. To verify this, we performed DFT calculations to determine the vibrational frequency of the ω_{8a} band of the pyridine adsorbed on *γ*-Al_2O_3 and Ag-loaded *γ*-Al_2O_3.

The side view of the surface slab model of *γ*-Al_2O_3 used in this study is shown in **Figure S1**. Previous studies have shown that the (110) surface dominates *γ*-Al_2O_3, occupying approximately 70% of the total area, followed by the (100) surface (~20% of the total area).[70,71,95] It is well established that the HO-μ^1-Al_{VI} sites are present only on the (100) surface, while strong Lewis acid (unsaturated Al_{IV}) sites are present on the (110) or (111) surface.[70] The proximity between the (100) and (110) or (111) surfaces is consistent with two types of step-edge models of *γ*-Al_2O_3 surfaces recently proposed by Batista et al.[80] and Lee et al.[72] In their models, the (100) and (110) surfaces are exposed alternately (the (100)–(110) step-edge model) or the (100) and (111) surfaces are exposed alternately (the (100)–(111) step-edge model). Based on our experimental results and the two step-edge models (**Figure S1**), DFT modeling of the Ag(I)-anchoring sites was attempted. Based on the OH coverage[59] under our pretreatment conditions (600 °C), the OH groups were located at all the coordinatively unsaturated Al_{III} and Al_{IV} sites of the bare *γ*-Al_2O_3 surfaces (edge, (110), and (111) surfaces) and at one of the Al_V sites near the edge site on the (100) surface. The surface densities of the OH groups were 3.5 OH/nm^2 in the (110)–(100) step-edge model and 3.4 OH/nm^2 in the (100)–(111) step-edge model.

The side view of the *γ*-Al_2O_3 step-edge model after structural relaxation by dissociative adsorption of H_2O is shown in **Figure 13a** and **S2**. In the (110)–(100) step-edge model, all the Al_{III} and Al_{IV} sites in the supercell were occupied by the HO-μ^1 groups because of the dissociative adsorption of the H_2O molecules, and HO-μ^3 groups were formed on the adjacent lattice oxygen (see **Figure 13a**). The HO-μ^1-Al_{VI} sites, which are anchor sites for the Ag^+ cations, were formed on the (100) surface. In contrast, in the (100)–(111) step-edge model, the edge site structure collapsed during structure optimization owing to the dissociative adsorption of H_2O, and the HO-μ^1-Al_{VI} site on the (100) surface changed to a HO-μ^2-$(Al_{VI})_2$ bridged structure (**Figure S2**). Therefore, the (100)–(111) step-edge model was not considered further in this study, and the (110)–(100) step-edge model was used for Ag anchoring. On the Ag-anchored *γ*-Al_2O_3 (**Figure 13b**), one Ag^+ cation is exchanged with H^+ at the HO-μ^1-Al_{VI} site. As listed in **Table S2**, the Bader charge of the Ag atom on *γ*-Al_2O_3 (0.44) is close to that of Ag_2O (0.41), indicating that the anchored Ag species exist as Ag(I) ions. To investigate whether Ag anchoring tends to occur near the edge site or not, the energy

change (Δ*E*) associated with Ag anchoring was calculated for the *γ*-Al_2O_3 (110)–(100) step-edge model and the *γ*-Al_2O_3 (100) slab model according to Eq. (13). The calculated Δ*E* (−4.03 eV) for the *γ*-Al_2O_3 (110)–(100) step-edge model was lower than Δ*E* (+0.27 eV) for the *γ*-Al_2O_3 (100) slab model, indicating that the AgO-μ^1-Al_{VI} species is more stable on the (110)–(100) step-edge than on the (100) plane.

To understand the experimentally observed decrease in the Lewis acid strength of the Al_{IV} sites caused by Ag(I) anchoring, the pyridine adsorption energies (E_{ads}) and vibrational frequencies of the pyridine adsorbed on the Al_{IV} edge sites were calculated for Ag-free and Ag-anchored *γ*-Al_2O_3 (110)–(100) step-edge surfaces (**Figure 13c, d, Table 1**). The Ag anchoring changes the E_{ads} value from −1.31 to −0.66 eV. In addition, the Al–N bond distance in *γ*-Al_2O_3 (2.02 Å) is shorter than that in Ag/*γ*-Al_2O_3 (2.05 Å), indicating that the exchange of Ag^+ to H^+ at the HO-μ^1-Al_{VI} site decreases the strength of the adjacent strong Lewis acid sites. The vibrational frequencies of the ω_{8a} bands for the pyridine adsorbed onto the Al_{IV} sites (1616 cm^{-1}) on the Ag-free surface are consistent with the values calculated by Digne et al. (1617 cm^{-1})[71] and are close to the experimental value (1621 cm^{-1}; **Figure 11**). The vibrational frequency of the pyridine adsorbed on the Al_{IV} edge site of the Ag-anchoring surface was calculated to be 1593 cm^{-1}. This is consistent with the IR spectra shown in **Figure 11b**, which suggest that the anchoring and redispersion of Ag(I) on *γ*-Al_2O_3 result in a decrease in the number of strong Lewis acid sites (1621 cm^{-1}) as well as the appearance of a new band (1597 cm^{-1}) due to the weak Lewis acid sites. The consistency in the experimental (IR) and DFT results strongly indicates that the exchange of Ag^+ to H^+ at the HO-μ^1-Al_{VI} site decreases the strength of the adjacent strong Lewis acid (Al_{IV}) sites. In other words, the anchoring sites of the isolated Ag(I) species on *γ*-Al_2O_3 are the HO-μ^1-Al_{VI} sites on the (100) surface adjacent to the strong Lewis acid (Al_{IV}) sites on the (110) surface, that is, the (100)–(100) step-edge sites. Despite the recent debate and proposal regarding the (surface) structure of *γ*-Al_2O_3,[80,81] we employed surface structures based on the bulk model proposed by Digne et al.[71] to investigate the relative changes in the properties of the representative surface sites by anchoring Ag species.

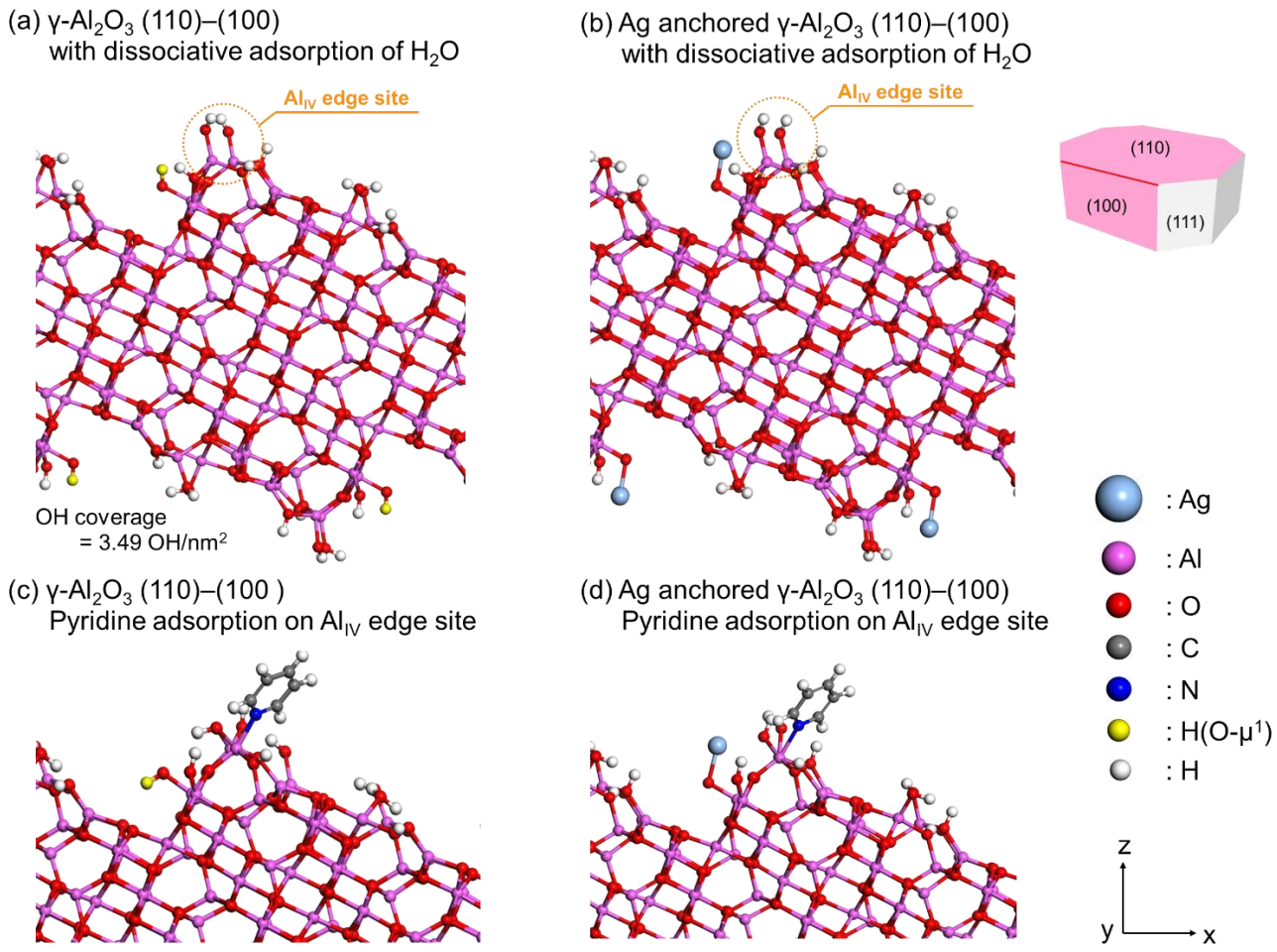

Figure 13. Side view of (a) γ-Al_2O_3 (110)–(100) and (b) Ag/γ-Al_2O_3 (110)–(100) step-edge surfaces and side view of pyridine adsorption on (c) γ-Al_2O_3 (110)–(100) and (d) Ag/γ-Al_2O_3 (110)–(100) edge Al_{IV} site (cyan: Ag atom, pink: Al atom, red: O atom, grey: C atom, blue: N atom, yellow: H atom in terminal hydroxyls, and white: H atom)

Table 1. Computed vibrational stretching frequencies of a pyridine (Pyr) molecule adsorbed on γ-Al_2O_3, adsorption energy (E_{ads}) of Pyr, and bond lengths between N (Pyr) and Al atoms (Al_{IV} sites).

	d (N-Al) (Å)	E_{ads} (eV)	ω_{8a} (cm^{-1})	ω_{8b} (cm^{-1})	ω_{19a} (cm^{-1})	ω_{19b} (cm^{-1})
Isolated Pyr (calculated by DFT)	-	-	1580	1579	1465	1430
Exp.	-	-	1581	1574	1482	1437
γ-Al_2O_3 (110)–(100)						
Fig.13c: Pyr -- Al_{IV} (edge site)	2.02	−1.31	1616	1577	1482	1445
Ag anchored γ-Al_2O_3 (110)–(100)						
Fig.13d Pyr -- Al_{IV} (edge site)	2.05	−0.66	1593	1565	1474	1438

Ab initio thermodynamic analysis for the stability of AgO-μ^1-Al_{VI} under redox conditions

The stability of the AgO-μ^1-Al_{VI} species at different temperatures and atmospheres was evaluated by *ab initio* thermodynamic analysis in reductive ((a) H_2+H_2O) and oxidative ((b) O_2+H_2O, (c) NO+O_2+HNO_3) atmospheres. **Figure 14** shows the phase diagram of the chemical species with the lowest relative Gibbs free energy (ΔG). The temperature (K) was measured on the horizontal axis, while the partial pressures of the reaction gases were measured on the vertical axis on a log scale. In the H_2 atmosphere, the aggregated Ag species (Ag NPs) were stable at all the temperatures and pressures (**Figure 14a**). This is in accordance with the fact that fresh Ag3/Al_2O_3 is easily sintered upon H_2 reduction. On the other hand, under an O_2 atmosphere, the dispersed Ag species are stable in the high-temperature region above approximately 400 °C. Furthermore, in the presence of NO and O_2, the dispersed species were stable except for the region where the NO partial pressure was low (less than 500 ppm) and the temperature was above 800 °C. **Figure S11** shows the conceptual model of dispersed and aggregated Ag species on the γ-Al_2O_3 (110)–(100) step-edge surface. The dispersed Ag is anchored by exchanging with H on the HO-μ^1-Al_{VI} site while the dispersed Ag can aggregate again with its de-anchoring and the HO-μ^1-Al_{VI} site regeneration. These results are in excellent agreement with our experimental observations, wherein O_2 or NO + O_2 treatment induced efficient dispersion of the Ag species.

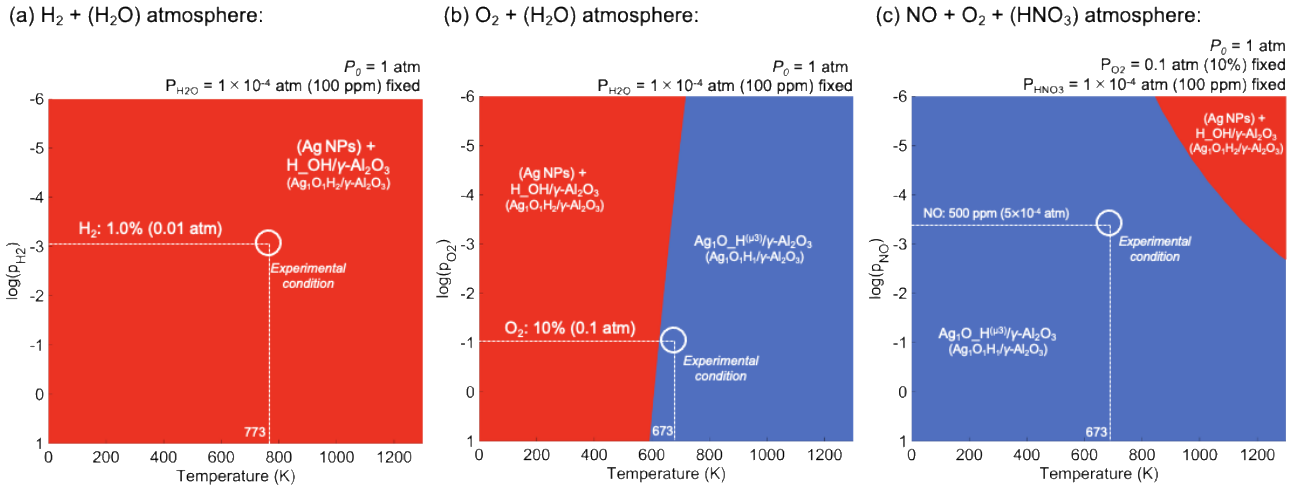

Figure 14. Partial pressure ((a) H_2, (b) O_2, and (c) NO) versus temperature plots for the species with the lowest relative Gibbs free energy (ΔG), as obtained by the *ab initio* thermodynamic analysis. H_2O (fixed at 100 ppm) is present as a coexistent gas for (a) and (b) while O_2 (fixed at 0.1%) and HNO_3 (fixed at 100 ppm) are present as coexistent gases for (c).

5.4. Conclusions

In summary, we have provided molecular-level insights into the reversible structural transformation between atomic Ag(I) and Ag metal NPs over *γ*-Al_2O_3 using *in situ* spectroscopy, electron microscopy, and DFT studies. The catalytic activity of fresh Ag3/Al_2O_3 decreased upon high temperature (800 ˚C) H_2-reduction (sintering of Ag) and was recovered upon subsequent oxidation under NO + O_2 (400 °C) flow due to the redispersion of the aggregated Ag NPs to the atomic Ag(I) species. The sintering and dispersion phenomena were reversible. The anchoring sites of the isolated Ag(I) species on *γ*-Al_2O_3 are the HO-μ^1-Al_{VI} sites on the (100) surface adjacent to the strong Lewis acid (Al_{IV}) sites on the (110) surface; thus, the (100)–(100) step-edge sites are the most likely structure of the anchoring site. During the sintering of Ag under H_2-reduction (de-anchoring), the isolated AgO-μ^1-Al_{VI} species aggregate to form Ag metal NPs, thereby regenerating the HO-μ^1-Al_{VI} sites on *γ*-Al_2O_3. In the process of oxidative dispersion (anchoring), the Ag metal NPs are oxidized by NO and O_2 to mobile $AgNO_3$ species, which move across the *γ*-Al_2O_3 surface and react with the anchoring site, HO-μ^1-Al_{VI}, to yield the original AgO-μ^1-Al_{VI} species and HNO_3; the latter reacts with the *γ*-Al_2O_3 surface to yield the adsorbed nitrate species. These findings provide molecular-level insights into the deactivation and reactivation of supported metal catalysts under reductive and oxidative conditions.

REFERENCES

(1) Hayashizaki, K.; Jibiki, T.; Inoue, K.; Koyanagi, Y.; Tanaka, S.; Tongu, H.; Hirabayashi, H.; Sato, S. After-Treatment System of Medium Duty Engines Using Diesel Fuel as a Reducing Agent for NO_x Reduction. *SAE Tech. Pap.* **2018**, *1*, 0345. https://doi.org/10.4271/2018-01-0345.

(2) Nishihata, Y.; Mizuki, J.; Akao, T.; Tanaka, H.; Uenishi, M.; Kimura, M.; Okamoto, T.; Hamada, N. Self-Regeneration of a Pd-Perovskite Catalyst for Automotive Emissions Control. *Nature* **2002**, *418*, 164–167. https://doi.org/10.1038/nature00893.

(3) Shinjoh, H. Noble Metal Sintering Suppression Technology in Three-Way Catalyst: Automotive Three-Way Catalysts with the Noble Metal Sintering Suppression Technology Based on the Support Anchoring Effect. *Catal. Surv. from Asia* **2009**, *13*, 184–190. https://doi.org/10.1007/s10563-009-9076-6.

(4) Datye, A. K.; Votsmeier, M. Opportunities and Challenges in the Development of Advanced Materials for Emission Control Catalysts. *Nature Materials*. 2020. https://doi.org/10.1038/s41563-020-00805-3.

(5) Beniya, A.; Higashi, S. Towards Dense Single-Atom Catalysts for Future Automotive Applications. *Nature Catalysis*. 2019. https://doi.org/10.1038/s41929-019-0282-y.

(6) Kaiser, S. K.; Chen, Z.; Faust Akl, D.; Mitchell, S.; Pérez-Ramírez, J. Single-Atom Catalysts across the Periodic Table. *Chemical Reviews*. 2020. https://doi.org/10.1021/acs.chemrev.0c00576.

(7) Lu, Y.; Zhang, Z.; Lin, F.; Wang, H.; Wang, Y. Single-Atom Automobile Exhaust Catalysts. *ChemNanoMat* **2020**, *6*, 1659–1682. https://doi.org/10.1002/cnma.202000407.

(8) Campbell, C. T.; Parker, S. C.; Starr, D. E. The Effect of Size-Dependent Nanoparticle Energetics on Catalyst Sintering. *Science (80-.).* **2002**, *298*, 811–814. https://doi.org/10.1126/science.1075094.

(9) Parkinson, G. S.; Novotny, Z.; Argentero, G.; Schmid, M.; Pavelec, J.; Kosak, R.; Blaha, P.; Diebold, U. Carbon Monoxide-Induced Adatom Sintering in a Pd-Fe_3O_4 Model Catalyst. *Nat. Mater.* **2013**, *12*, 724–728. https://doi.org/10.1038/nmat3667.

(10) Dessal, C.; Len, T.; Morfin, F.; Rousset, J. L.; Aouine, M.; Afanasiev, P.; Piccolo, L. Dynamics of Single Pt Atoms on Alumina during CO Oxidation Monitored by *Operando* X-Ray and Infrared Spectroscopies. *ACS Catal.* **2019**, *9*, 5752–5759. https://doi.org/10.1021/acscatal.9b00903.

(11) Maurer, F.; Jelic, J.; Wang, J.; Gänzler, A.; Dolcet, P.; Wöll, C.; Wang, Y.; Studt, F.; Casapu, M.; Grunwaldt, J. D. Tracking the Formation, Fate and Consequence for Catalytic Activity of Pt Single Sites on CeO_2. *Nat. Catal.* **2020**, *3*, 824–833. https://doi.org/10.1038/s41929-020-00508-7.

(12) Liu, L.; Corma, A. Evolution of Isolated Atoms and Clusters in Catalysis. *Trends Chem.* **2020**, *2*, 383–400. https://doi.org/10.1016/j.trechm.2020.02.003.

(13) Shimizu, K.; Shibata, J.; Yoshida, H.; Satsuma, A.; Hattori, T. Silver-Alumina Catalysts for Selective Reduction of NO by Higher Hydrocarbons: Structure of Active Sites and Reaction Mechanism. *Appl. Catal. B Environ.* **2001**, *30*, 151–162. https://doi.org/10.1016/S0926-3373(00)00229-0.

(14) Deng, H.; Yu, Y.; Liu, F.; Ma, J.; Zhang, Y.; He, H. Nature of Ag Species on Ag/γ-Al_2O_3 : A Combined Experimental and Theoretical Study. *ACS Catal.* **2014**, *4*, 2776–2784.

(15) Deng, H.; Yu, Y.; He, H. Discerning the Role of Ag-O-Al Entities on Ag/γ-Al_2O_3 Surface in NOx Selective Reduction by Ethanol. *J. Phys. Chem. C* **2015**, *119*, 3132–3142. https://doi.org/10.1021/jp5114416.

(16) Breen, J. P.; Burch, R.; Hardacre, C.; Hill, C. J.; Krutzsch, B.; Bandl-Konrad, B.; Jobson, E.; Cider, L.; Blakeman, P. G.; Peace, L. J.; Twigg, M. V.; Preis, M.; Gottschling, M. An Investigation of the Thermal Stability and Sulphur Tolerance of Ag/γ-Al_2O_3 Catalysts for the SCR of NO_x with Hydrocarbons and Hydrogen. *Appl. Catal. B Environ.* **2007**, *70*, 36–44. https://doi.org/10.1016/j.apcatb.2006.05.005.

(17) Shibata, J.; Shimizu, K.; Satokawa, S.; Satsuma, A.; Hattori, T. Promotion Effect of Hydrogen on Surface Steps in SCR of NO by Propane over Alumina-Based Silver Catalyst as Examined by Transient FT-IR. *Phys. Chem. Chem. Phys.* **2003**, *5*, 2154–2160. https://doi.org/10.1039/b302352d.

(18) Shimizu, K.; Katagiri, M.; Satokawa, S.; Satsuma, A. Applied Catalysis B : Environmental Sintering-Resistant and Self-Regenerative Properties of Ag/SnO_2 Catalyst for Soot Oxidation. *"Applied Catal. B, Environ.* **2011**, *108–109*, 39–46. https://doi.org/10.1016/j.apcatb.2011.08.003.

(19) Kannisto, H.; Skoglundh, M.; Arve, K.; Olsson, E.; Härelind, H. Direct Observation of Atomically-Resolved Silver Species on a Silver Alumina Catalyst Active for Selective Catalytic Reduction of Nitrogen Oxides. *Catal. Sci. Technol.* **2019**, *9*, 6213–6216. https://doi.org/10.1039/c9cy00940j.

(20) Tamm, S.; Vallim, N.; Skoglundh, M.; Olsson, L. The Influence of Hydrogen on the Stability of Nitrates during H_2-Assisted SCR over Ag/Al_2O_3 Catalysts - A DRIFT Study. *J. Catal.* **2013**, *307*, 153–161. https://doi.org/10.1016/j.jcat.2013.07.003.

(21) Korhonen, S. T.; Beale, A. M.; Newton, M. A.; Weckhuysen, B. M. New Insights into the Active Surface Species of Silver Alumina Catalysts in the Selective Catalytic Reduction of NO. *J. Phys. Chem. C* **2011**, *115*, 885–896. https://doi.org/10.1021/jp102530y.

(22) Bogdanchikova, N.; Meunier, F. C.; Avalos-Borja, M.; Breen, J. P.; Pestryakov, A. On the Nature of the Silver Phases of Ag/Al_2O_3 Catalysts for Reactions Involving Nitric Oxide. *Appl. Catal. B Environ.* **2002**, *36*, 287–297. https://doi.org/10.1016/S0926-3373(01)00286-7.

(23) Soon, P.; Kyu, M.; Cho, B. K.; Nam, I.; Oh, S. H. Effect of H_2 on $DeNO_x$ Performance of HC-SCR over Ag/Al_2O_3 : Morphological , Chemical , and Kinetic Changes. **2013**, *301*, 65–76. https://doi.org/10.1016/j.jcat.2013.01.026.

(24) Wang, F.; Ma, J.; Xin, S.; Wang, Q.; Xu, J.; Zhang, C.; He, H.; Cheng Zeng, X. Resolving the Puzzle of Single-Atom Silver Dispersion on Nanosized γ-Al_2O_3 Surface for High Catalytic Performance. *Nat. Commun.* **2020**, *11*, 1–11. https://doi.org/10.1038/s41467-019-13937-1.

(25) Richter, M.; Fricke, R.; Eckelt, R. Unusual Activity Enhancement of NO Conversion over Ag/Al_2O_3 by Using a Mixed NH_3/H_2 Reductant under Lean Conditions. *Catal. Lett.* **2004**, *94*, 115–118. https://doi.org/10.1023/b:catl.0000019340.51510.ba.

(26) Kondratenko, E. V; Kondratenko, V. A.; Richter, M.; Fricke, R. Influence of O_2 and H_2 on NO Reduction by NH_3 over Ag/Al_2O_3 : A Transient Isotopic Approach. **2006**, *239*, 23–33. https://doi.org/10.1016/j.jcat.2006.01.008.

(27) Kondratenko, V. A.; Bentrup, U.; Richter, M.; Hansen, T. W.; Kondratenko, E. V. Mechanistic Aspects of N_2O and N_2 Formation in NO Reduction by NH_3 over Ag/Al_2O_3: The Effect of O_2 and H_2. *Appl. Catal. B Environ.* **2008**, *84*, 497–504. https://doi.org/10.1016/j.apcatb.2008.05.007.

(28) Xu, G.; Ma, J.; Wang, L.; Lv, Z.; Wang, S.; Yu, Y. Mechanism of the H_2 Effect on NH_3-Selective Catalytic Reduction over Ag/Al_2O_3 : Kinetic and Diffuse Reflectance Infrared Fourier Transform Spectroscopy Studies. *ACS Catal.* **2019**, *9*, 10489–10498. https://doi.org/10.1021/acscatal.9b04100.

(29) Xu, G.; Wang, H.; Yu, Y.; He, H. Role of Silver Species in H_2-NH_3-SCR of NOx over Ag/Al_2O_3 Catalysts: *Operando* Spectroscopy and DFT Calculations. *J. Catal.* **2021**, *395*, 1–9. https://doi.org/10.1016/j.jcat.2020.12.025.

(30) Shimizu, K.; Satsuma, A. Hydrogen Assisted Urea-SCR and NH_3-SCR with Silver-Alumina as Highly Active and SO_2-Tolerant de-NO_x Catalysis. *Appl. Catal. B Environ.* **2007**, *77*, 202–205. https://doi.org/10.1016/j.apcatb.2007.07.021.

(31) Shimizu, K.; Satsuma, A. Reaction Mechanism of H_2-Promoted Selective Catalytic Reduction of NO with NH_3 over Ag/Al_2O_3. *J. Phys. Chem. C* **2007**, *111*, 2259–2264. https://doi.org/10.1021/jp0668100.

(32) Wan, Q.; Hu, S.; Dai, J.; Chen, C.; Li, W. X. First-Principles Kinetic Study for Ostwald Ripening of Late Transition Metals on TiO_2 (110). *J. Phys. Chem. C* **2019**, *123*, 1160–1169. https://doi.org/10.1021/acs.jpcc.8b08530.

(33) Narula, C. K.; Stocks, G. M. Ab Initio Density Functional Calculations of Adsorption of Transition Metal Atoms on θ-Al2O3(010) Surface. *J. Phys. Chem. C* **2012**, *116*, 5628–2636. https://doi.org/10.1021/jp209725a.

(34) Dietze, E. M.; Plessow, P. N. Predicting the Strength of Metal − Support Interaction with Computational Descriptors for Adhesion Energies. *J. Phys. Chem. C* **2019**, *123*, 20443–20450. https://doi.org/10.1021/acs.jpcc.9b06893.

(35) Agostini, G.; Usseglio, S.; Groppo, E.; Uddin, M. J.; Prestipino, C.; Bordiga, S.; Zecchina, A.; Solari, P. L.; Lamberti, C. From Isolated Ag+ Ions to Aggregated Ag0 Nanoclusters in Silver-Exchanged Engelhard Titanosilicate (ETS-10) Molecular Sieve: Reversible Behavior. *Chem. Mater.* **2009**, *21*. https://doi.org/10.1021/cm803216k.

(36) Goodman, E. D.; Schwalbe, J. A.; Cargnello, M. Mechanistic Understanding and the Rational Design of Sinter- Resistant Heterogeneous Catalysts. *ACS Catalysis*. 2017. https://doi.org/10.1021/acscatal.7b01975.

(37) Dai, Y.; Lu, P.; Cao, Z.; Campbell, C. T.; Xia, Y. The Physical Chemistry and Materials Science behind Sinter-Resistant Catalysts. *Chemical Society Reviews*. 2018. https://doi.org/10.1039/c7cs00650k.

(38) Hansen, T. W.; Delariva, A. T.; Challa, S. R.; Datye, A. K. Sintering of Catalytic Nanoparticles: Particle Migration or Ostwald Ripening? *Acc. Chem. Res.* **2013**, *46*, 1720–1730. https://doi.org/10.1021/ar3002427.

(39) Xu, Q.; Kharas, K. C.; Croley, B. J.; Datye, A. K. The Sintering of Supported Pd Automotive Catalysts. *ChemCatChem* **2011**, *3*, 1004–1014. https://doi.org/10.1002/cctc.201000392.

(40) Adibi, P. T. Z.; Zhdanov, V. P.; Langhammer, C.; Grönbeck, H. Transient Bimodal Particle Size Distributions during Pt Sintering on Alumina and Silica. *J. Phys. Chem. C* **2015**, *119*, 989–996. https://doi.org/10.1021/jp506586g.

(41) Monpezat, A.; Topin, S.; Thomas, V.; Pagis, C.; Aouine, M.; Burel, L.; Cardenas, L.; Tuel, A.; Malchère, A.; Epicier, T.; Farrusseng, D.; Roiban, L. Migration and Growth of Silver Nanoparticles in Zeolite Socony Mobil 5 (ZSM-5) Observed by Environmental Electron Microscopy: Implications for Heterogeneous Catalysis. *ACS Appl. Nano Mater.* **2019**, *2*, 6452–6461. https://doi.org/10.1021/acsanm.9b01407.

(42) Goodman, E. D.; Johnston-Peck, A. C.; Dietze, E. M.; Wrasman, C. J.; Hoffman, A. S.; Abild-Pedersen, F.; Bare, S. R.; Plessow, P. N.; Cargnello, M. Catalyst Deactivation via Decomposition into Single Atoms and the Role of Metal Loading. *Nat. Catal.* **2019**, *2*, 748–755. https://doi.org/10.1038/s41929-019-0328-1.

(43) Lai, X.; St. Clair, T. P.; Goodman, D. W. Oxygen-Induced Morphological Changes of Ag Nanoclusters Supported on TiO_2(110). *Faraday Discuss.* **1999**, *114*, 279–284. https://doi.org/10.1039/a902795e.

(44) Tabib Zadeh Adibi, P.; Pingel, T.; Olsson, E.; Grönbeck, H.; Langhammer, C. Pt Nanoparticle Sintering and Redispersion on a Heterogeneous Nanostructured Support. *J. Phys. Chem. C* **2016**, *120*, 14918–14925. https://doi.org/10.1021/acs.jpcc.6b03874.

(45) Dessal, C.; Sangnier, A.; Chizallet, C.; Dujardin, C.; Morfin, F.; Rousset, J. L.; Aouine, M.; Bugnet, M.; Afanasiev, P.; Piccolo, L. Atmosphere-Dependent Stability and Mobility of

Catalytic Pt Single Atoms and Clusters on γ-Al_2O_3. *Nanoscale* **2019**, *11*, 6897–6904. https://doi.org/10.1039/c9nr01641d.

(46) Wang, X.; Van Bokhoven, J. A.; Palagin, D. Ostwald Ripening versus Single Atom Trapping: Towards Understanding Platinum Particle Sintering. *Phys. Chem. Chem. Phys.* **2017**, *19*. https://doi.org/10.1039/c7cp05887j.

(47) Su, Y. Q.; Liu, J. X.; Filot, I. A. W.; Hensen, E. J. M. Theoretical Study of Ripening Mechanisms of Pd Clusters on Ceria. *Chem. Mater.* **2017**, *29*. https://doi.org/10.1021/acs.chemmater.7b03555.

(48) Gänzler, A. M.; Casapu, M.; Vernoux, P.; Loridant, S.; Cadete Santos Aires, F. J.; Epicier, T.; Betz, B.; Hoyer, R.; Grunwaldt, J. D. Tuning the Structure of Platinum Particles on Ceria In Situ for Enhancing the Catalytic Performance of Exhaust Gas Catalysts. *Angew. Chem. Int. Ed.* **2017**, *56*, 13078–13082. https://doi.org/10.1002/anie.201707842.

(49) Ferré, G.; Aouine, M.; Bosselet, F.; Burel, L.; Cadete Santos Aires, F. J.; Geantet, C.; Ntais, S.; Maurer, F.; Casapu, M.; Grunwaldt, J. D.; Epicier, T.; Loridant, S.; Vernoux, P. Exploiting the Dynamic Properties of Pt on Ceria for Low-Temperature CO Oxidation. *Catal. Sci. Technol.* **2020**, *10*, 3904–3917. https://doi.org/10.1039/d0cy00732c.

(50) Aylor, A. W.; Lobree, L. J.; Reimer, J. A.; Bell, A. T. Investigations of the Dispersion of Pd in H-ZSM-5. *J. Catal.* **1997**, *172*, 453–462. https://doi.org/10.1006/jcat.1997.1893.

(51) Jing, Y.; Cai, Z.; Liu, C.; Toyao, T.; Maeno, Z.; Asakura, H.; Hiwasa, S.; Nagaoka, S.; Kondoh, H.; Shimizu, K. Promotional Effect of La in the Three-Way Catalysis of La-Loaded Al_2O_3-Supported Pd Catalysts (Pd/La/Al_2O_3). *ACS Catal.* **2020**, *10*, 1010–1023. https://doi.org/10.1021/acscatal.9b03766.

(52) Yasumura, S.; Ide, H.; Ueda, T.; Jing, Y.; Liu, C.; Kon, K.; Toyao, T.; Maeno, Z.; Shimizu, K. Transformation of Bulk Pd to Pd Cations in Small-Pore CHA Zeolites Facilitated by NO. *JACS Au* **2021**, *1*, 201–211. https://doi.org/10.1021/jacsau.0c00112.

(53) Paredis, K.; Ono, L. K.; Behafarid, F.; Zhang, Z.; Yang, J. C.; Frenkel, A. I.; Cuenya, B. R. Evolution of the Structure and Chemical State of Pd Nanoparticles during the in Situ Catalytic Reduction of NO with H2. *J. Am. Chem. Soc.* **2011**, *133*. https://doi.org/10.1021/ja203709t.

(54) Li, R.; Xu, X.; Zhu, B.; Li, X. Y.; Ning, Y.; Mu, R.; Du, P.; Li, M.; Wang, H.; Liang, J.; Chen, Y.; Gao, Y.; Yang, B.; Fu, Q.; Bao, X. *In Situ* Identification of the Metallic State of Ag Nanoclusters in Oxidative Dispersion. *Nat. Commun.* **2021**, *12*, 1–9. https://doi.org/10.1038/s41467-021-21552-2.

(55) Inceesungvorn, B.; López-Castro, J.; Calvino, J. J.; Bernal, S.; Meunier, F. C.; Hardacre, C.; Griffin, K.; Delgado, J. J. Nano-Structural Investigation of Ag/Al_2O_3 Catalyst for Selective Removal of O_2 with Excess H_2 in the Presence of C_2H_4. *Appl. Catal. A Gen.* **2011**, *391*, 187–193. https://doi.org/10.1016/j.apcata.2010.07.035.

(56) Murata, K.; Ohyama, J.; Satsuma, A. Kinetic Analysis of Ag Particle Redispersion into ZSM-5 in the Presence of Coke Using *In Situ* XAFS. *Catal. Sci. Technol.* **2021**, *11*, 506–515. https://doi.org/10.1039/d0cy01989e.

(57) Shimizu, K.; Sawabe, K.; Satsuma, A. Self-Regenerative Silver Nanocluster Catalyst for CO Oxidation. *ChemCatChem* **2011**, *3*, 1290–1293. https://doi.org/10.1002/cctc.201100122.

(58) Busca, G. Structural, Surface, and Catalytic Properties of Aluminas. *Adv. Catal.* **2014**, *57*, 319–404. https://doi.org/10.1016/B978-0-12-800127-1.00003-5.

(59) Rascón, F.; Wischert, R.; Copéret, C. Molecular Nature of Support Effects in Single-Site Heterogeneous Catalysts: Silica vs. Alumina. *Chem. Sci.* **2011**, *2*, 1449–1456. https://doi.org/10.1039/c1sc00073j.

(60) Jang, E. J.; Lee, J.; Kwak, J. H. Morphology Change and Phase Transformation of Alumina Related to Defect Sites and Its Use in Catalyst Preparation. *Catal. Today* **2020**, *352*, 323–328. https://doi.org/10.1016/j.cattod.2019.09.043.

(61) Kwak, J. H.; Hu, J. Z.; Kim, D. H.; Szanyi, J.; Peden, C. H. F. Penta-Coordinated Al^{3+} Ions as Preferential Nucleation Sites for BaO on γ-Al_2O_3: An Ultra-High-Magnetic Field ^{27}Al MAS NMR Study. *J. Catal.* **2007**, *251*, 189–194. https://doi.org/10.1016/j.jcat.2007.06.029.

(62) Kwak, J. H.; Hu, J.; Lukaski, A.; Kim, D. H.; Szanyi, J.; Peden, C. H. F. Role of Pentacoordinated Al^{3+} Ions in the High Temperature Phase Transformation of γ-Al_2O_3. *J. Phys. Chem. C* **2008**, *112*, 9486–9492. https://doi.org/10.1021/jp802631u.

(63) Phung, T. K.; Lagazzo, A.; Rivero Crespo, M. Á.; Sánchez Escribano, V.; Busca, G. A Study of Commercial Transition Aluminas and of Their Catalytic Activity in the Dehydration of Ethanol. *J. Catal.* **2014**, *311*, 102–113. https://doi.org/10.1016/j.jcat.2013.11.010.

(64) Murata, K.; Shiotani, T.; Ohyama, J.; Wakabayashi, R.; Maruoka, H.; Kimura, T.; Satsuma, A. Relationship between Penta-Coordinated Al^{3+} Sites in the Al_2O_3 Supports and CH_4 Combustion Activity of Pd/Al_2O_3 Catalysts. *Catal. Sci. Technol.* **2021**, *11*, 2374–2378. https://doi.org/10.1039/d1cy00098e.

(65) Liu, X. DRIFTS Study of Surface of γ-Alumina and Its Dehydroxylation. *J. Phys. Chem. C* **2008**, *112*, 5066–5073. https://doi.org/10.1021/jp711901s.

(66) Srinivasan, S.; Narayanan, C. R.; Datye, A. K. The Role of Sodium and Structure on the Catalytic Behavior of Alumina: II. IR Spectroscopy. *Appl. Catal. A, Gen.* **1995**, *132*, 289–308. https://doi.org/10.1016/0926-860X(95)00162-X.

(67) Lundie, D. T.; McInroy, A. R.; Marshall, R.; Winfield, J. M.; Jones, P.; Dudman, C. C.; Parker, S. F.; Mitchell, C.; Lennon, D. Improved Description of the Surface Acidity of η-Alumina. *J. Phys. Chem. B* **2005**, *109*, 11592–11601. https://doi.org/10.1021/jp0405963.

(68) Phung, T. K.; Herrera, C.; Larrubia, M. Á.; García-Diéguez, M.; Finocchio, E.; Alemany, L. J.; Busca, G. Surface and Catalytic Properties of Some γ-Al_2O_3 Powders. *Appl. Catal. A Gen.* **2014**, *483*, 41–51. https://doi.org/10.1016/j.apcata.2014.06.020.

(69) Liu, X.; Truitt, R. E. DRFT-IR Studies of the Surface of γ-Alumina. *J. Am. Chem. Soc.* **1997**, *119*, 9856–9860. https://doi.org/10.1021/ja971214s.

(70) Morterra, C.; Magnacca, G. A Case Study: Surface Chemistry and Surface Structure of Catalytic Aluminas, as Studied by Vibrational Spectroscopy of Adsorbed Species. *Catal. Today* **1996**, *27*, 497–532. https://doi.org/10.1016/0920-5861(95)00163-8.

(71) Digne, M.; Sautet, P.; Raybaud, P.; Euzen, P.; Toulhoat, H. Use of DFT to Achieve a Rational Understanding of Acid-Basic Properties of γ-Alumina Surfaces. *J. Catal.* **2004**, *226*, 54–68. https://doi.org/10.1016/j.jcat.2004.04.020.

(72) Lee, J.; Jang, E. J.; Jeong, H. Y.; Kwak, J. H. Critical Role of (100) Facets on Γ-Al_2O_3 for Ethanol Dehydration: Combined Efforts of Morphology-Controlled Synthesis and TEM Study. *Appl. Catal. A Gen.* **2018**, *556*, 121–128. https://doi.org/10.1016/j.apcata.2018.02.018.

(73) Dyan, A.; Cenedese, P.; Dubot, P. Physical Properties of γ Alumina Surface Hydroxyls Revisited through a Large Scale Periodic Quantum-Chemistry Approach. *J. Phys. Chem. B* **2006**, *110*, 10041–10050. https://doi.org/10.1021/jp056825i.

(74) Kresse, G.; Hafner, J. Ab Initio Molecular Dynamics for Open-Shell Transition Metals. *Phys. Rev. B* **1993**, *48*, 13115–13118. https://doi.org/10.1103/PhysRevB.48.13115.

(75) Kresse, G.; Furthmüller, J. Efficiency of Ab-Initio Total Energy Calculations for Metals and Semiconductors Using a Plane-Wave Basis Set. *Comput. Mater. Sci.* **1996**, *6*, 15–50.

(76) Blöchl, P. E. Projector Augmented-Wave Method. *Phys. Rev. B* **1994**, *50*, 17953–17979.

(77) Perdew, J. P.; Burke, K.; Ernzerhof, M. Generalized Gradient Approximation Made Simple. *Phys. Rev. Lett.* **1996**, *77*, 3865–3868. https://doi.org/10.1103/PhysRevLett.77.3865.

(78) Grimme, S.; Ehrlich, S.; Goerigk, L. Effect of the Damping Function in Dispersion Corrected Density Functional Theory. *J. Comput. Chem.* **2011**, *32*, 1456–1465. https://doi.org/10.1002/jcc.21759.

(79) Grimme, S.; Antony, J.; Ehrlich, S.; Krieg, H. A Consistent and Accurate Ab Initio Parametrization of Density Functional Dispersion Correction (DFT-D) for the 94 Elements H-Pu. *J. Chem. Phys.* **2010**, *132*, 154104. https://doi.org/10.1063/1.3382344.

(80) Batista, A. T. F.; Wisser, D.; Pigeon, T.; Gajan, D.; Diehl, F.; Rivallan, M.; Catita, L.; Gay, A. S.; Lesage, A.; Chizallet, C.; Raybaud, P. Beyond Γ-Al2O3 Crystallite Surfaces: The Hidden Features of Edges Revealed by Solid-State 1H NMR and DFT Calculations. *J. Catal.* **2019**, *378*. https://doi.org/10.1016/j.jcat.2019.08.009.

(81) Batista, A. T. F.; Baaziz, W.; Taleb, A. L.; Chaniot, J.; Moreaud, M.; Legens, C.; Aguilar-Tapia, A.; Proux, O.; Hazemann, J. L.; Diehl, F.; Chizallet, C.; Gay, A. S.; Ersen, O.; Raybaud, P. Atomic Scale Insight into the Formation, Size, and Location of Platinum Nanoparticles Supported on γ-Alumina. *ACS Catal.* **2020**, *10*. https://doi.org/10.1021/acscatal.0c00042.

(82) Rozita, Y.; Brydson, R.; Comyn, T. P.; Scott, A. J.; Hammond, C.; Brown, A.; Chauruka, S.; Hassanpour, A.; Young, N. P.; Kirkland, A. I.; Sawada, H.; Smith, R. I. A Study of Commercial Nanoparticulate γ-Al2O3 Catalyst Supports. *ChemCatChem* **2013**, *5*. https://doi.org/10.1002/cctc.201200880.

(83) Khivantsev, K.; Jaegers, N. R.; Kwak, J. H.; Szanyi, J.; Kovarik, L. Precise Identification and Characterization of Catalytically Active Sites on the Surface of γ-Alumina**. *Angew. Chem. Int. Ed.* **2021**, *60*. https://doi.org/10.1002/anie.202102106.

(84) Dudarev, S.; Botton, G. Electron-Energy-Loss Spectra and the Structural Stability of Nickel Oxide: An LSDA+U Study. *Phys. Rev. B - Condens. Matter Mater. Phys.* **1998**, *57*, 1505–1509. https://doi.org/10.1103/PhysRevB.57.1505.

(85) Stevanović, V.; Lany, S.; Zhang, X.; Zunger, A. Correcting Density Functional Theory for Accurate Predictions of Compound Enthalpies of Formation: Fitted Elemental-Phase Reference Energies. *Phys. Rev. B Condens. Matter Mater. Phys.* **2012**, *85*, 115104. https://doi.org/10.1103/PhysRevB.85.115104.

(86) Henkelman, G.; Arnaldsson, A.; Jónsson, H. A Fast and Robust Algorithm for Bader Decomposition of Charge Density. *Comput. Mater. Sci.* **2006**, *36*, 354–360. https://doi.org/10.1016/j.commatsci.2005.04.010.

(87) Tang, W.; Sanville, E.; Henkelman, G. A Grid-Based Bader Analysis Algorithm without Lattice Bias. *J. Phys. Condens. Matter* **2009**, *21*, 084204. https://doi.org/10.1088/0953-8984/21/8/084204.

(88) Yu, M.; Trinkle, D. R. Accurate and Efficient Algorithm for Bader Charge Integration. *J. Chem. Phys.* **2011**, *134*, 1–8. https://doi.org/10.1063/1.3553716.

(89) Rogal, J.; Reuter, K. Ab Initio Atomistic Thermodynamics for Surfaces : A Primer. In Experiment, Modeling and Simulation of Gas Surface Interactions for Reactive Flows in Hypersonic Flights; Educational Notes RTO-EN-AVT-142. *Tech. Rep.* **2007**, *2*, 1–18.

(90) M.W. Chase, C.A.D Jr., J.J.R. Downey, D.J. Frurip, R.A. McDonald, A. N. S. NIST-JANAF Thermochemical Tables (2nd Ed.). *U.S. Dep. Commer. Washingt.* **1985**. https://doi.org/10.1063/1.555993.

(91) Shimizu, K.; Tsuzuki, M.; Kato, K.; Yokota, S.; Okumura, K. Reductive Activation of O_2 with H_2 -Reduced Silver Clusters as a Key Step in the H_2-Promoted Selective Catalytic Reduction of NO with C_3H_8 over Ag/Al_2O_3. *J. Phys. Chem. C* **2007**, *111*, 950–959.

(92) Kwak, J. H.; Hu, J.; Mei, D.; Yi, C. W.; Kim, D. H.; Peden, C. H. F.; Allard, L. F.; Szanyi, J. Coordinatively Unsaturated Al^{3+} Centers as Binding Sites for Active Catalyst Phases of Platinum on γ-Al_2O_3. *Science (80-.).* **2009**, *325*, 1670–1673. https://doi.org/10.1126/science.1176745.

(93) Wan, C.; Hu, M. Y.; Jaegers, N. R.; Shi, D.; Wang, H.; Gao, F.; Qin, Z.; Wang, Y.; Hu, J. Z. Investigating the Surface Structure of Î-Al_2O_3 Supported WO_X Catalysts by High Field ^{27}Al

MAS NMR and Electronic Structure Calculations. *J. Phys. Chem. C* **2016**, *120*, 23093–23103. https://doi.org/10.1021/acs.jpcc.6b09060.

(94) Shi, L.; Deng, G. M.; Li, W. C.; Miao, S.; Wang, Q. N.; Zhang, W. P.; Lu, A. H. Al_2O_3 Nanosheets Rich in Pentacoordinate Al^{3+} Ions Stabilize Pt-Sn Clusters for Propane Dehydrogenation. *Angew. Chem. Int. Ed.* **2015**, *54*, 13994–13998. https://doi.org/10.1002/anie.201507119.

(95) Busca, G. The Surface of Transitional Aluminas: A Critical Review. *Catal. Today* **2014**, *226*, 2–13. https://doi.org/10.1016/j.cattod.2013.08.003.

Supplementary Information

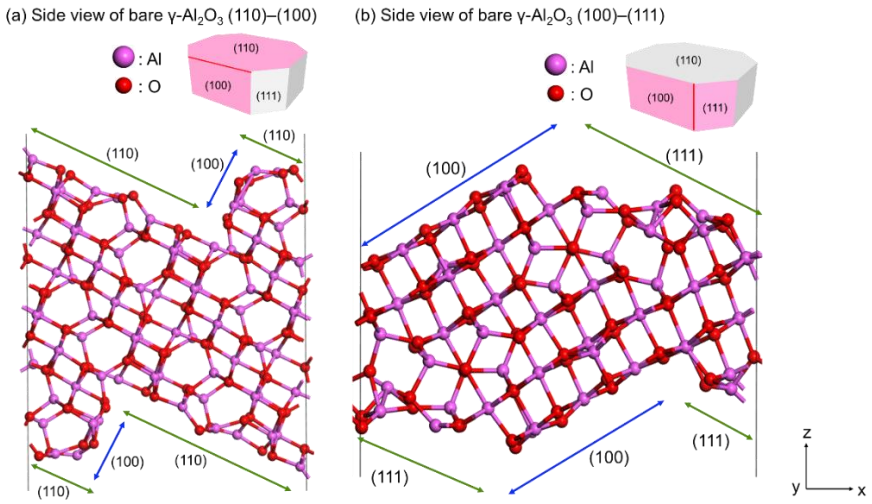

Figure S1. Side view of optimized periodic models of *γ*-Al_2O_3 surface. (a) *γ*-Al_2O_3 (110)–(100) surface, (b) *γ*-Al_2O_3 (100)–(111) surface. (pink: Al atom, red: O atom)

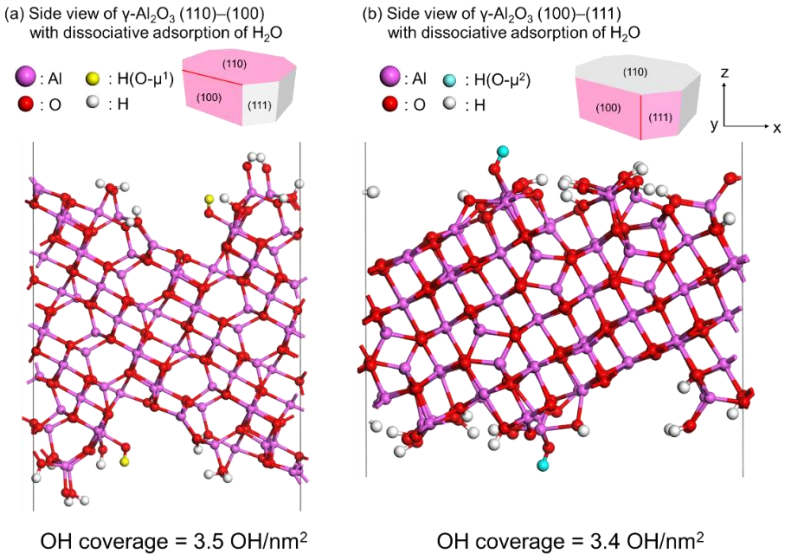

Figure S2. Side view of the optimized periodic model of a *γ*-Al_2O_3 surface with dissociative adsorbed H_2O. (a) *γ*-Al_2O_3 (110)–(100) surface, (b) *γ*-Al_2O_3 (100)–(111) surface. (pink: Al atom, cyan: Ag atom, red: O atom, white: H atom, blue: H atom in terminal hydroxyls on *γ*-Al_2O_3 (100) surface, and yellow: H atom in doubly bridging hydroxyls on *γ*-Al_2O_3 (100) surface.)

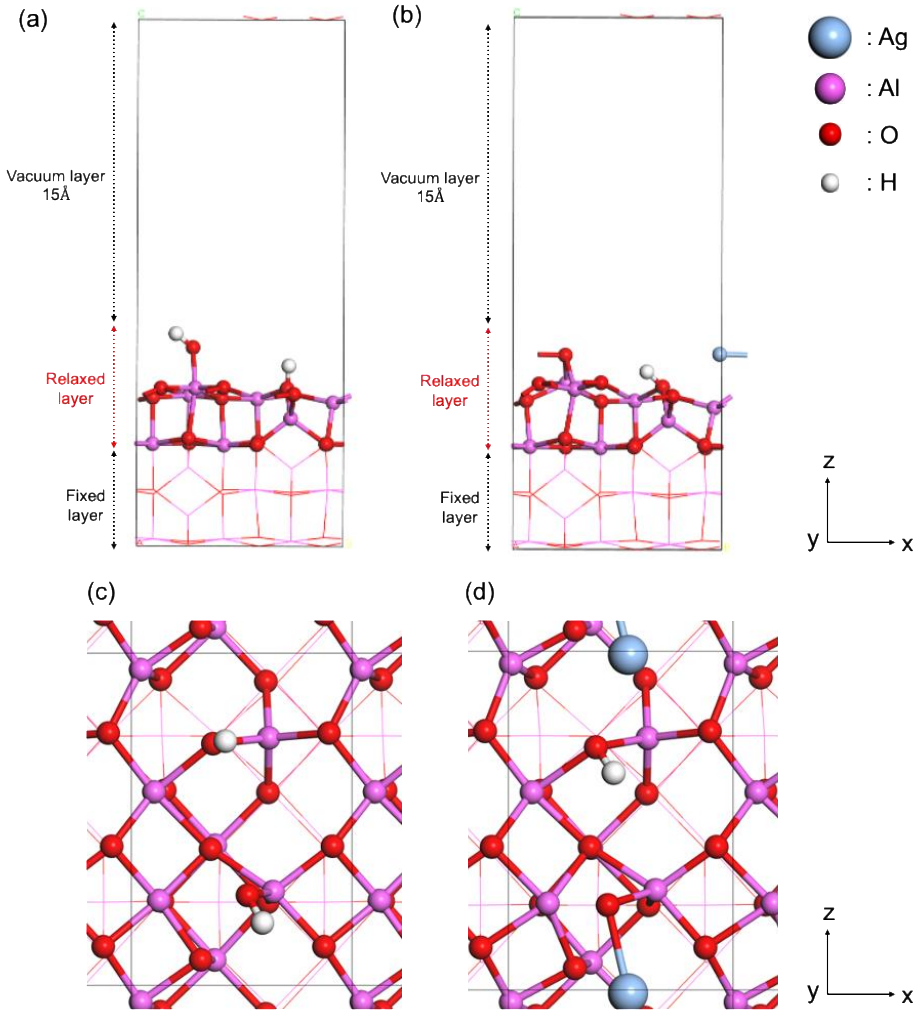

Figure S3. Optimized periodic models of γ-Al_2O_3 surface. Side and top view of (a), (c) γ-Al_2O_3 (100) surface and (b), (d) Ag/γ-Al_2O_3 (100) surface. Relaxed layers are represented by balls and sticks, and fixed layers are represented by lines. (pink: Al atom, cyan: Ag atom, red: O atom, and white: H atom.)

Table S1. Compositional formula and lattice parameters of the γ-Al_2O_3 step-edge models.

Step-edge model	Composition formula	a (Å)	b (Å)	c (Å)	α (°)	β (°)	γ (°)
γ-Al_2O_3 (110)–(100)	$(H_2O)_{10}/Al_{96}O_{144}$	17.02	8.41	37.35	90.00	97.02	90.00
γ-Al_2O_3 (100)–(111)	$(H_2O)_{14}/Al_{96}O_{144}$	18.66	11.17	36.40	89.48	88.08	90.26

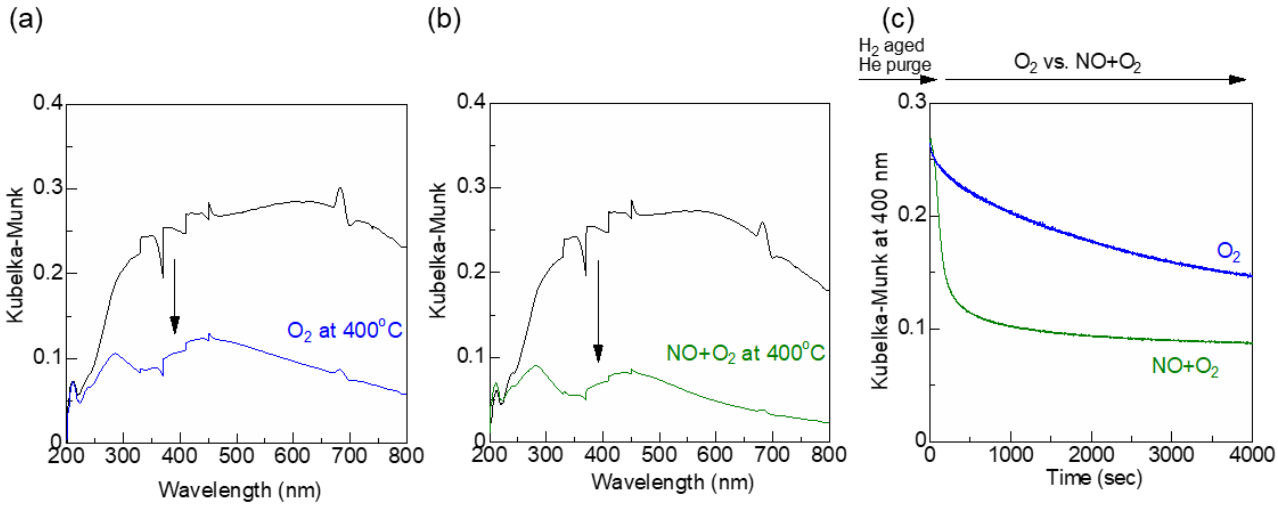

Figure S4. *In situ* UV-vis spectra of $Ag3/Al_2O_3$ after reduction by H_2 at 800 ˚C (black lines) and subsequent re-oxidation at 400 ˚C (4000 s) by (a) 10% O_2 and (b) 500 ppm NO + 10% O_2. (c) Time dependence of the UV-vis signal intensity due to Ag NPs during re-oxidation.

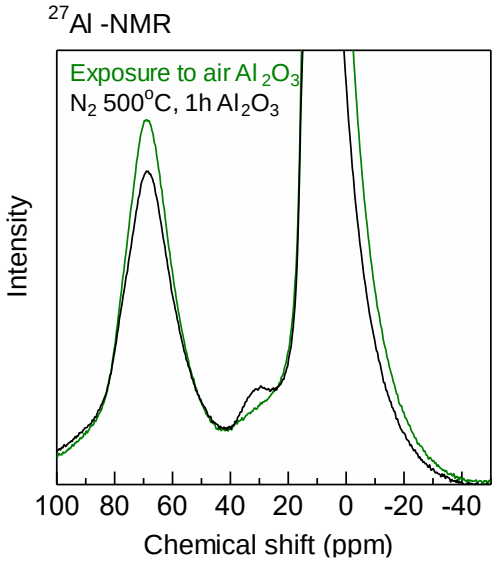

Figure S5. Normalized ^{27}Al NMR spectra of γ-Al_2O_3 dehydrated under N_2 at 500 ˚C for 1 h (black), followed by rehydration under ambient conditions for 1 h (green).

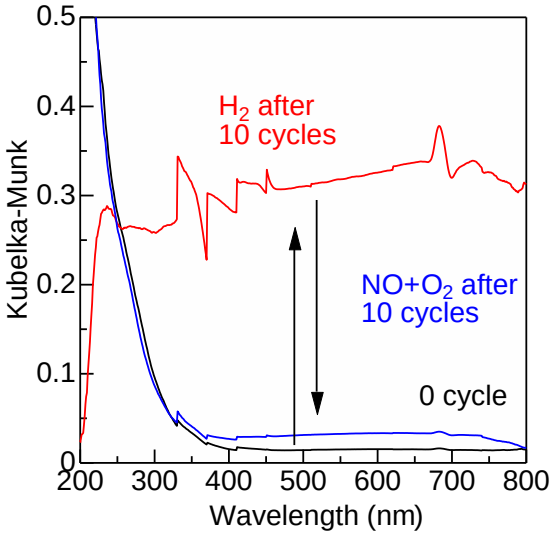

Figure S6. *In situ* UV-vis spectra (600 ˚C) of fresh Ag3/Al_2O_3 (black; in He), after 10 cycles under H_2 (red), and subsequent exposure to NO + O_2 (blue).

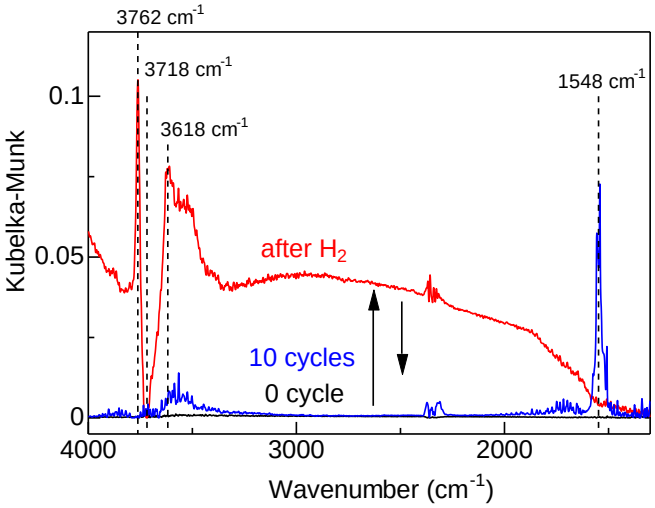

Figure S7. *In situ* DRIFT spectra (600 ˚C) of fresh Ag3/Al_2O_3 (black; in He), after 10 cycles under H_2 (red), and subsequent exposure to NO + O_2 (blue).

Table S2. Bader charge of Ag, O, and H.

Model	Bader charge		
	Ag	H	O
Ag_2O	0.41		-0.83
γ-Al_2O_3 (110)		0.67	-1.49
Ag on γ-Al_2O_3 (110)	0.44		-1.20

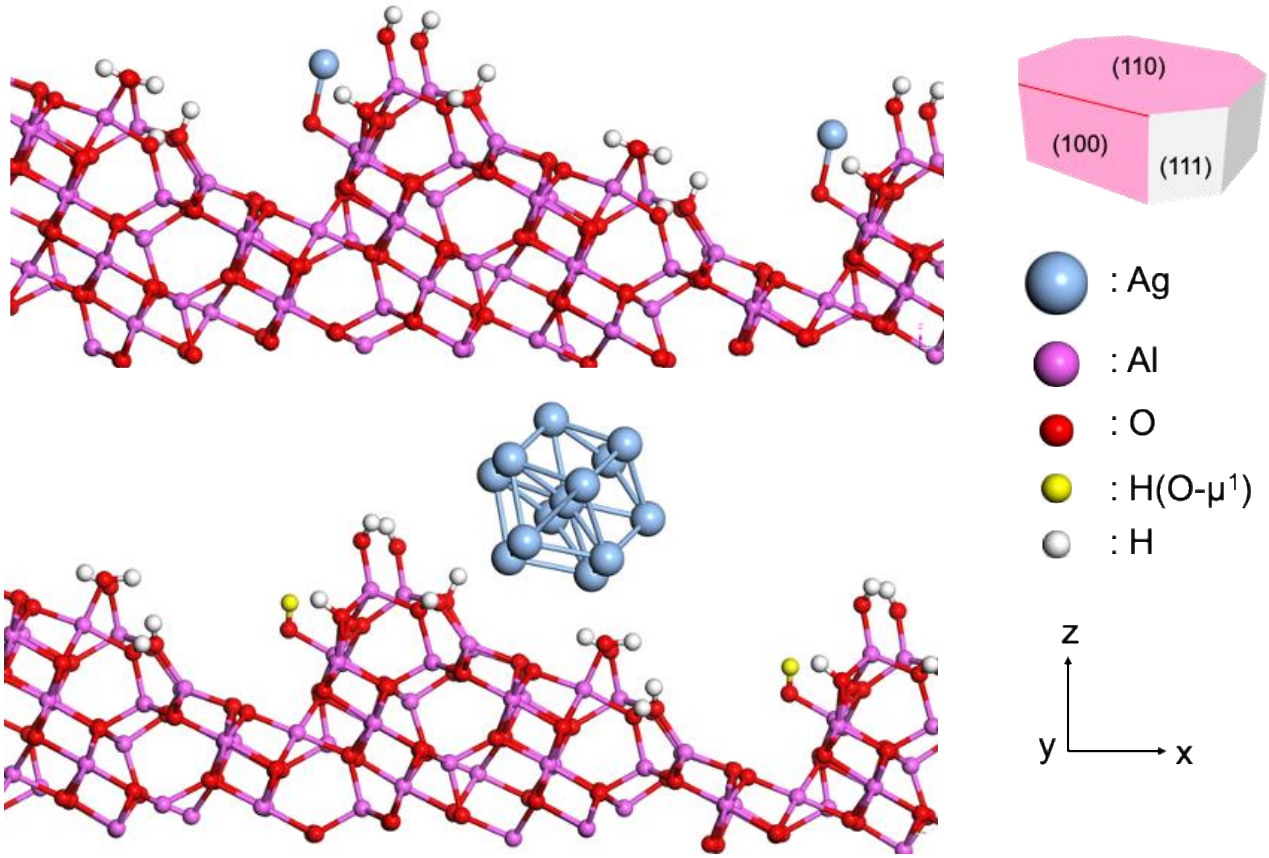

Figure S8. Surface structure models of (a) dispersed Ag species and (b) aggregated Ag species on a *γ*-Al_2O_3 (110)–(100) step-edge surface (cyan: Ag atom, pink: Al atom, red: O atom, yellow: H atom in terminal hydroxyls, and white: H atom). When Ag atoms aggregate, the H atoms of the terminal hydroxyl are regenerated.

Chapter 6
Regeneration of Atomic Ag Sites over Commercial γ-Aluminas by Oxidative Dispersion of Ag Metal Particles

6.1. INTRODUCTION

γ-Alumina-supported silver (Ag/Al_2O_3) catalysts have long been studied as promising catalysts for the selective catalytic reduction (SCR) of NO*x* by hydrocarbons (HC–SCR),[1–5] H_2-assisted HC–SCR,[6–13] and H_2-assisted SCR by NH_3 (H_2–NH_3–SCR).[14–20] After a long debate on the active Ag species in HC–SCR reactions,[1,6,13,20] it was concluded that isolated Ag(I) sites are indispensable for achieving high-performance Ag/Al_2O_3 catalysts for SCR.[13] Hence, Ag/Al_2O_3 for HC–SCR can be regarded as a rare example of a commercialized single-atom catalyst (SAC). Small $Ag_n^{\delta+}$ clusters generated from the *in situ* reduction of Ag(I) species by H_2 or HCs during SCR promoted the reaction under certain conditions, whereas Ag metal nanoparticles (NPs) had an adverse effect on NO*x* conversion as they promoted the non-selective oxidation of reductants.[17,20] Our previous study on H_2–NH_3–SCR[14–20] showed that isolated Ag(I) sites and small $Ag_n^{\delta+}$ clusters, which coexist under the reaction conditions, play important roles. Previous reports have suggested that compared to other transition metals, supported single-atom Ag and small Ag clusters are more susceptible to sintering at lower temperatures.[21–24] In commercial SCR systems, Ag/Al_2O_3 catalysts are exposed to high-temperature conditions, which could result in catalyst deactivation due to sintering of the isolated Ag(I) species to Ag metal NPs. Redispersion of the aggregated Ag NPs is a potential strategy for the regeneration of sintered Ag/Al_2O_3 catalysts. We previously reported the oxidative dispersion of large Ag metal NPs to isolated Ag(I) cations on *θ*-Al_2O_3.[25] However, the precise dispersion mechanism and nature of the anchoring sites remain elusive.

The structures of the metal anchoring sites on *γ*-Al_2O_3 were discussed.[26,27] Among various sites, recent studies employing Al nuclear magnetic resonance (NMR) spectroscopy[28–32] exclusively proposed the penta-coordinated Al_V^{3+} site as anchoring sites of various metal clusters. However, Al NMR is not a sufficient tool for complete characterization the of the anchoring sites as this technique is not suitable for identification of other sites such as surface octahedral (Al_{VI}^{3+}) and tetrahedral Al (Al_{IV}^{3+}) sites and Al-OH sites. In this regard, infrared (IR) spectroscopy using basic probe molecules[33–39] is useful for characterizing surface Al sites with different coordination environments (Al_{VI}^{3+}, Al_V^{3+}, and Al_{IV}^{3+}) and different Al-OH groups.[40,41] Based on NH_3-IR study on $Ag/γ$-Al_2O_3 and *γ*-Al_2O_3, Zeng et al.[13] proposed that the terminal hydroxyl (OH) groups on the (100) surface are the anchoring sites of the isolated Ag(I) cations, which act as catalytic sites for H_2-assisted HC–SCR. We recently studied the reversible structural transformation between atomic Ag(I) and large Ag metal NPs on a Ag/Al_2O_3 catalyst using various *in situ* spectroscopic techniques, *ex situ* microscopy, and theoretical calculations.[42] The on-top OH group on octahedral Al (HO-$μ_1$-Al_{VI}) adjacent to the unsaturated Al_{IV}^{3+} site anchors isolated Ag^+ in the form of AgO-$μ_1$-Al_{VI}, which can be converted to Ag metal NPs and HO-$μ_1$-Al_{VI} during sintering under H_2. Thereafter, under NO + O_2, the Ag metal NPs and HO-$μ_1$-Al_{VI} react to regenerate dispersed single-atomic AgO-$μ_1$-Al_{VI}.

Because the SCR activity of Ag/Al_2O_3 depends strongly on the type of Al_2O_3 source,[13] we hypothesized that the SCR activity of Ag/Al_2O_3 prepared with different alumina samples depends on the number of anchoring sites on the alumina samples.

Herein, we prepare Ag/Al_2O_3 catalysts with four types of commercial alumina and investigate the relationships between the relative number of HO-μ_1-Al_{VI} sites and (1) the number of unsaturated Al_{IV}^{3+} sites, (2) sintering resistance of Ag/Al_2O_3, (3) rate of Ag redispersion, and (4) catalytic activity of Ag/Al_2O_3. *In situ* X-ray absorption spectroscopy (XAS), ultraviolet-visible (UV-vis) spectroscopy, and infrared (IR) spectroscopy are employed to quantify these properties. We propose that our anchoring site model, the HO-μ_1-Al_{VI} site adjacent to the unsaturated Al_{IV}^{3+} site, is a universal model for different alumina samples, and that the SCR activity of Ag/Al_2O_3 increases with an increase in the number of anchoring sites.

6.2. Experimental methods

Preparation and characterization of catalysts

Ag/Al_2O_3 catalysts were prepared using the impregnation method, and four types of *γ*-AlOOH (CTB, PUR, VGL, and CFF in **Table 1**) were impregnated with an aqueous solution of $AgNO_3$, followed by evaporation to dryness at 60 °C, drying at 100 °C for 12 h, and calcination in air at 600 °C for 1 h. The Ag/Al_2O_3 catalysts are designated as Ag*x*/Al_2O_3 or Ag*x*/CTB, where *x* denotes the Ag loading amount (wt%). *γ*-Al_2O_3 was prepared by the calcination of *γ*-AlOOH at 600 °C (1 h).

X-ray diffraction (XRD) patterns were obtained using a Rigaku MiniFlex II/AP diffractometer with Cu-Kα radiation. Transmission electron microscopy (TEM) data were acquired using a JEOL JEM-2200FS electron microscope. ^{27}Al magic-angle spinning (MAS) NMR (^{27}Al-NMR) measurements were performed on a Bruker DSX-300 spectrometer operating at 300 MHz, with a 4 mm rotor. The Brunauer-Emmett-Teller (BET) surface areas of the *γ*-Al_2O_3 samples were determined using N_2 adsorption using AUTOSORB 6AG (Yuasa Ionics Co., Ltd., Japan).

Table 1. Properties of commercially available alumina and investigated catalysts

Sample	Product name	Manufacturer	S_{BET} [a]	Phase [b]	NO conversion in H_2–NH_3–SCR [%][c]	NO conversion in H_2–C_3H_6–SCR [%][c]
CTB	CATAPAL® B	Sasol	218	γ	55	34
PUR	PURALOX® SBa 200	Sasol	200	γ	38	30
VGL	Versal-Alumina VGL-15	UOP	166	γ	13	17
CFF	CFF-NP005-50	chemPUR	135	γ, (θ, α) [d]	13	14

[a]BET surface area ($m^2\ g^{-1}$) of *γ*-Al_2O_3 after calcination at 600 °C.

[b]Crystal phase of alumina estimated by XRD.

[c]NO conversion (%) by Ag(3 wt%)-loaded Al_2O_3 (40 mg) for H_2–NH_3–SCR at 150 °C and H_2–C_3H_6–SCR at 400 °C.

[d]*γ*-Al_2O_3 was the main phase, but XRD lines corresponding to *θ* and *α*-Al_2O_3 were observed as minor phases.

In situ spectroscopy

In situ diffuse reflectance UV-vis spectra were recorded on a JASCO V-750 UV-vis spectrometer. The sintered $Ag3/Al_2O_3$ (15 mg) catalyst powder was placed in a diffuse reflectance cell with a quartz window, connected to a gas flow system (100 mL min^{-1}). The light source was

directed to the center of the integrating sphere through an optical fiber. $BaSO_4$ was used to collect background spectra. The reflectance was converted to the Kubelka-Munk function.

In situ diffuse reflectance infrared Fourier-transform (DRIFT) spectra of the OH stretching region of the powder sample (ca. 40 mg) were recorded on a JASCO FT/IR-4600 instrument (mercury cadmium telluride detector) equipped with an *in situ* flow cell with a CaF_2 window. *In situ* IR spectra of the adsorbed pyridine were recorded in transmission mode using a JASCO FT/IR-4600 spectrometer. A 40 mg self-supporting wafer sample (20 mm ϕ) was mounted on a flow-type quartz IR cell (CaF_2 windows) connected to a flow system (100 mL min^{-1}). Twenty spectra were collected at a resolution of 4 cm^{-1} and averaged to obtain a spectrum. The spectrum of the catalyst wafer, acquired at the measurement temperature under He, was subtracted from each spectrum.

Ag K-edge X-ray absorption spectra were recorded in transmission mode using the BL-14B2 beamline at the SPring-8 synchrotron radiation facility (Harima, Japan). A Si(311) single crystal was used to obtain monochromatic X-ray beams. A self-supporting wafer of the sample (approximately 7 mm ϕ) was placed in an *in situ* quartz cell under a flow of a gas mixture diluted with He (500 mL min^{-1}) at atmospheric pressure. Normalization and linear combination fitting (LCF) analysis of the X-ray absorption near-edge structure (XANES) and curve-fitting analysis of the extended X-ray absorption fine structure (EXAFS) data were performed using the Athena software package.[43] For the LCF analysis, Ag^+-exchanged Ag-CHA (Si/Al = 11) and 10 wt% Ag-loaded low-surface-area Al_2O_3 were used as reference compounds for the isolated Ag(I) and Ag metal NPs, respectively.[42] Fourier-transformation of the k^3-weighted EXAFS data was carried out over the k range of 3−7 $Å^{-1}$ and R range of 1.05–3.2 $Å^{-1}$. Curve-fitting analysis was performed using Artemis, and the parameters for each shell were provided by FEFF6.

Catalytic reactions

H_2–NH_3–SCR (H_2 + NO + NH_3 + O_2) and H_2–C_3H_6–SCR (H_2 + NO + C_3H_6 + O_2) were performed using Ag3/Al_2O_3 powder in a fixed-bed flow reactor (flow rate = 100 mL min^{-1}). The composition of the feed gas, H_2/NO/(NH_3 or C_3H_6)/O_2/He, was 1%/500 ppm/500 ppm/10%/balance. The concentrations of the feed gas and products were measured using an online IR spectrometer (JASCO FT/IR-4600 with a TGS detector) equipped with a custom-built gas cell. The concentrations of NO, NO_2, N_2O, C_3H_6, and NH_3 were calculated based on calibration results. The reaction rates were estimated by changing the catalyst loading under conditions where the NO and NH_3 conversions were below 30%.

6.3. Results and discussion

SCR activity and structure of four Ag/Al_2O_3 catalysts

Four commercial alumina sources (CTB, PUR, VGL, and CFF) with different characteristics were used (**Table 1**). Ag(3 wt%)-loaded on alumina (designated as Ag3/CTB) was prepared by the conventional impregnation method.[42] The NO conversion (**Table 1**) achieved with these catalysts in the H_2-assisted SCR of NO by NH_3 and C_3H_6 was measured at 150 and 400 °C, respectively, using a flow reactor. For both reactions, the NO conversion of Ag-loaded alumina depended on the type of alumina and increased in the order: CTB > PUR > VGL ≥ CFF.

The Ag-loaded alumina catalysts were reduced under 2% H_2 flow at 800 °C (0.5 h) to prepare the sintered catalysts. The size distribution of the Ag NPs after sintering was estimated using *ex situ* TEM (**Figure 1**). The mean diameter of the Ag metal NPs after the sintering treatment increased in the order: CTB < PUR < VGL < CFF. The results indicate that the resistance to Ag sintering under reductive conditions depends on the type of alumina, and the sintering resistance decreased in the order: CTB > PUR > VGL > CFF. This order is consistent with the order of the catalytic activity of Ag/Al_2O_3 for SCR (**Table 1**).

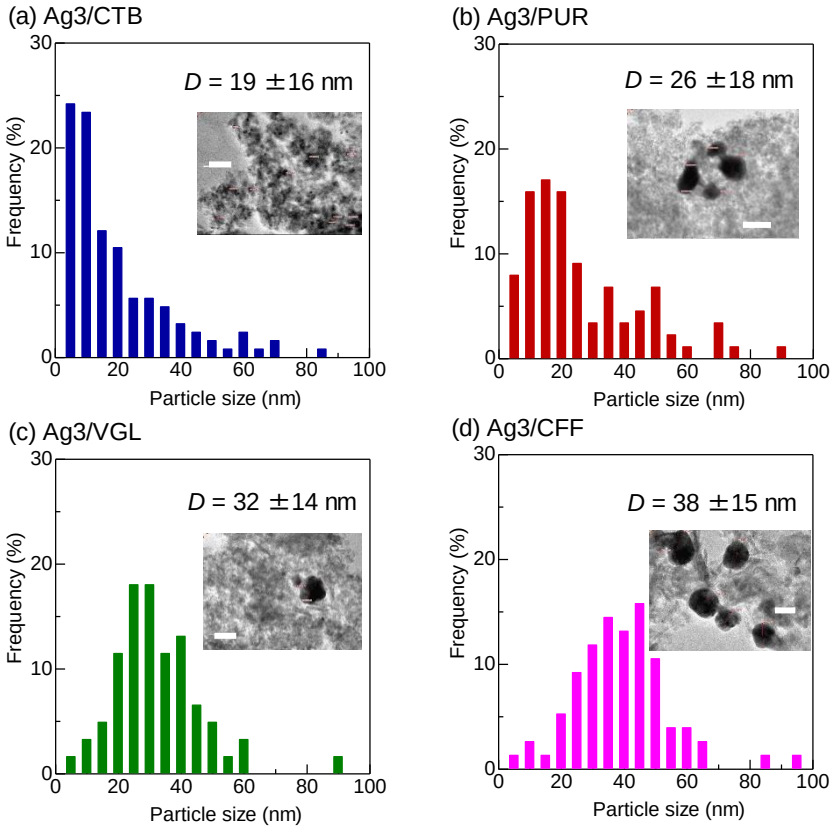

Figure 1. Particle size distribution and TEM images of (a) Ag3/CTB, (b) Ag3/PUR, (c) Ag3/VGL, and (d) Ag3/CFF after sintering treatment (2% H_2, 800 °C, 0.5 h).

Figure 2 shows the ^{27}Al NMR spectra of the alumina and Ag-loaded alumina samples dehydrated at 500 °C. To enhance the changes in the spectra caused by the loading of Ag, high-loading (10 wt%) samples were prepared and tested for ^{27}Al NMR measurements. The peaks with chemical shifts centered at 10, 33, and 67 ppm were assigned to Al_{IV}^{3+}, Al_{V}^{3+}, and Al_{VI}^{3+}, respectively. Previous ^{27}Al NMR studies of γ-Al_2O_3 have established that Al_{V}^{3+} ions are present only on the first surface layer.[29] Upon loading 10 wt% Ag on CTB, the Al_{V}^{3+} peak of CTB almost disappeared, indicating that some of the surface Al_{V}^{3+} sites interacted with the Ag species. However, loading 10 wt% Ag on the other alumina samples (PUR, VGL, CFF) did not markedly change the intensity of the Al_{V}^{3+} signals. These results demonstrate that ^{27}Al NMR is not a powerful method for investigating the anchoring sites of Ag species.

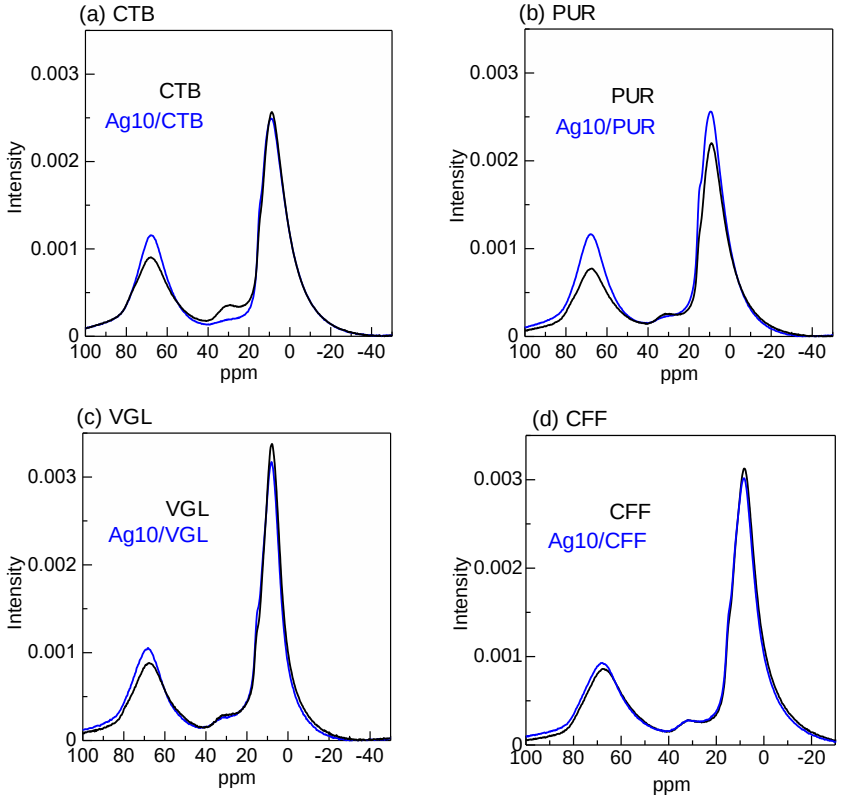

Figure 2. ^{27}Al NMR spectra of γ-Al_2O_3 (black) and Ag(10 wt%)-loaded Al_2O_3 (blue): (a) CTB, (b) PUR, (c) VGL and (d) CFF. The samples were dehydrated under N_2 at 500 °C before the measurements.

Our previous study[42] showed that the IR spectra of Ag/Al_2O_3 in the OH stretching region and 8a regions of pyridine adsorbed on Ag/Al_2O_3 and Al_2O_3 are useful for discussing the anchoring site of isolated Ag^+ on Al_2O_3. In brief, when Ag was loaded on Al_2O_3, the IR peak at 3770 cm^{-1}, assigned to the on-top OH group on octahedral Al (HO-μ^1-Al_{VI})[39] became less intense, the intensity of the band at 1621 cm^{-1} due to strong Lewis acid sites (unsaturated Al_{IV}^{3+} sites) also declined. Combined with STEM and DFT studies and a structural model of γ-Al_2O_3 in the literature, we

concluded that the anchoring sites of the isolated Ag(I) species on γ-Al_2O_3 are the HO-μ^1-Al_{VI} sites on the (100) surface adjacent to the strong Lewis acid (Al_{IV}) sites on the (110) surface.[42] Based on the consistent DFT and experimental IR data, it is concluded that the HO-μ^1-Al_{VI} site on the (100)–(110) step edge is the anchoring site of Ag. After sintering, the isolated AgO-μ^1-Al_{VI} species aggregate to form Ag metal NPs to regenerate the HO-μ^1-Al_{VI} sites. In the subsequent oxidative treatment, the Ag metal NPs undergo redispersion to regenerate the original AgO-μ^1-Al_{VI} species.[42] *In situ* DRIFT analysis of the four Ag/Al_2O_3 samples after sintering treatment was used for *in situ* monitoring of the changes in the HO-μ^1-Al_{VI} sites during the oxidative redispersion process. First, the sample was reduced in 2% H_2 at 500 °C (0.5 h), followed by He purging, and IR spectra of the reduced samples (black lines in **Figure 3a**) were obtained. The sample was then oxidized by 10% O_2 at 500 °C (0.5 h), and the IR spectra (blue lines in **Figure 3a**) were obtained. For the four samples, a negative band centered around 3762 cm^{-1} appeared after re-oxidization by O_2; the intensity of this negative band increased in the order: CTB > PUR > VGL > CFF. This order is consistent with the order of the catalytic activity (**Table 1**) and sintering resistance of supported Ag on alumina (**Figure 1**).

In separate IR (transmission) experiments, pyridine adsorption on pre-oxidized IR disks of Al_2O_3 and Ag/Al_2O_3 was studied at 200 °C. For all samples, the band intensities of pyridine on the strong Lewis acid (Al_{IV}) sites (1621 cm^{-1}) of Ag/Al_2O_3 (red lines in **Figure 3b**) were markedly lower than those of Al_2O_3 (black lines in **Figure 3b**). This suggests that the Ag species in the form of AgO-μ^1-Al_{VI} decreased the Lewis acidity of the adjacent Al_{IV}^{3+} sites because of the electronic effect of the Ag species. **Figure 4a** presents a plot of the intensity of the strong Lewis acid (Al_{IV}) sites (1621 cm^{-1}) of the Ag-free Al_2O_3 samples in **(Figure 3b**) versus the intensity of the negative band of HO-μ^1-Al_{VI} (3762 cm^{-1}) observed due to re-oxidation of the sintered Ag/Al_2O_3 samples (**Figure 3a**). A linear relationship was observed, providing additional evidence to support our previously reported conclusion[42] that the anchoring sites of Ag on γ-Al_2O_3 are the HO-μ^1-Al_{VI} sites on the (100) surface adjacent to the strong Lewis acid (Al_{IV}) sites on the (110) surface at the (100)–(110) step edge. **Figure 4b** presents a plot of the average sizes of the Ag NPs on the Ag/Al_2O_3 samples after sintering at 800 °C (**Figure 1**) *versus* the intensity of the negative band of HO-μ^1-Al_{VI} (**Figure 3a**). The size of the Ag metal NPs decreased with an increase in the number of HO-μ^1-Al_{VI} sites on the alumina surfaces, which demonstrates that the anchored Ag species in the form of AgO-μ^1-Al_{VI} play a significant role in the sintering resistance under reductive conditions at high temperatures.

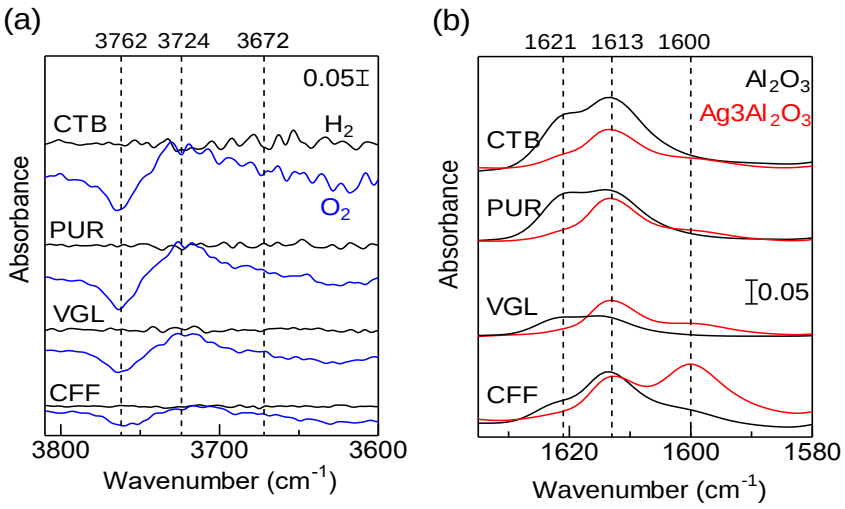

Figure 3. (a) *In situ* DRIFT spectra of OH stretching on four types of Ag(3 wt%)-loaded Al_2O_3 after H_2 (black) and O_2 (blue) treatment at 500 °C. (b) *In situ* IR spectra of pyridine adsorbed on four types of γ-Al_2O_3 (black) and Ag3/Al_2O_3 (red) at 200 °C.

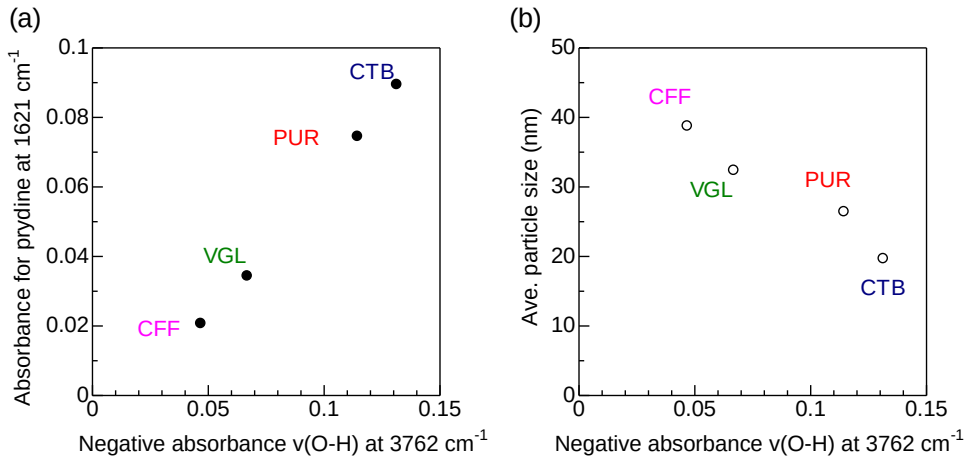

Figure 4. (a) IR intensity of adsorbed pyridine (**Figure 3b**) and (b) average particle size of Ag NPs (**Figure 1**) *versus* IR intensity of negative peak due to HO-μ^1-Al_{VI} sites (**Figure 3a**) on Ag(3 wt%)-loaded Al_2O_3.

In situ observation of oxidative dispersion

In situ time-resolved Ag K-edge XANES spectroscopy was used to characterize the structure of the Ag species during oxidative redispersion. Two Ag catalysts loaded on alumina with a relatively large amount (CTB) and a low number of HO-μ^1-Al_{VI} sites (VGL), Ag3/CTB and Ag3/VGL, pre-reduced by H_2 (800 °C), were exposed to NO + O_2 at 500 °C, while monitoring the XANES spectra as a function of time (**Figure 5**). The EXAFS features (**Figure 5(a,b)** and **Table 2**) of the sintered Ag3/CTB (9.3 Ag−Ag bonds at 2.78 Å) and Ag3/VGL (7.4 Ag−Ag bonds at 2.82 Å) show

the absence of Ag^+ species on alumina and the presence of Ag metal NPs as major species. According to the method described in our previous study, [42] LCF analysis of the spectra was performed in the energy range of 25500–25650 eV using the spectra of the two reference samples: Ag^+ ion-exchanged CHA zeolite for the isolated Ag(I) species and Ag(10 wt%)-loaded low surface area *α*, *θ*-Al_2O_3 for the Ag metal NPs. LCF analysis of the samples at t = 0 s shows that Ag metal NPs are the dominant Ag species in the sintered catalysts. With an increase in the time of oxidation by NO + O_2, the fraction of Ag(I) species increased and that of Ag metal NPs decreased. This indicates that the Ag metal NPs undergo oxidative dispersion to form isolated Ag(I) species. Most of the Ag metal NPs on Ag3/CTB were converted to isolated Ag(I) species within 48 s, whereas the oxidative dispersion was completed in 96 s for Ag3/VGL. This indicates that oxidative redispersion of the Ag metal NPs is faster for alumina with a larger number of surface HO-μ^1-Al_{VI} sites (CTB). Oxidation by NO + O_2 treatment for 300 s decreased the intensity of the Ag−Ag contribution to the EXAFS peak, accompanied by the appearance of peaks corresponding to Ag−O coordination (**Figure 5(a),(b)**, and **Table 2**). The EXAFS results indicate that some of the Ag metal NPs were converted to isolated Ag(I) species bonded to alumina, which is consistent with the XANES results.

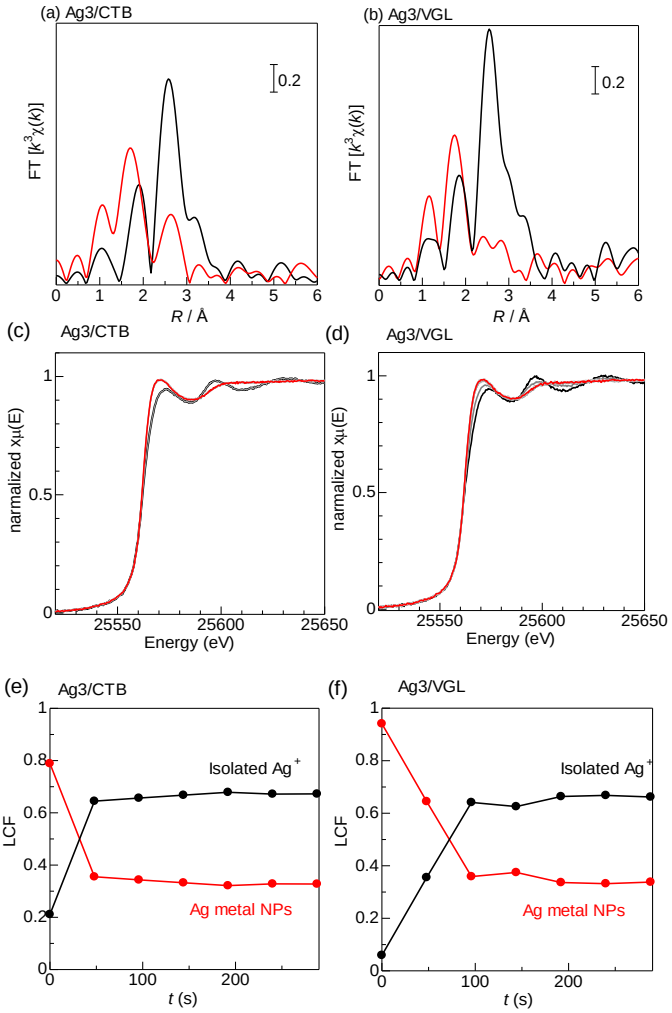

Figure 5 *In situ* Ag K-edge EXAFS (a, b) and XANES (c, d) profiles of (a) Ag3/CTB and (b) Ag3/VGL during re-oxidation by NO + O_2 (300 s) at 500 °C. LCF fraction of Ag metal NPs and isolated Ag^+ in (c) Ag3/CTB and (d) Ag3/VGL. Flow rate = 1000 mL min^{-1}; sample weight = 136.8 mg.

Table 2. Ag K-edge EXAFS curve-fitting analysis of $Ag3/Al_2O_3$

Sample	Shell	CN [a]	R [b] / Å	σ^2 [c] / $Å^2$	R_f [d] / %
Sintered Ag3/CTB	Ag-Ag	8.9	2.89	0.0237	2.9
Re-oxidized Ag3/CTB	Ag-O	1.1	2.25	0.0682	2.1
	Ag-Ag	1.6	2.71	0.0208	2.4
Sintered Ag3/VGL	Ag-Ag	8.3	2.76	0.0247	2.9
Re-oxidized Ag3/VGL	Ag-O	1.1	2.22	0.0060	2.1
	Ag-Ag	4.6	2.74	0.0382	2.4

[a]Coordination number. [b]Bond distance. [c]Debye-Waller factor. [d]Residual factor.

Similar experiments for the redispersion process were performed using *in situ* diffuse reflectance UV-vis spectroscopy.[19,44] The UV-vis spectra of the four different Ag/Al_2O_3 samples pre-reduced at 800 °C showed a broad band around 400–800 nm, assignable to the small Ag metal NPs (black lines in **Figure 6**). The intensity of the band at 750 nm was monitored as a function of time under NO + O_2 at 400 °C (**Figure 7a**). Oxidation by NO + O_2 for 0.5 h decreased the intensity of the band at 400–800 nm due to the Ag metal NPs (blue lines in **Figure 6**). **Figure 8a** presents a plot of the decrease in the intensity of the UV-vis band at 750 nm (relative amount of re-dispersed Ag NPs) *versus* the intensity of the negative peak in the IR profile arising from the HO-μ^1-Al_{VI} sites. Conversion of Ag the metal NPs to Ag(I) species increased with increasing the number of HO-μ^1-Al_{VI} sites on alumina, indicating that the HO-μ^1-Al_{VI} sites act as anchoring sites for the dispersed Ag(I) species.

The kinetic curves in **Figure 7a** were numerically differentiated to obtain the plots of the initial slope of the kinetic curve ($\Delta KM/\Delta t$) *versus* time (**Figure 7b**). The maximum values of $\Delta KM/\Delta t$ in the initial period correspond to the initial rates for redispersion of the Ag metal NPs into Ag(I) species. The rates depend on the type of alumina support and changed in the order: CTB > PUR > VGL > CFF. This order is consistent with the order of the catalytic activity (**Table 1**) and sintering-resistance of Ag supported on alumina **(Figure 1**). **Figure 8a** presents the plot of the initial rates for the redispersion of Ag metal NPs (**Figure 7b**) as a function of the intensity of the negative band of HO-μ^1-Al_{VI}. The rate of redispersion of the Ag metal NPs increased with an increase in the number of HO-μ^1-Al_{VI} sites, which shows that alumina with a larger number of HO-μ^1-Al_{VI} sites leads to more rapid redispersion under oxidative conditions.

In the H_2–NH_3–SCR and H_2–C_3H_6–SCR employing the Ag/Al_2O_3 catalysts, reductive aggregation ($Ag^+ \rightarrow$ Ag metal) by H_2 and oxidative dispersion (Ag metal $\rightarrow Ag^+$) by NO + O_2 may compete with each other; hence, the relative amount of Ag metal and Ag(I) species depends on the number of HO-μ^1-Al_{VI} sites on the different alumina types. To quantitatively discuss the effect of the number of anchoring sites on the SCR activity of the Ag/Al_2O_3 catalysts, the NO conversion (**Table 1**) in the H_2–NH_3–SCR at 150 °C and H_2–C_3H_6–SCR at 400 °C was plotted versus the IR intensity of the negative peak due to the HO-μ^1-Al_{VI} sites (**Figure 9**). For both reactions, the NO conversion increased with increasing number of HO-μ^1-Al_{VI} sites, which clearly indicates that Al_2O_3 with a larger number of surface HO-μ^1-Al_{VI} sites is preferable as a support material for the H_2-assisted SCR promoted by Ag/Al_2O_3 catalysts. A larger number of anchoring sites should lead to a higher fraction of highly dispersed Ag(I) species as active species for the SCR, rather than Ag metal NPs, resulting

in higher NO conversion.

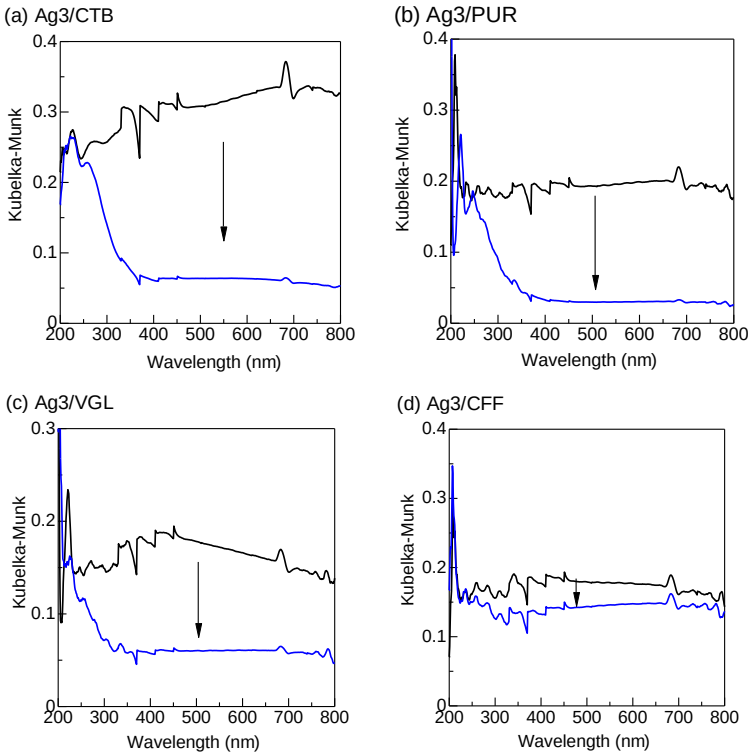

Figure 6. (a) *In situ* UV spectra of (a) Ag3/CTB, (b) Ag3/PUR, (c) Ag3/VGL, and (d) Ag3/CFF after sintering treatment (black), followed by NO + O_2 treatment at 400 °C for 0.5 h (blue).

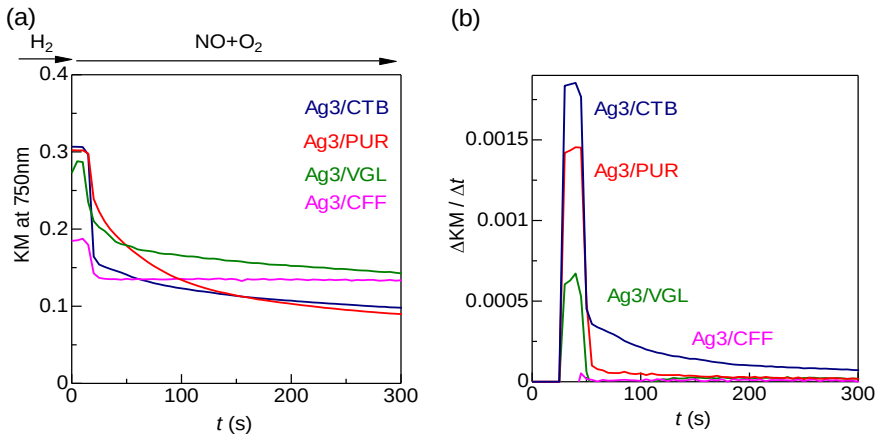

Figure 7. (a) Time-dependence of relative amount of Ag NPs (UV-vis intensity (KM) at 750 nm) on Ag3/Al_2O_3 samples under NO + O_2 at 400 °C and (b) redispersion rate of Ag NPs, estimated by numerical differentiation ($\Delta KM/\Delta t$) of the kinetic curves *vs*. time.

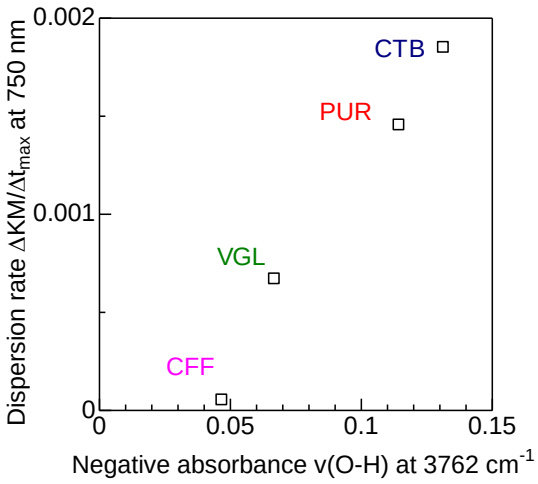

Figure 8. Initial rate of Ag NP redispersion (maximum ΔKM/Δ*t* value in **Figure 7b**) *versus* IR intensity of negative peak due to HO-μ^1-Al$_{VI}$ sites (**Figure 3a**) for Ag3/Al_2O_3 samples.

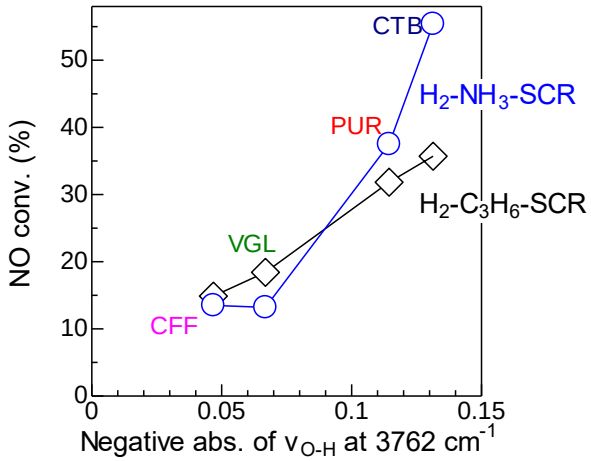

Figure 9. NO conversion (from **Table 1**) for H_2–NH_3–SCR at 150 °C and H_2–C_3H_6–SCR at 400 °C *versus* IR intensity of negative peak due to HO-μ^1-Al$_{VI}$ sites (**Figure 3a**) for Ag3/Al_2O_3 samples. Flow rate = 100 mL min^{-1}; sample weight = 15 mg.

6.4. Conclusions

Ag/Al_2O_3 catalysts were prepared using four types of commercial alumina sources. The effect of the relative amount of on-top OH groups on octahedral Al ($HO\text{-}\mu_1\text{-}Al_{VI}$) on (1) the amount of unsaturated Al_{IV}^{3+} sites, (2) sintering resistance of Ag/Al_2O_3, (3) rate of Ag redispersion, and (4) catalytic activity of Ag/Al_2O_3 was investigated. The number of strong Lewis acid (unsaturated Al_{IV}^{3+}) sites on the Ag-free γ-Al_2O_3 supports increased with an increase in the number of $HO\text{-}\mu^1\text{-}Al_{VI}$ sites. Combined with the results in our previous report,[42] the data demonstrate that the $HO\text{-}\mu^1\text{-}Al_{VI}$ site on the (100) surface adjacent to the unsaturated Al_{IV}^{3+} site on the (110) surface at the (100)–(110) step edge is a general model for the anchoring sites of Ag on γ-Al_2O_3. The anchored Ag species, $AgO\text{-}\mu^1\text{-}Al_{VI}$, underwent sintering to yield Ag metal NPs after H_2-reduction at 800 °C. The mean size of the Ag metal NPs after sintering decreased with an increase in the number of anchoring sites on the alumina surface. Under NO + O_2, the sintered Ag/Al_2O_3 catalysts undergo oxidative redispersion to regenerate the $AgO\text{-}\mu^1\text{-}Al_{VI}$ sites. The amount of re-dispersed Ag metal and the initial rate of the redispersion process increase with the number of $HO\text{-}\mu^1\text{-}Al_{VI}$ sites, which demonstrates that the anchored Ag species are in the form of $AgO\text{-}\mu^1\text{-}Al_{VI}$. These results show that the $HO\text{-}\mu^1\text{-}Al_{VI}$ site adjacent to the unsaturated Al_{IV}^{3+} site on γ-Al_2O_3 (anchoring site of Ag) plays an important role in the sintering resistance and redispersion of the supported Ag species. The activity of these catalysts for H_2-assisted SCR of NO by NH_3 or C_3H_6 increased with an increase in the number of $HO\text{-}\mu^1\text{-}Al_{VI}$ sites. In summary, the present results provide a simple concept for designing sintering-resistant Ag/Al_2O_3 catalysts for SCR; γ-Al_2O_3 with a larger amount of surface $HO\text{-}\mu^1\text{-}Al_{VI}$ sites is a preferable support for H_2-assisted SCR by Ag/Al_2O_3 catalysts because the support with a larger number of anchoring sites provides a larger number of $AgO\text{-}\mu^1\text{-}Al_{VI}$ sites, as active sites for H_2-assisted SCR, possibly *via* dynamic sintering/redispersion cycles.

References

(1) Shimizu, K.; Shibata, J.; Yoshida, H.; Satsuma, A.; Hattori, T. Silver-Alumina Catalysts for Selective Reduction of NO by Higher Hydrocarbons: Structure of Active Sites and Reaction Mechanism. *Appl Catal B* **2001**, *30*, 151–162.

(2) Deng, H.; Yu, Y.; Liu, F.; Ma, J.; Zhang, Y.; He, H. Nature of Ag Species on Ag/γ-Al_2O_3 : A Combined Experimental and Theoretical Study. *ACS Catal* **2014**, *4*, 2776–2784.

(3) Deng, H.; Yu, Y.; He, H. Discerning the Role of Ag-O-Al Entities on Ag/γ-Al_2O_3 Surface in NOx Selective Reduction by Ethanol. *Journal of Physical Chemistry C* **2015**, *119*, 3132–3142.

(4) Breen, J. P.; Burch, R.; Hardacre, C.; Hill, C. J.; Krutzsch, B.; Bandl-Konrad, B.; Jobson, E.; Cider, L.; Blakeman, P. G.; Peace, L. J.; Twigg, M. V.; Preis, M.; Gottschling, M. An Investigation of the Thermal Stability and Sulphur Tolerance of Ag/γ-Al_2O_3 Catalysts for the SCR of NO_x with Hydrocarbons and Hydrogen. *Appl Catal B* **2007**, *70*, 36–44.

(5) Hayashizaki, K.; Jibiki, T.; Inoue, K.; Koyanagi, Y.; Tanaka, S.; Tongu, H.; Hirabayashi, H.; Sato, S. After-Treatment System of Medium Duty Engines Using Diesel Fuel as a Reducing Agent for NO_x Reduction. *SAE Technical Papers* **2018**, *1*, 0345.

(6) Shibata, J.; Shimizu, K.; Satokawa, S.; Satsuma, A.; Hattori, T. Promotion Effect of Hydrogen on Surface Steps in SCR of NO by Propane over Alumina-Based Silver Catalyst as Examined by Transient FT-IR. *Physical Chemistry Chemical Physics* **2003**, *5*, 2154–2160.

(7) Shimizu, K.; Katagiri, M.; Satokawa, S.; Satsuma, A. Applied Catalysis B : Environmental Sintering-Resistant and Self-Regenerative Properties of Ag/SnO_2 Catalyst for Soot Oxidation. *Appl Catal B* **2011**, *108–109*, 39–46.

(8) Kannisto, H.; Skoglundh, M.; Arve, K.; Olsson, E.; Härelind, H. Direct Observation of Atomically-Resolved Silver Species on a Silver Alumina Catalyst Active for Selective Catalytic Reduction of Nitrogen Oxides. *Catal Sci Technol* **2019**, *9*, 6213–6216.

(9) Tamm, S.; Vallim, N.; Skoglundh, M.; Olsson, L. The Influence of Hydrogen on the Stability of Nitrates during H_2-Assisted SCR over Ag/Al_2O_3 Catalysts - A DRIFT Study. *J Catal* **2013**, *307*, 153–161.

(10) Korhonen, S. T.; Beale, A. M.; Newton, M. A.; Weckhuysen, B. M. New Insights into the Active Surface Species of Silver Alumina Catalysts in the Selective Catalytic Reduction of NO. *Journal of Physical Chemistry C* **2011**, *115*, 885–896.

(11) Bogdanchikova, N.; Meunier, F. C.; Avalos-Borja, M.; Breen, J. P.; Pestryakov, A. On the Nature of the Silver Phases of Ag/Al_2O_3 Catalysts for Reactions Involving Nitric Oxide. *Appl Catal B* **2002**, *36*, 287–297.

(12) Soon, P.; Kyu, M.; Cho, B. K.; Nam, I.; Oh, S. H. Effect of H_2 on DeNO_x Performance of HC-SCR over Ag/Al_2O_3 : Morphological , Chemical , and Kinetic Changes. **2013**, *301*, 65–76.

(13) Wang, F.; Ma, J.; Xin, S.; Wang, Q.; Xu, J.; Zhang, C.; He, H.; Cheng Zeng, X. Resolving the Puzzle of Single-Atom Silver Dispersion on Nanosized γ-Al_2O_3 Surface for High Catalytic Performance. *Nat Commun* **2020**, *11*, 1–11.

(14) Richter, M.; Fricke, R.; Eckelt, R. Unusual Activity Enhancement of NO Conversion over Ag/Al_2O_3 by Using a Mixed NH_3/H_2 Reductant under Lean Conditions. *Catal Letters* **2004**, *94*, 115–118.

(15) Kondratenko, E. V; Kondratenko, V. A.; Richter, M.; Fricke, R. Influence of O_2 and H_2 on NO Reduction by NH_3 over Ag/Al_2O_3 : A Transient Isotopic Approach. **2006**, *239*, 23–33.

(16) Kondratenko, V. A.; Bentrup, U.; Richter, M.; Hansen, T. W.; Kondratenko, E. V. Mechanistic Aspects of N_2O and N_2 Formation in NO Reduction by NH_3 over Ag/Al_2O_3: The Effect of O_2 and H_2. *Appl Catal B* **2008**, *84*, 497–504.

(17) Xu, G.; Wang, H.; Yu, Y.; He, H. Role of Silver Species in H_2-NH_3-SCR of NOx over Ag/Al_2O_3 Catalysts: *Operando* Spectroscopy and DFT Calculations. *J Catal* **2021**, *395*, 1–9.

(18) Shimizu, K.; Satsuma, A. Hydrogen Assisted Urea-SCR and NH_3-SCR with Silver-Alumina as Highly Active and SO_2-Tolerant de-NO_x Catalysis. *Appl Catal B* **2007**, *77*, 202–205.

(19) Shimizu, K.; Satsuma, A. Reaction Mechanism of H_2-Promoted Selective Catalytic Reduction of NO with NH_3 over Ag/Al_2O_3. *Journal of Physical Chemistry C* **2007**, *111*, 2259–2264.

(20) Xu, G.; Ma, J.; Wang, L.; Lv, Z.; Wang, S.; Yu, Y. Mechanism of the H2 Effect on NH3-Selective Catalytic Reduction over Ag/Al2O3 : Kinetic and Diffuse Reflectance Infrared Fourier Transform Spectroscopy Studies. *ACS Catal* **2019**, *9*, 10489–10498.

(21) Wan, Q.; Hu, S.; Dai, J.; Chen, C.; Li, W. X. First-Principles Kinetic Study for Ostwald Ripening of Late Transition Metals on TiO_2 (110). *Journal of Physical Chemistry C* **2019**, *123*, 1160–1169.

(22) Narula, C. K.; Stocks, G. M. Ab Initio Density Functional Calculations of Adsorption of Transition Metal Atoms on θ-Al2O3(010) Surface. *Journal of Physical Chemistry C* **2012**, *116*, 5628–2636.

(23) Dietze, E. M.; Plessow, P. N. Predicting the Strength of Metal − Support Interaction with Computational Descriptors for Adhesion Energies. *Journal of Physical Chemistry C* **2019**, *123*, 20443–20450.

(24) Agostini, G.; Usseglio, S.; Groppo, E.; Uddin, M. J.; Prestipino, C.; Bordiga, S.; Zecchina, A.; Solari, P. L.; Lamberti, C. From Isolated Ag+ Ions to Aggregated Ag0 Nanoclusters in Silver-Exchanged Engelhard Titanosilicate (ETS-10) Molecular Sieve: Reversible Behavior. *Chemistry of Materials* **2009**, *21*.

(25) Shimizu, K.; Sawabe, K.; Satsuma, A. Self-Regenerative Silver Nanocluster Catalyst for CO Oxidation. *ChemCatChem* **2011**, *3*, 1290–1293.

(26) Busca, G. Structural, Surface, and Catalytic Properties of Aluminas. *Advances in Catalysis* **2014**, *57*, 319–404.

(27) Rascón, F.; Wischert, R.; Copéret, C. Molecular Nature of Support Effects in Single-Site Heterogeneous Catalysts: Silica vs. Alumina. *Chem Sci* **2011**, *2*, 1449–1456.

(28) Jang, E. J.; Lee, J.; Kwak, J. H. Morphology Change and Phase Transformation of Alumina Related to Defect Sites and Its Use in Catalyst Preparation. *Catal Today* **2020**, *352*, 323–328.

(29) Kwak, J. H.; Hu, J. Z.; Kim, D. H.; Szanyi, J.; Peden, C. H. F. Penta-Coordinated Al^{3+} Ions as Preferential Nucleation Sites for BaO on γ-Al_2O_3: An Ultra-High-Magnetic Field ^{27}Al MAS NMR Study. *J Catal* **2007**, *251*, 189–194.

(30) Kwak, J. H.; Hu, J.; Lukaski, A.; Kim, D. H.; Szanyi, J.; Peden, C. H. F. Role of Pentacoordinated Al^{3+} Ions in the High Temperature Phase Transformation of γ-Al_2O_3. *Journal of Physical Chemistry C* **2008**, *112*, 9486–9492.

(31) Phung, T. K.; Lagazzo, A.; Rivero Crespo, M. Á.; Sánchez Escribano, V.; Busca, G. A Study of Commercial Transition Aluminas and of Their Catalytic Activity in the Dehydration of Ethanol. *J Catal* **2014**, *311*, 102–113.

(32) Murata, K.; Shiotani, T.; Ohyama, J.; Wakabayashi, R.; Maruoka, H.; Kimura, T.; Satsuma, A. Relationship between Penta-Coordinated Al^{3+} Sites in the Al_2O_3 Supports and CH_4 Combustion Activity of Pd/Al_2O_3 Catalysts. *Catal Sci Technol* **2021**, *11*, 2374–2378.

(33) Liu, X. DRIFTS Study of Surface of γ-Alumina and Its Dehydroxylation. *Journal of Physical Chemistry C* **2008**, *112*, 5066–5073.

(34) Srinivasan, S.; Narayanan, C. R.; Datye, A. K. The Role of Sodium and Structure on the Catalytic Behavior of Alumina: II. IR Spectroscopy. *Appl Catal A Gen* **1995**, *132*, 289–308.

(35) Lundie, D. T.; McInroy, A. R.; Marshall, R.; Winfield, J. M.; Jones, P.; Dudman, C. C.; Parker, S. F.; Mitchell, C.; Lennon, D. Improved Description of the Surface Acidity of η-Alumina. *Journal of Physical Chemistry B* **2005**, *109*, 11592–11601.

(36) Phung, T. K.; Herrera, C.; Larrubia, M. Á.; García-Diéguez, M.; Finocchio, E.; Alemany, L. J.; Busca, G. Surface and Catalytic Properties of Some γ-Al_2O_3 Powders. *Appl Catal A Gen* **2014**, *483*, 41–51.

(37) Liu, X.; Truitt, R. E. DRFT-IR Studies of the Surface of γ-Alumina. *J Am Chem Soc* **1997**, *119*, 9856–9860.

(38) Morterra, C.; Magnacca, G. A Case Study: Surface Chemistry and Surface Structure of Catalytic Aluminas, as Studied by Vibrational Spectroscopy of Adsorbed Species. *Catal Today* **1996**, *27*, 497–532.

(39) Digne, M.; Sautet, P.; Raybaud, P.; Euzen, P.; Toulhoat, H. Use of DFT to Achieve a Rational Understanding of Acid-Basic Properties of γ-Alumina Surfaces. *J Catal* **2004**, *226*, 54–68.

(40) Lee, J.; Jang, E. J.; Jeong, H. Y.; Kwak, J. H. Critical Role of (100) Facets on Γ-Al_2O_3 for Ethanol Dehydration: Combined Efforts of Morphology-Controlled Synthesis and TEM Study. *Appl Catal A Gen* **2018**, *556*, 121–128.

(41) Dyan, A.; Cenedese, P.; Dubot, P. Physical Properties of γ Alumina Surface Hydroxyls Revisited through a Large Scale Periodic Quantum-Chemistry Approach. *Journal of Physical Chemistry B* **2006**, *110*, 10041–10050.

(42) Kubota, H.; Mine, S.; Toyao, T.; Maeno, Z.; Shimizu, K. I. Redox-Driven Reversible Structural Evolution of Isolated Silver Atoms Anchored to Specific Sites on γ-Al2O3. *ACS Catal* **2022**, *12*.

(43) Ravel, B.; Newville, M. ATHENA, ARTEMIS, HEPHAESTUS: Data Analysis for X-Ray

Absorption Spectroscopy Using IFEFFIT. In *Journal of Synchrotron Radiation*; 2005; Vol. 12.

(44) Inceesungvorn, B.; López-Castro, J.; Calvino, J. J.; Bernal, S.; Meunier, F. C.; Hardacre, C.; Griffin, K.; Delgado, J. J. Nano-Structural Investigation of Ag/Al_2O_3 Catalyst for Selective Removal of O_2 with Excess H_2 in the Presence of C_2H_4. *Appl Catal A Gen* **2011**, *391*, 187–193.

Chapter 7
General Conclusion

In this research, I focused on selective catalytic reduction of nitrogen oxides (NO_x) using NH_3 as the reducing agent (NH_3–SCR) is commercially utilized to control the NO_x emissions from exhausts in the presence of O_2.

Chapters 2 conclude that *In situ/operando* IR, UV–vis, and XAS experiments were performed on the V(V)↔V(IV) and Cu(II)↔Cu(I) redox cycles with V- and Cu-based NH_3–SCR catalysts under similarly transient reaction conditions. The results provide comprehensive evidence for a general mechanism of NH_3–SCR that is common to V and Cu catalysts. Under transient conditions, B-NH_3 was confirmed to be a reservoir of NH_3 that migrates to the metal cation sites and participates in the second reduction half-cycle.

Chapters 3 conclude that steady-state kinetics shows that the SCR of NO_2 or NO/NO_2 mixture is more than two orders of magnitude faster than the SCR of NO over H-AFX zeolite. For NO_2 involved SCR over H-AFX, Brønsted acid sites (BAS) play an essential role, which promote the reaction of the adsorbed NH_3 with NO_2 to yield N_2, H_2O, and adsorbed NH_4NO_3 at low temperatures (50–150 ˚C).

Chapters 4 conclude that the reduction/oxidation half-cycles in the NH_3–SCR over WO_3/CeO_2. Ce^{4+} species is reduced by NO + NH_3 to yield N_2 and Ce^{3+} species (reduction half cycle), which is then is reoxidized by O_2 (oxidation half cycle). The oxidation state of W^{6+} species remains unchanged under the redox conditions. Reduction half cycle and oxidation half cycle over WO_3/CeO_2 under transient reaction conditions were studied using time-resolved *operando* IR, UV-vis, and XAS in combination with the observation of gas-phase products. IR and theoretical results suggest that the reduction half cycle starts with the reaction of W^{6+}-OH and adjacent Ce^{4+}-O with NO to afford Ce^{3+} species and a gaseous HONO, which is converted to NO^+ species on the catalyst. The NO^+ species reacts with NH_3 to yield N_2.

Chapters 5,6 concludes that reversible structural changes between atomic Ag(I) and large Ag metal nanoparticles (NPs) on γ-Al_2O_3-supported Ag (Ag/Al_2O_3) catalysts and anchoring mechanism of Ag species over γ-Al_2O_3 using in situ/operando spectroscopies, electron microscopes, DFT and ab initio thermodynamics studies. Sintering and regeneration of the atomic Ag(I) species are reversibly and leading to recovering of catalytic activity for H_2-assisted NO_x selective catalytic reduction SCR by NH_3 (H_2–NH_3–SCR). We have found that the catalytic activity in H_2–NH_3–SCR is depended on the reversibly degree of dispersion of Ag NPs. The sintering/dispersion phenomena were reversibly observed of redox repeating H_2 ↔ NO + O_2 treatments. we report the relationships between the relative number of anchoring sites (HO-μ_1-Al_{VI}) of Ag/Al_2O_3 and (1) the number of unsaturated Al_{IV}^{3+} sites, (2) sintering resistance of Ag/Al_2O_3, (3) rate of Ag redispersion, and (4)

catalytic activity of Ag/Al_2O_3 which prepared by four types of commercial alumina sources (CTB, PUR, VGL, and CFF). Combined with the two results, the data demonstrate that the HO-μ^1-Al_{VI} site on the (100) surface adjacent to the unsaturated Al_{IV}^{3+} site on the (110) surface at the (100)–(110) step edge is a general model for the anchoring sites of Ag on γ-Al_2O_3.

In summary, using operando spectroscopy and computational science, this thesis provides a molecular-level insight into the NH_3-SCR mechanism of lean de-NOx catalysts and the regeneration mechanism of isolated metal species on the catalyst surface. This thesis proposes a new guideline for the design of reaction fields at the molecular level in the field and makes a significant contribution to catalytic chemistry.

Acknowledgments

I am extremely grateful to all those who helped me to concentrate on the study the Institute for Catalysis at Hokkaido University as a doctoral student.

First of all, I would like to express my deep and sincere gratitude to my research supervisor Prof. Dr. Ken-ichi Shimizu. It was a great privilege to be one of the members of the Catalyst Material Research Division. The two projects of AGS-short-visit program from Hokkaido university and Japanese-Swiss Science and Technology Programme (grant no. JP_EG_04_042021) from ETH zurich have provided me a study abroad opportunity to Paul Scherrer Institute (PSI), Switzerland, which is one of the top institutes on *in situ* spectroscopic study for catalysis. I cannot express thanks to my committee for their support and encouragement: Dr. Davide Ferri and group member of Energy and Environment Research Division. Thank you for the great opportunity.

In addition, thanks to the projects promoted by Research Association of Automobile Internal Combustion Engines (AICE) and the Japan Society for the Promotion of Science (JSPS), Grant no. 21J11913.

Hiroe Kubota